

RESBOS2: PRECISION RESUMMATION FOR THE LHC ERA

By

Joshua Paul Isaacson

A DISSERTATION

Submitted to  
Michigan State University  
in partial fulfillment of the requirements  
for the degree of

Physics—Doctor of Philosophy

2017

# ABSTRACT

## RESBOS2: PRECISION RESUMMATION FOR THE LHC ERA

By

Joshua Paul Isaacson

With the precision of data at the LHC, it is important to advance theoretical calculations to match it. Previously, the ResBos code was insufficient to adequately describe the data at the LHC. This requires an advancement in the ResBos code, and led to the development of the ResBos2 package. This thesis discusses some of the major improvements that were implemented into the code to advance it and prepare it for the precision of the LHC.

The resummation for color singlet particles is improved from approximate NNLL+NLO accuracy to an accuracy of N<sup>3</sup>LL+NNLO accuracy. The ResBos2 code is validated against the calculation of the total cross-section for Drell-Yan processes against fixed order calculations, to ensure that the calculations are performed correctly. This allows for a prediction of the transverse momentum and  $\phi_\eta^*$  distributions for the  $Z$  boson to be consistent with the data from ATLAS at a collider energy of  $\sqrt{s} = 8$  TeV. Also, the effects of choice of resummation scheme are investigated for the Collins-Soper-Sterman and Catani-deFlorian-Grazzini formalisms. It is shown that as long as the calculation of each of these is performed such that the order of the  $B$  coefficient is exactly 1 order higher than that of the  $C$  and  $H$  coefficients, then the two formalisms are consistent. Additionally, using the improved theoretical prediction will help to reduce the theoretical uncertainty on the mass of the  $W$  boson, by reducing the uncertainty in extrapolating the  $\frac{d\sigma}{dp_T^W}$  distribution from the data for the  $\frac{d\sigma}{dp_T^Z}$  distribution by taking the ratio of the theory predictions for the  $Z$  and  $W$  transverse momentum.

In addition to improving the accuracy of the color singlet final state resummation calculations, the ResBos2 code introduces the resummation of non-color singlet states in the

final state. Here the details for the Higgs plus jet calculation are illustrated as an example of one such process. It is shown that it is possible to perform this resummation, but the resummation formalism needs to be modified in order to do so. The major modification that is made is the inclusion of the jet cone-size dependence in the Sudakov form factor. This result resolves, analytically, the Sudakov shoulder singularity. The results of the ResBos2 prediction are compared to both the fixed order and parton shower calculations. The calculations are shown to be consistent for all of the distributions considered up to the theoretical uncertainty. As the LHC continues to increase their data, and their precision on these observables, the ability to have analytic resummation calculations for non-color singlet final states will provide a strong check of perturbative QCD.

Finally, the calculation of the terms needed to match to N<sup>3</sup>LO are done in this work. Once the results become sufficiently publicly available for the perturbative calculation, the ResBos2 code can easily be extended to include these corrections, and be used as a means to predict the total cross-section at N<sup>3</sup>LO as well.

Dedicated to: My parents and Laurel DiPucchio.

## ACKNOWLEDGMENTS

Throughout the process of obtaining my Ph.D, there have been many influential people to help me along the way. My thanks goes to all of you who have helped me along the way to achieve my dream of becoming a physicist.

My parents have played an important role in helping me to learn all of the skills I would need to be successful in school from an early age. Additionally, they have always been there for me in times of struggle throughout my education. I would not have been able to make it through graduate school without them.

Also, Laurel DiPucchio has been a great support in my times of struggle throughout this process. I know that I have caused her so much stress with this work, and I couldn't be more thankful to have her with me throughout this journey. I am thankful for all the sacrifices she has made for me and continues to make for me.

I would also like to thank my thesis advisor, C.-P. Yuan, for giving me the tools needed to perform this research, and as a guiding hand throughout. The main discussions that we have had over the years has helped to develop me as a physicist, and taught me how to approach complex research questions in a way to make them less daunting. C.-P.'s guiding idea that his Ph.D students should teach him something new by the end of their work, has really helped me to understand the topics that are presented in this thesis to the depth that I now do, along with many other topics that I have learned along the way. His dedication to always learning new ideas being presented in the community, and to develop my skills in such a way to provide a needed insight into the world of physics has become my guiding principle as I move forward in my career.

In addition to C.-P., I would like to acknowledge the help from the rest of the professors

in the High Energy Group at MSU. Specifically, Wade Fisher, Joey Huston, Carl Schmidt, Wayne Repko, Andreas von Manteuffel, and Chip Brock, for their discussions of physics topics throughout my career at MSU. Wade always had an open door to come and discuss topics with, and his knowledge of statistics has been invaluable to me. Joey Huston has always made sure that I know what is going on in the community that I can contribute to, and has helped me to understand the way experimentalists think about the same problems I am trying to tackle. This has allowed me to approach the problems, and the solutions in a way that benefits not only the theorists, but are also helpful to experimentalists. Carl Schmidt has always been available to discuss the details of calculations with when I would get stuck on some of the more technical details. Wayne Repko was always interested to learn about the status of my work, and to provide thought provoking questions to myself and officemates that really made us think about the underlying physics. While Andreas von Manteuffel arrived late in my career, his helpful discussions since his arrival has helped me to understand the complexities of higher loop calculations, and has given me many interesting directions of research as I begin my post doctoral career. Finally, Chip Brock has been paramount in helping me develop my communication skills with experimentalists throughout our discussions over the intricate details of Parton Distribution Functions and their need to be improved for the precision of the LHC.

My coworkers throughout my time at MSU have been a valuable resource in terms of learning what is happening in the field, outside my immediate focus. I would especially like to thank Kirtimaan Mohan, Jan Winter, and Chris Willis. Kirtimaan has always provided advice when I would be struggling with my own research, and also helped me to learn about effective field theories and developing Beyond the Standard Model theories to understand the anomalies found at the LHC. Chris was the experimentalist who I had the most discussions

with, and without him I would not have the same level of appreciation for the work the experimentalists in this field do that I now have. Finally, Jan has been helpful in terms of helping me to work through different difficult situations that have arisen while trying to get my Ph.D. He always has ideas on things to look into, and is always willing to help look into the setup of the numerical calculations to make sure everything comes out correctly. His help with getting the Sherpa predictions throughout this work has been invaluable.

Finally, I would like to thank Kim Crosslan and Brenda Wenzlick for being the amazing people that they are. Both of them have been helpful in navigating the bureaucracy of MSU and the wider physics community,

# TABLE OF CONTENTS

<b>LIST OF TABLES</b> . . . . .	<b>xi</b>
<b>LIST OF FIGURES</b> . . . . .	<b>xii</b>
<b>Chapter 1 Standard Model</b> . . . . .	<b>1</b>
1.1 Electroweak . . . . .	4
1.1.1 Higgs Mechanism . . . . .	7
1.1.2 Broken Electroweak Sector . . . . .	12
1.1.3 Electroweak Precision Observables . . . . .	16
1.1.4 Electroweak Parameters . . . . .	19
1.2 Renormalization and Regularization . . . . .	20
1.3 Quantum Chromodynamics . . . . .	25
1.3.1 Introduction . . . . .	25
1.3.2 Asymptotic Freedom and Confinement . . . . .	28
1.3.3 Soft and Collinear QCD . . . . .	32
1.3.4 Factorization . . . . .	33
<b>Chapter 2 Experimental Measurements</b> . . . . .	<b>44</b>
2.1 Basic Concepts . . . . .	44
2.2 Detecting Particles . . . . .	46
2.2.1 Trackers . . . . .	47
2.2.2 Electromagnetic Calorimeters . . . . .	49
2.2.3 Hadronic Calorimeters . . . . .	50
2.2.4 Muon Spectrometers . . . . .	51
2.3 Physics Objects . . . . .	53
2.3.1 Jets . . . . .	53
2.3.1.1 B-Tagging . . . . .	54
2.3.2 Leptons . . . . .	55
2.3.3 Missing Transverse Energy . . . . .	56
<b>Chapter 3 Resummation</b> . . . . .	<b>58</b>
3.1 Collins-Soper Frame . . . . .	59
3.2 Fixed-Order Calculations . . . . .	63
3.2.1 Real Corrections . . . . .	66
3.2.2 Virtual Correction . . . . .	68
3.3 NLO DY Total Cross-Section . . . . .	69
3.3.1 Breakdown of Fixed-Order . . . . .	73
3.4 Resummation Formalisms . . . . .	74
3.4.1 Collins-Soper-Sterman Formalism . . . . .	79
3.4.2 Catani-deFlorian-Grazzini Formalism . . . . .	80



3.4.3	Comparison of CSS to CFG . . . . .	82
3.4.4	Non-Perturbative Contribution . . . . .	83
3.5	The Asymptotic Piece and Obtaining Fixed-Order Cross-Sections from Re- summed Results . . . . .	90
3.5.1	$\mathcal{O}(\alpha_s)$ Singular, Asymptotic Piece, and NLO Result . . . . .	94
3.5.2	$\mathcal{O}(\alpha_s^2)$ Singular, Asymptotic, and the NNLO Total Cross-Section . . . . .	97
3.6	Scale Dependence . . . . .	101
<b>Chapter 4</b>	<b><math>Z</math> Boson Resummed Predictions . . . . .</b>	<b>105</b>
4.1	$Z$ $p_T$ Distribution . . . . .	105
4.2	$Z$ $\phi_\eta^*$ Distribution . . . . .	110
4.3	Angular Functions . . . . .	113
<b>Chapter 5</b>	<b><math>W</math> Mass . . . . .</b>	<b>119</b>
5.1	SM EW Precision Fit . . . . .	119
5.2	Experimental Measurement . . . . .	122
5.3	ResBos2 Results . . . . .	125
<b>Chapter 6</b>	<b>Color Singlet Boson Plus Jet Resummation at Hadron Colliders</b>	<b>128</b>
6.1	Higgs Plus Jet Resummation . . . . .	129
6.1.1	Virtual Corrections . . . . .	130
6.1.2	Jet Corrections . . . . .	133
6.1.3	Collinear Corrections . . . . .	134
6.1.4	Soft Corrections . . . . .	134
6.1.5	Total Real Correction . . . . .	140
6.1.6	Resummation Calculation . . . . .	142
6.1.7	Results . . . . .	146
6.1.7.1	Comparison to Fixed Order . . . . .	147
6.1.7.2	Comparison to Parton Showers . . . . .	149
6.1.8	Future of Higgs Plus Jet Resummation . . . . .	155
<b>Chapter 7</b>	<b>Conclusion . . . . .</b>	<b>158</b>
7.1	Color Singlet Resummation . . . . .	159
7.1.1	Resummation Schemes . . . . .	159
7.1.2	$Z$ Boson Predictions . . . . .	159
7.1.3	$W$ Boson Predictions . . . . .	160
7.2	Non-Color Singlet Resummation . . . . .	161
7.3	Final Remarks . . . . .	162
<b>APPENDICES . . . . .</b>		<b>163</b>
APPENDIX A	The Dirac Equation and $\gamma$ Matrices . . . . .	164
APPENDIX B	Spin, Helicity, and Chirality . . . . .	167
APPENDIX C	Standard Model Higgs Boson and Higgs Mechanism . . . . .	169
APPENDIX D	Structure of $SU(3)$ . . . . .	172
APPENDIX E	QCD Feynman Rules . . . . .	173

APPENDIX F Calculation Details . . . . .	191
APPENDIX G Higgs Plus Jet Resummation Calculation Details . . . . .	218
<b>BIBLIOGRAPHY . . . . .</b>	<b>220</b>

## LIST OF TABLES

Table 1.1: Standard Model of Particle Physics . . . . .	3
Table 1.2: Electroweak quantum number for the first family of fermions . . . . .	17
Table 1.3: The current best fit results for the $S, T, U$ parameters, along with their uncertainties and correlation coefficients. Reproduced from [1] . . . . .	18
Table 2.1: Representative cross section scales (cross sections are not exact). Reproduced from Ref. [2] . . . . .	45
Table 3.1: The organization of fixed-order and resummed calculations. Going across a row is the fixed-order calculation included at a given order of $\alpha_s$ , while going down the columns is the resummed calculation up the the given power of the logs included. . . . .	58
Table 3.2: The non-perturbative functions parameters fitting results. Here, $N_{fit}$ is the fitted normalization factor for each experiment. . . . .	86
Table 3.3: Total inclusive NLO Drell-Yan Cross-sections for $66 \text{ GeV} < M_{ll} < 116 \text{ GeV}$ . MCFM calculation using version 8.0 [3]. FEWZ calculation using version 3.1_rc [4] . . . . .	97
Table 3.4: Total inclusive NNLO Drell-Yan Cross-sections for $66 \text{ GeV} < M_{ll} < 116 \text{ GeV}$ . MCFM calculation using version 8.0 [3]. FEWZ calculation using version 3.1_rc [4] . . . . .	101
Table 5.1: Electroweak fit. The fourth column gives the fit results without using any experimental or phenomenological estimate for the parameter when performing the fit. The fifth column is the same as the fourth, but ignores all theory uncertainties. The table is reproduced from Ref. [5]. . . . .	121
Table 5.2: The values are reported in GeV, and taken from Ref. [5] . . . . .	121
Table F.1: Table of the results of calculating the area of a $d$ -Sphere . . . . .	196

## LIST OF FIGURES

Figure 1.1:	The two different scenarios for the value of $\mu^2$ . . . . .	8
Figure 1.2:	The best fit in the $TS$ plane with $U$ free to float on the left and $U$ fixed to zero on the right. Additionally, $m_H = 126$ GeV and $m_t = 173$ GeV in this fit. Reproduced from [1] . . . . .	19
Figure 1.3:	An example of a loop diagram, $p_1$ , $p_2$ , and $p_3$ are the momentums of the external particles, and $k$ is the momentum of the loop. . . . .	21
Figure 1.4:	The first order correction to the strong coupling constant can be calculated from this vertex correction diagram. . . . .	29
Figure 1.5:	The comparison between the theoretical calculation of the strong coupling compared to experimental data. The plot is reproduced from Ref. [6] . . . . .	32
Figure 1.6:	Electron scattering off of a proton with an energy of 188 MeV. Results show data is inconsistent with a point-like proton. Reproduced from [7]. . . . .	33
Figure 1.7:	Depiction of the $F_2$ proton structure function, showing Bjorken scaling. This was the motivation for the parton model proposed by Richard Feynman. Plot is reproduced from [8]. . . . .	34
Figure 1.8:	Test of the Callan-Gross relation, with $K_0 = F_2/(2xF_1) - 1$ . Results are consistent with spin-1/2 predictions. Reproduced from [9]. . . . .	36
Figure 1.9:	The splitting kernels that occur at $\alpha_s$ . Note that to obtain the missing kernels, take fermions to anti-fermions and vice-versa. . . . .	37
Figure 1.10:	Plots of the CT14 NNLO Parton Distributions at 2 GeV (left) and 100 GeV (right). The plots are reproduced from Ref. [10] . . . . .	40
Figure 1.11:	(a) Anti- $k_t$ algorithm. (b) $k_t$ Algorithm. (c) Cambridge-Aachen algorithm. Reproduced from Ref. [11] . . . . .	43
Figure 2.1:	Depiction of particles traveling through the CMS Detector. Reproduced from Ref. [12] . . . . .	46
Figure 2.2:	Fractional energy loss per radiation length in lead as a function of electron or positron energy. Reproduced from Ref. [6] . . . . .	50

Figure 2.3:	Performance curves obtained for different $b$ -tagging algorithms using simulated data. (Left) The mis-identification for light jets. (Right) The mis-identification for $c$ jets. Plots are reproduced from Ref. [13] . . . . .	55
Figure 3.1:	Depiction of the Collins-Soper Frame. Reproduced from [14]. . . . .	60
Figure 3.2:	The diagrams that contribute to the $\alpha_s$ correction to Drell-Yan. (a) is the born diagram. (b) is the virtual coupling correction. (c) is the wave function correction. (d) and (e) are the real corrections . . . . .	64
Figure 3.3:	Plot showing fixed-order versus resummed predictions. The dashed curves correspond to fixed-order calculations, and the solid curves correspond to resummed predictions. The plot is reproduced from Ref. [15] . . . . .	73
Figure 3.4:	A diagrammatic representation of the factorized cross-section for Drell-Yan, broken into a soft, collinear, and hard factor. The soft factor is labeled by the $S$ , the collinear factors are labeled by the $C$ 's, and the hard factor is labeled by the $H$ . . . . .	75
Figure 3.5:	Fit to the differential cross section for Drell-Yan lepton pair production in hadronic collisions from E288 Collaboration [16]. . . . .	87
Figure 3.6:	Fit to the Drell-Yan data from the E605 Collaboration [17]. . . . .	88
Figure 3.7:	Fit to the Drell-Yan data from the R209 Collaboration [18]. . . . .	88
Figure 3.8:	Fit to the Tevatron Run I data from the CDF and D0 Collaborations [19, 20]. The fits include only the $A^{(1,2)}$ , $B^{(1,2)}$ , and $C^{(1)}$ contributions. . . . .	89
Figure 3.9:	Fit to the Tevatron Run II data from the CDF and D0 Collaborations [21, 22]. . . . .	89
Figure 3.10:	Comparison of the SIYY1 and SIYY2 fit to the ATLAS data. . . . .	89
Figure 3.11:	$\Delta\chi^2$ distribution scanning $g_2$ parameter in SIYY1 fit (left), and $\Delta\chi^2$ distribution scanning $g_2$ parameter in SIYY2 fit (right). . . . .	90
Figure 4.1:	Comparison of $p_T^{ll}$ data from ATLAS compared to ResBos predictions, reproduced from Ref. [23] . . . . .	106
Figure 4.2:	Comparison of the ResBos2 calculation with a scale choice of $\mu^2 = M_{ll}^2 + p_T^2$ to the ATLAS data given in Ref. [23], focusing on the high transverse momentum region . . . . .	107

Figure 4.3: Comparison of the CSS and CFG formalisms, focusing on only the small transverse momentum, and not including the $Y$ -piece. . . . .	108
Figure 4.4: Comparison of the fixed order piece up to $\mathcal{O}(\alpha_s^2)$ to the asymptotic piece up to $\mathcal{O}(\alpha_s^2)$ . The cutoff on the transverse momentum of both calculations is set to 2 GeV. . . . .	108
Figure 4.5: Comparison of the Asymptotic piece to $\mathcal{O}(\alpha_s^3)$ to the N <sup>3</sup> LL resummed piece. . . . .	109
Figure 4.6: Comparison of both the CSS(left) and CFG(right) prediction to data. The PDF and scale uncertainty is given by the error bands. The lighter error band is the PDF uncertainty, and the darker error band is the combination of the scale and PDF uncertainty. . . . .	109
Figure 4.7: Comparison of the fixed order calculation of $Z$ +jet to NNLO compared to the ATLAS data. Reproduced from [24]. . . . .	111
Figure 4.8: The frame definition for $\phi_\eta^*$ , reproduced from [25]. . . . .	111
Figure 4.9: Comparison of $\phi_\eta^*$ data from ATLAS compared to ResBos predictions, reproduced from Ref. [23] . . . . .	112
Figure 4.10: Comparison of both the CSS(left) and CFG(right) prediction to data. The PDF and scale uncertainty is given by the error bands. The lighter error band is the PDF uncertainty, and the darker error band is the combination of the scale and PDF uncertainty. . . . .	113
Figure 4.11: Comparison of the fixed order calculation of $Z$ +jet to NNLO compared to the ATLAS data. Reproduced from [24]. . . . .	114
Figure 4.12: The predictions for $A_2 - A_0$ for the DYNNLO code [26], at NLO and NNLO. Reproduced from [27]. . . . .	116
Figure 4.13: Theoretical prediction from the ResBos2 program for the angular coefficients of $A_0$ , $A_2$ , $A_4$ , and the breaking of the Lam-Tung Relationship for the CSS Scheme. The lighter error band is the PDF uncertainty, and the darker error band is the combination of the scale and PDF uncertainty. . . . .	117
Figure 4.14: Theoretical prediction from the ResBos2 program for the angular coefficients of $A_0$ , $A_2$ , $A_4$ , and the breaking of the Lam-Tung Relationship for the CFG Scheme. The lighter error band is the PDF uncertainty, and the darker error band is the combination of the scale and PDF uncertainty. . . . .	118

Figure 5.1:	Results of the EW Fit, reproduced from Ref. [5] . . . . .	123
Figure 5.2:	The ratio of the normalized transverse momentum distributions of the $W$ boson to the $Z$ boson. . . . .	126
Figure 5.3:	An example of the $\chi^2$ distribution for an error set, others are similar to this. The central input mass was $M_W = 80.358$ GeV. The minimum here occurs around 80.372, a shift of 14 MeV. . . . .	127
Figure 6.1:	Feynman diagrams for the gluon-gluon scattering channel to a Higgs Boson.	135
Figure 6.2:	Rapidity dependence of the hard factor for Higgs+Jet for different scale choices . . . . .	146
Figure 6.3:	The differential cross sections of Higgs boson plus one jet production at the LHC as functions of the total transverse momentum $q_\perp$ (left) and the Higgs boson transverse momentum $P_{H\perp}$ (right). The resummation predictions (resum) with resummation scale set to be $P_{J\perp}$ (black line) and $Q$ (green line) respectively are compared to the LO result from MCFM (pink line) with non-zero $q_\perp$ , and the NLO result from MCFM (red line) which is the production rate of Higgs boson plus two separate jets up to one-loop in QCD. . . . .	148
Figure 6.4:	The central predictions(left panel) and with theoretical uncertainties (right panel) for the inclusive jet multiplicities as predicted by fixed-order calculations, resummed calculations, NNLO and NLO Monte Carlos. The bottom panel is divided up into three subplots all showing the ratios with respect to the POWHEG NNLOPS prediction. The upper of these plots contains the HEJ and SHERPA NNLOPS ratios, while the middle one includes all NLO merged predictions ( <b>Madgraph5_aMC@NLO</b> , <b>Herwig 7.1</b> and <b>SHERPA</b> ) and the lower one shows all those listed in the bottom left legend of the main panel. Reproduced from [28]. . . . .	151
Figure 6.5:	The Higgs boson transverse momentum in the presence of at least one jet central predictions(left) with uncertainty bands(right). The ratio plot panel is divided into six parts where the upper four exhibit the ratios to the POWHEG NNLOPS result while the lower two show them to the NLO calculation for $h + 1$ jet as provided by GOSAM+SHERPA. Reproduced from [28]. . . . .	152

Figure 6.6:	The leading jet transverse momentum distribution for $h + \geq 1$ -jet production, to the right (left) shown with (without) the uncertainty bands provided by the various calculations. The part below the main plot contains four ratio plots taken wrt. the NNLO result of the BFGLP group following the same strategy for grouping the predictions as before (NNLOPS versus NLO ME+PS versus fixed-order and resummation results). Reproduced from [28]. . . . .	153
Figure 6.7:	The rapidity distribution for the leading jet in $h + \geq 1$ -jet production, shown without (left) and with (right) theoretical uncertainties. Ratio plots are displayed in the lower part of the plot using the POWHEG NNLOPS result for Higgs boson production as their reference. Predictions are grouped, from top to bottom, according to the categories NNLOPS, ME+PS at NLO and NLO fixed order as well as resummation. Reproduced from [28]. . .	154
Figure 6.8:	The transverse momentum of the Higgs-boson-leading-jet system in the presence of at least one jet. For better visibility, results are shown without (left) and with (right) theoretical uncertainties. The plot layout exactly corresponds to that of Figure 6.7, except for the extended $\hat{y}$ -axis range in the ratio plots. Reproduced from [28]. . . . .	156
Figure 6.9:	Normalized distributions of the vector boson fusion and gluon-fusion contributions to the Higgs boson plus two jets production in the typical kinematics at the LHC with $\sqrt{S} = 13TeV$ , where the jet transverse momenta $k_{1\perp} = k_{2\perp} = 30GeV$ , $y_{j1} = -y_{j2} = 2$ and $y_h = 0$ : as functions of the total transverse momentum $q_{\perp}$ (left); the total rate as function of the upper limit of $q_{\perp}$ (right). Reproduced from [29]. . . . .	157
Figure F.1:	The hadronic virtual correction Feynman Diagram to Drell-Yan at NLO.	193
Figure F.2:	Multiplicity distribution as function of transverse momentum in semi-inclusive hadron production in deep inelastic scattering compared to the experimental data from HERMES Collaboration at $Q^2 = 3.14GeV^2$ . . . .	203
Figure F.3:	Connection of a soft/collinear gluon between two colored particles. . . .	214



# Chapter 1

## Standard Model

The Standard Model (SM) of Particle Physics is almost a complete description of all of the phenomena observed in high energy physics, including interactions of the strong and electroweak forces. With the discovery of the Higgs Boson on July 4th, 2012 [30, 31, 32], the standard model is now complete. Although experimental data appears to agree with the SM quite precisely, there are certain phenomena that cannot be explained in the framework of the SM (such as gravity [33], dark matter [34, 35, 36], neutrino masses [37], and the matter-antimatter asymmetry [38]). Additionally, there are some problems that arise from a theoretical standpoint, such as the hierarchy problem [39, 40] and the strong CP problem [41]. Therefore, the SM is anticipated to be an effective theory of some complete higher energy theory. The precision of agreement between the experimental results and theoretical predictions forces the discovery of any new physics to either be through searches at high energies or through the study of small effects on specific observables. To study small effects on observables requires precise experimental measurements. Observables that can be measured precisely and that are sensitive to the parameters of the SM are considered precision observables. One such observable is the  $g - 2$  of the electron, which is currently measured to a precision of  $\approx 10^{-13}$  and calculated theoretically to a similar precision. Despite the success of the SM, there are many unanswered questions pertaining to particle physics, such as the exact nature of the Higgs Boson, and what new physics can explain dark matter. In

order to search for new physics, the parameters of the SM must be measured as precisely as possible and any deviations from the expected value will hint at the presence of new physics.

Calculational accuracy of the SM can be improved in either of two forces: the electroweak force, which unifies both the weak and electromagnetic forces (details can be found in Section 1.1), and the strong force (details can be found in Section 1.3). These predictions are calculated using Quantum Field Theory (QFT). QFT is a mathematical framework based on the physically motivated assumptions that the theory incorporates Poincare invariance, point-particles, local interactions (no actions at a distance), causality, unitarity (the quantum mechanical evolution conserves probability), and is free of divergences (also known as a renormalizable theory) [42]. These restrictions define the underlying principles of the standard model.

The standard model is traditionally expressed via the Lagrangian formalism, in which all physical interactions are encoded into a Lagrangian. The form of the Lagrangian, is determined by demanding the Lagrangian be invariant under a set of local symmetries. These symmetry transformations correspond to locally conserved quantities as detailed by Noether's Theorem [43]: Noether's theorem states that for each symmetry of the Lagrangian there is a corresponding conserved quantity of the form,

$$\frac{\partial \mathcal{L}}{\partial \dot{q}_\alpha} \gamma_\alpha, \tag{1.1}$$

where  $\mathcal{L}$  is the Lagrangian density,  $\dot{q}_\alpha$  is the time derivative of a coordinate, and  $\gamma_\alpha$  is some function (note the use of Einstein summation notation). Through Noether's theorem, quantities that are experimentally conserved are used to introduce symmetries of the SM Lagrangian and greatly constrain its form. The SM symmetries are the Poincare symmetry,

Fermions			Bosons
First Generation	Second Generation	Third Generation	
$u$	$c$	$t$	$\gamma$
$d$	$s$	$b$	$g$
$e$	$\mu$	$\tau$	$W^\pm, Z$
$\nu_e$	$\nu_\mu$	$\nu_\tau$	H

Table 1.1: Standard Model of Particle Physics

$SO(3, 1)$ , and the gauge symmetries  $SU(3)_C \times SU(2)_L \times U(1)_Y$ . Generally, a gauge symmetry is a symmetry that is space-time dependent, or local. Gauge symmetries are responsible for all of the SM forces and as such can be broken into two groups: the  $SU(2)_L \times U(1)_Y$  gauge groups generate the electroweak force, while the  $SU(3)$  gauge group generates the strong force.

In addition to the gauge symmetries that define the forces of the standard model, the fermionic content of the standard model needs to be introduced by hand, but must still obey the symmetries of the standard model. Therefore, for a particle to interact with the gauge field it must be in a non-singlet representation of the group, or in other words, has to have a special transformation property under the group symmetry<sup>1</sup>. The full particle content of the standard model can be found in Table 1.1. The details for the electroweak sector can be found in the following section (Sec. 1.1), and the details of the strong force can be found in the section on QCD (Sec. 1.3).

The following sections discuss the Electroweak sector and the QCD sector of the SM. Additionally, in the Electroweak section the Higgs Boson and spontaneous symmetry breaking is discussed. The symmetry groups that make up the SM will be discussed, along with the experimental evidence that supports these observations through the discussion of conserved

---

<sup>1</sup>In the SM outside of the gauge fields and the Higgs boson, all other particles are fermions. Details of the equation of motion for fermions can be found in App. A.

quantities as described in Noether's theorem.

## 1.1 Electroweak

The electroweak force is the unification of the electromagnetic force, and the weak nuclear force. The quantum description of electromagnetism (QED) arose in the 1920s and 1930s, through work by Dirac, Pauli, Heisenberg, and Fermi [44, 45, 46, 47]. One of the major accomplishments in QED was the calculation of the electron gyromagnetic ratio, known as  $g-2$ . Currently, the most accurate measurement was done by Hanneke et. al. [48], obtaining a value of  $g/2 = 1.00115965218073(28)$ . This is consistent with the theoretical prediction given as:  $g/2 = 1.00115965218182(6)(4)(2)(78)$ , where the uncertainties in the theoretical prediction, arise from the eighth order QED correction, tenth order QED correction, Hadronic Electroweak corrections, and the Atomic Physics determination of  $\alpha$ , respectively [49].

In 1896, Henri Becquerel discovered  $\beta$ -decay [50], based off of the penetration of the decays through material. In modern language,  $\beta$  decay is the process in which a proton turns into a neutron and emits a positron and a neutrino. This phenomenon is unable to be explained in QED, and thus a new theory was needed to explain it. At first, Fermi developed the four point interaction to describe  $\beta$ -decays, and introduced a new particle known as the neutrino, in order to conserve momentum [51]. In the 1970s, Weinberg, Glashow, and Salam developed a theory that could explain both QED and  $\beta$  decay through a single theory, the Electroweak theory [52, 53, 54]. In addition, it predicted that  $\beta$  decay is mediated by a  $W$  boson, and further predicted the existence of a massive neutral gauge boson,  $Z$ . The first evidence of the neutral current in this theory was discovered by the Gargamelle collaboration in 1973 in neutrino scattering [55]. The direct detection of the  $W$  and  $Z$

bosons was first done by the UA1 and UA2 collaborations in 1983 at the Super Proton Synchrotron [56, 57, 58, 59]. Finally, 't Hooft and Veltman showed that the Electroweak theory is renormalizable in 1972 [60]. The discussion that follows explains the theory that was proposed, along with the definition of renormalizable.

Any fermion can be described by the direction of its spin in relation to the direction of its momentum. If its spin is parallel to its momentum, then the particle is said to be right-handed, and if its spin is anti-parallel to its momentum then the particle is left-handed<sup>2</sup>. The electroweak (EW) sector of the standard model is described by the gauge symmetries of  $SU(2)_L \times U(1)_Y$ . Experimentally, it was discovered that the weak force ( $\beta$ -decay for example) only interacts with left-handed particles. Secondly, the  $U(1)_Y$  gauge group interacts with a particle's hypercharge. The  $SU(2)_L$  group has three gauge mediating bosons,  $W^i$  where  $i = 1, 2, 3$ , and the  $U(1)_Y$  group has one gauge mediating boson,  $B$ .

To understand how the gauge bosons interact with the fermions, consider how the infinitesimal gauge transformations affect the fermions. Namely,

$$\delta\psi_{L,R} = \left( igT_i\theta_i(x) + ig'\frac{Y}{2}\theta(x) \right) \psi_{L,R}, \quad (1.2)$$

where  $g$  and  $g'$  are the gauge couplings,  $T_i$  and  $Y$  are the generators of for  $SU(2)_L$  and  $U(1)_Y$  respectively, and  $\theta_i(x)$  and  $\theta(x)$  are space-time dependent transformation variables.

The commutators for the two groups are given by:

$$[T_i, T_j] = i\epsilon^{ijk}T_k, \quad (1.3)$$

$$[T_i, Y] = 0 \quad \text{for all } i, \quad (1.4)$$

---

<sup>2</sup>For more details on spin and the difference between spin and helicity one can reference Appendix B

where  $\epsilon^{ijk}$  is the fully anti-symmetric tensor in three dimensions, and  $T_i = \sigma_i/2$ , where  $\sigma_i$  are the two dimensional Pauli matrices. A Lagrangian composed of fermionic fields that remains invariant under this transformation rule is:

$$\mathcal{L}_f = i\bar{\psi}\not{D}\psi, \quad (1.5)$$

where  $\psi$  is the fermionic field,  $\bar{\psi} = \psi^\dagger\gamma^0$ ,  $\not{D} = \gamma^\mu D_\mu$ , and  $D$  is the covariant derivative which is defined in such a way to maintain the gauge invariance. The covariant derivative for the electroweak sector is:

$$D_\mu = \partial_\mu - igP_L T_i W_\mu^i - ig'\frac{Y}{2}B_\mu. \quad (1.6)$$

In addition to dynamical fermionic terms, the SM Lagrangian also requires dynamical bosonic terms. The gauge bosons transform under the adjoint representation of the gauge groups, according to:

$$\delta W_\mu^i = \partial_\mu\theta^i(x) - g\epsilon^{ijk}\theta^j(x)W_\mu^k, \quad (1.7)$$

$$\delta B_\mu = \partial_\mu\theta(x). \quad (1.8)$$

The kinetic term for the gauge bosons (which is invariant under the above transformations) is given as:

$$\mathcal{L}_V = -\frac{1}{4}B^{\mu\nu}B_{\mu\nu} - \frac{1}{4}W^{i\mu\nu}W_{i\mu\nu}, \quad (1.9)$$

where  $B^{\mu\nu}$  and  $W^{i\mu\nu}$  are known as the field strength tensors given by:

$$B^{\mu\nu} = \partial^\mu B^\nu - \partial^\nu B^\mu, \quad (1.10)$$

$$W^{i\mu\nu} = \partial^\mu W^{i\nu} - \partial^\nu W^{i\mu} + g\epsilon^{ijk}W^{j\mu}W^{k\nu}. \quad (1.11)$$

Because  $SU(2)_L$  is non-Abelian, the  $W$ -boson kinetic Lagrangian contains self-interaction terms. Additionally, the interaction Lagrangian between fermions and these gauge fields is given by:

$$\mathcal{L}_{\text{int}} = -\frac{g'}{2}\bar{\psi}_R Y_R \not{B} \psi_R - \bar{\psi}_L \left( \frac{g' Y_L}{2} \not{B} + \frac{g}{2} \vec{T} \cdot \vec{W} \right) \psi_L, \quad (1.12)$$

where  $\bar{\psi}_{L/R}$  and  $\psi_{L/R}$  are the left and right handed fermion wavefunctions,  $Y_{R/L}$  is the right- and left-handed hypercharge respectively.

However, these gauge bosons are all massless. Introducing a mass term by hand explicitly breaks the gauge symmetry. This issue is resolved through the use of the Higgs Mechanism and spontaneous symmetry breaking.

### 1.1.1 Higgs Mechanism

The Higgs Mechanism is a means of breaking spontaneously the Electroweak  $SU(2)_L \times U(1)_Y$  gauge symmetry, and through which massless gauge fields and massless Nambu-Goldstone bosons combine to produce massive bosons [61, 62, 63, 64]. To illustrate this mechanism, consider a  $U(1)$  gauge example.

A symmetry can be spontaneously broken by simply adding a complex scalar field ( $\Phi$ ),

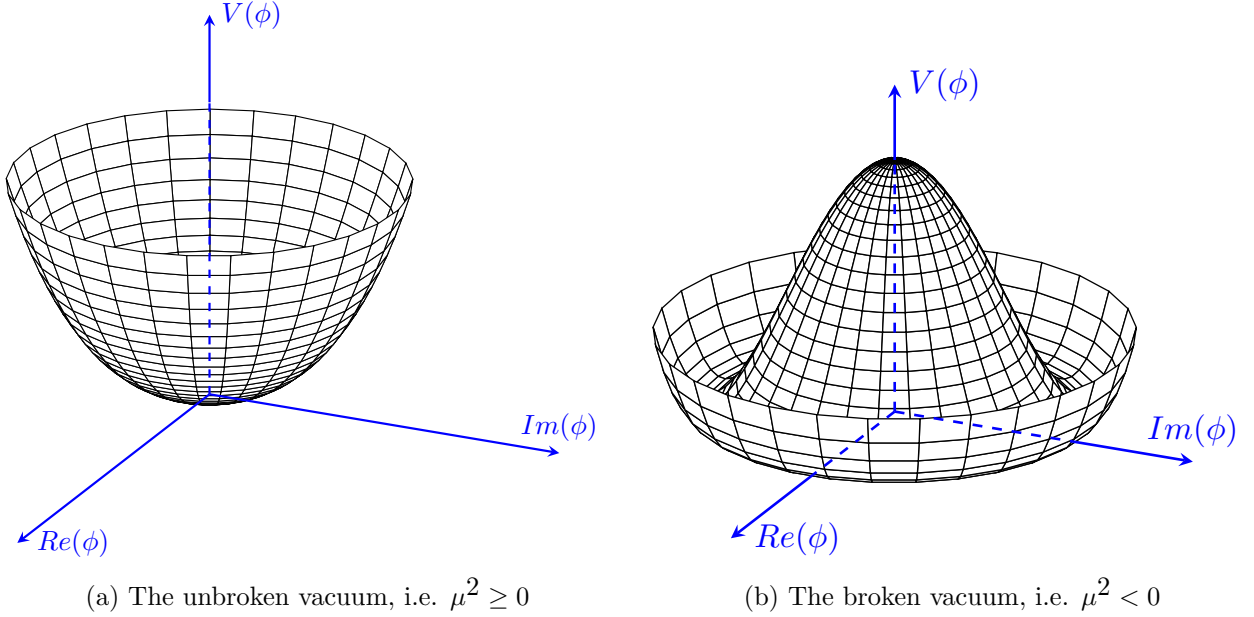


Figure 1.1: The two different scenarios for the value of  $\mu^2$

with a Lagrangian given by:

$$\mathcal{L} = (\partial_\mu \Phi)^\dagger \partial^\mu \Phi - \mu^2 |\Phi|^2 - \lambda |\Phi|^4. \quad (1.13)$$

The physical interpretation of this Lagrangian depends on the sign of  $\mu^2$ . When  $\mu^2 > 0$ , the symmetry remains unbroken. The classical potential of this case is illustrated in Fig. 1.1a. The minimum of the vacuum state occurs at the origin and furthermore, the Lagrangian expanded around small oscillations of the minimum reproduces Eq. 1.13. However, when  $\mu^2 < 0$ , the minimum of the vacuum is no longer unique as shown in Fig. 1.1b, with a minimum given by:

$$\langle \Phi^2 \rangle_0 = -\frac{\mu^2}{2\lambda} e^{i\theta} = \frac{\nu^2}{2} e^{i\theta}, \quad (1.14)$$

where  $\theta$  is any real number, for simplicity  $\theta$  will be taken to be zero. The  $U(1)$  degeneracy of this minima reflects the  $U(1)$  symmetry of the initial Lagrangian. Defining a shifted field:



$$\Phi' = \Phi - \langle \Phi \rangle_0 = \frac{\eta + i\xi}{\sqrt{2}}, \quad (1.15)$$

the Lagrangian takes the form of:

$$\mathcal{L} = \frac{1}{2}(\partial_\mu \eta)(\partial^\mu \eta) + \frac{1}{2}(\partial_\mu \xi)(\partial^\mu \xi) + \mu^2 \left( \frac{\eta^4}{4\nu^2} + \frac{\eta^3}{\nu} + \frac{\eta^2 \xi^2}{2\nu^2} + \eta^2 + \frac{\eta \xi^2}{\nu} + \frac{\xi^4}{4\nu^2} - \frac{\nu^2}{4} \right) \quad (1.16)$$

and looking at small oscillations about the minimum of the potential (keeping terms that are quadratic in the fields), the following Lagrangian is obtained:

$$\mathcal{L}_{SO} = \frac{1}{2}(\partial_\mu \eta \partial^\mu \eta + 2\mu^2 \eta^2) + \frac{1}{2} \partial_\mu \xi \partial^\mu \xi, \quad (1.17)$$

plus a constant term. There are two particles in the Lagrangian, one of which is massless ( $\xi$ ), and one which has a mass given by  $m_\eta = -2\mu^2 > 0$ . The  $\xi$  particle is called a Nambu-Goldstone Boson(NGB), and the general outcome is known as the Goldstone phenomenon [62, 65]. In general, there exists one NGB for each broken generator of the original symmetry group. As such, when applied to the Standard Model, the breaking of symmetry groups of  $SU(2)_L \times U(1)_Y$  to  $U(1)_Q$  will generate three NGBs.

The appearance of NGBs during the Higgs Mechanism significantly impacts the massless gauge fields. For simplicity, consider the  $U(1)$  example again, but now extend the Lagrangian with a gauged  $U(1)$  symmetry:

$$\mathcal{L} = |D^\mu \Phi|^2 - \mu^2 |\Phi|^2 - \lambda |\Phi|^4 - \frac{1}{4} F^{\mu\nu} F_{\mu\nu}, \quad (1.18)$$

where  $\Phi = \frac{\phi_1 + i\phi_2}{\sqrt{2}}$  is a complex scalar field,  $D^\mu$  is the covariant derivative as defined pre-

viously, and  $F^{\mu\nu}$  is the field strength tensor for a  $U(1)$  symmetry as defined in Eqs. 1.9, 1.10. Consider when  $\mu^2 < 0$ . In this case, the absolute minimum corresponds to the vacuum expectation value given as:

$$\langle |\Phi|^2 \rangle_0 = \frac{-\mu^2}{2\lambda} e^{i\theta} = \frac{\nu^2}{2} e^{i\theta}. \quad (1.19)$$

To produce a viable quantum theory, the complex scalar field must be expanded around this minimum. By choosing the vacuum expectation value to be real and positive ( $\theta = 0$ ), and expanding around the minimum,  $\Phi$  is given by the following formula:

$$\Phi = \frac{\nu + \phi_1 + i\phi_2}{\sqrt{2}}. \quad (1.20)$$

After plugging this into Eq. 1.18, the Lagrangian becomes:

$$\mathcal{L} = \frac{1}{2}(\partial^\mu \phi_1 \partial_\mu \phi_1 + 2\mu^2 \phi_1^2) + \frac{1}{2} \partial^\mu \phi_2 \partial_\mu \phi_2 - \frac{1}{4} F^{\mu\nu} F_{\mu\nu} + q\nu A_\mu \partial^\mu \xi + \frac{q^2 \nu^2}{2} A_\mu A^\mu. \quad (1.21)$$

In addition to the massive scalar resulting from the Goldstone phenomenon, the "photon" gains a mass term. Furthermore, the gauge transformation given by:

$$A_\mu \rightarrow A'_\mu = A_\mu + \frac{1}{q\nu} \partial_\mu \xi, \quad (1.22)$$

$$\Phi \rightarrow \Phi' = e^{-i\xi/\nu} \Phi = \frac{\nu + \eta}{\sqrt{2}}, \quad (1.23)$$

greatly simplifies the Lagrangian to:

$$\mathcal{L} = \frac{1}{2}(\partial_\mu \eta \partial^\mu \eta + 2\mu^2 \eta^2) - \frac{1}{4} F^{\mu\nu} F_{\mu\nu} + \frac{q^2 \nu^2}{2} A'_\mu A'^\mu, \quad (1.24)$$

plus terms that are not of interest to this discussion. Note there are only two fields appearing in the above equation: a massive scalar field ( $m_\eta = -2\mu^2$ ) and a massive "photon" field ( $m_{A'} = q\nu$ ). There is no Nambu-Goldstone Boson field. This is colloquially described as the massless gauge boson "eating" the Nambu-Goldstone Boson in order to become massive. Details of how this simple example may be extended to an  $SU(2) \times U(1)$  symmetry can be found in Appendix C.

The above mechanism resolves the issue of describing massive gauge bosons in the Standard Model, yet leaves the fermions massless. To resolve this issue, consider a fermionic mass term:

$$\mathcal{L}_{m_f} = m_f \bar{\psi}_R \psi_L + h.c., \quad (1.25)$$

where  $m_f$  is the mass of the fermion, and  $h.c.$  is the hermitian conjugate of the previous term. The mass term mixes left-handed and right-handed fermions. This explicitly breaks the  $SU(2)_L$  symmetry because  $\bar{\psi}_R \psi_L$  does not form an  $SU(2)_L$  singlet, and thus the Lagrangian does not respect  $SU(2)_L$  symmetry. This can be resolved by introducing a Higgs doublet under transformations of  $SU(2)$ ,

$$\Phi = \begin{pmatrix} \phi^+ \\ \frac{v+H+i\phi_0}{\sqrt{2}} \end{pmatrix}, \quad (1.26)$$

which is already in the appropriate form to expand about a classical vacuum and subsequently including the following  $SU(2)_L$  invariant interaction in the SM Lagrangian:

$$\mathcal{L}_{int} = y \bar{\psi}_R \Phi^\dagger \psi_L + h.c. \quad (1.27)$$

When expanded, the above interaction generates terms that are related to the interaction of the fermion to the Higgs boson, and the Goldstone bosons associated with the  $W$  and  $Z$  bosons, along with a mass term. The interactions with the Goldstone bosons can be absorbed into the  $W$  and  $Z$  interactions, and are discussed below. The interaction of the Higgs boson with the fermion and the fermion's mass term are given by"

$$\mathcal{L}_{int} = y_u \bar{u}_R \frac{(v + H + i\phi_0)}{\sqrt{2}} u_L + h.c. \quad (1.28)$$

This includes a fermionic mass term (compare the above to Eq. 1.25), where the mass may be identified as  $m_u = y_u \frac{v}{\sqrt{2}}$ .

Therefore, the Higgs Mechanism introduces masses into the Standard Model without entirely destroying the symmetry structures admitted by gauge symmetries.

### 1.1.2 Broken Electroweak Sector

After symmetry breaking through the Higgs Mechanism, the gauge bosons now obtain a mass. Defining the electric charge as:

$$Q = T_3 + \frac{Y}{2}, \quad (1.29)$$

where  $T_3$  is the third component of the weak isospin generator,  $Y$  is the hypercharge, and  $Q$  is the electric charge of the operator. Applying the isospin, hypercharge, and electric charge operators to the ground state of the  $SU(2)_L \otimes U(1)_Y$  after spontaneous symmetry breaking

$\langle\phi\rangle_0 = \begin{pmatrix} 0 \\ \nu/\sqrt{2} \end{pmatrix}$  gives the following results:

$$T_1\langle\phi\rangle_0 = \begin{pmatrix} 0 & 1 \\ 1 & 0 \end{pmatrix} \begin{pmatrix} 0 \\ \nu/\sqrt{2} \end{pmatrix} = \begin{pmatrix} \nu/\sqrt{2} \\ 0 \end{pmatrix} \quad (1.30)$$

$$T_2\langle\phi\rangle_0 = \begin{pmatrix} 0 & -i \\ i & 0 \end{pmatrix} \begin{pmatrix} 0 \\ \nu/\sqrt{2} \end{pmatrix} = \begin{pmatrix} -i\nu/\sqrt{2} \\ 0 \end{pmatrix} \quad (1.31)$$

$$T_3\langle\phi\rangle_0 = \begin{pmatrix} 1 & 0 \\ 0 & -1 \end{pmatrix} \begin{pmatrix} 0 \\ \nu/\sqrt{2} \end{pmatrix} = \begin{pmatrix} 0 \\ -\nu/\sqrt{2} \end{pmatrix} \quad (1.32)$$

$$Y\langle\phi\rangle_0 = +1\langle\phi\rangle_0 = \begin{pmatrix} 0 \\ \nu/\sqrt{2} \end{pmatrix} \quad (1.33)$$

$$Q\langle\phi\rangle_0 = \begin{pmatrix} Y+1 & 0 \\ 0 & Y-1 \end{pmatrix} \begin{pmatrix} 0 \\ \nu/\sqrt{2} \end{pmatrix} = \begin{pmatrix} 0 \\ 0 \end{pmatrix}. \quad (1.34)$$

In the above equations, only the combination of the electric charge corresponds to a zero, implying that this symmetry is unbroken, while the remaining symmetries are broken. In other words, the original four bosons correspond to broken symmetries, but the linear combination given in Eq. 1.29 is unbroken. This combination can be recognized as the photon, and remains massless, while the other three gain masses. Furthermore, the  $W^1$  and  $W^2$  bosons can be exchanged for the  $W^+$  and  $W^-$  bosons through the following relationship:

$$W_\mu^\pm = \frac{W_\mu^1 \mp iW_\mu^2}{\sqrt{2}}. \quad (1.35)$$

This combination is similar to the raising and lowering operators for angular momentum often seen when discussing the hydrogen atom in introductory quantum mechanics<sup>3</sup>. Plugging this transformation back into the Lagrangian results in a mass term of the form:

$$\frac{g^2\nu^2}{4} (|W_\mu^+|^2 + |W_\mu^-|^2), \quad (1.36)$$

and the  $W$  mass can be defined as:  $M_W = \frac{g\nu}{2}$ . Additionally, the  $W_\mu^0$  and  $B_\mu$  bosons mix into two experimentally observable bosons using the orthogonal combinations:

$$Z_\mu = \frac{-g'B^\mu + gW_\mu^3}{\sqrt{g^2 + g'^2}} \quad (1.37)$$

$$A_\mu = \frac{gB^\mu + g'W_\mu^3}{\sqrt{g^2 + g'^2}}, \quad (1.38)$$

where  $g$  is the coupling of the  $SU(2)_L$  gauge group, and  $g'$  is the coupling of the  $U(1)_Y$  gauge group. It is convenient to relate these couplings through the use of a mixing angle, given by:

$$g' \equiv g \tan \theta_w. \quad (1.39)$$

Using the above equation the relationship can be rewritten as:

$$Z_\mu = \cos \theta_w W_\mu^3 - \sin \theta_w B_\mu \quad (1.40)$$

$$A_\mu = \sin \theta_w W_\mu^3 + \cos \theta_w B_\mu, \quad (1.41)$$

---

<sup>3</sup>The angular momentum of the hydrogen atom also has an  $SU(2)$  symmetry.

where  $\theta_w$  is the experimentally measured weak mixing angle<sup>4</sup>. Finally, the interaction Lagrangian in Eq. 1.12 can be rewritten into the charge current interaction and the neutral current interactions. The charged current in the lepton sector is given by:

$$\mathcal{L}_{\text{int},W} = -\frac{g}{\sqrt{2}} \left( \bar{\nu} W^+ P_L e + \bar{e} W^- P_L \nu \right), \quad (1.42)$$

where  $\nu, e$  are the neutrino and electron wavefunctions respectively, and  $P_L$  is the left-handed projection operators. The left(right)-handed projection operators project the fermion onto a left(right)-handed state. The projection operators are defined as:

$$P_L = \frac{1 - \gamma_5}{2}, \quad P_R = \frac{1 + \gamma_5}{2}, \quad (1.43)$$

where  $\gamma_5 = i\gamma_0\gamma_1\gamma_2\gamma_3$ . The coupling of the  $W$  boson can be identified in terms of measurable observables as  $\frac{G_F M_W^2}{\sqrt{2}}$ , where  $G_F$  is the Fermi constant, and will be discussed in detail later.

The neutral current interaction for the lepton sector is given by:

$$\begin{aligned} \mathcal{L}_{\text{int,neutral}} = & \frac{gg'}{\sqrt{g^2 + g'^2}} \bar{e} \not{A} e \\ & - \frac{\sqrt{g^2 + g'^2}}{2} \bar{\nu} \not{Z} P_L \nu \\ & + \frac{1}{\sqrt{g^2 + g'^2}} \left( -g'^2 \bar{e} \not{Z} P_R e + \frac{g^2 - g'^2}{2} \bar{e} \not{Z} P_L e \right). \end{aligned} \quad (1.44)$$

Identifying the coupling of the photon with the fundamental electric charge  $e$ , gives:

$$e = \frac{gg'}{\sqrt{g^2 + g'^2}}. \quad (1.45)$$

---

<sup>4</sup>Details of measuring this angle can be found in Sec. 1.1.3.

It is important to note that this also gives a definitive prediction for the  $Z$  boson mass given by:

$$M_Z^2 = \frac{M_W^2}{\cos^2 \theta_w}, \quad (1.46)$$

which implies that the  $Z$  boson mass must be greater than the  $W$  boson mass, which is confirmed experimentally.

Similar to angular momentum in the hydrogen atom, the square of the weak isospin generator ( $T^2$ ) and the third component of the isospin generator can be used to distinguish the components of the doublet after symmetry breaking. All of the fermions are in the fundamental representation of the  $U(1)_Y$  gauge group, and are each assigned a hypercharge. Furthermore, the left-handed fermions combine into doublets of  $SU(2)$  (i.e.  $\psi^T = \begin{pmatrix} u_L & d_L \end{pmatrix}$  for the left-handed up and down quarks), while the right-handed fermions are singlets. The quantum numbers for the first generation of fermions are summarized in Table 1.2. It is important to note that while  $\nu_R$  is included in Table 1.2, it does not interact with anything, and is therefore also acceptable to completely drop right-handed neutrinos from the theory. However, if the neutrinos are to have a Dirac mass term, then right-handed neutrinos need to be included in the theory. As of the writing of this work, neutrinos are known to have mass, but the origin of mass is unknown<sup>5</sup>. The quantum numbers for the first generation are also the same for the respective members in the second and third generation of fermions.

### 1.1.3 Electroweak Precision Observables

In the electroweak sector, a set of three measurable quantities known as the  $S, T,$  and  $U$  parameters are able to test the nature of the electroweak theory [67]. The parameters are

---

<sup>5</sup>For additional details on the status of neutrinos, the reader is referred to [66].



Fermion	Q	$T_3$	Y
$\nu_L^e$	0	$\frac{1}{2}$	-1
$e_L$	-1	$-\frac{1}{2}$	-1
$u_L$	$\frac{2}{3}$	$\frac{1}{2}$	$\frac{1}{3}$
$d_L$	$-\frac{1}{3}$	$-\frac{1}{2}$	$\frac{1}{3}$
$\nu_R^e$	0	0	0
$e_R$	-1	0	-2
$u_R$	$\frac{2}{3}$	0	$\frac{4}{3}$
$d_R$	$-\frac{1}{3}$	0	$-\frac{2}{3}$

Table 1.2: Electroweak quantum number for the first family of fermions

extracted from the precise data from the LEP experiment and include the recent Higgs mass measurement by ATLAS and CMS [1]. The parameters are defined using the oblique (vacuum polarization) corrections to the gauge bosons. Current measurements are consistent with the Standard Model prediction.

The vacuum polarization functions for the Electroweak bosons can be expanded in terms of the four momentum transfer,  $q^2$ . Keeping only up to  $\mathcal{O}(q^2)$ , the vacuum polarizations can be expressed as:

$$\Pi_{\gamma\gamma}(q^2) = q^2 \Pi'_{\gamma\gamma}(0) + \mathcal{O}(q^4), \quad (1.47)$$

$$\Pi_{Z\gamma}(q^2) = q^2 \Pi'_{Z\gamma}(0) + \mathcal{O}(q^4), \quad (1.48)$$

$$\Pi_{ZZ}(q^2) = \Pi_{ZZ}(0) + q^2 \Pi'_{ZZ}(0) + \mathcal{O}(q^4), \quad (1.49)$$

$$\Pi_{WW}(q^2) = \Pi_{WW}(0) + q^2 \Pi'_{WW}(0) + \mathcal{O}(q^4), \quad (1.50)$$

where  $\Pi'$  represents a derivative of the vacuum polarization with respect to  $q^2$ . Furthermore, the constant terms for  $\Pi_{\gamma\gamma}$  and  $\Pi_{Z\gamma}$  are zero due to the renormalization conditions of the Electroweak sector, namely that the photon should have zero mass and that the mass matrix for the mixing of the photon and  $Z$  is diagonal. In the above equations, there are six different

Variable	Value	$S$ Correlation	$T$ Correlation
S	$0.03 \pm 0.10$		
T	$0.05 \pm 0.12$	0.89	
U	$0.03 \pm 0.10$	-0.54	-0.83

Table 1.3: The current best fit results for the  $S, T, U$  parameters, along with their uncertainties and correlation coefficients. Reproduced from [1]

quantities,  $\Pi'_{\gamma\gamma}(0)$ ,  $\Pi'_{Z\gamma}(0)$ ,  $\Pi_{ZZ}(0)$ ,  $\Pi'_{ZZ}(0)$ ,  $\Pi_{WW}(0)$ , and  $\Pi'_{WW}(0)$ . Three of these can be fixed by input parameters, in this work they are the fine structure constant ( $\alpha$ ), the Fermi coupling constant ( $G_F$ ), and the  $Z$  boson mass. This leaves three parameters that can be measured. These are the  $S, T, U$  parameters, and are defined as:

$$\alpha S = 4s_w^2 c_w^2 \left( \Pi'_{ZZ}(0) - \frac{c_w^2 - s_w^2}{s_w c_w} \Pi'_{Z\gamma}(0) - \Pi'_{\gamma\gamma}(0) \right), \quad (1.51)$$

$$\alpha T = \frac{\Pi_{WW}(0)}{M_W^2} - \frac{\Pi_{ZZ}(0)}{M_Z^2}, \quad (1.52)$$

$$\alpha U = 4s_w^2 \left( \Pi'_{WW}(0) - c_w^2 \Pi'_{ZZ}(0) - 2s_w c_w \Pi'_{Z\gamma}(0) - s_w^2 \Pi'_{\gamma\gamma}(0) \right), \quad (1.53)$$

where  $s_w$  and  $c_w$  are the sine and cosine of the weak mixing angle respectively. In most observables, the effect of the  $U$  parameter is small, and it is also predicted to be small in most new physics models. Therefore, typically a two parameter space is used with  $U$  being set to zero. The fit to current data for both  $U$  non-zero and  $U$  zero can be seen in Figure 1.2a and 1.2b, respectively. The current best fit values for  $S, T, U$  are given in [1], and reproduced in Table 1.3. The SM predictions for the  $S, T, U$  parameters are all zero, and the data currently is consistent with the SM.

The  $W$  mass is an important observable in constraining these parameters, and the discussion of how to precisely measure this observable can be found in Chap. 5

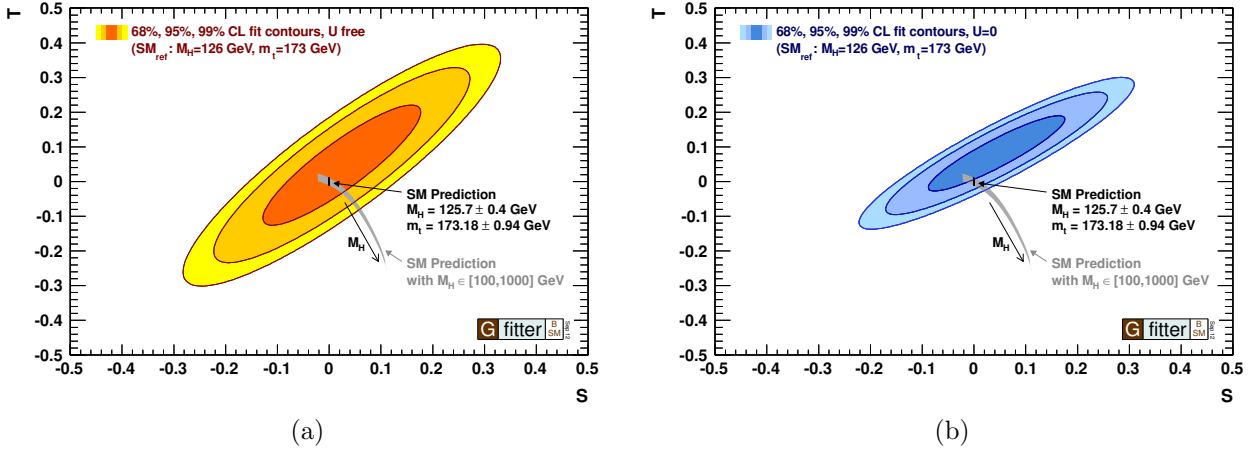


Figure 1.2: The best fit in the  $TS$  plane with  $U$  free to float on the left and  $U$  fixed to zero on the right. Additionally,  $m_H = 126$  GeV and  $m_t = 173$  GeV in this fit. Reproduced from [1]

### 1.1.4 Electroweak Parameters

While this work focuses on the QCD corrections for given processes, the processes themselves contain Electroweak couplings. Therefore, it is important to discuss the parameters in the electroweak sector, the different schemes to set the parameters, and the scheme and values of input parameters used for the results in this work.

In the electroweak sector, typically, the values of  $M_Z$ , the fine structure constant  $\alpha$ , and Fermi's constant  $G_F$  are used as input parameters. The reason that these three are chosen is due to the fact that these are the most precisely measured parameters. It is possible to trade out  $G_F$  for  $M_W$ , and other such exchanges. These would result in slightly different predictions that should only differ by higher order corrections. In this work, the choice of parameters follows that detailed in Section 3.1 of [68], and are detailed below for simplicity. The constant width approach is used, and thus the  $W$  and  $Z$  masses and widths need to be adjusted from that measured in the  $s$ -dependent width approach [69, 70]. This results in the

inputs for the  $W$  and  $Z$  boson to be:

$$M_Z = 91.1535\text{GeV}, \quad \Gamma_Z = 2.4943\text{GeV} \quad (1.54)$$

$$M_W = 80.358\text{GeV}, \quad \Gamma_W = 2.084\text{GeV}, \quad (1.55)$$

where  $\Gamma_{Z,W}$  is the width of the  $Z$  and  $W$  boson respectively. Additionally, the value of  $\alpha(0)$  is replaced by the effective coupling  $\alpha_{G_F} = \sqrt{2}G_F M_W^2 \left(1 - \frac{M_W^2}{M_Z^2}\right) / \pi$ . The input value for  $G_F = 1.1663787 \times 10^{-5} \text{ GeV}^{-2}$ . In all numerical results, these input parameters are used for all the calculations, to ensure that any difference is not due to different choices of input parameters.

There are three schemes for the measurement of the EW parameters that are discussed in the literature, the on-shell scheme [71], the  $\overline{MS}$  scheme, and the  $\sin\theta_w$  scheme. In the on-shell scheme, the weak mixing angle is fixed to be given by the following equation to all orders:

$$\sin^2\theta_w = 1 - \frac{M_W^2}{M_Z^2}. \quad (1.56)$$

In the  $\overline{MS}$  scheme, all parameters develop a scale dependence and the parameters run as a function of the hard scale. Finally, the effective angle scheme determines the mixing angle by using  $Z$  pole observables to obtain the  $Z$  couplings to fermions, and thus fixing  $\sin\theta_w$ . These schemes will have small deviations in the calculated parameters.

## 1.2 Renormalization and Regularization

In Quantum Field Theories, calculations are usually performed as a series expansion of a small coupling constant. However, when calculating an observable beyond the leading

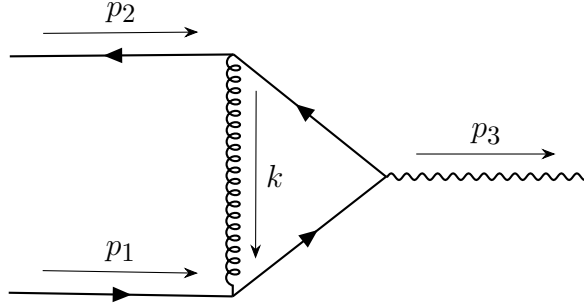


Figure 1.3: An example of a loop diagram,  $p_1$ ,  $p_2$ , and  $p_3$  are the momentums of the external particles, and  $k$  is the momentum of the loop.<sup>6</sup>

term in the expansion, the theory generates infinities. Because the physical observables are finite, physicists developed a procedure to ensure that predictions are similarly finite. This procedure consists of regularization and renormalization.

Regularization is a means to isolate the divergences in the theoretical calculation. The present work focuses on Dimensional Regularization, the most commonly used regularization scheme [72]. In Dimensional Regularization, field theory equations are calculated in  $D = 4 - 2\epsilon$  spacetime dimensions, where  $\epsilon$  is eventually taken to 0. The divergences will show up in the form of  $\epsilon^{-n}$  poles, where  $n$  is a positive integer. Consider the Feynman Diagram in Fig. 1.3. From conservation of momentum, the values of  $p_1$ ,  $p_2$ , and  $p_3$  are all related, but  $k$  is left arbitrary. Therefore, all possible values for  $k$  need to be considered, resulting in an integral over the four momentum of  $k$ . In general the set of one-loop diagrams can be expressed in integrals of the form:

$$\int \frac{d^D k}{(2\pi)^D} \frac{N(k^2)}{(k^2 - \Delta)^n}, \quad (1.57)$$

where the numerator and denominator must each be constructed exclusively from even pow-

---

<sup>6</sup>Drawn using TikZ-Feynman [73]

ers of  $k$ , since any odd powers of  $k$  will integrate to zero since it would be an integration of an odd function over symmetric bounds. If the power of  $k$  in the denominator is greater than that in the numerator by at least 4, then the subsequent integral is divergent in 4 dimensions as the loop momentum goes to infinity. This divergence is known as an ultraviolet(UV) divergence. In dimensional regularization, this divergence is regulated by moving to a dimension slightly smaller than 4 and results in simple poles in  $\epsilon$ . Similarly, it is possible that a divergence appears as the loop momentum goes to zero. Such a divergence is called an infrared(IR) divergence, and is discussed in more detail in Section 1.3.3. For now, note IR divergences are regulated in dimensions larger than 4. Any poles in the resulting calculation need to be removed in order to obtain a physical result, this is known as renormalization. Additionally, Dimensional Regularization causes couplings to gain a mass dimension. However, this is undesirable, so the coupling is traditionally modified to be dimensionless, and an additional dimensionful parameter  $\mu$  is introduced to ensure the proper dimensions in the Lagrangian ( $g^2 \rightarrow g^2 \mu^{4-D}$ ). The above discussion can be generalized to higher order loops, by modifying Eq. 1.57 to:

$$\int \prod_{i=1}^n \frac{d^D k_i}{(2\pi)^D} \frac{N(k_1^2, \dots, k_n^2)}{D(k_1^2, \dots, k_n^2)}, \quad (1.58)$$

where the  $k_i$ 's are the loop momenta, and  $N$  and  $D$  are some function of the momenta squared.

Renormalization modifies the Lagrangian parameters from so-called bare parameters into renormalized parameters. When redefining these bare parameters into renormalized parameters, the UV divergences are absorbed. Because the renormalized parameters must be able to absorb a divergent contribution yet obtain a finite result, the bare parameters must also be divergent. There are many different renormalization schemes. This work utilizes the Modi-

fied Minimal Subtraction ( $\overline{MS}$ ) Scheme [74, 75]. To illustrate the renormalization procedure, consider the bare QED Lagrangian:

$$\mathcal{L} = -\frac{1}{4}F^{\mu\nu}F_{\mu\nu} + i\bar{\psi}^0\cancel{\partial}\psi^0 - m_0\bar{\psi}^0\psi^0 - e_0\bar{\psi}^0A^0\psi^0, \quad (1.59)$$

where  $m_0$  is the bare electron mass,  $e_0$  is the bare electron charge,  $\psi^0$  is the bare electron field, and  $A^0$  is the bare photon field. By defining renormalized quantities, the Lagrangian can be rewritten in terms of renormalized quantities plus counterterms. To begin, rewrite the bare electron field according to:

$$\psi^R = \frac{1}{\sqrt{Z_2}}\psi^0, \quad (1.60)$$

where  $\psi^R$  is the renormalized field, and  $Z_2$  is some infinite number. Because the calculations will be performed order by order, it is more convenient to express  $Z_2$  as 1 (its tree level value) plus a counterterm. Thus,  $Z_2$  can be written as  $1 + \delta_2$ , where  $\delta_2$  is the counterterm, and is expressed as a Taylor series expansion in the coupling of the theory. Furthermore, the process can be repeated with the mass, thereby yielding an additional counterterm  $\delta_m$  and a renormalized mass  $m_R$ . These terms are used to absorb the divergences in the calculation as well as some finite portion of the calculation. The form of the finite piece absorbed is determined by the renormalization scheme used. As mentioned above, this work utilizes the  $\overline{MS}$  scheme, wherein counterterms are chosen to remove the aforementioned poles, along with constants proportional to  $\ln(4\pi e^{-\gamma}E)$ , arising from any loop calculation performed using dimensional regularization. The renormalization of the coupling constant will be discussed in relation to QCD in detail in Subsection 1.3.2, and is discussed in terms of the running of

the coupling, in which the coupling gains an energy dependence.

In all of the above discussion, it was assumed all the divergences could be absorbed by a finite number of counterterms. A QFT for which this is true is said to be a renormalizable theory. However, it is not guaranteed that any theory can be renormalized using a finite number of counterterms. To show that a theory is completely renormalizable is quite complicated. t'Hooft [76] showed this is true for spontaneously broken non-Abelian gauge theories, thus paving the path for the Standard Model. A rough sketch of proving that a theory is renormalizable is described below. Firstly, it is necessary to show that it is true not only for one loop calculations, but for all loop orders. Bogoliubov, Parasiuk, Hepp, and Zimmermann developed a theorem describing the conditions needed for a QFT to be renormalizable to all orders [77, 78, 79]. The BPHZ Theorem states a theory is renormalizable if all divergences in the theory can be removed by counterterms corresponding to superficially divergent one-loop irreducible amplitudes. Therefore, it is sufficient to show that there are only a finite number of superficially divergent one-loop processes and that the number of superficially divergent amplitudes does not increase with increasing orders of perturbation theory. Showing there are a finite number of counterterms at one-loop is a straight forward calculation. Ensuring no new superficially divergent amplitudes appear at higher perturbative orders is more difficult, and involves a proof by induction. The details of this proof for the Standard Model are in Ref. [80].



## 1.3 Quantum Chromodynamics

### 1.3.1 Introduction

The theory of Quantum Chromodynamics was developed in order to study the strong force that holds hadrons together. As mentioned at the start of this chapter, there are 6 quarks that interact through the strong force.

Gell-Mann and Zweig introduced the quark model to describe the many hadrons being observed [81, 82]. However, the model possessed a major problem. Consider the  $\Delta^{++}$  particle:

$$\Delta^{++} = |u^\uparrow u^\uparrow u^\uparrow\rangle. \quad (1.61)$$

Because the up quarks are identical and all spin up, multiple fermions occupy the same state, and this spin 3/2 particle violates Fermi-Dirac statistics. This problem was solved by introducing what is now called “color charge”. Using this new idea, the  $\Delta^{++}$  can be expressed with a completely anti-symmetric expression by including three different colors of quarks, and requiring the new object to be colorless:

$$\Delta^{++} = \frac{1}{\sqrt{6}} \sum_{ijk} \epsilon_{ijk} |u_i^\uparrow u_j^\uparrow u_k^\uparrow\rangle. \quad (1.62)$$

Motivated by the color theory of optical light, colorless refers to the fact that the  $\Delta^{++}$  contains one of each color (named red, green, and blue). Another way to create a colorless object is to have one color and the same anti-color (e.g. red and anti-red). Quarks are

defined in a color triplet as follows:

$$|q\rangle = \begin{pmatrix} |q_r\rangle \\ |q_g\rangle \\ |q_b\rangle \end{pmatrix}. \quad (1.63)$$

It is important to note that experimentally, observables must depend on the complete triplet e.g.,

$$\mathcal{O} \sim \langle q|\mathcal{O}|q\rangle \sim \left( \|q_r\|^2 + \|q_g\|^2 + \|q_b\|^2 \right). \quad (1.64)$$

The above equation is invariant under the transformation  $q \rightarrow q' = Uq$ , where  $U$  is an unitarity 3 x 3 matrix ( $U^\dagger U = \mathbb{1}$ ). This matrix includes Abelian transformations that do not mix  $q_r, q_g$ , and  $q_b$ . These transformations are not desired (this type of transformation is included in QED). To single out the transformations between  $q_r, q_g$ , and  $q_b$  the matrix is required to be special ( $\det(U) = 1$ ).

These transformations form the group of special unitary transformations of degree 3, labeled SU(3). For a group SU(N), the number of generators are given by  $N^2 - 1$ . Therefore, SU(3) has 8 generators resulting in 8 different force mediators (gluons). Let us define the Gell-Mann matrices<sup>7</sup>  $\lambda^a$ , and the T matrices,  $T^a = \frac{\lambda^a}{2}$ .

The properties that follow here are general to SU(N):

1. The  $T^a$  are traceless and hermitian:

$$\text{Tr}(T^a) = 0 \quad (T^a)^\dagger = T^a \quad (1.65)$$

---

<sup>7</sup>A representation for the Gell-Mann matrices can be found in Appendix D.

2. Lie-Algebra of SU(N):

$$[T^a, T^b] = if_{abc}T^c \quad [\lambda^a, \lambda^b] = 2if_{abc}\lambda^c \quad (1.66)$$

3. Structure Constants:

$$f^{abc} = -2i \text{Tr} \left( [T^a, T^b] T^c \right) \quad (1.67)$$

4. Traces:

$$\text{Tr} \left( T^a T^b \right) = \frac{1}{2} \delta^{ab} \quad \text{Tr} \left( \lambda^a \lambda^b \right) = 2\delta^{ab} \quad (1.68)$$

5. Fierz Identity:

$$T_{ij}^a T_{kl}^a = \frac{1}{2} \left( \delta_{il} \delta_{jk} - \frac{1}{N} \delta_{ij} \delta_{kl} \right) \quad (1.69)$$

The covariant derivative for quarks under the strong force is given by:

$$D_\mu = \partial_\mu - ig_s T_a G_\mu^a, \quad (1.70)$$

where  $g_s$  is the strong coupling constant and  $G^a$  is the gluonic field. The introduction of the gluonic field is needed to ensure that a local  $SU(3)$  transformation of the quark fields remains invariant. Under the gauge transformation, the gluonic fields transform as:

$$G_\mu^a \rightarrow G_\mu^a + \partial_\mu \theta^a(x) - g_s f^{abc} \theta^b(x) G_\mu^c. \quad (1.71)$$

The kinetic term in the Lagrangian for the gluon fields is given by:

$$\mathcal{L}_G = -\frac{1}{4} G_{\mu\nu}^a G_a^{\mu\nu}, \quad (1.72)$$

where the field strength tensor is given by:

$$G_{\mu\nu}^a = \partial_\mu G_\nu^a - \partial_\nu G_\mu^a + g_s f^{abc} G_\mu^b G_\nu^c. \quad (1.73)$$

Since  $SU(3)$  is a non-Abelian group, the gluons are allowed to self-interact. The Lagrangian for the cubic and quartic coupling are given by:

$$\mathcal{L}_c = -\frac{1}{2} g_s \left[ f_{abc} (\partial^\mu A^{a,\nu}) A_\mu^b A_\nu^c - f_{abc} (\partial^\nu A^{a,\mu}) A_\mu^b A_\nu^c \right], \quad (1.74)$$

$$\mathcal{L}_q = g_s^2 f_{abc} f_{ab'c'} A^{\mu,b} A^{\nu,c} A_\mu^{b'} A_\nu^{c'}, \quad (1.75)$$

respectively. The fact that the gluons self-interact leads to many interesting properties of QCD. These properties are asymptotic freedom and confinement, which are discussed in the following section.<sup>8</sup>

### 1.3.2 Asymptotic Freedom and Confinement

In Quantum Field Theories, the coupling in the theory is dependent upon the energy scale at which the theory is being calculated. In this section, the low energy and high energy properties of Quantum Chromodynamics are discussed.

Asymptotic freedom is the phenomenon that occurs in QCD at high energies, while confinement is the phenomenon that occurs in QCD at very low energies. Both of these phenomena are the result of the running of the strong coupling constant. As mentioned in Subsection 1.2, the couplings in the gauge theory gain an energy dependence when performing loop corrections to the coupling (an example diagram for corrections to a coupling is shown

---

<sup>8</sup>Details on the derivation of the QCD Feynman Rules can be found in App. E.

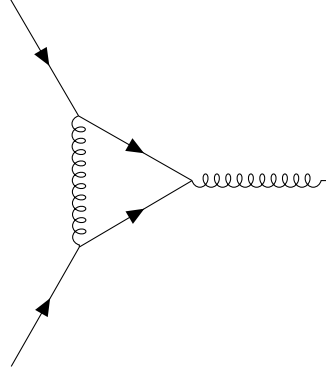


Figure 1.4: The first order correction to the strong coupling constant can be calculated from this vertex correction diagram.

in Figure 1.4). The bare coupling should be independent of the scale of the calculation, which leads to the following equation:

$$\frac{d\alpha_{\text{bare}}}{d\mu} = 0 \rightarrow \frac{\partial\alpha(\mu^2)}{\partial\ln(\mu^2)} = \beta(\alpha), \quad (1.76)$$

where  $\alpha = \frac{g^2}{4\pi}$ , with  $g$  being the coupling of the theory, and  $\beta$  is given by:

$$\beta(\alpha) = -\alpha\frac{\alpha}{\pi}\beta_0 - \alpha\left(\frac{\alpha}{\pi}\right)^2\beta_1 + \mathcal{O}(\alpha\alpha^2). \quad (1.77)$$

For QED, the leading term in the  $\beta$ -function is given by:

$$\beta_0^{QED} = -\frac{2}{3}. \quad (1.78)$$

With this running of coupling constant, at low energy scales the coupling is small, but as the energy is taken to be larger and larger, the coupling grows. At a certain point the coupling divergences, this is referred to as the Landau pole [83], and occurs around  $10^{286}$  eV for QED.

For QCD, the leading term in the  $\beta$ -function is given by:

$$\beta_0^{QCD} = \frac{11C_A - 2n_f}{12}, \quad (1.79)$$

where  $C_A$  is the number of colors in the theory, and  $n_f$  is the number of active flavors. The number of active flavors is determined by the scale at which the calculation is being performed. For example, if  $\mu^2 < m_c^2$  then  $n_f = 3$ , and if  $m_b^2 < \mu^2 < m_t^2$  then  $n_f = 5$ . Furthermore, it is interesting to note that if  $n_f$  is less than 6, than the value of  $\beta_0$  is greater than zero. In QCD, this condition is satisfied, which leads to a running of the coupling which is the opposite of QED. So while the QED coupling grows as a function of energy, the QCD coupling decreases as a function of energy. This leads to a running coupling that asymptotically approaches zero at high energies, and therefore QCD asymptotically approaches a free theory [84, 85]. On the other hand, the coupling grows for small energy scales and eventually becomes non-perturbative ( $\alpha_s > 4\pi$ ), and it is no longer reasonable to describe QCD using quarks and gluons, but rather using hadrons. Calculations in this regime are done either using Chiral Perturbation Theory [86] or Lattice QCD [87].<sup>9</sup> Since the coupling becomes so strong the quarks and gluons become confined into the hadrons that are used to describe the theory, this describes the phenomena of confinement found in QCD.

It is possible to analytically solve the running of the coupling at the lowest order, the

---

<sup>9</sup>Both ChPT and Lattice QCD are beyond the scope of this work. For additional information, the reader is referred to [86, 88, 89] for ChPT and to [87, 90, 91, 92, 93] for Lattice QCD.

result given in terms of  $\beta_0$  is:

$$\alpha(\mu) = \frac{\alpha(\mu_0)}{1 + \frac{\alpha(\mu_0)}{\pi} \beta_0 \ln \frac{\mu^2}{\mu_0^2}}, \quad (1.80)$$

where  $\mu$  is the scale the coupling is being evaluated, and  $\mu_0$  is the input scale at which the coupling was measured at. While  $\beta_1$  and  $\beta_2$ <sup>10</sup> have been calculated [94], it is not possible to solve the running of the coupling analytically, and is traditionally done numerically.

Given the value of the coupling at a given scale, it is possible to predict the coupling at any other scale. For QCD, the experimental measurements of the coupling are shown to be consistent with the theoretical predictions as seen in Fig. 1.5. Typically, the starting scale is chosen to be the mass of the  $Z$  boson, and is given as  $\alpha_s(M_Z) = 0.118 \pm 0.0011$  [6]. As mentioned previously, the value of  $n_f$  is dependent upon the scale that one is evaluating the coupling at, and thus leads to the need to create a matching procedure in order to ensure that the coupling is a continuous function. This results in choosing  $\alpha_s(m_q - \epsilon) = \alpha_s(m_q + \epsilon)$  at the scale of  $m_q$ .

When using the renormalization group equation (Eq. 1.76) to obtain the running of the coupling, the large logarithmic terms that appear at all orders are resummed in order to improve the theoretical prediction of this quantity. Later in this work, there will be a large focus on the methodology of resummation in the case of the transverse momentum of a given system.

---

<sup>10</sup>The expressions for  $\beta_1$  and  $\beta_2$  can be found in App. E.

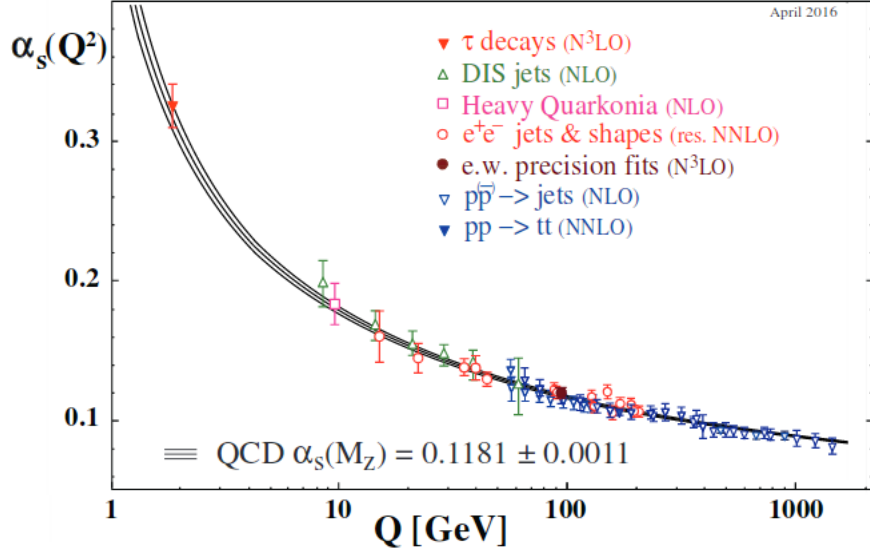


Figure 1.5: The comparison between the theoretical calculation of the strong coupling compared to experimental data. The plot is reproduced from Ref. [6]

### 1.3.3 Soft and Collinear QCD

As mentioned in the previous section, all physical results must be finite. However, during the calculations there can be an IR divergence that is the result of two particles being emitted collinear to each other, or in the case of a massless particle, the momentum can be very small, which is referred to as a soft divergence. To see these divergences from a mathematical standpoint consider the denominator of a massless and massive propagator given as:

$$\frac{1}{(p+k)^2} = \frac{1}{2p \cdot k}, \quad (1.81)$$

and

$$\frac{1}{(p+k)^2 - m^2} = \frac{1}{2p \cdot k + p^2 + k^2 - m^2}, \quad (1.82)$$

respectively. In the massless case, in the limit that  $k^\mu \rightarrow 0$  or  $k^\mu \rightarrow ap^\mu$ , where  $a$  is some scaling constant, the propagator diverges. However, when considering the second equation,



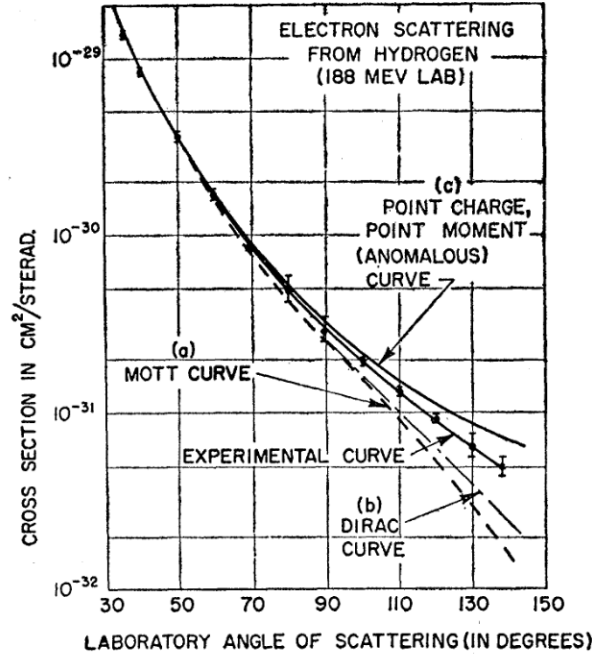


Figure 1.6: Electron scattering off of a proton with an energy of 188 MeV. Results show data is inconsistent with a point-like proton. Reproduced from [7].

only the limit that  $k^\mu \rightarrow ap^\mu$  results in a divergence. This is a result of having a momentum cutoff due to the mass of the particle.

### 1.3.4 Factorization

The QCD cross-sections can be broken into a long distance piece and a short distance piece. While the short distance piece is the major discussion of the rest of this work, here the long distance physics needed in order to compare a theoretical calculation with data is briefly discussed. The two major long distance physics phenomena that will be discussed here are the parton distribution functions (PDFs), and hadronization along with jet algorithms.

The parton model (Richard Feynman, 1969) [95] is the idea that a proton is composed of many smaller pieces, that are essentially free point-like particles. This was supported by data showing that indeed the proton was not a point particle and the validation of Bjorken

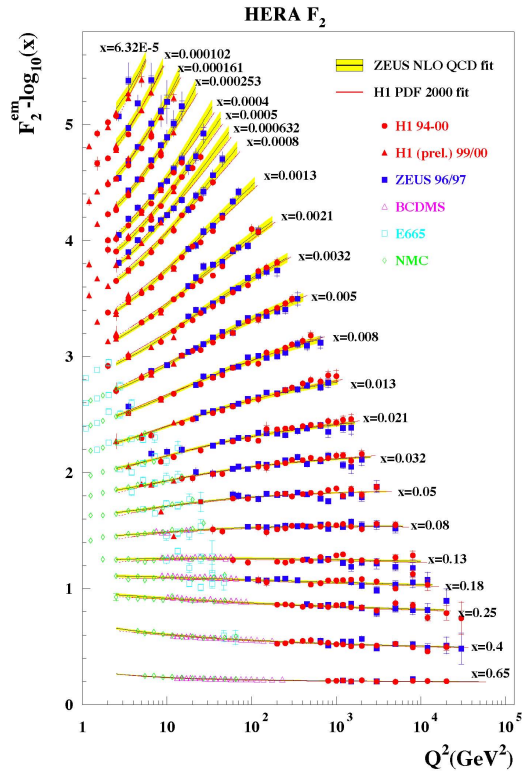


Figure 1.7: Depiction of the  $F_2$  proton structure function, showing Bjorken scaling. This was the motivation for the parton model proposed by Richard Feynman. Plot is reproduced from [8].

Scaling [96] (See Fig. 1.7). If the proton was a point particle, then proton electron collisions should follow the predictions made by Mott Scattering [97]. However, as seen from the results of [7] and reproduced in Fig. 1.6, it is clear that electron-proton scattering does not follow the prediction for Mott Scattering. To resolve this issue, proton structure functions are introduced. For further simplicity the calculations are performed in the "infinite momentum frame," where  $p^\mu \approx (E, 0, 0, E)$  with  $E \gg M_p$ , where  $M_p$  is the mass of the proton. It is then possible to write the scattering as the following cross-section:

$$\frac{d^2\sigma}{dx dQ^2} = \frac{4\pi\alpha^2}{Q^4} \left[ \left(1 + (1-y)^2\right) F_1(x, Q^2) + \frac{1-y}{x} \left(F_2(x, Q^2) - 2xF_1(x, Q^2)\right) \right], \quad (1.83)$$

where  $Q^2$  is the energy transferred by the photon being exchanged,  $y = 1 - \frac{E'}{E}$ , with  $E'$  the outgoing energy of the electron, and  $E$  the incoming energy of the electron. Also,  $x = \frac{Q^2}{2M_p(E-E')}$ , and  $F_1$  and  $F_2$  are the two structure functions that appear. Furthermore, there exists the Callan-Gross relation [98], that states for a spin- $\frac{1}{2}$  particle,  $F_2 = 2xF_1$ . This can be tested experimentally, and the results can be seen in Fig. 1.8. It is clear that the results are close to zero and thus the proton is made of spin-1/2 particles. However, this is not the complete story, and at higher energies there is a deviation away from zero as a result of higher order QCD corrections, and interactions with the gluon.

From these results, the picture of the proton becomes one of a set of valence quarks, sea quarks, and gluons. When calculating a theoretical prediction, it is necessary to know the probability of removing a given parton from the proton at a set energy. These distributions are known as Parton Distribution Functions (PDFs) and a detailed discussion follows in the subsequent section. However, because these distributions are related to the proton composition at low energies, it is non-perturbative. Therefore, to obtain a calculation, factorization

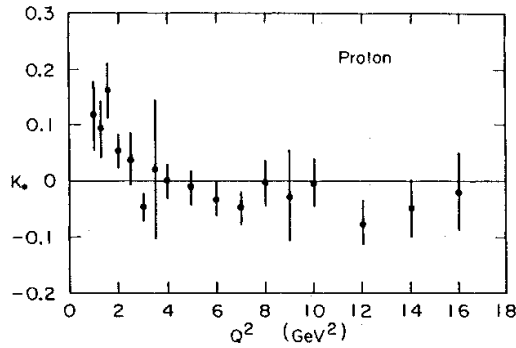


Figure 1.8: Test of the Callan-Gross relation, with  $K_0 = F_2/(2xF_1) - 1$ . Results are consistent with spin-1/2 predictions. Reproduced from [9].

was introduced. The idea behind factorization is that one can introduce an arbitrary scale to separate the non-perturbative contributions from the perturbative contributions. Because the scale is arbitrary, the final result should be independent of scale, if the calculation can be performed to all orders. However, this is not the case and therefore a scale dependence is introduced, which is used for estimating theoretical uncertainties, referred to as the factorization scale ( $\mu_F$ ).

The factorization of the long distance physics from the short distance physics is given schematically for deep inelastic scattering ( $e + p \rightarrow e + X$ ) as:

$$\sigma = \int f(x) \hat{\sigma} dx, \quad (1.84)$$

where  $\sigma$  is the total measured cross-section,  $f(x)$  is the PDF, and  $\hat{\sigma}$  is the calculation of a quark interacting with an electron. A similar technique is used to describe final state quarks. In this case, since only hadrons are physically observed, there needs to be a function that takes quarks into hadrons. This is known as the fragmentation function, and is again defined using an arbitrary scale. Additional details for fragmentation functions can be found

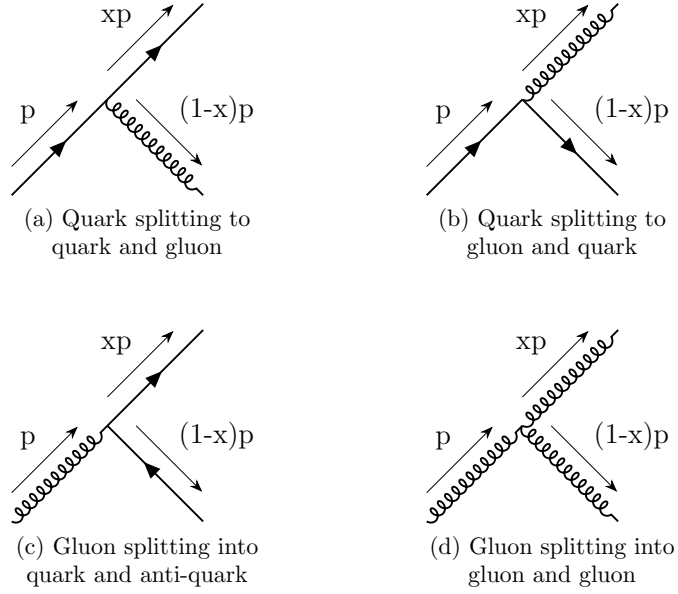


Figure 1.9: The splitting kernels that occur at  $\alpha_s$ . Note that to obtain the missing kernels, take fermions to anti-fermions and vice-versa.

in [99, 100]. However, if the details of the hadrons in the final state are unimportant, a jet algorithm can be used to create theoretically manipulable objects. Details on jets and jet algorithms are provided below.

## Parton Distribution Functions

In order to perform calculations at a hadron collider, it is necessary to use Parton Distribution Functions. However, it is possible to extend the basic purely non-perturbative picture of the PDFs to include the improved parton model. In the improved parton model, it is possible to calculate the energy dependence of the PDFs. In order to calculate these effects, consider diagrams of the forms found in Fig. 1.9. The results of these calculations can be represented

by the following equations at leading order:

$$P_{qq}(z) = C_F \left( \frac{1+z^2}{(1-z)_+} + \frac{3}{2} \delta(1-z) \right), \quad (1.85)$$

$$P_{qg}(z) = C_F \left( \frac{1+(1-z)^2}{z} \right), \quad (1.86)$$

$$P_{gq}(z) = \frac{1}{2} \left( z^2 + (1-z)^2 \right), \quad (1.87)$$

$$P_{gg}(z) = 2C_A \left( \frac{z}{(1-z)_+} + \frac{1-z}{z} \right) + \beta_0 \delta(1-z), \quad (1.88)$$

where  $P_{ij}$  is the splitting kernel from  $j$  to  $i$ . Also, the  $\frac{1}{(1-z)_+}$  is the plus-distribution and is discussed in detail in Appendix F. Similar to the summation that was performed for the running of the coupling, it is possible to define bare PDFs which are independent of scale. This results in a set of  $2N_f + 1$  coupled differential equations, known as the full form DGLAP evolution equations [101, 102, 103], given by:

$$\frac{\partial}{\partial \ln \mu^2} \begin{pmatrix} q(x, \mu^2) \\ g(x, \mu^2) \end{pmatrix} = \frac{\alpha_s(\mu^2)}{2\pi} \int_z^1 \frac{dz}{z} \begin{pmatrix} P_{qq}(z) & P_{qg}(z) \\ P_{gq}(z) & P_{gg}(z) \end{pmatrix} \begin{pmatrix} q(\frac{x}{z}, \mu^2) \\ g(\frac{x}{z}, \mu^2) \end{pmatrix}, \quad (1.89)$$

up to  $\mathcal{O}(\alpha_s)$ . To solve these equations, it is convenient to define a new set of PDFs, defined using the valence quark, singlet, non-singlet, and gluon contributions. There are  $N_f$  valence quark contributions,  $N_f - 1$  non-singlet contributions, and one of both the singlet and gluon contributions. The valence quark distribution is

$$q_i^V = q_i - \bar{q}_i, \quad (1.90)$$

the non-singlet distribution is

$$q_i^F = \sum_{n=1}^{i-1} (q_n + \bar{q}_n - q_i - \bar{q}_i), \quad (1.91)$$

and the singlet distribution is

$$q^S = \sum_{n=1}^{N_f} (q_n + \bar{q}_n). \quad (1.92)$$

This change of variables leads to a set of  $2N_f - 1$  decoupled and two coupled differential equations given up to  $\mathcal{O}(\alpha_s)$  as:

$$\frac{\partial q_i^V}{\partial \ln \mu^2} = \frac{\alpha_s(\mu^2)}{2\pi} P_{qq} \otimes q_i^V \quad (1.93)$$

$$\frac{\partial q_i^F}{\partial \ln \mu^2} = \frac{\alpha_s(\mu^2)}{2\pi} P_{qq} \otimes q_i^F \quad (1.94)$$

$$\frac{\partial q^S}{\partial \ln \mu^2} = \frac{\alpha_s(\mu^2)}{2\pi} \left( P_{qq} \otimes q^S + 2N_f P_{qg} \otimes g \right) \quad (1.95)$$

$$\frac{\partial g}{\partial \ln \mu^2} = \frac{\alpha_s(\mu^2)}{2\pi} \left( P_{gq} \otimes q^S + P_{gg} \otimes g \right) \quad (1.96)$$

Additionally, there are constraints on the solutions implemented by sum rules. The momentum sum rule forces that the total momentum of the partons to be the momentum of the hadron,

$$\sum_{q, \bar{q}, g} \int_0^1 x f(x) = 1. \quad (1.97)$$

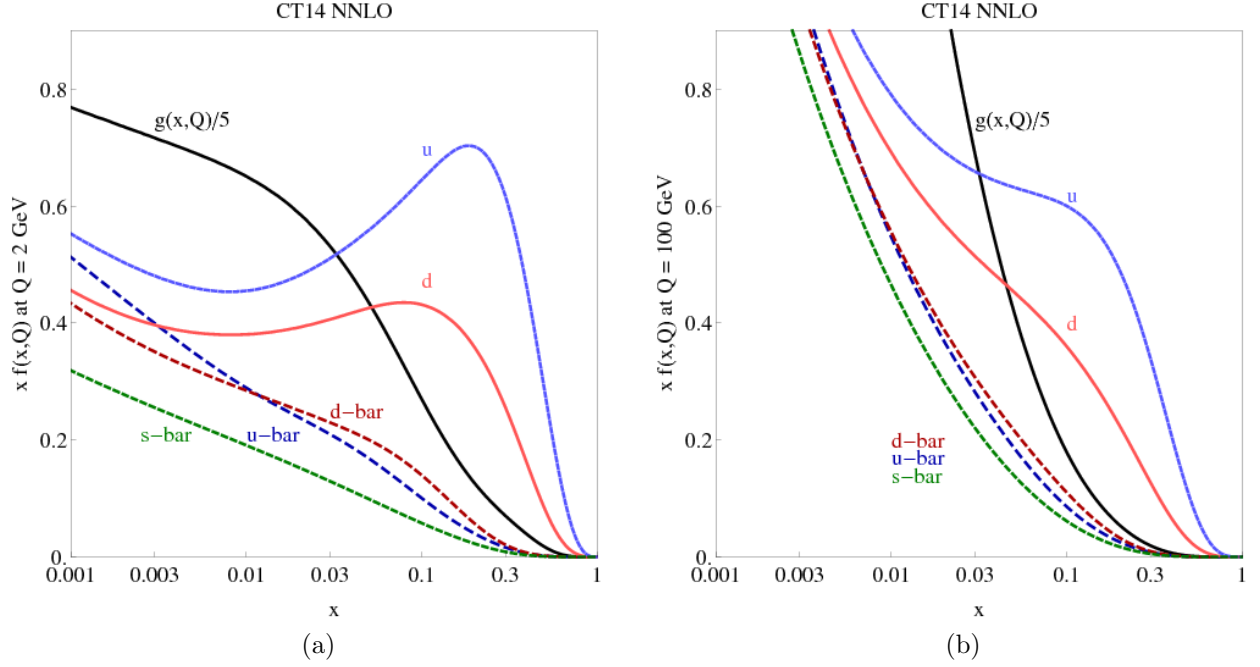


Figure 1.10: Plots of the CT14 NNLO Parton Distributions at 2 GeV (left) and 100 GeV (right). The plots are reproduced from Ref. [10]

The other sum rule is the valence quark sum rule, which for a proton is given by:

$$\int_0^1 (f_u - f_{\bar{u}}) = 2, \quad (1.98)$$

$$\int_0^1 (f_d - f_{\bar{d}}) = 1, \quad (1.99)$$

$$\int_0^1 (f_q - f_{\bar{q}}) = 0, \quad \text{for } q \neq u, d. \quad (1.100)$$

The DGLAP equations can be extended order by order in QCD, and currently have been calculated to NNLO [104, 105]. An example of a PDF can be found in Figure 1.10, where the energy dependence can be seen between the two subfigures.



## Jet Algorithms

A true observable must be an infrared safe observable which means the observable is unchanged by the addition of a soft or collinear contribution. If this is not the true, then the result will suffer from IR divergences and is known as an IR unsafe observable. In the case of final state partons, an infrared safe observable is constructed by collecting the partons into jets. The method of combining the final state partons into jets is known as a Jet Algorithm, and must satisfy the following two conditions:

1. If two particles become collinear then the observable must not change:

$$\mathcal{O}_n(p_1, p_2, \dots, p_n) \rightarrow \mathcal{O}_{n-1}(p_1 + p_2, \dots, p_n) \quad (1.101)$$

2. If one particle is soft then the observable must not change:

$$\mathcal{O}_n(p_1, p_2, \dots, p_n) \rightarrow \mathcal{O}_{n-1}(p_2, \dots, p_n) \quad (1.102)$$

Currently, there is one major class of jet algorithms used to ensure the final state is infrared safe. This class of algorithms is known as sequential recombination algorithms, which contains anti- $k_t$ ,  $k_t$ , and Cambridge-Aachen algorithms [106, 107, 108, 11]. For this class of algorithms, the methodology of forming jets is the same, but the measure to determine when to combine two subjects together varies from one to the other. The steps of the algorithm is as follows:

1. Calculate the distance between all sets of two partons ( $d_{ij}$ ) and between all partons and the beam ( $d_{iB}$ )

2. Find the smallest distance. If  $d_{ij}$  is the smallest, combine  $i$  and  $j$  into a subset, else if  $d_{iB}$  is smallest remove subset  $i$  from the list and mark as a jet
3. Repeat until all particles are clustered into a set of jets

The definition of the distance varies from one algorithm to another, but can be represented in general by:

$$\begin{aligned}
 d_{ij} &= \min \left( k_{ti}^{2p}, k_{tj}^{2p} \right) \frac{R_{ij}}{R} \\
 d_{iB} &= k_{ti}^{2p},
 \end{aligned}
 \tag{1.103}$$

where,  $k_{ti}$  is the transverse momentum of the  $i^{th}$  particle,  $p$  is the power factor that depends on the scheme (-1 for anti- $k_t$ , 1 for  $k_t$ , and 0 for Cambridge-Aachen),  $R_{ij}$  is the distance between the two particles given by  $R_{ij}^2 = (y_i - y_j)^2 + (\phi_i - \phi_j)^2$ , and  $R$  is a parameter that determines the radius of a typical jet. The anti- $k_T$ ,  $k_T$ , and Cambridge-Aachen algorithms can be compared by looking at how they cluster the same event as shown in Figure 1.11. It is interesting to note that the anti- $k_T$  algorithm tends to have the most cone like jets. In recent years, there has been work to begin delving into the sub-structure of jets to obtain more information about them. While that discussion is beyond the scope of this work, the reader is referred to [109, 110, 111, 112, 113, 114] for some of the recent advancements.

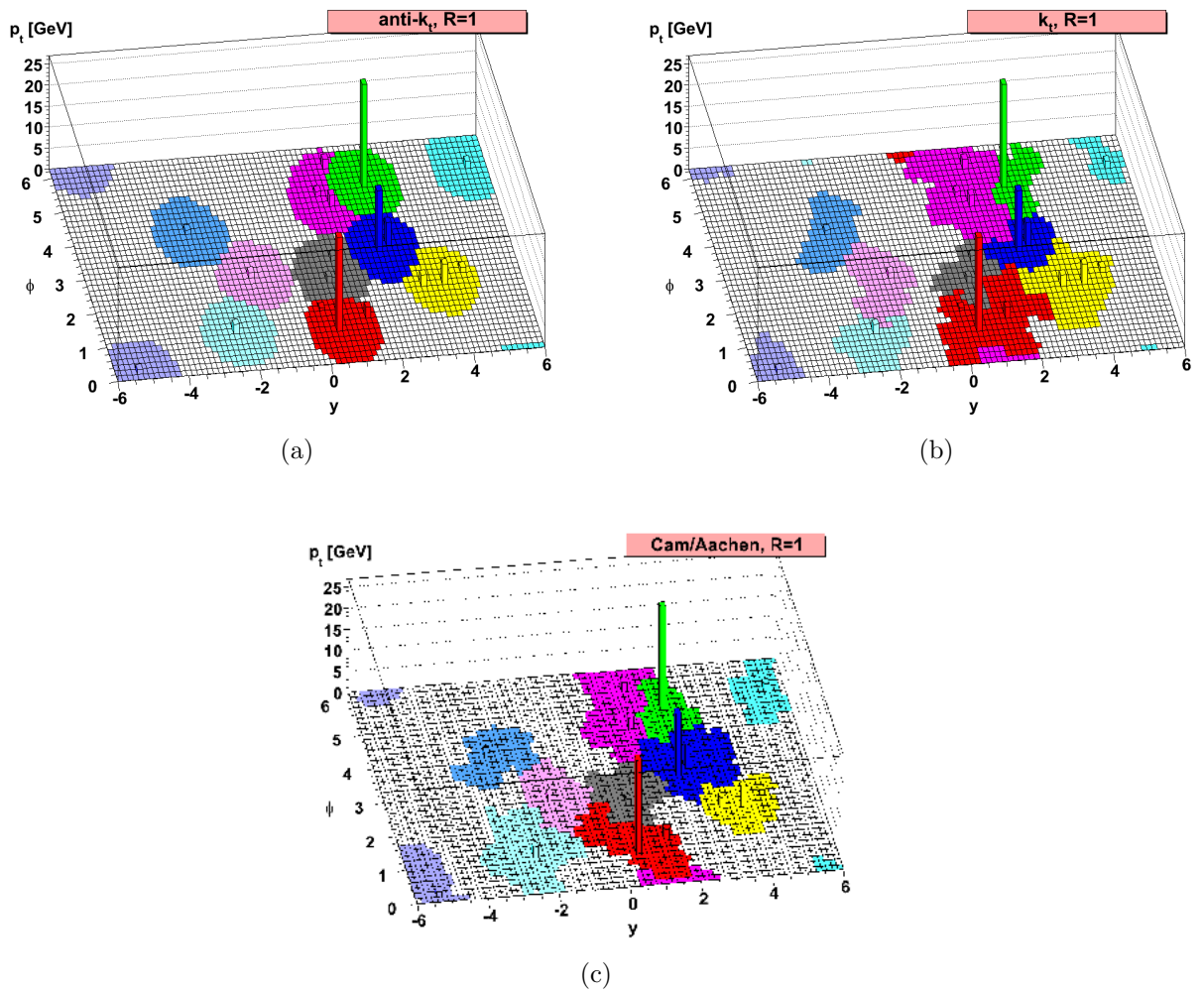


Figure 1.11: (a) Anti- $k_t$  algorithm. (b)  $k_t$  Algorithm. (c) Cambridge-Aachen algorithm. Reproduced from Ref. [11]

# Chapter 2

## Experimental Measurements

Since the true test of any theory is how it compares to experimental data, it is important to understand how the data is collected and analyzed. The purpose of this chapter is to discuss the most important pieces needed to understand the data used in future chapters, and how it was obtained. The main focus will be only on applications to hadron colliders, however, some of the topics are general to all colliders. In this chapter, the needed concepts that are general to all hadron colliders will first be introduced, along with the details that are unique to both the ATLAS and CMS detectors at the LHC.

### 2.1 Basic Concepts

There are many experimental concepts and methods that are general to all hadron colliders. These include the types of data that are collected, the variables that are used to describe the momenta of the particles, and methods of determining particle identities.

Firstly, data is collected in terms of events. An event is an interesting collision between the two incoming hadrons that gets recorded for further analysis. To compare the events that are collected by the experiments, it is necessary to convert either the experimentally measured events into cross-sections, or take the theoretically calculated cross-sections and convert that to the number of expected events. In either case, there is a conversion factor

Cross Section	Process
1 b	cross section of heavy nuclei
30 mb	proton size ( $\pi r^2$ , where $r = 1$ fm)
50 mb	proton-proton inelastic cross-section at the LHC
50 nb	W and Z boson production at the LHC
20 pb	inclusive Higgs boson production at the LHC: $pp \rightarrow H + anything$
100 fb	inclusive $t\bar{t}H$ production at the LHC: $pp \rightarrow t\bar{t}H + anything$

Table 2.1: Representative cross section scales (cross sections are not exact). Reproduced from Ref. [2]

that is used, defined as the luminosity. The instantaneous luminosity is a quantity that measures the intensity, density, and thickness of the beams. The integrated luminosity is simply the integral of the luminosity over a given period of time. The conversion between events and cross-section is given by:

$$\sigma = N \times \mathcal{L}_{int}, \quad (2.1)$$

where  $\sigma$  is the cross-section,  $N$  is the number of events, and  $\mathcal{L}_{int}$  is the integrated luminosity. This however is not the complete picture. This assumes that for every single bunch crossing all of the data is recorded. Since the detector does not cover the full  $4\pi$  region of the collisions an additional factor, called the efficiency ( $\epsilon$ ), needs to be included in Eq. 2.1. The efficiency of the gaps in the detector is modeled through programs such as GEANT4 [115]. Additionally, due to the large number of collisions that occur at these colliders, it is impossible to record every collision. Therefore, there are minimum cuts placed on the momenta of the final state particles, to ensure that the recorded events are of physical interest. This reduces the cross-section and needs to be included in the efficiency factor. In order to understand the need for the momentum cuts, some examples of cross-sections are listed in Table 2.1.

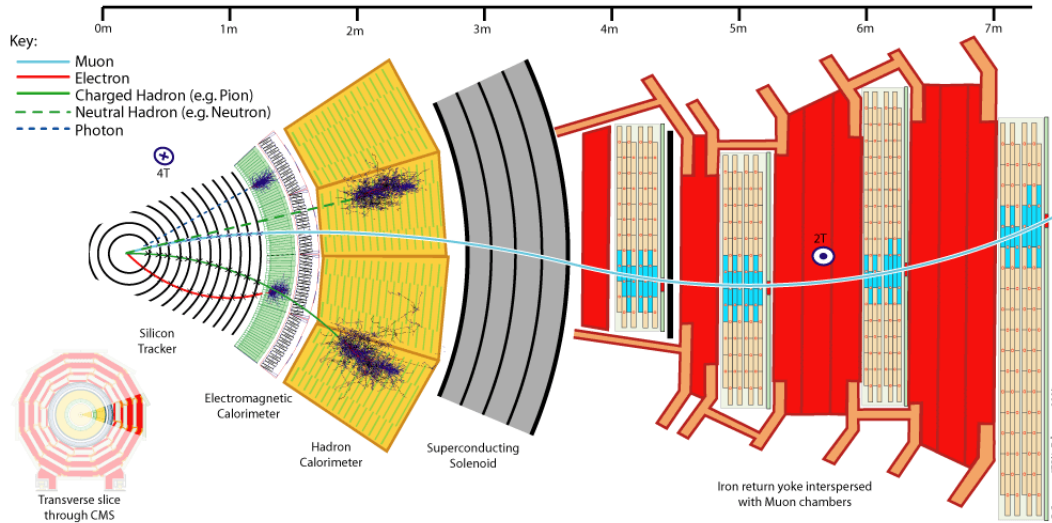


Figure 2.1: Depiction of particles traveling through the CMS Detector. Reproduced from Ref. [12]

## 2.2 Detecting Particles

When recording events, only certain particles can actually be recorded by the detector. These particles are relatively stable, with lifetimes that allow the particle to make it from the collision point to the detector. This reduces the number of particles that can be detected to a list of only seven particles. These include: electrons, muons, photons, pions, kaons, protons, and neutrons. The remaining particles that are produced in the hard interaction either cannot be detected (neutrinos), or decay before they hit the detector (top quarks,  $b$  hadrons). A depiction of a cross-section of the CMS detector at the LHC is shown in Fig. 2.1 to show which pieces of the detector each of the particles interact with. In the previously mentioned figure, the curved tracks are due to charged particles traveling through a toroidal magnetic field. The direction of the curvature is used to determine whether the particle is positively or negatively charged. Additionally, the curvature of the tracks allows the

momentum of the particle to be calculated, recalling from classical Electromagnetism:

$$r = \frac{p}{qB}, \quad (2.2)$$

where  $r$  is the radius,  $p$  and  $q$  are the momentum and charge of the particle respectively, and  $B$  is the strength of the magnetic field.

Another handle on the energy and momentum of the particles is through the use of calorimeters. The calorimeters are classified into two classes, electromagnetic and hadronic. These two classes focus on two different mechanisms to stop the particles. The electromagnetic calorimeter focuses on stopping lighter particles (electrons and photons) through the use of electromagnetic interactions. The hadronic calorimeter is used to stop hadrons, as the name implies, through the use of nuclear interactions. The typical property to define the material used in a calorimeter is the radiation length ( $X_0$ ) and nuclear interaction length ( $\lambda_I$ ) for the electromagnetic and hadronic calorimeters respectively. The typical size of an electromagnetic calorimeter is 15-30  $X_0$ , and for an hadronic calorimeter 5-8  $\lambda_I$  [6]. These detectors tend to be segmented in both azimuthal and rapidity segments in order to obtain direction information and improve reconstruction. The details of how each calorimeter works can be found in Sections 2.2.2, 2.2.3.

### 2.2.1 Trackers

The inner most layer of the detector is known as the tracking system. This layer is used to obtain track paths of charged particles and aid in vertex reconstruction. Furthermore, the tracker is helpful in determining the momentum of charged particles as previously mentioned. The curvature of the path allows for momentum and charge information to be collected. How-

ever, the momentum and charge determined becomes inaccurate at very high momentum, due to the radius becoming too large to detect. The ability to reconstruct the vertex allows the ability to distinguish between particles that come from the hard process versus some background event (underlying event) or from a secondary decay. The beams consist of large bunches of protons, and many may collide in each crossing. An underlying event is another interaction that occurred in the crossing, but is not related to the hard interaction being studied. A secondary decay results in a displaced vertex, and usually arises from events containing  $b$  or  $t$  quarks. Experimentalists have developed techniques to determine massive particles such as  $b$  and  $t$  quarks from these displaced vertices called "tagging". Details on tagging can be found in Section 2.3.1.1.

At ATLAS, the tracking system is formed from three sub-systems. The first layer is the pixel detector [116], which is made up of 92 million silicon pixels covering a rapidity range of  $|\eta| < 2.5$ . As particles pass through the pixels, ionization occurs by creating electron/hole pairs. The resolution of the tracks formed by this system are  $10\mu\text{m}$  in the  $r - \phi$  plane and  $115\mu\text{m}$  along the  $z$ -axis. The next layer is the semiconductor tracker [117, 118], which covers the same rapidity region. However, this system is formed by strips of silicon instead of pixels. This system provides position resolution of  $17\mu\text{m}$  in the  $r - \phi$  plane and  $580\mu\text{m}$  along the  $z$ -axis. Finally, the last sub-system is the transition radiation tracker [119, 120, 121], which covers a rapidity range of  $|\eta| < 2$ . The transition radiation tracker contains a gaseous medium used for producing ionizing radiation needed to obtain tracking information. The resolution of this system is approximately  $170\mu\text{m}$  in the  $r - \phi$  plane, but does not provide information about the particles position along the  $z$ -axis. Through the use of vertex finding algorithms and the tracking data, the resolution of the location of the vertex is about  $10\mu\text{m}$  in the  $r - \phi$  plane, and between  $36\text{-}40\mu\text{m}$  in the  $z$ -axis [122].



At CMS, the tracking system also consists of multiple sub-systems [123, 124]. The first layer is again a silicon pixel detector containing 66 million pixels with a resolution of the tracks at the  $10\text{-}15\mu\text{m}$  level in the  $r - \phi$  plane, and a resolution of  $150\mu\text{m}$  in the  $z$ -direction, covering the rapidity range of  $|\eta| < 2.5$ . The second layer is a silicon strip tracker, consisting of  $70\text{ m}^2$  silicon micro-strips. The strip tracker also covers the same rapidity range as the pixel detector, and has a resolution on position of approximately  $20\mu\text{m}$  in the  $r - \phi$  plane, and a resolution of about  $500\mu\text{m}$  in the  $z$ -axis. The CMS collaboration decided to not use a gas system for position measurements in order to have their tracking system all of the same material. The combination of all of these systems, along with the algorithms implemented to determine track information results in a vertex resolution of  $10\text{-}12\mu\text{m}$  in all three spacial directions [125].

### 2.2.2 Electromagnetic Calorimeters

The method of stopping particles in electromagnetic calorimeters is through electromagnetic showers. The primary method of energy loss is through ionization, but Møller scattering, Bhabha scattering, and annihilation also play a role, as seen in Fig. 2.2 for lead [6]. The energy resolution of an electromagnetic calorimeter ( $\sigma/E$ ) can be parameterized as:

$$\frac{\sigma}{E} = \frac{a}{\sqrt{E}} \oplus b \oplus \frac{c}{E}, \quad (2.3)$$

where  $E$  is the energy of the particle in GeV, and  $\oplus$  means that the terms are added in quadrature. For the LHC, the electromagnetic calorimeter resolution is:  $2.8\%/\sqrt{E} \oplus 0.3\% \oplus 12\%/E$  for CMS [126] and  $10\%/\sqrt{E} \oplus 0.7\% \oplus 0.170/E$  for ATLAS [127]. The response of electromagnetic calorimeters is well understood, and is simulated accurately in both the

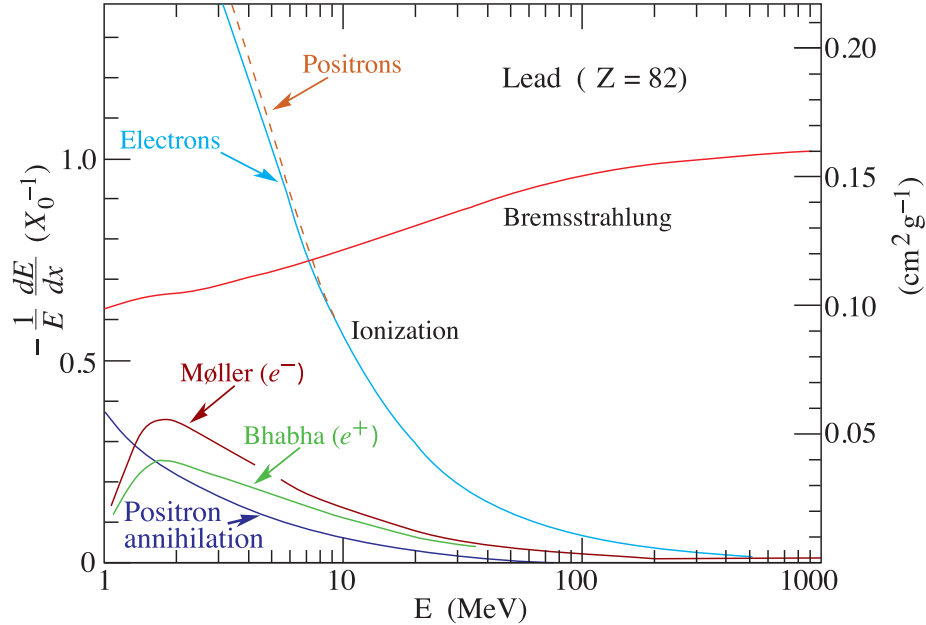


Figure 2.2: Fractional energy loss per radiation length in lead as a function of electron or positron energy. Reproduced from Ref. [6]

EGS4 [128] and GEANT [115] Monte Carlo detector simulators.

### 2.2.3 Hadronic Calorimeters

Unlike electromagnetic calorimeters, hadronic calorimeters are more difficult. The size of the calorimeter needs to be approximately 30 times larger than the electromagnetic calorimeter in order to absorb the same fraction of the particle's energy. Additional complications in measuring energy deposits arise from large fluctuations in neutron production, undetectable energy loss to nuclear disassociation, and other effects [6]. At both the ATLAS and CMS detector, the hadronic calorimeters are behind the electromagnetic calorimeters. The type of calorimeters used at the LHC are known as sampling calorimeters. This means that the calorimeter is made up of alternating layers of dense absorbers and plastic scintillators.

The absorber layers allow for the hadrons to interact, creating secondary particles. These

particles form a hadronic shower. When the particles pass through the scintillators, light is created and then through the use of wavelength-shifting fibers are transmitted to electronic readout equipment [6].

Furthermore, the resolution of hadronic calorimeters are lower than the resolution of electromagnetic calorimeters, due to the fact that the hadronic showers are broader than electromagnetic showers. The energy response of hadronic calorimeters tend not to be linear since the energy deposited arises from both hadronic and electromagnetic showers. This further adds to the complexity of measuring final state jets. The energy resolution at CMS is given by a stochastic term,  $a = 84.7\%$ , and a constant term,  $b = 7.4\%$  [129]. The energy resolution at ATLAS is given by a stochastic term,  $a = 41.9\%$ , a constant term,  $b = 1.8\%$ , and with  $c = 1.8$  [130].

## 2.2.4 Muon Spectrometers

As mentioned in Sec. 1, muons are second generation leptons. Muons have a lifetime of  $2.2\mu\text{s}$ , and are about 200 times heavier than an electron. Due to these properties, muons escape from the colliders with minimal energy loss as it transitions through the trackers and calorimeters. Therefore, it is necessary to have additional detectors outside of these systems to gain additional information on the muons in order to accurately determine their momentum.

The momentum and charge of a muon is determined by the sagitta of the tracks formed in magnetic fields. A sagitta is the distance from the center of a circular arc to the center of the base. The measurement of the sagitta in the inner tracker is combined with that from the muon spectrometer in order to improve the precision of the measurement.

In the ATLAS detector, the muon spectrometer is made up of four main sub-systems.

These systems consist of the Monitored Drift Tube (MDT) chambers, the Cathode Strip Chambers (CSC), the Resistive Plate Chambers (RPC), and the Thin Gap Chambers (TGC) [131]. These sub-systems can be divided into two sub-groups. The first group, consisting of the MDT chambers and the CSC, is responsible for high precision tracking and momenta measurements. The second group, consisting of the RPC and the TGC, is used as inputs for the trigger system. The goal of the precision tracking components are to be able to measure the momentum of a 1 TeV muon to an accuracy of 10%, resulting in a requirement on the accuracy of the sagitta to be measured to a resolution of approximately  $50\mu\text{m}$ . The MDT chambers cover the rapidity region  $|\eta| < 2.7$ , and are used to obtain the z component of the position, while the CSC is responsible for the R component in the range of  $2.0 < |\eta| < 2.7$  for muon rapidity. The need for the CSC is to measure the high flux of muons in the forward direction, which is unable to be handled by the MDT chambers. Finally, the RPC and TGC do not have very accurate position determination, but are optimized instead for fast response times in order to interface with the muon trigger electronics. This allows for accurate bunch-crossing identifications in order to properly reconstruct events. However, this means that these systems need to provide coverage over  $|\eta| < 2.4$  and over the entire  $\phi$  range.

In the CMS detector, the muon spectrometer is made up of three main sub-systems. These systems consist of a RPC, a CSC, and a Drift Tube Chambers (DT) [132]. The RPCs are used in both the barrel and the endcap solely for the purpose of being used for the trigger system. The response time is approximately 1.3ns, guaranteeing a precise identification of the bunch crossing. The endcaps use the CSC to provide precise time and position measurements, and are able to handle the high flux and complex magnetic field. This system is able to obtain a spatial resolution by approximately  $100 - 240\mu\text{m}$ . Finally,

the DT chambers are used in the barrel region to obtain precise position measurements, and from a single hit is able to obtain a precision of approximately  $190\mu\text{m}$ . Combining these systems into many stations, CMS is able to obtain a resolution on the momentum between 5 – 13% for momentums of 1 TeV if the inner tracker information is also used.

## 2.3 Physics Objects

Experimentally, all that is measured are energy deposits. Therefore, it is important to separate these contributions into the fundamental particles that lead to the energy deposits, in order to study the underlying physics. The major objects that these deposits or lack of a deposit can be grouped into: jets, leptons, and missing energy. It is also possible to use tracks to measure particles with a short but non-negligible lifetime through the use of offset vertices from the major interaction point, this is known as tagging.

### 2.3.1 Jets

The definition of jets for experimentalists, is a collimated spray of hadrons that fall within a given cone. Typically, the reconstruction of jets at the LHC is through the use of the anti-kt algorithm, see Section 1.3.4 for details. The dominant uncertainties arise from the absolute energy scale and the jet energy resolution, or in other words, the relationship between jets formed in simulations and from those actually reconstructed in the detector [2]. To help validate this, a comparison between dijet events, and photon plus jet events are compared. In addition to understanding the jets as a complete object, it is important at the LHC to begin to probe into the substructure of jets. Some of these techniques are described below.

### 2.3.1.1 B-Tagging

There are a few different algorithms that are implemented in tagging the decay of  $b$  hadrons. These include techniques that range from looking at signed significance of the decay length to ones that use both secondary vertex and impact parameters [133]. These are combined using multivariate methods to obtain the best discrimination possible.

One class of algorithms are known as lifetime-based tagging, which is based on the fact that a  $b$  hadron with a  $p_T \approx 50$  GeV will travel approximately 3mm before decaying [133]. This will leave behind a displaced vertex inside the tracker from which the charge particles produced from the decay of the  $b$  hadron lead back to. The algorithms in this class try to identify this topology in the events, and are broken into two sub-categories: impact parameter algorithms, and vertex algorithms.

Impact parameter algorithms compute the impact parameters with respect to the primary vertex. The transverse impact parameter is assigned to separate the tracks from the decay from the hard interaction tracks. The sign of the momentum is positive if the secondary vertex is in front of the primary vertex, and negative otherwise. An implementation of this algorithm is known as JetProp [134], which was used at LEP and the Tevatron.

The vertex algorithm uses a three dimensional reconstruction of the vertex formed by the decay products of the  $b$  hadron. The invariant mass of the charged tracks are used to help reject vertices due to decays of  $K_s$  and  $\Lambda$  particles, along with photon conversions [133]. An example implementation of an algorithm which uses the secondary vertex to tag  $b$ -jets is known as JetFitter [135].

Another class of algorithms that are used to tag  $b$ -jets is muon-based algorithms. Muons are produced from the decay of the  $b$  hadrons either directly, or indirectly through the decay

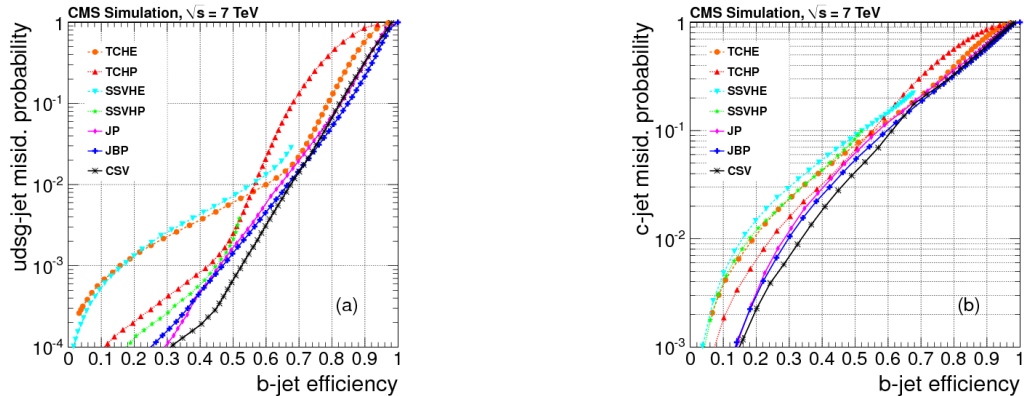


Figure 2.3: Performance curves obtained for different  $b$ -tagging algorithms using simulated data. (Left) The mis-identification for light jets. (Right) The mis-identification for  $c$  jets. Plots are reproduced from Ref. [13]

of the subsequent  $c$  hadrons. The efficiency of these types of algorithms tend to be lower than that of lifetime-based algorithms, due to the fact that the branching ratio to muons is only about 20%. However, the Soft Muon Tagger used by ATLAS does not use any lifetime information, therefore making it a complementary method [133]. This method looks for muons that are within  $\Delta R(jet, \mu) < 0.5$  and other additional selection criteria.

These sets of algorithms are then combined using multivariate techniques as previously mentioned. The results for the combined tagging efficiency to mis-identified jets and tagging efficiency to mis-tagging  $c$  jets at CMS can be found in Fig. 2.3.

### 2.3.2 Leptons

When measuring leptons, there are a few sub-groups that are used in order to classify them more thoroughly. This list consists of prompt, non-prompt, tight, loose, and fake leptons.

Prompt leptons are those that come from the decays of a  $W$ ,  $Z$ ,  $\gamma$ , top, Higgs, or some new physics and not associated with a jet. A lepton that is associated with a jet is the result of the decay of a short lived hadron and is known as a non-prompt lepton.

The identification of tight and loose leptons refer to the set of selection criteria that are applied to an experimental object during reconstruction. Tight criteria are used to help ensure that the object is more likely to be a prompt lepton, and therefore prompt leptons should pass tight selection criteria with a very high efficiency and non-prompt should not. Loose selection criteria would be able to reconstruct both prompt and non-prompt leptons, but also have the chance to identify an object that is not a lepton as a lepton. This leads to the last identity, fake leptons. Since the tight selection criteria will not guarantee that the object is a prompt lepton let alone an electron at all, a fake lepton is used to describe such objects. Experimentally, there is not much that can be done to handle fake leptons. The best method is to estimate the probability of fake leptons passing the tight lepton criteria and to remove the contributions from the final result on average. However, removing fake leptons is impossible on an event-by-event basis.

### **2.3.3 Missing Transverse Energy**

As mentioned above, there are means to detect charged particles, photons, and neutral hadrons. However, particles that are neutral and have lifetimes that are long enough to escape from the detector before decaying are not detected at all. In the SM, the only such particle is the neutrino, but there may exist additional particles that also have these properties. It is still possible to interpret the energy in the transverse direction that these particles had, and to know its azimuthal angle, but not its rapidity. The transverse components are simply obtained through the use of conservation of momentum, since the beams only have momentum along the beam axis, the total transverse momentum must sum to zero. Complications arise for this measurement due to gaps in the detector, and imperfect energy resolution. The accuracy on the missing transverse energy at ATLAS has a stochastic



behavior with  $a = 0.55$  [136] and CMS has a stochastic behavior with  $a = 0.63$  [137].

The particles that are inferred from the missing transverse energy measurement are neutrinos, dark matter candidates, and other exotic particles that may or may not exist. In this work, the missing transverse energy will be solely used for neutrinos in determining the  $W$  boson mass (Chap. 5). The  $W$  boson mass is an important measurement that strongly depends on both resummation and an ability to accurately measure the missing transverse energy.

# Chapter 3

## Resummation

When performing fixed-order calculations, the calculation is organized by the power of  $\alpha_s$ . fixed-order calculations make sense when each term in the series is smaller than the previous term. However, there are certain phase space points that result in each subsequent term being larger than the previous one, causing the breakdown of the fixed-order calculation. To resolve this, resummation is introduced. Resummation reorganizes that calculation by noticing that there are certain terms that appear at every order in  $\alpha_s$  [138]. These terms that appear in a specific form at each order are logarithms of two scales, e.g.  $\log\left(\frac{Q^2}{q_T^2}\right)$ . The number of logarithmic terms included in the calculation is denoted by leading log for having only the leading term, and adding next-to for each additional log term included. Table 3.1 shows the difference between the organization of a fixed-order calculation and a resummed calculation.

	LL	NLL	NNLL	NNNLL	...	$N^k$ LL
LO	1					
NLO	$\alpha_s \log^2$	$\alpha_s \log$	$\alpha_s$			
NNLO	$\alpha_s^2 \log^4$	$\alpha_s^2 \log^3$	$\alpha_s^2 \log$	$\alpha_s^2$		
$\vdots$	$\vdots$	$\vdots$	$\vdots$	$\vdots$	$\ddots$	
$N^k$ LO	$\alpha_s^k \log^{2k}$	$\alpha_s^k \log^{2k-1}$	$\alpha_s^k \log^{2k-2}$	$\alpha_s^k \log^{2k-3}$	...	$\alpha_s^k$

Table 3.1: The organization of fixed-order and resummed calculations. Going across a row is the fixed-order calculation included at a given order of  $\alpha_s$ , while going down the columns is the resummed calculation up to the given power of the logs included.

This chapter introduces the Collins-Soper frame, which resummation is typically performed in, followed by the calculation of Drell-Yan to next-to-leading order as an example of a fixed-order calculation. Additionally, it will be shown how the fixed-order calculation breaks down at each order in perturbation theory for the transverse momentum of the vector boson. This will then lead into the derivation of the resummation formalism, a discussion of the resummation scheme, and the non-perturbative function. Reproducing the fixed-order calculation from the resummed calculation is an important cross-check of the resummation formalism, and also the asymptotic piece needs to be obtained to allow the resummed piece to properly match to the fixed-order result at high transverse momentum. Finally, the scale dependence of the resummation formalism is calculated.

### 3.1 Collins-Soper Frame

The Collins-Soper (CS) Frame is a special reference frame in which  $q_T$  resummation is typically performed [139]. Here the details of the Lorentz transformations between lab and  $CS$  frame are given for completeness. The lab frame is the the center of mass frame of the colliding hadrons. In this frame, the momentum of the two colliding hadrons are given by:

$$p_{h_1, h_2}^\mu = \frac{\sqrt{S}}{2} (1, 0, 0, \pm 1), \quad (3.1)$$

where  $h_1, h_2$  are the two incoming hadrons and  $\sqrt{S}$  is the center of mass energy of the collider. The Collins-Soper frame is a special rest frame of the vector boson. In this frame, the z-axis is defined to bisect the angle between the hadron momentum  $p_{h_1}$ , and the negative of the hadron momentum  $p_{h_2}$  in the CS frame, shown in Fig. 3.1.

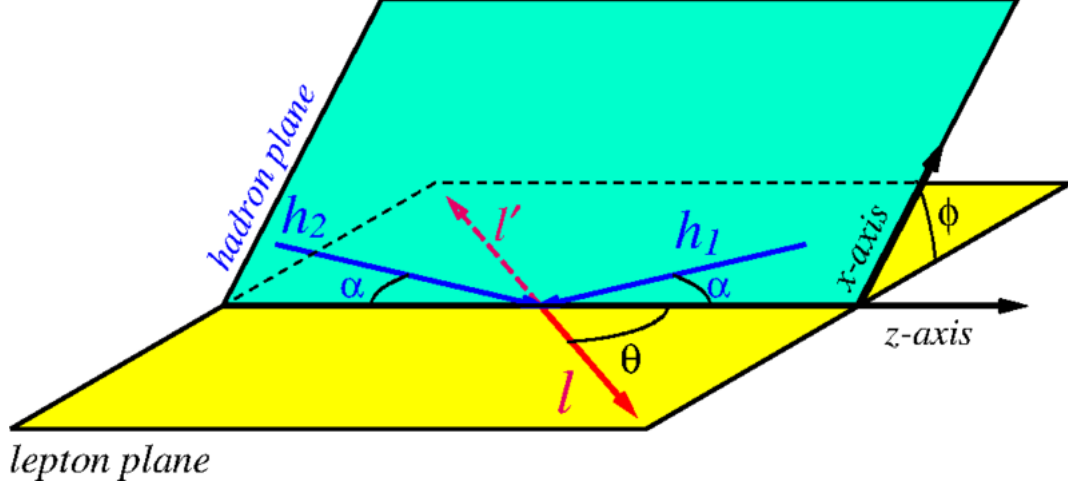


Figure 3.1: Depiction of the Collins-Soper Frame. Reproduced from [14].

Define the Lorentz transformation between the lab and CS frames as  $\Lambda_{\nu}^{\mu}$ :

$$p_{CS}^{\mu} = \Lambda_{\nu}^{\mu} p_{lab}^{\nu}. \quad (3.2)$$

Since the amplitude is independent of the  $\phi$  angle in the lab frame, without loss of generality, the  $\phi$  angle will be taken to be zero. The transformation can be performed in two-steps. First, the lab frame is boosted to the rest frame of the vector boson. Secondly, the frame is then rotated such that the z-axis bisects the angle formed by the momentum  $p_{h_1}^{\mu}$  and  $-p_{h_2}^{\mu}$ .

The boost factor from the lab frame to the rest frame is defined by  $\vec{\beta} = \frac{\vec{q}}{q_0}$ , where  $\vec{q}$  is the 3 momentum, and  $q_0$  is the energy of the vector boson in the lab frame. Boosting by  $\vec{\beta}$  brings any four vector from the lab frame to the rest frame of the vector boson. The explicit Lorentz transformation matrix in terms of the momentum of the vector boson in the lab

frame, is given by:

$$\Lambda_{\nu}^{\mu} = \frac{1}{Q} \begin{pmatrix} q^0 & -q_T & 0 & -q^3 \\ -q_T & Q + \frac{q_T^2}{q^0+Q} & 0 & \frac{q_T q^3}{q^0+Q} \\ 0 & 0 & Q & 0 \\ -q^3 & \frac{q_T q^3}{q^0+Q} & 0 & Q + \frac{(q^3)^2}{q^0+Q} \end{pmatrix}, \quad (3.3)$$

where  $Q = \sqrt{(q^0)^2 - q_T^2 - (q^3)^2}$  is the invariant mass of the vector boson,  $q_3$  is the momentum along the z-axis, and  $q_t$  is the transverse momentum of the vector boson in the lab frame.

After the boost, a rotation is applied to ensure that the z-axis bisects the angle formed between  $p_{h_1}$  and  $-p_{h_2}$ . Once the boost given in Eq. 3.3 is performed, the momentum of the incoming hadrons are given by:

$$p_{h_1, h_2}^{\mu} = \frac{\sqrt{S}}{2} \left( \frac{q^0 \mp q^3}{Q}, -\frac{q_T}{Q} \frac{q^0 + Q \mp q^3}{q^0 + Q}, 0, \frac{(\pm Q - q^3)(q^0 + Q) \pm (q^3)^2}{Q(q^0 + Q)} \right). \quad (3.4)$$

In the case that  $q_T$  is zero, there is no needed rotation. However, in general  $q_T \neq 0$ , and an additional rotation is needed. To keep the hadronic momentum in the  $x - z$  plane, the rotation should be made around the y-axis. The angle for the rotation is given by:

$$\alpha = \arccos \left[ Q \left( q^0 + M_T \right) / \left( M_T \left( q^0 + Q \right) \right) \right], \quad (3.5)$$

where  $M_T$  is the transverse mass given by  $M_T = \sqrt{Q^2 + q_T^2}$ .

Combining the two transformations given in Eqs. 3.3 and 3.5 into a single Lorentz transform gives the full transformation from the CS to the lab frame, which is given by the

Lorentz matrix:

$$\Lambda_{\nu}^{\mu}(CS \rightarrow lab) = (\Lambda_{\nu}^{\mu}(lab \rightarrow CS))^{-1} = \frac{1}{QM_T} \begin{pmatrix} q^0 M_T & q^0 q_T & 0 & q^3 Q \\ q_T M_T & M_T^2 & 0 & 0 \\ 0 & 0 & Q M_T & 0 \\ q^3 M_T & q^3 q_T & 0 & q^0 Q \end{pmatrix}. \quad (3.6)$$

The kinematics of the leptons from the decay of the vector boson are completely determined by two angles (polar and azimuthal) defined in the Collins-Soper frame. Taking the lepton momentum in the CS frame, and using the transformation given in Eq. 3.6, gives the lepton momentum in the lab frame. The momentum for the fermion and the anti-fermion in the lab frame are given by:

$$p^{\mu} = \frac{Q}{2} \left( \frac{q^{\mu}}{Q} + \sin \theta \cos \phi X^{\mu} + \sin \theta \sin \phi Y^{\mu} + \cos \theta Z^{\mu} \right), \bar{p}^{\mu} = q^{\mu} - p^{\mu},$$

where  $p^{\mu}(\bar{p}^{\mu})$  is the (anti-)fermion momentum,  $q^{\mu}$  is the vector boson momentum in the lab frame,  $X$ ,  $Y$ , and  $Z$  are the axes in the CS frame given by the lab frame momentum. The anti-fermion momentum is simply obtained by conservation of momentum. The vector boson momentum and axes in the lab frame are defined as:

$$\begin{aligned} q^{\mu} &= (M_t \cosh y, q_t \cos \phi_V, q_t \sin \phi_V, M_t \sinh y), \\ X^{\mu} &= -\frac{Q}{q_t M_t} \left( q_+ n^{\mu} + q_- \bar{n}^{\mu} - \frac{M_t^2}{Q^2} q^{\mu} \right), \\ Z^{\mu} &= \frac{1}{M_t^2} (q_+ n^{\mu} - q_- \bar{n}^{\mu}), \\ Y^{\mu} &= \epsilon^{\mu\nu\alpha\beta} \frac{q_{\nu}}{Q} Z_{\alpha} X_{\beta}, \end{aligned} \quad (3.7)$$

where,  $q_{\pm} = \frac{1}{\sqrt{2}}(q^0 \pm q^3)$ ,  $y = \ln(q_+/q_-)$ ,  $n^{\nu} = \frac{1}{\sqrt{2}}(1, 0, 0, 1)$ ,  $\bar{n}^{\nu} = \frac{1}{\sqrt{2}}(1, 0, 0, -1)$ , and  $\epsilon^{\mu\nu\alpha\beta}$  is the completely anti-symmetric Levi-Civita tensor. With the derivation of the Collins-Soper frame, the act of resummation can now be performed. Next the motivation for resummation will be discussed, followed by the means to perform resummation.

## 3.2 Fixed-Order Calculations

In Quantum Field Theory, calculations are performed order by order in perturbation theory. Calculating the first term in the series is referred to as leading order (LO). Adding an additional term is referred to as next-to-leading order (NLO), etc. The Drell-Yan process ( $pp \rightarrow e^+e^-$ ) is calculated to NLO below in order to illustrate the steps of a fixed-order calculation.

The Feynman diagrams that represent this calculation are shown in Fig. 3.2. Feynman diagrams are a means to pictorially represent the calculation of the scattering matrix element. To simplify the calculation, the hadronic matrix element is separated from the leptonic matrix element. The leptonic matrix element is the same for both the leading order calculation and the next-to-leading order calculation, and the diagram is represented by the right half of each diagram of Fig. 3.2. The result for the leptonic matrix element is given by:

$$L_{\mu\nu} = 4 \left[ 2 \left( f_L^2 + f_R^2 \right) (l_{1\mu}l_{2\nu} + l_{2\mu}l_{1\nu} - g_{\mu\nu} (l_1 \cdot l_2)) + \left( f_L^2 - f_R^2 \right) i\epsilon_{\mu\nu\rho\sigma} q^{\rho} l_{12}^{\sigma} \right], \quad (3.8)$$

where  $q_{\mu} = l_{1\mu} + l_{2\mu}$ ,  $l_{12\mu} = l_{1\mu} - l_{2\mu}$ ,  $l_{1\mu}/l_{2\mu}$  is the momentum of the lepton and anti-lepton respectively, and  $f_{L/R}$  are the left and right handed couplings respectively.

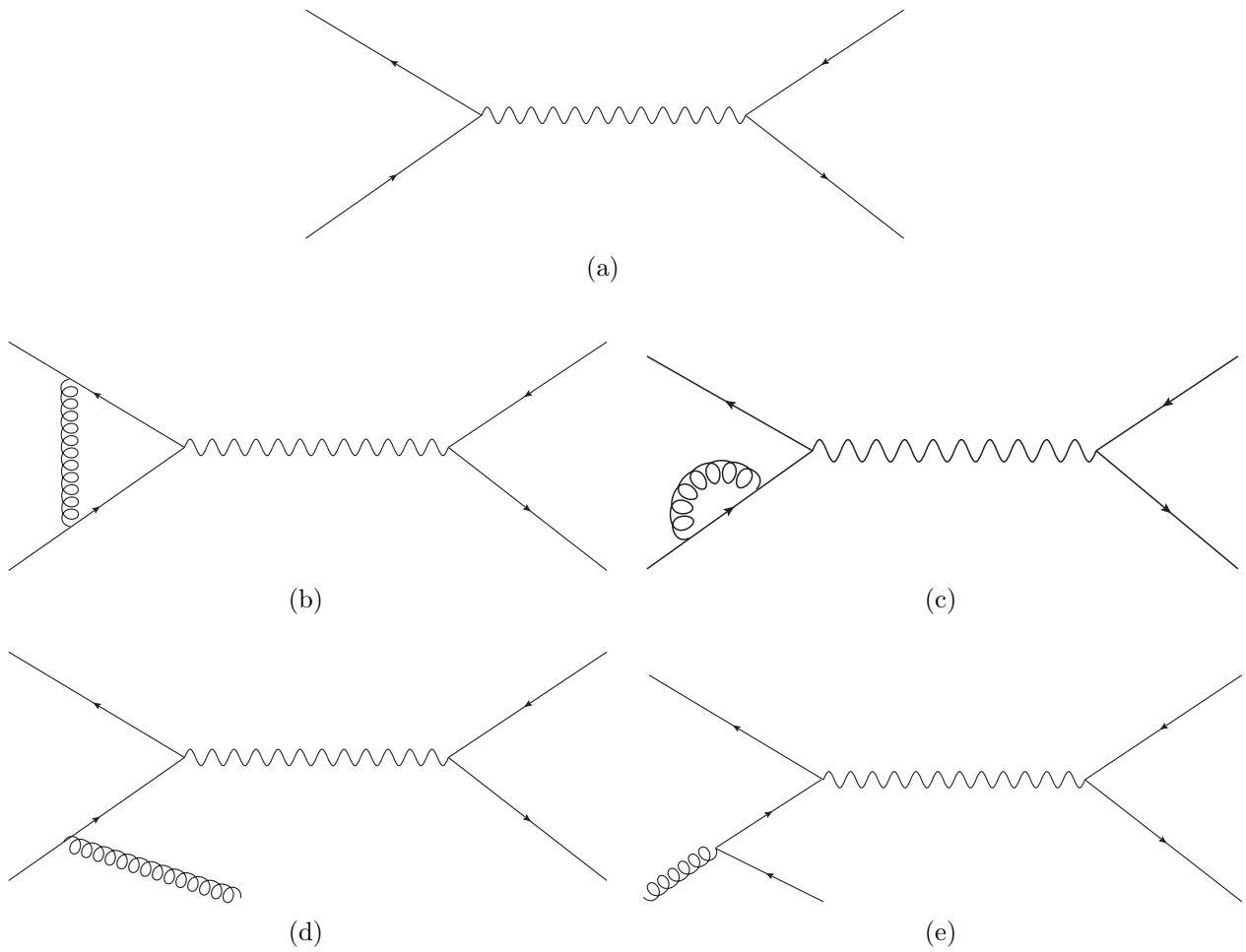


Figure 3.2: The diagrams that contribute to the  $\alpha_s$  correction to Drell-Yan. (a) is the born diagram. (b) is the virtual coupling correction. (c) is the wave function correction. (d) and (e) are the real corrections



The leading order calculation for the hadronic matrix element is done in  $d$ -dimensions, with  $d = 4 - 2\epsilon$ , since this dependence will be needed to obtain the correct result after calculating the virtual correction. The hadronic matrix element is given by:

$$\begin{aligned}
H^{\mu\nu} = 4 & \left[ 2 \left( g_L^2 + g_R^2 \right) \left( p_1^\mu p_2^\nu + p_1^\nu p_2^\mu - g^{\mu\nu} p_1 \cdot p_2 \right) \right. \\
& \left. + \left( g_L^2 - g_R^2 \right) i\epsilon^{\mu\nu\alpha\beta} p_{2\alpha} p_{1\beta} \right], \tag{3.9}
\end{aligned}$$

where  $g_{L/R}$  are the left and right handed coupling of the quarks to the vector boson,  $p_1$  is the momentum of the incoming quark, and  $p_2$  is the momentum of the incoming anti-quark.

At next-to-leading order, both the virtual corrections and real corrections are required. The virtual corrections contain a virtual gluon connecting the two initial state partons (vertex correction, Fig. 3.2b), as well as a virtual gluon connecting one initial parton to itself (self-energy, Fig. 3.2c). However, in Dimensional Regularization the self-energy diagrams do not contribute if the quark is massless, which is the case here. The real correction contains a real gluon being radiated off of one of the external legs, and also a gluon splitting into a quark anti-quark pair, as seen in Figs. 3.2d, and 3.2e respectively. Both of these contributions are required in order to ensure that the soft divergences cancel according to the KLN theorem [140, 141]. The KLN theorem states that in the SM that all IR divergences that arise from loop integrals (virtual corrections), must be canceled by phase space corrections. In addition to these two contributions, the renormalization of the Parton Distribution Function needs to be included to ensure that the final result is completely IR finite.

### 3.2.1 Real Corrections

In performing the calculations of the born contribution, the virtual contribution, and the real contribution, it is possible to separate the leptonic piece of the matrix element from the hadronic piece of the matrix element. First, consider the vector boson gluon final state hadronic matrix element. The matrix element is the sum of the left hand sides of the diagrams in Figs. 3.2d, and 3.2e. Defining the Mandelstam variables as:  $t = (k - q)^2$ ,  $u = (q - l)^2$ , and  $s = (k + l)^2$ , the hadronic matrix element is expressed by:

$$\begin{aligned}
H^{\mu\nu} = & \frac{8}{ut} \left( g_L^2 + g_R^2 \right) \left[ (p_2^\mu p_2^\nu + p_1^\mu p_1^\nu) \left( -4g^2 \right) (1 - \epsilon) \right. \\
& + 4sq^\mu q^\nu \epsilon - g^{\mu\nu} \left( (q^2 - u)^2 + (q^2 - t)^2 \right) (1 - \epsilon) \\
& - g^{\mu\nu} \left( 2q^2 s - 2tu \right) \epsilon + (p_1^\mu q^\nu + q^\mu p_1^\nu) \left( 2 \left( q^2 - t \right) (1 - \epsilon) + 2 \left( -q^2 + u \right) \epsilon \right) \\
& + (p_2^\mu q^\nu + q^\mu p_2^\nu) \left( 2 \left( q^2 - u \right) (1 - \epsilon) + 2 \left( -q^2 + t \right) \epsilon \right) + (p_1^\mu p_2^\nu + p_2^\mu p_1^\nu) \left( 4q^2 \epsilon \right) \left. \right] \\
& + \frac{8}{ut} i \left( g_L^2 - g_R^2 \right) \left[ \epsilon^{\mu\nu\alpha\beta} p_{1\alpha} q_\beta \left( 2(s + u) \right) + \epsilon^{\mu\nu\alpha\beta} p_{2\alpha} q_\beta \left( -2(s + t) \right) \right]. \quad (3.10)
\end{aligned}$$

The hadronic matrix element can be separated into a symmetric and anti-symmetric piece under the change of  $p_1 \rightarrow -p_1$ ,  $p_2 \rightarrow -p_2$ . The symmetric piece is thus:

$$\begin{aligned}
H^{[S]\mu\nu} = & \frac{8}{ut} \left( g_L^2 + g_R^2 \right) \left[ (l^\mu l^\nu + k^\mu k^\nu) \left( -4g^2 \right) (1 - \epsilon) \right. \\
& + 4sq^\mu q^\nu \epsilon - g^{\mu\nu} \left( (q^2 - u)^2 + (q^2 - t)^2 \right) (1 - \epsilon) \\
& - g^{\mu\nu} \left( 2q^2 s - 2tu \right) \epsilon + (k^\mu q^\nu + q^\mu k^\nu) \left( 2 \left( q^2 - t \right) (1 - \epsilon) + 2 \left( -q^2 + u \right) \epsilon \right) \\
& + (l^\mu q^\nu + q^\mu l^\nu) \left( 2 \left( q^2 - u \right) (1 - \epsilon) + 2 \left( -q^2 + t \right) \epsilon \right) + (k^\mu l^\nu + l^\mu k^\nu) \left( 4q^2 \epsilon \right) \left. \right], \quad (3.11)
\end{aligned}$$

and the anti-symmetric piece is:

$$H^{[A]\mu\nu} = \frac{8}{ut} i \left( g_L^2 - g_R^2 \right) \left[ \epsilon^{\mu\nu\alpha\beta} k_\alpha q_\beta (2(s+u)) + \epsilon^{\mu\nu\alpha\beta} l_\alpha q_\beta (-2(s+t)) \right] \quad (3.12)$$

With both the leptonic and hadronic matrix element, the amplitude squared is:

$$\begin{aligned} |M|_{q\bar{q}}^2 &= H^{\mu\nu} L_{\mu\nu} = \frac{64 Q^2}{ut} \frac{1}{2} \\ &\left[ \left( g_L^2 + g_R^2 \right) \left( f_L^2 + f_R^2 \right) \left( a \left( (t - Q^2)^2 + (u - Q^2)^2 \right) + 4 \left( (k \cdot l_{12})^2 + (l \cdot l_{12})^2 \right) \right. \right. \\ &\quad \left. \left. \epsilon \left( -a (t+u)^2 - 4 (k \cdot l_{12} + l \cdot l_{12})^2 \right) \right) \right. \\ &\quad \left. + \left( g_L^2 - g_R^2 \right) \left( f_L^2 - f_R^2 \right) \left( 4 (t - Q^2) (k \cdot l_{12}) - 4 (u - Q^2) (l \cdot l_{12}) \right) \right], \quad (3.13) \end{aligned}$$

where  $a = 1$  in 4-dimensions, and  $a = 1 - \epsilon$  in  $d$ -dimensions. Finally, the color average factor  $(\frac{1}{3} \times \frac{1}{3})$  and the spin average factor  $(\frac{1}{2} \times \frac{1}{2})$ , in addition to a sum over the initial state colors (3) needs to be included in the final result.

To obtain the calculation for quark-gluon initial states, crossing symmetry can be used, which is defined by the following transformation for this process:

$$p_1 \rightarrow p_2, \quad q \rightarrow q, \quad p_1 \rightarrow q - p_1 - p_2, \quad -(p_1 + p_2 - q) \rightarrow p_1, \quad (3.14)$$

$$u \rightarrow s, \quad s \rightarrow t, \quad t \rightarrow u. \quad (3.15)$$

Additionally, the color and spin factors need to be modified since there is now a gluon in the initial state. In  $d$ -dimensions, the spin factor goes from  $\frac{1}{2} \times \frac{1}{2} \rightarrow \frac{1}{2(1-\epsilon)} \times \frac{1}{2}$ , and the color factor is  $\frac{1}{3} \times \frac{1}{3} \rightarrow \frac{1}{8} \times \frac{1}{3}$ . Finally, since there is an exchange of an outgoing particle with an incoming anti-particle, the final result needs to be multiplied by  $(-1)$ . This gives

the amplitude squared as:

$$\begin{aligned}
|M|_{gq}^2 = & 64 \frac{1}{su} \frac{Q^2}{2} \left( (g_L^2 + g_R^2) (f_L^2 + f_R^2) \left( a \left( - (u - Q^2)^2 - (s - Q^2)^2 \right) \right. \right. \\
& - 4 \left( (k \cdot l_{12} + l \cdot l_{12})^2 + (l \cdot l_{12})^2 \right) + \epsilon \left( a (u + s)^2 + 4 (k \cdot l_{12})^2 \right) \left. \right) \\
& + \left( g_L^2 - g_R^2 \right) \left( f_L^2 - f_R^2 \right) \left( -4 (u - Q^2) (l \cdot l_{12}) - 4 (s - Q^2) (k \cdot l_{12} + l \cdot l_{12}) \right).
\end{aligned} \tag{3.16}$$

Similarly, for the anti-quark-gluon initial states, again crossing symmetry can be taken advantage of to obtain the same result as Eq. 3.16, but with a change of sign for the anti-symmetric piece. With the real corrections calculated, the virtual corrections are needed to complete the NLO correction to the Drell-Yan process.

### 3.2.2 Virtual Correction

Finally, to obtain the complete NLO correction to the total cross-section to the Drell-Yan process, the virtual corrections need to be calculated. The diagram that contributes a non-zero result up to one-loop in the strong coupling are given in Fig. 3.2b. When using dimensional regularization to calculate the loop contributions, the loops on massless external legs lead to a contribution of zero, since the loop integral obtained is a scaleless integral, and thus must be zero. From a physics standpoint, this can be seen by the fact that the UV-divergences exactly cancel the IR-divergences in dimensional regularization ( $\epsilon_{UV} = -\epsilon_{IR}$ ). Therefore, only one diagram remains to be calculated. Additionally, when performing the calculation, only the terms proportional to  $\alpha_s$  need to be considered. From this, the virtual matrix element squared does not contribute, but the interference of the one-loop diagram

with the tree-level diagram does. The hadronic matrix element is given by:

$$H_{\text{virtual}}^{\mu\nu} = 4(1 + 2f(\epsilon)) \left( 2 \left( g_L^2 + g_R^2 \right) (k^\mu l^\nu + k^\nu l^\mu - g^{\mu\nu} (k \cdot l)) - 2i \left( g_L^2 - g_R^2 \right) \epsilon^{\mu\nu\alpha\beta} l_\alpha k_\beta \right), \quad (3.17)$$

where

$$f(\epsilon) = \frac{\alpha_s}{4\pi} C_F \left( \frac{4\pi\mu^2}{Q^2} \right)^\epsilon \frac{1}{\Gamma(1-\epsilon)} \left( -\frac{2}{\epsilon^2} - \frac{3}{\epsilon} - 8 + \pi^2 \right). \quad (3.18)$$

Details of obtaining  $f(\epsilon)$  can be found in App. F. The one-loop matrix element squared is thus:

$$|M|_{\text{virtual}}^2 = 16(1 + 2f(\epsilon)) Q^4 \left( \left( g_L^2 + g_R^2 \right) \left( f_L^2 + f_R^2 \right) \left( 2a - 1 + \cos^2(\theta) \right) + \left( g_L^2 - g_R^2 \right) \left( f_L^2 - f_R^2 \right) 2 \cos(\theta) \right). \quad (3.19)$$

Eventually, the limit of  $\epsilon$  to zero will be taken and the divergences in  $f(\epsilon)$  will cancel with those in the real correction once the additional radiation is integrated out and also with the corrections to the PDF.

### 3.3 NLO DY Total Cross-Section

It is convenient to express the matrix elements in terms of angular functions in the Collins-Soper Frame. At this order, the matrix element can be expressed using the following angular

functions:

$$\mathcal{L} = 1 + \cos^2 \theta, \quad (3.20)$$

$$\mathcal{A}_0 = \frac{1}{2} \left( 1 - \cos^2 \theta \right), \quad (3.21)$$

$$\mathcal{A}_1 = \sin 2\theta \cos \phi, \quad (3.22)$$

$$\mathcal{A}_2 = \frac{1}{2} \sin^2 \theta \cos 2\phi, \quad (3.23)$$

$$\mathcal{A}_3 = \cos \theta, \quad (3.24)$$

$$\mathcal{A}_4 = \sin \theta \cos \phi. \quad (3.25)$$

Rewriting the real matrix elements in terms of these angular functions gives the following for the  $q\bar{q}$  channel:

$$|M|_{q\bar{q}}^2 = 64 \frac{(Q^2 - t)^2 + (Q^2 - u)^2}{ut} \frac{Q^2}{2} \left( (g_L^2 + g_R^2) (f_L^2 + f_R^2) (H_1 - \tilde{H}_1 \epsilon) + (g_L^2 - g_R^2) (f_L^2 - f_R^2) H_2 \right), \quad (3.26)$$

where the  $H$  functions are given by:

$$H_1 = \mathcal{L} + \frac{q_T^2}{Q^2 + q_T^2} (\mathcal{A}_0 + \mathcal{A}_2) + \frac{(Q^2 - u)^2 - (Q^2 - t)^2}{(Q^2 - u)^2 + (Q^2 - t)^2} \frac{q_T Q}{Q^2 + q_T^2} \mathcal{A}_1 \quad (3.27)$$

$$\tilde{H}_1 = \mathcal{L} \frac{(t + u)^2}{(Q^2 - u)^2 + (Q^2 - t)^2} + \frac{(Q^2 + s)^2}{(Q^2 - u)^2 + (Q^2 - t)^2} \frac{q_T^2}{Q^2 + q_T^2} (\mathcal{A}_0 + \mathcal{A}_2) \quad (3.28)$$

$$H_2 = \frac{2Q}{\sqrt{Q^2 + q_T^2}} \mathcal{A}_3 + \frac{(Q^2 - u)^2 - (Q^2 - t)^2}{(Q^2 - u)^2 + (Q^2 - t)^2} \frac{2q_T}{\sqrt{Q^2 + q_T^2}} \mathcal{A}_4. \quad (3.29)$$

There is a similar set of relations for the quark-gluon and anti-quark-gluon initial state processes, see App. F. It is important to note that the coefficient of  $\mathcal{A}_0$  and  $\mathcal{A}_2$  is identical at

NLO. This is known as the Lam-Tung relation [142, 143, 144]. A more detailed discussion of the angular functions for Drell-Yan, the breaking of the Lam-Tung relation, and a comparison of the ResBos2 code to LHC data can be found in Sec. 4.3.

In the real diagram, the divergences come from when the gluon becomes soft or collinear to an initial parton. In other words when the transverse momentum of the vector boson goes to zero. In the limit  $q_T \rightarrow 0$ , the terms proportional to  $\frac{1}{q_T^2}$  for the  $q\bar{q}$  channel are:

$$|M|_{\text{singular}}^2 = 64 \frac{Q^2}{2} \left( (g_L^2 + g_R^2) (f_L^2 + f_R^2) \mathcal{K}_1 \mathcal{L} + (g_L^2 - g_R^2) (f_L^2 - f_R^2) 2\mathcal{K}_2 \mathcal{A}_3 \right), \quad (3.30)$$

with

$$\begin{aligned} \mathcal{K}_1 = & \frac{1}{q_T^2} \delta(1 - z_A) \delta(1 - z_B) \left( \ln \left( \frac{Q^2}{q_T^2} \right) - \frac{3}{2} \right) \\ & + \frac{1}{q_T^2} \left( \left( \frac{1 + z_A^2}{1 - z_A} \right)_+ \delta(1 - z_B) \right) \\ & - \frac{\epsilon}{q_T^2} ((1 - z_A) \delta(1 - z_B)) + z_A \leftrightarrow z_B, \end{aligned} \quad (3.31)$$

$$\begin{aligned} \mathcal{K}_2 = & \frac{2}{q_T^2} \delta(1 - z_A) \delta(1 - z_B) \left( \ln \left( \frac{Q^2}{q_T^2} \right) - \frac{3}{2} \right) \\ & + \frac{1}{q_T^2} \left( \left( \frac{1 + z_A^2}{1 - z_A} \right)_+ \delta(1 - z_B) + z_A \leftrightarrow z_B \right), \end{aligned} \quad (3.32)$$

where  $z_{A/B}$  is the partonic momentum fraction of the parton from hadron  $A/B$  respectively, and  $\frac{1}{(1-z)_+}$  is the plus-function and its properties can be found in App. F. There are similar expressions for the quark-gluon and anti-quark-gluon initial states (App. F). The most important difference between the quark-anti-quark and (anti-)quark-gluon expressions is that there are no terms proportional to  $\delta(1 - z_A)\delta(1 - z_B)$  for those with gluons in the initial

state. Integrating out the transverse momentum of the vector boson results in the poles that are needed to cancel the double poles in the virtual correction. In order to obtain a full cancellation of the poles, the parton distribution functions need to be renormalized. Once the poles for the PDF renormalization are included, then all of the poles will be canceled, and a finite result will remain. To obtain the singularities from the real correction, an integral over the phase space is needed. Details on  $d$ -dimensional phase space integrals can be found in App. F. The results of the phase space integration are shown below for the singular terms.

$$\begin{aligned} \frac{d\sigma_{q\bar{q}}^R}{dQ^2} = & \sigma_0 C_F \frac{\alpha_s}{\pi} \left( \frac{4\pi\mu^2}{-Q^2} \right)^\epsilon \frac{1}{\Gamma(1-\epsilon)} \left( \frac{2}{\epsilon^2} \delta(1-z) - \frac{2(1+z)^2}{\epsilon(1-z)_+} \right. \\ & \left. + 4(1+z^2) \left( \frac{\ln(1-z)}{1-z} \right)_+ - 2 \left( \frac{1+z^2}{1-z} \right) \ln z \right). \end{aligned} \quad (3.33)$$

Similarly, performing the phase space integration over the virtual result gives the following results:

$$\frac{d\sigma_{q\bar{q}}^V}{dQ^2} = \sigma_0 C_F \frac{\alpha_s}{\pi} \left( \frac{4\pi\mu^2}{-Q^2} \right)^\epsilon \frac{1}{\Gamma(1-\epsilon)} \left( -\frac{2}{\epsilon^2} - \frac{3}{\epsilon} - 8 + \pi^2 \right) \delta(1-z). \quad (3.34)$$

Comparing Eqs. 3.33 and 3.34 the terms proportional to  $1/\epsilon^2$  cancel, as required by the KLN theorem. However, there remains a divergence which is canceled by the definition of the parton distribution functions. The singularities of the PDFs are:

$$\frac{2}{\epsilon} C_F \frac{\alpha_s}{\pi} \left( \frac{(1+z)^2}{(1-z)_+} + \frac{3}{2} \delta(1-z) \right), \quad (3.35)$$

which exactly cancels the remaining poles. Combining the real and virtual correction results in the total cross-section for Drell-Yan at NLO. At this order, the result is completely UV



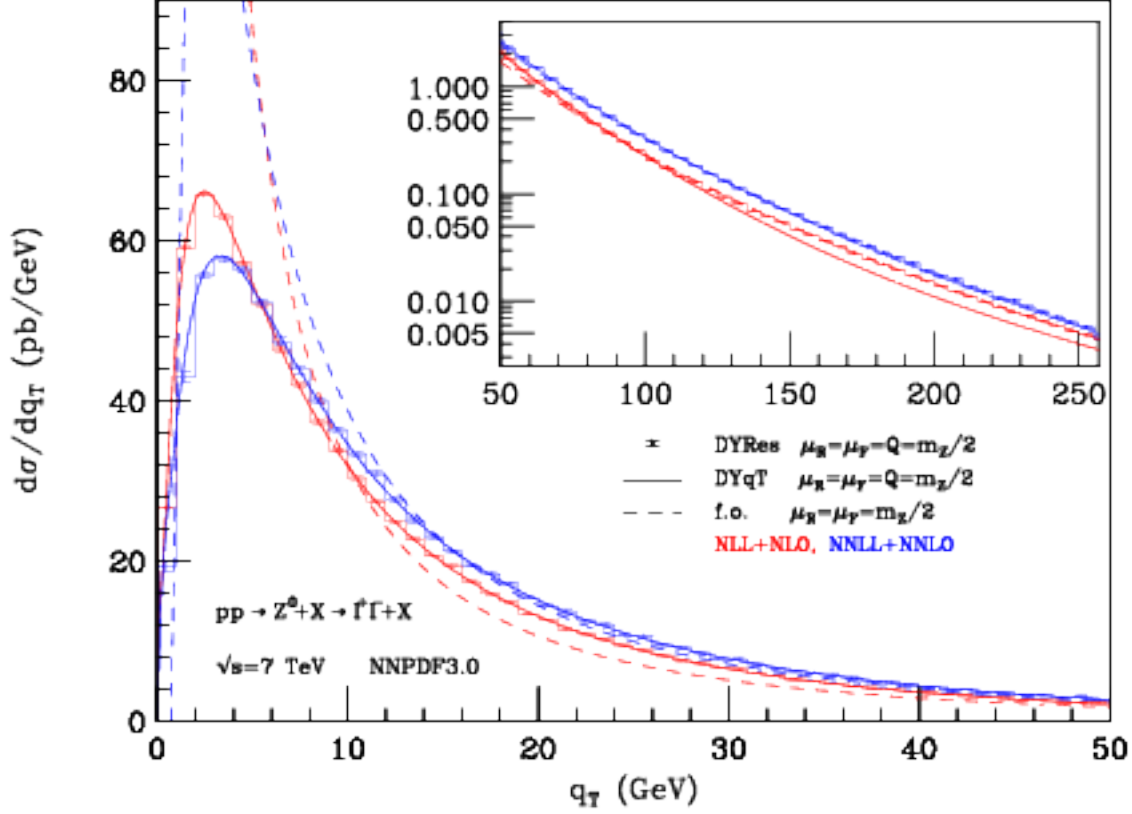


Figure 3.3: Plot showing fixed-order versus resummed predictions. The dashed curves correspond to fixed-order calculations, and the solid curves correspond to resummed predictions. The plot is reproduced from Ref. [15]

finite. At higher corrections in  $\alpha_s$  this is no longer true, and requires the strong coupling to be renormalized as discussed in Section 1.3.2. Details on the calculations to NNLO can be found in [145], and parts of the calculations to N<sup>3</sup>LO can be found in [146, 147, 148].

### 3.3.1 Breakdown of Fixed-Order

When using fixed-order calculations, certain distributions contain integrable singularities, resulting in nonsense theoretical predictions in certain kinematical regions. For example, the transverse momentum distribution of the vector boson in Drell-Yan displays such properties. This is seen in the  $q_T$  distribution at NLO and NNLO for Drell-Yan in Fig. 3.3.

As the calculation is performed at higher and higher orders the small  $q_T$  region will

oscillate, as seen in Fig. 3.3 comparing the red dashed (NLO) and blue dashed (NNLO) predictions. As the orders increase, the result continues to oscillate, but will never reach a stable result until all orders of the calculation are included. The solution to this problem is the introduction of the resummation formalism, which sums up the large logarithms that appear at each order in the fixed-order calculation.

### 3.4 Resummation Formalisms

The dynamics of multiple soft-gluon radiation in scattering processes is treated through the use of the resummation formalism [149, 150, 151, 152, 153]. There are many applications of resummation at modern colliders. In this work, the focus will be on the treatment of transverse momentum resummation. The formalism was originally shown to be possible for all the large logarithms (leading and subleading) to all orders by Collins, Soper, and Sterman [138]. The formalism developed in their work will be referred to as the CSS Formalism. A more recent formalism was developed by Catani, de Florian, and Grazzini, which is known as the CFG Formalism [154]. The details of the two formalisms are explained in Sec. 3.4.1 and Sec. 3.4.2 respectively. The differences between the two formalisms are highlighted in Sec. 3.4.3. The remainder of this section will focus on the general outline of  $q_T$  resummation.

Firstly, resummation is a means to relate the different scales of a multi-scale process to a single scale, which also removes the large logarithms that result from the large difference between the scales. Therefore, the first step is to factorize the cross-section calculation into the different scale regions that are involved in the calculation. The regions that are important to this work are known as the hard factor, the soft factor, and the collinear or jet factors. A diagrammatic representation of each piece for the Drell-Yan process can be seen in Fig. 3.4,

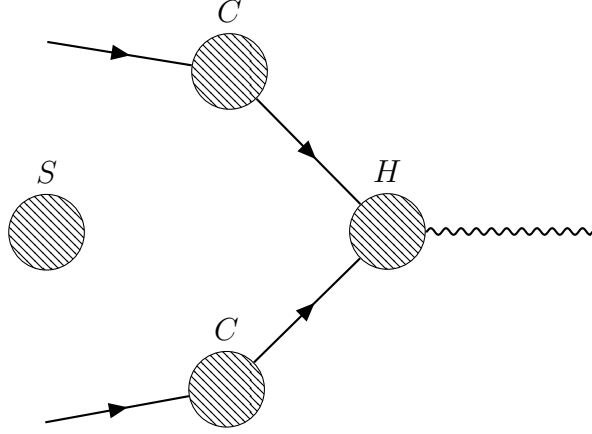


Figure 3.4: A diagrammatic representation of the factorized cross-section for Drell-Yan, broken into a soft, collinear, and hard factor. The soft factor is labeled by the  $S$ , the collinear factors are labeled by the  $C$ 's, and the hard factor is labeled by the  $H$

and can be expressed as:

$$\frac{d\sigma}{dQ^2 dy dq_T^2} \propto H(\mu) S(\mu, \mu_R) C_1(\mu, \mu_F) C_2(\mu, \mu_F) J(\mu, R\mu'), \quad (3.36)$$

where  $H$  is the hard factor,  $S$  is the soft factor,  $C_1$  and  $C_2$  are the collinear factors for each incoming hadron, and  $J$  is the jet factor. The remainder of the section is to discuss the calculation of the soft factor, and derive the well known Sudakov factor. Starting from the fixed-order calculation up to the  $n^{\text{th}}$  order in  $\alpha_s$ , the result can be split into a singular piece, and a regular piece. The singular piece are terms that are proportional to  $\frac{1}{q_T^2} \log^m \left( \frac{Q^2}{q_T^2} \right)$  ( $m = 0, 1, \dots, 2n - 1$ ) and  $\delta(q_T)$ , and the regular terms are less singular than those previously mentioned. As detailed in Sec. 3.3.1, this calculation breaks down when  $\alpha_s^n \frac{1}{q_T^2} \log^m \left( \frac{Q^2}{q_T^2} \right)$  becomes large.

To resolve this issue, the logarithms need to be summed to all orders to obtain a finite result in the limit  $q_T \rightarrow 0$ , and remove all large logarithms from the final result. In order to perform the resummation correctly, the cross-section needs to be Fourier transformed into

impact parameter ( $b$ ) space. In impact parameter space, the total transverse momentum is explicitly conserved [155]. After the Fourier transform, the cross section can be expressed as:

$$\frac{d\sigma}{dQ^2 dq_T^2 dy} = \frac{1}{(2\pi)^2} \int d^2b e^{i\vec{q}_T \cdot \vec{b}} \tilde{W}(b, Q, x_1, x_2) + Y(q_T, Q, x_1, x_2), \quad (3.37)$$

where  $\tilde{W}$  contains the resummation of the singular pieces of the cross section, and  $Y$  contains the regular pieces of the cross section defined by taking the fixed-order calculation and subtracting the asymptotic piece. The asymptotic piece contains the terms that are at least as singular as  $\frac{1}{q_T^2}$  in the fixed-order calculation in the limit  $q_T \rightarrow 0$ . The calculation of the asymptotic piece up to  $\alpha_s^3$  can be found in Secs. 3.5.1- 3.5.2.

By studying the form of the singular piece, the  $x_1$  and  $x_2$  dependence in  $\tilde{W}$  can be factorized into:

$$\tilde{W}(b, Q, x_1, x_2) = \sum_j C_j(b, Q, x_1) C_j(b, Q, x_2) \tilde{W}(b, Q), \quad (3.38)$$

where  $C_j$  is a convolution of the PDFs with a collinear Wilson coefficient, with the convolution defined as:

$$C_j = \sum_a \int_x^1 \frac{dz}{z} C_{ja} \left( \frac{x}{z}, b, \mu, Q \right) f_a(z, \mu), \quad (3.39)$$

where  $C_{ja}$  is the Wilson coefficient,  $f_a$  is the PDF, the sum  $a$  runs over all incoming partons, and  $j$  represents the parton that enters into the hard cross section calculation. These functions are the collinear factors as previously mentioned. The remaining term contains the hard factor, and the soft factors.

$\tilde{W}$  is determined by solving the evolution equation [156]:

$$\frac{\partial}{\partial \log Q^2} \tilde{W}(Q, b) = [K(b\mu, g_s(\mu)) + G(Q/\mu, g_s(\mu))] \tilde{W}(Q, b), \quad (3.40)$$

where  $K(b\mu, g_s(\mu))$  and  $G(Q/\mu, g_s(\mu))$  satisfy the renormalization group equations (RGEs),

$$\frac{d}{d \log \mu} K(b\mu, g_s(\mu)) = -\gamma_K(g_s(\mu)), \quad (3.41)$$

$$\frac{d}{d \log \mu} G(b/\mu, g_s(\mu)) = \gamma_K(g_s(\mu)), \quad (3.42)$$

where  $\gamma_K$  is the anomalous dimension, calculated from the singular terms of the cross section []. Through the RGE equations,  $K(b\mu, g_s(\mu))$  and  $G(b/\mu, g_s(\mu))$  can be evolved independently to scales of order  $1/b$  and  $Q$  respectively, removing all large logarithms from the calculation. After solving these equations, the  $A$  and  $B$  functions can be defined such that Eq. 3.40 can be rewritten as:

$$\frac{\partial}{\partial \log Q^2} \tilde{W}(Q, b) = - \left( \int_{C_1^2/b^2}^{C_2^2 Q^2} \frac{d\mu^2}{\mu^2} \left( A(g_s(\mu), C_1) \log \frac{C_2^2 Q^2}{\mu^2} + B(\mu, C_1, C_2) \right) \right) \tilde{W}(Q, b), \quad (3.43)$$

where  $C_1$  and  $C_2$  are arbitrary constants of integration arising from solving the RGEs. It is possible to calculate the values for the  $A$  and  $B$  functions order by order in perturbation theory.

Finally, to obtain a result that can be used to make predictions of the cross section, the evolution equation of  $\tilde{W}$  needs to be solved. The solution can be written as

$$\tilde{W}(Q, b) = e^{-S(Q, b)} \tilde{W} \left( \frac{C_1}{C_2 b}, b \right), \quad (3.44)$$

where  $\mathcal{S}$  is known as the Sudakov factor, and is given by

$$\mathcal{S}(Q, b) = \int_{C_1^2/b^2}^{C_2^2 Q^2} \frac{d\mu^2}{\mu^2} \left( A(g_s(\mu), C_1) \log \frac{C_2^2 Q^2}{\mu^2} + B(\mu), C_1, C_2 \right). \quad (3.45)$$

Putting all of the results above together, the resummed cross section can be written as:

$$\frac{d\sigma}{dQ^2 dq_T^2 dy} = \frac{H}{(2\pi)^2} \int d^2 b e^{i\vec{q}_T \cdot \vec{b}} e^{-\mathcal{S}(Q, b)} \sum_j C_j \left( \frac{C_1}{C_2 b}, Q, x_1 \right) C_j \left( \frac{C_1}{C_2 b}, Q, x_2 \right) + Y(q_T, Q, x_1, x_2). \quad (3.46)$$

This is the general form for transverse momentum resummation. However, this form is not the final form used in calculations, due the fact that when the impact parameter becomes large, the scale of resummation goes below  $\Lambda_{QCD}$ . Therefore the calculation becomes non-perturbative. To prevent using a scale below  $\Lambda_{QCD}$ , the  $b^*$  prescription is introduced, where:

$$b^* = \frac{b}{\sqrt{1 + \frac{b^2}{b_{max}^2}}}, \quad (3.47)$$

where  $b_{max}$  is chosen such that  $1/b_{max}$  is of order  $\Lambda_{QCD}$ . The lower bound of the Sudakov integral is then modified from  $C_1^2/b^2$  to  $C_1^2/b_*^2$ . This functional form prevents  $b^*$  from ever being large than  $b_{max}$ , preventing scales below  $\Lambda_{QCD}$ . However, this causes the prediction to be inaccurate at low  $q_T$ , since a piece is removed by the  $b^*$  prescription. To resolve this, a non-perturbative function needs to be introduced.

There are many different proposals for the form of the non-perturbative function [157, 158, 159, 160]. In this section, the general concepts of the non-perturbative function will be covered. The method of obtaining this function is through fits to data. It is believed that the non-perturbative function should be universal, and only depend on the color structure

of the initial states. Details on a specific proposed non-perturbative function can be found in Section 3.4.4. This then gives the final form of the resummation formalism in a scheme independent way as:

$$\frac{d\sigma}{dQ^2 dq_T^2 dy} = \sum_{i,j} \frac{H}{(2\pi)^2} \int d^2b e^{iq_T \cdot \vec{b}} e^{-S_{\text{pert}}} e^{-S_{NP}} C \otimes f_i C \otimes f_j, \quad (3.48)$$

where  $S_{\text{pert}}$  is the Sudakov factor, while  $S_{NP}$  is the non-perturbative Sudakov factor. Finally, up to this point the integration coefficients ( $C_1, C_2$ , and  $C_3$ ) were left to be arbitrary. The canonical choice for these scales are given by  $C_1 = b_0$ ,  $C_2 = 1$ , and  $C_3 = b_0$ , where  $b_0 = 2e^{-\gamma E}$ . In Section 3.6, the relationship between the canonical scale choice and any arbitrary choice is calculated. The theory uncertainty due to the missing higher order corrections can be estimated by modifying the values of  $C_1, C_2$ , and  $C_3$  as discussed later in this chapter.

### 3.4.1 Collins-Soper-Sterman Formalism

So far, the resummation formalism has been developed in a resummation scheme independent way. Here, the Collins-Soper-Sterman Formalism is introduced [138]. In this formalism, the hard matrix element,  $H$ , is taken to be 1, with no corrections as a function of  $\alpha_s$ , and the  $B$  and  $C$  coefficients become process dependent. The  $A$ ,  $B$ , and  $C$  coefficients can be expanded as a series in  $\alpha_s$  as:

$$A = \sum_n \left(\frac{\alpha_s}{\pi}\right)^n A^{(n)}, \quad (3.49)$$

$$B = \sum_n \left(\frac{\alpha_s}{\pi}\right)^n B^{(n)}, \quad (3.50)$$

$$C_{ij} = \delta_{ij} + \sum_n \left(\frac{\alpha_s}{\pi}\right)^n C_{ij}^{(n)}. \quad (3.51)$$

For Drell-Yan, the coefficients for  $A$  up to  $\alpha_s^3$ ,  $B$  up to  $\alpha_s^2$  and  $C$  up to  $\alpha_s$  are given with the canonical scale choice as [161, 162, 163, 164, 165, 166]:

$$A^{(1)} = C_F, \quad (3.52)$$

$$A^{(2)} = \frac{1}{2}C_F \left( \left( \frac{67}{18} - \frac{\pi^2}{6} \right) C_A - \frac{5}{9}N_f \right), \quad (3.53)$$

$$A^{(3)} = C_F \left( \frac{C_F N_f}{2} \left( \zeta_3 - \frac{55}{48} \right) - \frac{N_f^2}{108} + C_A^2 \left( \frac{11\zeta_3}{24} + \frac{11\pi^4}{720} - \frac{67\pi^2}{216} + \frac{245}{96} \right) + C_A N_f \left( \frac{-7\zeta_3}{12} + \frac{5\pi^2}{108} - \frac{209}{432} \right) \right), \quad (3.54)$$

$$B^{(1)} = -\frac{3}{2}C_F, \quad (3.55)$$

$$B^{(2)} = C_F^2 \left( \frac{\pi^2}{4} - \frac{3}{16} - 3\zeta_3 \right) + C_F C_A \left( \frac{11}{36}\pi^2 - \frac{193}{48} + \frac{3}{2}\zeta_3 \right) + C_F N_f \left( \frac{17}{24} - \frac{\pi^2}{18} \right), \quad (3.56)$$

$$C_{qq}^{(1)}(z) = \frac{1}{2}C_F(1-z) + \delta(1-z)\frac{1}{4}C_F(\pi^2 - 8), \quad (3.57)$$

$$C_{qg}^{(1)}(z) = \frac{1}{2}z(1-z), \quad (3.58)$$

$$C_{q\bar{q}}^{(1)}(z) = C_{qq'}^{(1)}(z) = C_{q\bar{q}'}^{(1)}(z) = 0, \quad (3.59)$$

where  $C_F = 4/3$ ,  $C_A = 3$ , and  $N_f$  is the number of active quarks. The results for  $B^{(3)}$  can be found in Ref. [167], and for  $C^{(2)}$  can be found in Ref. [168].<sup>1</sup>

### 3.4.2 Catani-deFlorian-Grazzini Formalism

Catani, deFlorian, and Grazzini realized that the behavior of soft gluons is independent of the hard process, and developed a resummation formalism in which the hard factor which is process dependent can be pulled out of the Fourier Transform [169]. This then leads to the

---

<sup>1</sup>The results for  $B^{(3)}$  and  $C^{(2)}$  can be found in App. F.



calculation in impact parameter space only depending on the initial state partons, and not the hard factor. Like in CSS, the  $A$ ,  $B$ , and  $C$  functions can be expanded as a series in  $\alpha_s$ . However, in addition to these three, the hard factor  $H$  is not fixed to one, but can also be expanded as a series in  $\alpha_s$ . In the CFG formalism, the  $A$ ,  $B$ , and  $C$  coefficients are given by:

$$A^{(1)} = C_F, \quad (3.60)$$

$$A^{(2)} = \frac{1}{2}C_F \left( \left( \frac{67}{18} - \frac{\pi^2}{6} \right) C_A - \frac{5}{9}N_f \right), \quad (3.61)$$

$$A^{(3)} = C_F \left( \frac{C_F N_f}{2} \left( \zeta_3 - \frac{55}{48} \right) - \frac{N_f^2}{108} + C_A^2 \left( \frac{11\zeta_3}{24} + \frac{11\pi^4}{720} - \frac{67\pi^2}{216} + \frac{245}{96} \right) + C_A N_f \left( \frac{-7\zeta_3}{12} + \frac{5\pi^2}{108} - \frac{209}{432} \right) \right), \quad (3.62)$$

$$B^{(1)} = -\frac{3}{2}C_F, \quad (3.63)$$

$$B^{(2)} = \left( (-3 + 24\zeta_2 - 48\zeta_3) C_F^2 + \left( \frac{-17}{3} - \frac{88}{3}\zeta_2 + 24\zeta_3 \right) C_F C_A + \left( \frac{2}{3} + \frac{16}{3}\zeta_2 \right) C_F N_f \right) / 16 + C_F \beta_0 \zeta_2, \quad (3.64)$$

$$C_{qq}^{(1)}(z) = \frac{1}{2}C_F(1-z), \quad (3.65)$$

$$C_{gq}^{(1)}(z) = \frac{1}{2}C_F z, \quad (3.66)$$

$$C_{qg}^{(1)}(z) = \frac{1}{2}z(1-z), \quad (3.67)$$

$$C_{q\bar{q}}^{(1)}(z) = C_{q\bar{q}'}^{(1)}(z) = C_{q\bar{q}'}^{(1)}(z) = 0. \quad (3.68)$$

The relationship for obtaining the  $A$ ,  $B$ , and  $C$  coefficients in the CFG formalism from the coefficients in the CSS formalism can be found in Sec. 3.4.3. The hard factor is process

dependent, and for Drell-Yan are given as:

$$H^{DY(1)} = C_F \left( \frac{\pi}{2} - 4 \right), \quad (3.69)$$

$$H^{DY(2)} = C_F C_A \left( \frac{59\zeta_3}{18} - \frac{1535}{192} + \frac{215\pi^2}{216} - \frac{\pi^4}{240} \right) + \frac{1}{4} C_F^2 \left( -15\zeta_3 + \frac{511}{16} - \frac{67\pi^2}{12} + \frac{17\pi^4}{45} \right) + \frac{1}{864} C_F N_f \left( 192\zeta_3 + 1143 - 152\pi^2 \right), \quad (3.70)$$

up to  $\mathcal{O}(\alpha_s^2)$  [154].

### 3.4.3 Comparison of CSS to CFG

The conversion between the CSS and CFG Formalisms can be given using the all orders relations [169]:

$$C_{ab}^F(z) = \left[ H_a^F \right]^{\frac{1}{2}} C_{ab}(z), \quad (3.71)$$

$$B_c^F = B_c - \beta \frac{d \ln H_c^F}{d \ln \alpha_s}, \quad (3.72)$$

where the  $F$  superscript is used to indicate which pieces are process dependent, and  $\beta$  is the function that describes the running of  $\alpha_s^2$ . This can be expanded order by order to give a conversion between explicit CSS and CFG coefficients. It is important to note that the  $A$  coefficients are always universal, and  $B^{(1)}$  is also universal (only depends on the color

---

<sup>2</sup>See Section 1.3.2 for a detailed discussion of the  $\beta$  function.

structure of the initial state). The conversions up to N<sup>3</sup>LL resummation are listed below:

$$C_{ab}^{(1)F}(z) = C_{ab}^{(1)}(z) + \delta_{ab}\delta(1-z)\frac{1}{2}H_a^{(1)F}, \quad (3.73)$$

$$C_{ab}^{(2)F}(z) = C_{ab}^{(2)}(z) + \frac{1}{2}H_a^{(1)F}C_{ab}^{(1)}(z) + \delta_{ab}\delta(1-z)\frac{1}{2}\left(H_a^{(2)F} - \frac{1}{4}\left(H_a^{(1)F}\right)^2\right), \quad (3.74)$$

$$B_c^{(2)F} = B_c^{(2)} + \beta_0 H_c^{(1)F}, \quad (3.75)$$

$$B_c^{(3)F} = B_c^{(3)} + \beta_1 H_c^{(1)F} + 2\beta_0\left(H_a^{(2)F} - \frac{1}{2}\left(H_a^{(1)F}\right)^2\right), \quad (3.76)$$

with  $\beta_0 = \frac{11C_A - 2N_f}{12}$  and  $\beta_1 = \frac{17C_A^2 - 5C_A N_f - 3C_F N_f}{24}$ .

Comparisons between the numerical results, and how each compare to data can be found in Section 4.1 and 4.2.

### 3.4.4 Non-Perturbative Contribution

As mentioned above, the resummation formalism needs to be cut-off at large values of impact parameter. Originally, the functional form was taken to be solely for the calculation of Drell-Yan. However, recent work in the transverse-momentum dependent PDF community (TMD) propose that the functional form should be universal.

The most successful form for the non-perturbative function is the Brock-Landry-Nadolsky-Yuan (BLNY) fit to the transverse momentum dependent Drell-Yan lepton pair production in hadronic collisions [157, 170]. The BLNY fit parameterizes the non-perturbative form factors as  $(g_1 + g_2 \ln(Q/2Q_0) + g_1 g_3 \ln(100x_1 x_2))b^2$  in the impact parameter space with  $x_1$  and  $x_2$  being the longitudinal momentum fractions of the incoming nucleons carried by the initial state quark and antiquark. These parameters are constrained from the combined fit to the low transverse momentum distributions of Drell-Yan lepton pair production with

$4\text{GeV} < Q < 12\text{GeV}$  in fixed target experiments and  $W/Z$  production ( $Q \sim 90\text{GeV}$ ) at the Tevatron. However, this parameterization does not apply to the semi-inclusive deep inelastic scattering (SIDIS) processes measured by HERMES and COMPASS collaborations: extrapolating the above parameterization down to the typical HERMES kinematics where  $Q^2$  is around  $3\text{GeV}^2$ , the transverse momentum distribution of hadron production in the experiments cannot be described [171, 172].

A parametrization form that can consistently describe the Drell-Yan data and SIDIS data in the CSS resummation formalism with a universal non-perturbative TMD function is proposed below. In order to describe the SIDIS data, it is necessary to modify the original BLNY parameterization. In the original BLNY parameterization, there is a strong correlation between the  $x$ -dependence and the  $Q^2$ -dependence [157, 170], since  $x_1 x_2 = Q^2/S$  where  $S$  is the center of mass energy squared of the incoming hadrons. Therefore, the  $x$ -dependence will be separated out, and assumed to follow a power law behavior:  $(x_0/x)^\lambda$ . These two parameterizations (logarithmic and power law) differ strongly in the intermediate  $x$  range. Secondly, the  $\ln Q$  term in the non-perturbative form factor is modified by following the observation of Ref. [171, 172], which has shown that a direct integral of the evolution kernel can describe the SIDIS and Drell-Yan data of  $Q^2$  range from a few to hundreds of  $\text{GeV}^2$ . Direct integration of the evolution kernel leads to a functional form proportional to  $\ln(b/b_*) \ln(Q)$ , instead of  $b^2 \ln(Q^2)$ . Therefore, the experimental data will be fit with the proposed non-perturbative function defined as:

$$g_1 b^2 + g_2 \ln(b/b_*) \ln(Q/Q_0) + g_3 b^2 \left( (x_0/x_1)^\lambda + (x_0/x_2)^\lambda \right) , \quad (3.77)$$

where  $Q_0^2 = 2.4\text{GeV}^2$ ,  $x_0 = 0.01$  and  $\lambda = 0.2$ , and are fixed in the fit. This new non-

perturbative function will be referred to as the Sun-Isaacson-Yuan-Yuan (SIYY) non-perturbative function. The  $x$ -dependence is motivated by a saturation picture for parton distributions at small- $x$ . This functional form also has mild dependence on  $x$  in the intermediate  $x$ -range as compared to the original BLNY parameterization.

After obtaining the TMD non-perturbative function from the fit to the Drell-Yan data, the fit is applied to the transverse momentum distributions in SIDIS processes from HERMES and COMPASS.

In the BLNY parameterization, the  $g_2$  term is responsible for the  $Q^2$  dependence, which is modified in order to describe the Drell-Yan and SIDIS processes simultaneously. At small- $b$ , the above function reduces to  $b^2$  behavior, which is consistent to the power counting analysis in Ref. [160]. However, at large  $b$ , the logarithmic behavior will lead to different predictions from BLNY.

To constrain the values of  $g_1, g_2$ , and  $g_3$  a global fit is performed on the Drell-Yan data. The data that is included in the fit is listed below:

- Drell-Yan lepton pair production from fixed target hadronic collisions, including R209, E288 and E605 [16, 18, 17].
- $Z$  boson production in hadronic collisions from Tevatron Run I and Run II [19, 20, 21, 22].

In total, 7 Drell-Yan data sets from 3 fixed target experiments and 4 Tevatron experiments are included. While the LHC data was not included in the fit, the fit is compared to data from the LHC afterwards, and is shown to be in good agreement. In total, there are 140 experimental data points, and  $g_1, g_2$ , and  $g_3$  as free parameters in the global fit, with  $b_{max} = 1.5 GeV^{-1}$ . In the numerical calculations, the CT10-NLO parton distributions at

Parameter	SIYY1 fit	SIYY2 fit
$g_1$	0.200	0.18084
$g_2$	0.810	0.16741
$g_3$	0.0204	0.00323
E288 (28 points) (Norm Err = 0.25)	$N_{fit} = 0.82$ $\chi^2 = 52.6$	$N_{fit} = 0.757$ $\chi^2 = 38$
E605 (35 points) (Norm Err = 0.15)	$N_{fit} = 0.86$ $\chi^2 = 63.5$	$N_{fit} = 0.824$ $\chi^2 = 61$
R209 (10 points) (Norm Err = 0.1)	$N_{fit} = 1.02$ $\chi^2 = 3$	$N_{fit} = 0.956$ $\chi^2 = 5$
CDF Run I (20 points) (Norm Err = 0.04)	$N_{fit} = 1.06$ $\chi^2 = 10$	$N_{fit} = 1.048$ $\chi^2 = 9.3$
D0 Run I (10 points) (Norm Err = 0.04)	$N_{fit} = 0.93$ $\chi^2 = 7$	$N_{fit} = 0.94$ $\chi^2 = 6.3$
CDF Run II (29 points) (Norm Err = 0.04)	$N_{fit} = 0.990$ $\chi^2 = 30$	$N_{fit} = 0.992$ $\chi^2 = 26.2$
D0 Run II (8 points) (Norm Err = 0.04)	$N_{fit} = 0.94$ $\chi^2 = 3.7$	$N_{fit} = 0.939$ $\chi^2 = 3.6$
$\chi^2$	169	150
$\chi^2/\text{DOF}$	1.21	1.07

Table 3.2: The non-perturbative functions parameters fitting results. Here,  $N_{fit}$  is the fitted normalization factor for each experiment.

the scale  $\mu = b_0/b_*$  are used [173]. An additional fitting parameter ( $N_{fit}$ ) is assigned for each experiment to account for the luminosity uncertainties.

In Figs. 3.5, 3.6, 3.7, 3.8, and 3.9, the best fits to the Drell-Yan data from E288, E605, and R209 Collaborations, and  $Z$  boson production from the CDF and D0 Collaborations at the Tevatron Run I and II are shown. The fitting results and  $\chi^2$  distributions are listed in Table 3.2. The plots and the table show that the SIYY non-perturbative function provides a reasonable fit to all 7 experimental data with 3 non-perturbative parameters  $g_{1,2,3}$  and 7 independent normalization factors.

In the above fit, SIYY2 is an update fit to the BLNY fit, with the choice of  $b_{max} = 1.5$  instead of the traditional value of 0.5. This fit is updated as well to estimate the uncertainty

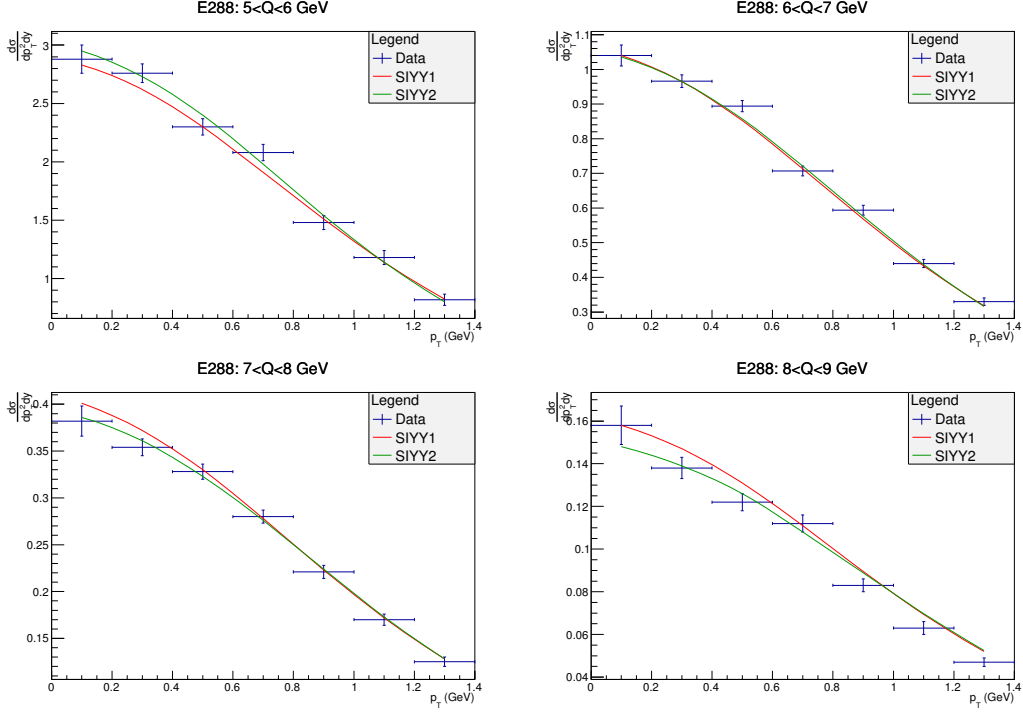


Figure 3.5: Fit to the differential cross section for Drell-Yan lepton pair production in hadronic collisions from E288 Collaboration [16].

in the non-perturbative fit due to the parameterization of the non-perturbative function.

Among these parameters, the most important one, relevant to the LHC  $W$  and  $Z$  boson physics, is  $g_2$  which controls the  $Q^2$  dependence in the non-perturbative form factors. From the  $\chi^2$  distribution in scanning the  $g_2$  parameter as shown in the left panel of Fig. 3.11, its uncertainty is given as:

$$g_2 = 0.81 \pm 0.06 \quad (\text{at } 90\% \text{ C.L.}) . \quad (3.78)$$

In order to demonstrate the sensitivity of  $g_2$  on different experiments, in the right panel of Fig. 3.11, the  $\Delta\chi^2$  distributions are plotted as functions of  $g_2$  from separate data sets: one from the Drell-Yan experiment E288, the combined contribution from all other Drell-Yan experiments, and one from Tevatron  $Z$ -boson experiments. From this figure, it is clear that the strongest constraints come from the precise Drell-Yan data at fixed target experiments,

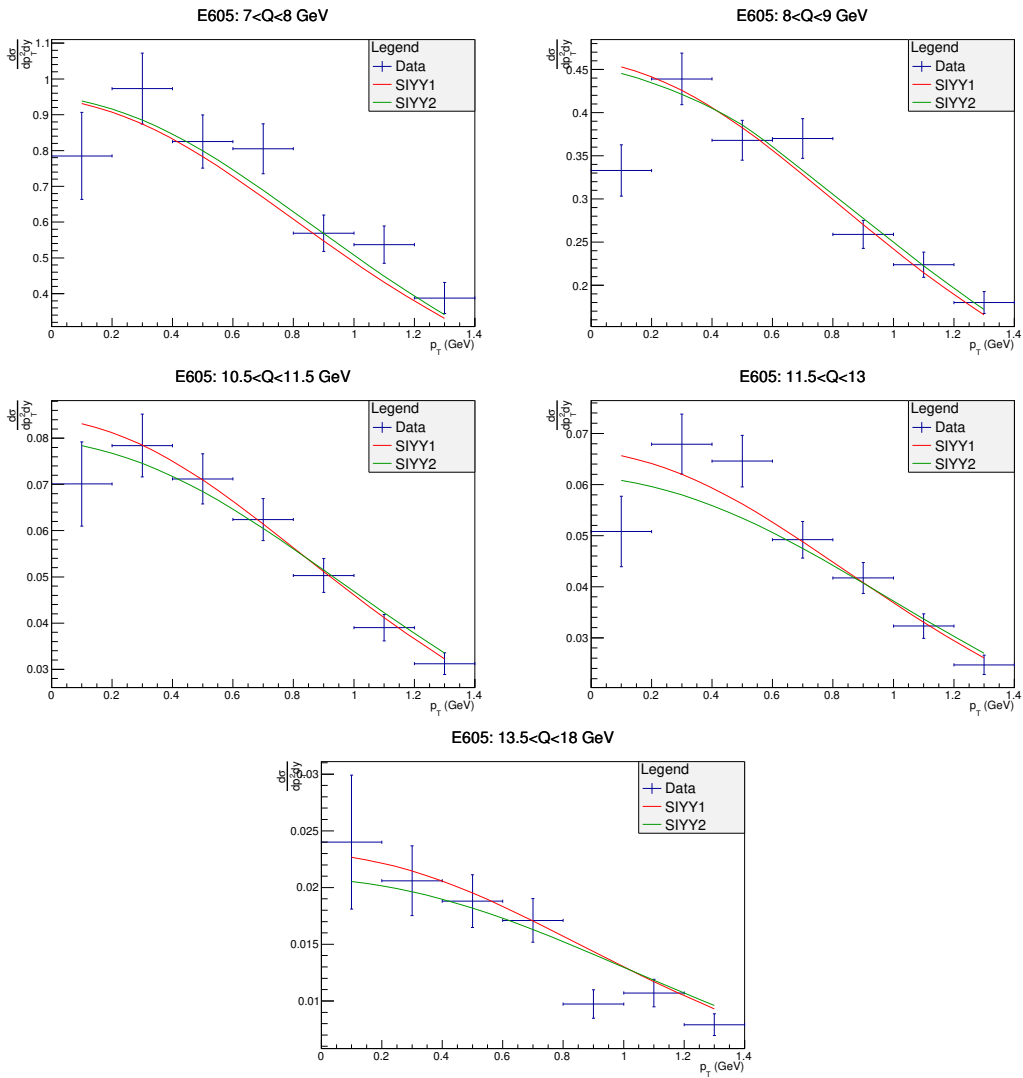


Figure 3.6: Fit to the Drell-Yan data from the E605 Collaboration [17].

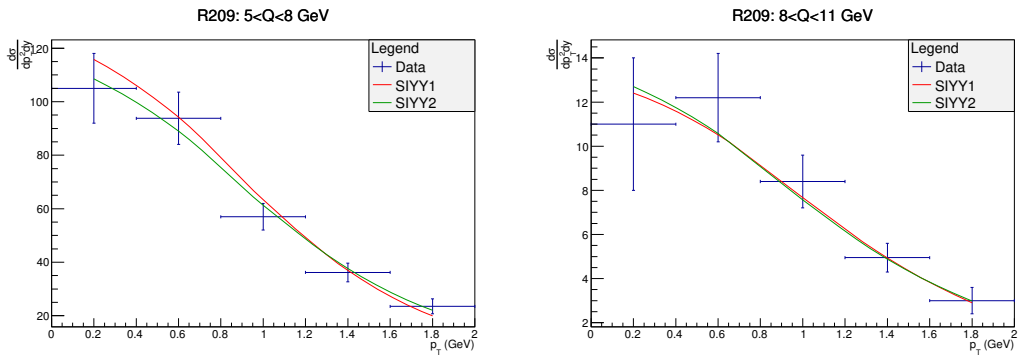


Figure 3.7: Fit to the Drell-Yan data from the R209 Collaboration [18].



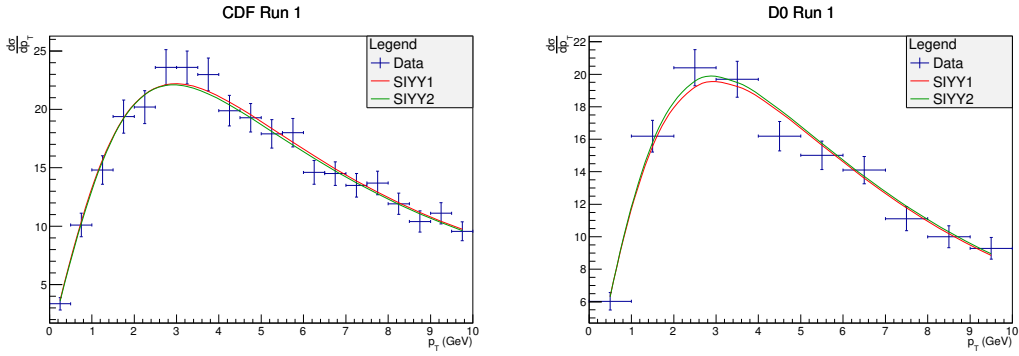


Figure 3.8: Fit to the Tevatron Run I data from the CDF and D0 Collaborations [19, 20]. The fits include only the  $A^{(1,2)}$ ,  $B^{(1,2)}$ , and  $C^{(1)}$  contributions.

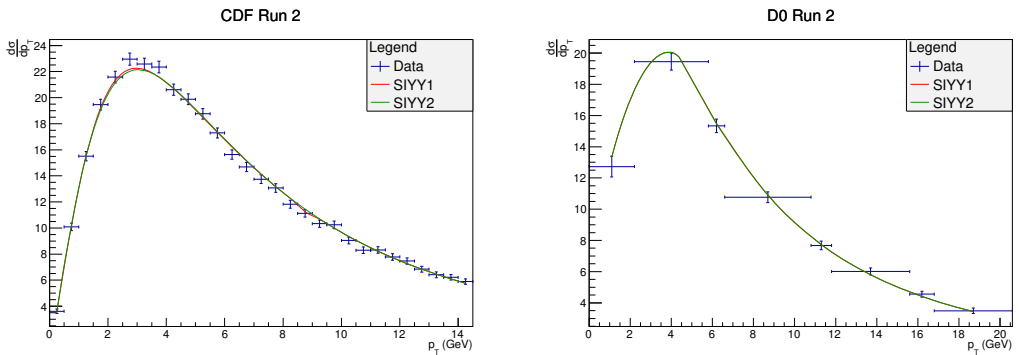


Figure 3.9: Fit to the Tevatron Run II data from the CDF and D0 Collaborations [21, 22].

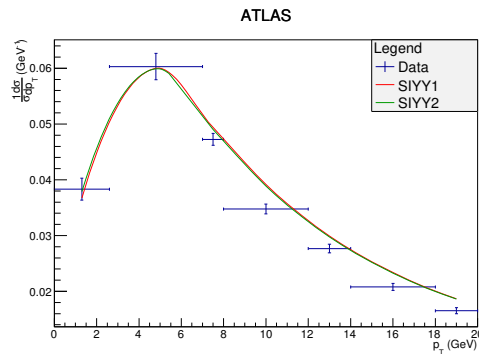


Figure 3.10: Comparison of the SIYY1 and SIYY2 fit to the ATLAS data.

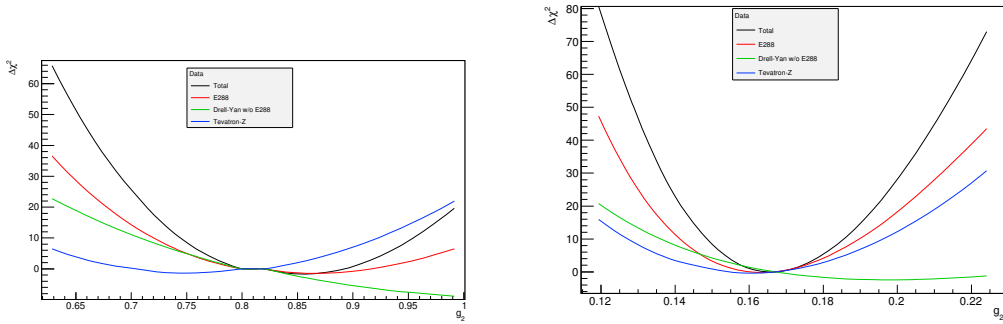


Figure 3.11:  $\Delta\chi^2$  distribution scanning  $g_2$  parameter in SIYY1 fit (left), and  $\Delta\chi^2$  distribution scanning  $g_2$  parameter in SIYY2 fit (right).

i.e., the E288 experiment. It is also interesting to note that, although the Tevatron data for  $Z$ -boson production is the most precise data, it does not pose a strong constraint on the  $g_2$  parameter. This can be understood as a result of the dominance of the perturbative contribution to the transverse momentum distribution of  $W/Z$  boson productions at these collider energies. A similar observation was made in Ref. [174, 159] with a different prescription to introduce the non-perturbative form factors. However, in the original BLNY fit, the Gaussian form of the  $g_2$  term ( $g_2 b^2 \ln Q$ ) leads to a stronger effect on the  $W/Z$  boson production as shown in Ref. [158]. The comparison of this non-perturbative fit to the SIDIS data can be found in App. F. As seen in the figures, the updated Gaussian fit is also consistent with the data, and the two fits give a good estimate of the uncertainty due to the form of the non-perturbative function.

### 3.5 The Asymptotic Piece and Obtaining Fixed-Order Cross-Sections from Resummed Results

The asymptotic piece contains the terms that are at least as singular as  $\frac{1}{q_T^2}$ , and can be obtained in two manners. One way to obtain the asymptotic piece is to take the limit of

$q_T$  goes to zero of the real correction. However, this explicitly involves integrating out all the kinematic variables of the additional radiations, with the requirement that the boson  $q_T$  is the desired value, i.e. adding in a  $\delta^{(2)}(q_T - \sum_i p_{T_i})$ , where  $i$  is over all additional radiations. The other method of obtaining the asymptotic piece is to perform an expansion of the resummation formalism to a fixed-order in  $\alpha_s$ . The expansion of the resummation formalism reproduces all of the divergences that exist in the real correction, and thus the two should cancel as  $q_T$  goes to zero. The second method is detailed below up to  $\alpha_s^3$ .

An important cross check of the calculations, is to ensure that when the appropriate expansions are made, the fixed-order total cross section is reproduced. In order to calculate the fixed-order total cross section three pieces are needed, the singular piece below  $p_T^{\text{cut}}$ , the real correction for  $q_T > p_T^{\text{cut}}$ , and the regular piece below  $p_T^{\text{cut}}$ . The regular piece is the difference between the real correction and the asymptotic piece. The contribution to the total cross-section from the regular piece is small if  $p_T^{\text{cut}}$  is taken to be small. Throughout this work,  $p_T^{\text{cut}}$  will be chosen to be small such that the regular piece provides a negligible contribution and will therefore be ignored. For the leading order calculation, obtaining the fixed-order calculation from the resummed result is trivial, and therefore the first order discussed will be NLO. Throughout the following calculation, without loss of generality, the choices for the resummation constants ( $C_1$ ,  $C_2$ , and  $C_3$ ) will be chosen to be the canonical values for simplicity ( $C_1 = C_3 = b_0$ ,  $C_2 = 1$ ). As will be discussed in the following section (Sec. 3.6), all  $C_1$ ,  $C_2$ , and  $C_3$  dependence should cancel in the expansion of the resummation formalism to some fixed-order in  $\alpha_s$ . Therefore, the asymptotic, singular, and real piece do not depend on the choice of resummation constants.

The asymptotic piece consists of terms that are at least as singular as  $q_T^{-2}$ . The singular piece consists of terms that are at least as singular as  $q_T^{-2}$  plus it also includes the  $\delta(q_T)$  terms.

The expansion of the  $A$ ,  $B$ ,  $C$ , and  $H$  coefficients to  $\mathcal{O}(\alpha_s^n)$  can be explicitly found up to  $\mathcal{O}(\alpha_s^3)$  in Section 3.4.1, Section 3.4.2, and Appendix F for the CSS and CFG formalisms. The expansion of both the CSS and CFG formalism result in the same singular and asymptotic piece, so it is sufficient to only consider the CSS formalism. The lepton variables and angle between  $\vec{b}$  and  $\vec{q}_T$  are integrated out to simplify the discussion, but do not modify the results. After these simplifications, the resummation formalism becomes:

$$\lim_{q_T \rightarrow 0} \frac{d\sigma}{dQ^2 dy dq_T^2} \propto \frac{1}{2\pi q_T^2} \int_0^\infty d\eta \eta J_0(\eta) e^{-S(\eta/q_T, Q)} \times C \otimes f_j(x_1, q_T^2/\eta^2) C \otimes f_{\bar{k}}(x_2, q_T^2/\eta^2) + j \leftrightarrow \bar{k}, \quad (3.79)$$

where terms that are not of importance in the derivation have been dropped, and terms that are less singular than  $\frac{1}{q_T^2}$  or  $\delta(q_T)$  have also been dropped. The asymptotic piece is obtained by integrating over  $\eta = bq_T$ . This can be performed by using the following integration by parts identity:

$$\int_0^\infty d\eta \eta J_0(\eta) F(\eta) = - \int_0^\infty d\eta \eta J_1(\eta) \frac{dF(\eta)}{d\eta}, \quad (3.80)$$

which is true given that the boundary term vanishes,  $(\eta J_1(\eta) F(\eta))_{\eta=0}^\infty = 0$ . Additionally, the following integral results will be important in obtaining both the asymptotic and singular

piece up to  $\mathcal{O}(\alpha_s^3)$ :

$$\int_0^\infty d\eta J_1(\eta) \ln^m \left( \frac{\eta^2 Q^2}{b_0^2 q_T^2} \right) = \begin{cases} 1, & \text{if } m = 0 \\ \ln \frac{Q^2}{q_T^2}, & \text{if } m = 1 \\ \ln^2 \frac{Q^2}{q_T^2}, & \text{if } m = 2 \\ \ln^3 \frac{Q^2}{q_T^2} - 4\zeta(3), & \text{if } m = 3 \\ \ln^4 \frac{Q^2}{q_T^2} - 16\zeta(3) \ln \frac{Q^2}{q_T^2}, & \text{if } m = 4 \\ \ln^5 \frac{Q^2}{q_T^2} - 40\zeta(3) \ln^2 \frac{Q^2}{q_T^2} - 48\zeta(5), & \text{if } m = 5, \\ \ln^6 \frac{Q^2}{q_T^2} - 80\zeta(3) \ln^3 \frac{Q^2}{q_T^2} - 288\zeta(5) \ln \frac{Q^2}{q_T^2} + 160\zeta(3)^2, & \text{if } m = 6, \end{cases} \quad (3.81)$$

where  $b_0 = e^{-\gamma_E}$ , and  $\gamma_E$  is the Euler constant. Up through  $m = 2$  is needed for the  $\mathcal{O}(\alpha_s)$  calculations, through  $m = 4$  is needed for the  $\mathcal{O}(\alpha_s^2)$  calculations, and all of the above will be needed for the  $\mathcal{O}(\alpha_s^3)$  calculations.

Secondly, the singular piece is obtained by taking the integral of  $q_T$  for the  $\mathcal{O}(\alpha_s^n)$  corrections from 0 to  $p_T^{cut}$ , and is calculated in a manner similar to the asymptotic piece, with one key modification. Instead of using the integration by parts identity, the order of integration between  $q_T$  and  $b$  is interchanged, giving us the following relationship:

$$\frac{1}{(2\pi)^2} \int_0^{(p_T^{cut})^2} dq_T^2 \int d^2 b e^{i\vec{q}_T \cdot \vec{b}} F(b) = \frac{1}{2\pi} \int_0^\infty db p_T^{cut} J_1(b p_T^{cut}) F(b). \quad (3.82)$$

Finally, the calculation of the real corrections is needed. The additional jets then need to be integrated out, and the singularities need to be canceled in order to obtain a finite prediction. For NLO this is straightforward, and there is an analytic form. However, at

NNLO this is not possible, and an external code with the parameters tuned to match that of the ResBos2 code will be used to obtain this contribution. Additionally, to ensure the external code is tuned correctly, it will be validated against the total cross-section at NLO. Once the functional form for  $C^{(3)}$  is calculated, the ResBos2 code along with the Z plus jet to NNLO calculation will be able to predict the N<sup>3</sup>LO total cross-section.

### 3.5.1 $\mathcal{O}(\alpha_s)$ Singular, Asymptotic Piece, and NLO Result

In this subsection, the computational details of obtaining the singular and asymptotic piece needed for the NLO calculation are shown. Firstly, to obtain the asymptotic piece the Sudakov factor is expanded to  $\mathcal{O}(\alpha_s)$ ,  $S(b, Q) = S^{(1)}(b, Q) + \mathcal{O}(\alpha_s^2)$ , with  $S^{(1)}$  given as:

$$S^{(1)}(b, Q) = \frac{\alpha_s(Q^2)}{\pi} \left[ \frac{1}{2} A^{(1)} \ln^2 \frac{Q^2 b^2}{b_0^2} + B^{(1)} \ln \frac{Q^2 b^2}{b_0^2} \right]. \quad (3.83)$$

Also, the convolution of the PDF with the  $C$  function needs to be expanded to  $\mathcal{O}(\alpha_s)$ . At  $\mathcal{O}(\alpha_s)$ , the  $C$  function does not appear in the asymptotic piece at this order, but will appear at higher orders. For the asymptotic piece, at this order it is sufficient to use the PDF evolution equation given as:

$$\frac{df_j(x, \mu^2)}{d \ln \mu^2} = \frac{\alpha_s(\mu^2)}{2\pi} \left( P_{j \leftarrow a}^{(1)} \otimes f_a \right) (x, \mu^2) + \mathcal{O}(\alpha_s^2). \quad (3.84)$$

Using the integration by parts identity in Eq. 3.80, requires the derivatives with respect to  $\eta$  of the Sudakov factor and the PDF, given as:

$$\frac{d}{d\eta} e^{-S(\eta/q_T, Q)} = \frac{-2}{\eta} \frac{\alpha_s(Q^2)}{\pi} \left[ A^{(1)} \ln \frac{Q^2 \eta^2}{b_0^2 q_T^2} + B^{(1)} \right] + \mathcal{O}(\alpha_s^2), \quad (3.85)$$

and

$$\frac{d}{d\eta} f_j \left( x, b_0^2 q_T^2 / \eta^2 \right) = \frac{-2 \alpha_s(Q^2)}{\eta} \frac{1}{2\pi} \left( P_{j \leftarrow a}^{(1)} \otimes f_a \right) \left( x, \mu^2 \right) + \mathcal{O} \left( \alpha_s^2 \right). \quad (3.86)$$

Combining these results with those from Eq. 3.81, the final results for the asymptotic piece is given as:

$$\begin{aligned} \lim_{q_T \rightarrow 0} \frac{d\sigma}{dQ^2 dy dq_T^2} &= \frac{\sigma_0}{S} \frac{1}{2\pi q_T^2} \frac{\alpha_s(Q^2)}{\pi} \left\{ \left[ f_j \left( x_1, Q^2 \right) \left( P_{\bar{k} \leftarrow b} \otimes f_b \right) \left( x_2, Q^2 \right) \right. \right. \\ &+ \left. \left. f_{\bar{k}} \left( x_2, Q^2 \right) \left( P_{j \leftarrow a} \otimes f_a \right) \left( x_1, Q^2 \right) \right] \right. \\ &+ \left. 2 \left[ A^{(1)} \ln \frac{Q^2}{q_T^2} + B^{(1)} \right] f_j \left( x_1, Q^2 \right) f_{\bar{k}} \left( x_2, Q^2 \right) + j \leftrightarrow \bar{k} \right\} + \mathcal{O} \left( \alpha_s^2 \right). \end{aligned} \quad (3.87)$$

For simplicity, it is useful to introduce the following definition,

$$\frac{d\sigma}{dQ^2 dy dq_T^2} = \frac{\sigma_0}{S} \frac{1}{2\pi q_T^2} \sum_{i,j} \sum_{n=1}^{\infty} \sum_{m=0}^{2n-1} \left( \frac{\alpha_s(\mu^2)}{\pi} \right)^n {}_n C_m^{(i,j)} \ln^m \left( \frac{Q^2}{q_T^2} \right), \quad (3.88)$$

which becomes very useful for organization beyond  $\mathcal{O}(\alpha_s)$ . The definition above differs from that found in Ref. [175] by expanding in factors of  $\frac{\alpha_s}{\pi}$  instead of  $\frac{\alpha_s}{2\pi}$ , and the overall factor for the  $\frac{1}{q_T^2}$  term is  $\frac{1}{2\pi}$  instead of  $\frac{1}{\pi}$ . Using these definitions the above results are given as:

$$\begin{aligned} {}_1 C_1^{(i,j)} &= 2A^{(1)} f_i f_j, \\ {}_1 C_0^{(i,j)} &= 2B^{(1)} f_i f_j + \left[ f_j \left( P_{i \leftarrow b} \otimes f_b \right) f_i \left( P_{j \leftarrow a} \otimes f_a \right) \right]. \end{aligned}$$

Secondly, calculating the singular piece begins by expanding the Sudakov factor in the same manner. However, instead of using the evolution of the PDF as a shortcut to obtain

the derivative with respect to  $\eta$ , the PDF is directly expanded to  $\mathcal{O}(\alpha_s)$  as:

$$f_j(x, \mu^2) = f_j(x, Q^2) + \frac{\alpha_s(Q^2)}{2\pi} \ln\left(\frac{\mu^2}{Q^2}\right) (P_{j \rightarrow a \otimes f_a})(x, Q^2) + \mathcal{O}(\alpha_s^2), \quad (3.89)$$

where  $\mu^2$  is the factorization scale<sup>3</sup>. It will be convenient to again introduce the following definition:

$$\int_0^{(p_T^{cut})^2} dq_T^2 \frac{d\sigma}{dQ^2 dy dq_T^2} = \frac{\sigma_0}{S} \sum_{i,j} \sum_{n=0}^{\infty} \sum_{m=0}^{2n} \left(\frac{\alpha_s(\mu^2)}{\pi}\right)^n {}_nV_m^{(i,j)} \ln^m\left(\frac{Q^2}{q_T^2}\right) \quad (3.90)$$

Combining this with Eq. 3.82 we obtain the following results using the above definition of  ${}_nV_m^{(i,j)}$ :

$$\begin{aligned} {}_0V_0^{(i,j)} &= f_i f_j, \\ {}_1V_2^{(i,j)} &= -\frac{1}{2} A^{(1)} f_i f_j, \\ {}_1V_1^{(i,j)} &= -B^{(1)} f_i f_j - \frac{1}{2} [f_j (P_{i \leftarrow b} \otimes f_b) + f_i (P_{j \leftarrow a} \otimes f_a)], \\ {}_1V_0^{(i,j)} &= f_j (C_{i \leftarrow b}^{(1)} \otimes f_b) + f_i (C_{j \leftarrow a}^{(1)} \otimes f_a). \end{aligned}$$

Finally, the regular terms and real corrections can be found in Ref. [176] in Section 2.2.5. By combining these pieces, the NLO prediction can be calculated, and is implemented into the ResBos2 code. As mentioned above, there is a  $p_T^{cut}$  that is artificially introduced to separate the singular region from the regular region. The numerical result at NLO is for the total cross section for Drell-Yan in the invariant mass region of  $66 \text{ GeV} < M_{ll} < 116 \text{ GeV}$  at a collider energy of  $\sqrt{S} = 8 \text{ TeV}$ . Furthermore, comparisons to other publicly available codes tuned to have the same Electroweak parameters as defined in Ref. [68], and mentioned

---

<sup>3</sup>The higher order expansion for the PDF is detailed in App. F



NLO Calculation	Cross-Section
ResBos2 ( $q_T^{cut} = 0.1\text{GeV}$ )	1113.3 pb
ResBos2 ( $q_T^{cut} = 3\text{GeV}$ )	1115.1 pb
MCFM	1112.6 pb
FEWZ	1113.2 pb

Table 3.3: Total inclusive NLO Drell-Yan Cross-sections for  $66 \text{ GeV} < M_{ll} < 116 \text{ GeV}$ . MCFM calculation using version 8.0 [3]. FEWZ calculation using version 3.1\_rc [4]

in Sec. 1.1.4, and using the CT14nnlo PDF [10], can be seen in Table 3.3.

### 3.5.2 $\mathcal{O}(\alpha_s^2)$ Singular, Asymptotic, and the NNLO Total Cross-Section

At NNLO, the procedure above is extended to the next order in  $\alpha_s$ . The most important difference from NLO is that the expansion of  $\alpha_s(\mu^2)$  needs to be considered. This expansion is given by the following to  $\mathcal{O}(\alpha_s^3)$ :

$$\frac{\alpha_s(\mu^2)}{\pi} = \frac{\alpha_s(\mu_R^2)}{\pi} - \left(\frac{\alpha_s(\mu_R^2)}{\pi}\right)^2 \beta_0 \ln \frac{\mu^2}{\mu_R^2} + \left(\frac{\alpha_s(\mu_R^2)}{\pi}\right)^3 \left( \beta_0^2 \log^2 \frac{\mu^2}{\mu_R^2} - \beta_1 \log \frac{\mu^2}{\mu_R^2} \right) + \mathcal{O}(\alpha_s^4), \quad (3.91)$$

where  $\beta_0$  and  $\beta_1$  are defined in App. E, and  $\mu_R$  is the renormalization scale<sup>4</sup>. The Sudakov factor then can be expressed as  $S = S^{(1)} + S^{(2)} + \mathcal{O}(\alpha_s^3)$  with:

$$S^{(2)}(b, Q) = \frac{\alpha_s^2(Q^2)}{\pi^2} \left[ \frac{1}{2} A^{(2)} \ln^2 \frac{Q^2 b^2}{b_0^2} + B^{(2)} \ln \frac{Q^2 b^2}{b_0^2} \right], \quad (3.92)$$

---

<sup>4</sup>The complete derivation of the result can be found in Appendix F

and after expanding  $\alpha_s$ , the Sudakov factor is

$$\begin{aligned}
S &= \frac{\alpha_s}{\pi} \left( \frac{1}{2} A^{(1)} \ln^2 \frac{Q^2 b^2}{b_0^2} + B^{(1)} \ln \frac{Q^2 b^2}{b_0^2} \right) \\
&+ \left( \frac{\alpha_s}{\pi} \right)^2 \left( \frac{1}{4} A^{(1)} \beta_0 \ln^2 \frac{Q^2 b^2}{b_0^2} \ln \frac{\mu_R^2}{Q^2} + \frac{1}{6} A^{(1)} \beta_0 \ln^3 \frac{Q^2 b^2}{b_0^2} + \frac{1}{2} A^{(2)} \ln^2 \frac{Q^2 b^2}{b_0^2} \right. \\
&+ \left. \frac{1}{2} B^{(1)} \beta_0 \ln \frac{Q^2 b^2}{b_0^2} \ln \frac{\mu_R^2}{Q^2} + \frac{1}{4} B^{(1)} \beta_0 \ln^2 \frac{Q^2 b^2}{b_0^2} + B^{(2)} \ln \frac{Q^2 b^2}{b_0^2} \right) + \mathcal{O}(\alpha_s^3). \quad (3.93)
\end{aligned}$$

A similar expansion as above is carried out for the convolution of the  $C$  function with the PDF. The results can then be expressed as:

$$\begin{aligned}
C \otimes f &= f + \frac{\alpha_s}{\pi} \left( C^{(1)} \otimes f - \frac{1}{2} P^{(1)} \otimes f \left( \ln \frac{Q^2 b^2}{b_0^2} + \ln \frac{\mu_F^2}{Q^2} \right) \right) \\
&+ \frac{1}{8} \left( \frac{\alpha_s}{\pi} \right)^2 \left( 4\beta_0 C^{(1)} \otimes f \left( \ln \frac{Q^2 b^2}{b_0^2} + \ln \frac{\mu_F^2}{Q^2} \right) \right. \\
&- 2\beta_0 P^{(1)} \otimes f \left( \ln \frac{Q^2 b^2}{b_0^2} + \ln \frac{\mu_F^2}{Q^2} \right) \left( \ln \frac{Q^2 b^2}{b_0^2} + \ln \frac{\mu_R^2}{Q^2} \right) + \beta_0 P^{(1)} \otimes f \left( \ln \frac{Q^2 b^2}{b_0^2} + \ln \frac{\mu_F^2}{Q^2} \right)^2 \\
&+ 4C^{(1)} \otimes P^{(1)} \otimes f \left( \ln \frac{Q^2 b^2}{b_0^2} + \ln \frac{\mu_F^2}{Q^2} \right) + 8C^{(2)} \otimes f \\
&+ \left. P^{(1)} \otimes P^{(1)} \otimes f \left( \ln \frac{Q^2 b^2}{b_0^2} + \ln \frac{\mu_F^2}{Q^2} \right)^2 + 2P^{(2)} \otimes f \left( \ln \frac{Q^2 b^2}{b_0^2} + \ln \frac{\mu_F^2}{Q^2} \right) \right) + \mathcal{O}(\alpha_s^3), \quad (3.94)
\end{aligned}$$

where  $\mu_F$  is the factorization scale.

Following the procedure used at NLO, the  ${}_n C_m$ 's for the asymptotic piece, are given as:

$$\begin{aligned}
{}_2 C_3^{(i,j)} &= -2 \left( A^{(1)} \right)^2 f_i f_j, \\
{}_2 C_2^{(i,j)} &= \left( -6A^{(1)}B^{(1)} + 2A^{(1)}\beta_0 \right) f_i f_j - 3A^{(1)} \left( f_j (P_{i \leftarrow b} \otimes f_b) f_i (P_{j \leftarrow a} \otimes f_a) \right), \\
{}_2 C_1^{(i,j)} &= \left( A^{(1)}\beta_0 \ln \frac{\mu_R^2}{Q^2} + 2A^{(2)} - 2 \left( B^{(1)} \right)^2 + B^{(1)}\beta_0 \right) f_i f_j + 4A^{(1)} \left( C^{(1)} \otimes f_i \right) f_j \\
&\quad - 2A^{(1)} \left( P^{(1)} \otimes f_i \right) f_j \ln \frac{\mu_F^2}{Q^2} - 4B^{(1)} \left( P^{(1)} \otimes f_i \right) f_j \\
&\quad + \beta_0 \left( P^{(1)} \otimes f_i \right) f_j - \left( P^{(1)} \otimes P^{(1)} \otimes f_i \right) f_j - \left( P^{(1)} \otimes f_i \right) \left( P^{(1)} \otimes f_j \right) + i \leftrightarrow j, \\
{}_2 C_0^{(i,j)} &= \left( 4 \left( A^{(1)} \right)^2 \zeta(3) + B^{(1)}\beta_0 \ln \frac{\mu_R^2}{Q^2} + 2B^{(2)} \right) f_i f_j \\
&\quad + B^{(1)} \left( 4 \left( C^{(1)} \otimes f_i \right) f_j - 2 \left( P^{(1)} \otimes f_i \right) f_j \ln \frac{\mu_F^2}{Q^2} \right) \\
&\quad - \beta_0 \left( 4 \left( C^{(1)} \otimes f_i \right) f_j - 2 \left( P^{(1)} \otimes f_i \right) f_j \ln \frac{\mu_R^2}{Q^2} \right) \\
&\quad + 2 \left( C^{(1)} \otimes P^{(1)} \otimes f_i \right) f_j + 2 \left( C^{(1)} \otimes f_i \right) \left( P^{(1)} \otimes f_j \right) - \left( P^{(1)} \otimes P^{(1)} \otimes f_i \right) f_j \ln \frac{\mu_F^2}{Q^2} \\
&\quad + \left( P^{(1)} \otimes f_i \right) \left( P^{(1)} \otimes f_j \right) \ln \frac{\mu_F^2}{Q^2} + \left( P^{(2)} \otimes f_i \right) f_j + i \leftrightarrow j,
\end{aligned}$$

where the  $i \leftrightarrow j$  corresponds to the same terms with  $i$  and  $j$  interchanged. These results above are consistent with the results of [177]. Also, using the expansions above, the singular

piece is given by

$$\begin{aligned}
{}_2V_4^{(i,j)} &= \frac{1}{8} \left( A^{(1)} \right)^2 f_i f_j, \\
{}_2V_3^{(i,j)} &= \left( \frac{1}{2} A^{(1)} B^{(1)} - \frac{1}{6} A^{(1)} \beta_0 \right) f_i f_j + \frac{1}{4} A^{(1)} \left( \left( P^{(1)} \otimes f_i \right) f_j + \left( P^{(1)} \otimes f_j \right) f_i \right), \\
{}_2V_2^{(i,j)} &= \left( -\frac{1}{8} \beta_0 A^{(1)} \ln \left( \frac{\mu_R^2}{Q^2} \right) + \frac{\left( B^{(1)} \right)^2}{4} - \frac{\beta_0 B^{(1)}}{8} - \frac{A^{(2)}}{4} \right) f_i f_j \\
&\quad + \left( \frac{1}{4} A^{(1)} \ln \left( \frac{\mu_F^2}{Q^2} \right) + \frac{B^{(1)}}{2} - \frac{\beta_0}{8} \right) f_j \left( P^{(1)} \otimes f_i \right) + \frac{1}{8} \left( P^{(1)} \otimes P^{(1)} \otimes f_i \right) f_j \\
&\quad - \frac{1}{2} A^{(1)} \left( C^{(1)} \otimes f_i \right) f_j + \frac{1}{8} \left( P^{(1)} \otimes f_i \right) \left( P^{(1)} \otimes f_j \right) + i \leftrightarrow j, \\
{}_2V_1^{(i,j)} &= \left( -\zeta(3) \left( A^{(1)} \right)^2 - \frac{1}{4} \beta_0 B^{(1)} \ln \left( \frac{\mu_R^2}{Q^2} \right) - \frac{B^{(2)}}{2} \right) f_i f_j - B^{(1)} \left( C^{(1)} \otimes f_i \right) f_j \\
&\quad + \frac{1}{2} B^{(1)} \ln \left( \frac{\mu_F^2}{Q^2} \right) \left( P^{(1)} \otimes f_i \right) f_j + \frac{1}{2} \beta_0 \left( C^{(1)} \otimes f_i \right) f_j - \frac{1}{2} \left( C^{(1)} \otimes P^{(1)} \otimes f_i \right) f_j \\
&\quad + \frac{1}{4} \ln \left( \frac{\mu_F^2}{Q^2} \right) \left( P^{(1)} \otimes f_i \right) \left( P^{(1)} \otimes f_j \right) + \frac{1}{4} \ln \left( \frac{\mu_F^2}{Q^2} \right) \left( P^{(1)} \otimes P^{(1)} \otimes f_i \right) f_j \\
&\quad - \frac{1}{4} \beta_0 \ln \left( \frac{\mu_R^2}{Q^2} \right) \left( P^{(1)} \otimes f_i \right) f_j - \frac{1}{4} \left( P^{(2)} \otimes f_i \right) f_j + i \leftrightarrow j, \\
{}_2V_0^{(i,j)} &= \left( \frac{1}{3} \beta_0 \zeta(3) A^{(1)} - \zeta(3) A^{(1)} B^{(1)} \right) f_i f_j - \zeta(3) A^{(1)} \left( P^{(1)} \otimes f_i \right) f_j \\
&\quad - \frac{1}{2} \ln \left( \frac{\mu_F^2}{Q^2} \right) \left( C^{(1)} \otimes f_i \right) \left( P^{(1)} \otimes f_j \right) - \frac{1}{2} \ln \left( \frac{\mu_F^2}{Q^2} \right) \left( C^{(1)} \otimes P^{(1)} \otimes f_i \right) f_j \\
&\quad + \frac{1}{2} \beta_0 \ln \left( \frac{\mu_F^2}{Q^2} \right) \left( C^{(1)} \otimes f_i \right) f_j + \frac{1}{2} \left( C^{(1)} \otimes f_i \right) \left( C^{(1)} \otimes f_j \right) \\
&\quad + \frac{1}{8} \beta_0 \ln^2 \left( \frac{\mu_F^2}{Q^2} \right) \left( P^{(1)} \otimes f_i \right) f_j \\
&\quad + \frac{1}{8} \ln^2 \left( \frac{\mu_F^2}{Q^2} \right) \left( P^{(1)} \otimes f_i \right) \left( P^{(1)} \otimes f_j \right) + \frac{1}{8} \ln^2 \left( \frac{\mu_F^2}{Q^2} \right) \left( P^{(1)} \otimes P^{(1)} \otimes f_i \right) f_j \\
&\quad - \frac{1}{4} \beta_0 \ln \left( \frac{\mu_F^2}{Q^2} \right) \ln \left( \frac{\mu_R^2}{Q^2} \right) \left( P^{(1)} \otimes f_i \right) f_j + \left( C^{(2)} \otimes f_i \right) f_j \\
&\quad - \frac{1}{4} \ln \left( \frac{\mu_F^2}{Q^2} \right) \left( P^{(2)} \otimes f_i \right) f_j + i \leftrightarrow j.
\end{aligned}$$

NNLO Calculation	Cross-Section
ResBos2 ( $q_T^{cut} = 1.5\text{GeV}$ )	1111.0 pb
ResBos2 ( $q_T^{cut} = 4.5\text{GeV}$ )	1115.6 pb
MCFM	1116.6 pb
FEWZ	1111.0 pb

Table 3.4: Total inclusive NNLO Drell-Yan Cross-sections for  $66 \text{ GeV} < M_{ll} < 116 \text{ GeV}$ . MCFM calculation using version 8.0 [3]. FEWZ calculation using version 3.1\_rc [4]

Similar to the NLO calculation, the results can be compared to that from other publicly available tools. Everything in the comparison is the same as it was in the NLO calculation, with the exception that the real correction is obtained from SHERPA [178]. The results are shown in Tab. 3.4.

The results for the  $\mathcal{O}(\alpha_s^3)$  calculation can be found in the App. F.

## 3.6 Scale Dependence

In the resummation formalism, there exists three constants that are a result of solving the renormalization group equations. These constants are arbitrary, and should therefore not appear in the expansion of the resummation formalism to a fixed-order in  $\alpha_s$ . This implies that the resummation coefficients,  $A$ ,  $B$ ,  $C$ , and  $H$  should depend on these parameters. Here the calculation is done in the CSS scheme, but the CFG scale dependence can be obtained using Eq. 3.73.

To obtain the coefficients, the resummation formalism is expanded for arbitrary scales and is compared to the canonical choice, ( $C_1 = C_3 = b_0$ , and  $C_2 = 1$ ). In other words:

$$W(b, Q, C_1, C_2, C_3) |_{\mathcal{O}(\alpha_s^n)} = W(b, Q, C_1 = b_0, C_2 = 1, C_3 = b_0) |_{\mathcal{O}(\alpha_s^n)}, \quad (3.95)$$

where the definitions of  $C_1, C_2$ , and  $C_3$  can be found in the scale dependent resummation formalism given as:

$$W = \exp \left( - \int_{C_1^2/b^2}^{C_2^2 Q^2} \frac{d\mu^2}{\mu^2} A(\mu; C_1) \log \left( \frac{C_2^2 Q^2}{\mu^2} \right) + B(\mu; C_1, C_2) \right) \\ C \otimes f_a \left( x_1, \frac{C_1}{C_2}, \frac{C_3}{b} \right) C \otimes f_b \left( x_2, \frac{C_1}{C_2}, \frac{C_3}{b} \right). \quad (3.96)$$

performing the series expansion of the previous equation, and using Eq. 3.95, to  $\mathcal{O}(\alpha_s^3)$ , the scale dependence is given by:

$$A^{(1)} = A^{(1,c)} \quad (3.97)$$

$$A^{(2)} = A^{(2,c)} - \beta_0 A^{(1,c)} \log \left( \frac{b_0^2}{C_1^2} \right) \quad (3.98)$$

$$A^{(3)} = A^{(3,c)} + 4\beta_0^2 A^{(1,c)} \log^2 \left( \frac{b_0}{C_1} \right) - 2 \log \left( \frac{b_0}{C_1} \right) \left( \beta_1 A^{(1,c)} + 2\beta_0 A^{(2,c)} \right) \quad (3.99)$$

$$B^{(1)} = B^{(1,c)} - A^{(1,c)} \log \left( \frac{b_0^2 C_2^2}{C_1^2} \right) \quad (3.100)$$

$$B^{(2)} = B^{(2,c)} - A^{(2,c)} \log \left( \frac{b_0^2 C_2^2}{C_1^2} \right) \\ + \beta_0 \left( 2A^{(1,c)} \log^2 \left( \frac{b_0}{C_1} \right) - 2A^{(1,c)} \log^2 (C_2) + 2B^{(1,c)} \log (C_2) \right) \quad (3.101)$$

$$B^{(3)} = B^{(3,c)} - A^{(3,c)} \log \left( \frac{b_0^2 C_2^2}{C_1^2} \right) \\ + 2\beta_1 \left( A^{(1,c)} \log^2 \left( \frac{b_0}{C_1} \right) + \log (C_2) \left( B^{(1,c)} - A^{(1,c)} \log (C_2) \right) \right) \\ - \frac{4}{3} \beta_0^2 \left( 2A^{(1,c)} \log^3 \left( \frac{b_0}{C_1} \right) + \log^2 (C_2) \left( 2A^{(1,c)} \log (C_2) - 3B^{(1,c)} \right) \right) \\ + 4\beta_0 \left( A^{(2,c)} \log^2 \left( \frac{b_0}{C_1} \right) + \log (C_2) \left( B^{(2,c)} - A^{(2,c)} \log (C_2) \right) \right) \quad (3.102)$$

$$\begin{aligned}
C^{(1)} &= C_{ja}^{(1,c)}(\xi) + \delta_{ja}\delta(1-\xi) \left( -\frac{1}{4}A^{(1,c)} \log^2 \left( \frac{b_0^2 C_2^2}{C_1^2} \right) + \frac{1}{2}B^{(1,c)} \log \left( \frac{b_0^2 C_2^2}{C_1^2} \right) \right) \\
&\quad - \frac{1}{2}P_{ja}^{(1)} \log \frac{C_3^2}{b_0^2}
\end{aligned} \tag{3.103}$$

$$\begin{aligned}
C^{(2)} &= C_{ja}^{(2,c)}(\xi) + \delta_{ja}\delta(1-\xi) \left( -\frac{1}{4}\beta_0 A^{(1,c)} \log^2 \left( \frac{b_0^2 C_2^2}{C_1^2} \right) \log \left( \frac{b^2 \mu_F^2}{b_0^2} \right) \right. \\
&\quad + \frac{1}{2}\beta_0 B^{(1,c)} \log \left( \frac{b_0^2 C_2^2}{C_1^2} \right) \log \left( \frac{b^2 \mu_F^2}{b_0^2} \right) + \frac{1}{32} \left( A^{(1,c)} \right)^2 \log^4 \left( \frac{b_0^2 C_2^2}{C_1^2} \right) \\
&\quad - \frac{1}{12}\beta_0 A^{(1,c)} \log^3 \left( \frac{b_0^2 C_2^2}{C_1^2} \right) - \frac{1}{8}A^{(1,c)}B^{(1,c)} \log^3 \left( \frac{b_0^2 C_2^2}{C_1^2} \right) + \frac{1}{2}B^{(2,c)} \log \left( \frac{b_0^2 C_2^2}{C_1^2} \right) \\
&\quad - \frac{1}{4}A^{(2,c)} \log^2 \left( \frac{b_0^2 C_2^2}{C_1^2} \right) + \frac{1}{8} \left( B^{(1,c)} \right)^2 \log^2 \left( \frac{b_0^2 C_2^2}{C_1^2} \right) + \frac{1}{4}\beta_0 B^{(1,c)} \log^2 \left( \frac{b_0^2 C_2^2}{C_1^2} \right) \\
&\quad + \frac{1}{2}B^{(1,c)}C_{ja}^{(1,c)} \log \left( \frac{b_0^2 C_2^2}{C_1^2} \right) - \frac{1}{4}A^{(1,c)}C_{ja}^{(1,c)} \log^2 \left( \frac{b_0^2 C_2^2}{C_1^2} \right) \\
&\quad + \left( \beta_0 C_{ja}^{(1,c)} - \frac{1}{2}C_{jb}^{(1,c)} \otimes P_{ba}^{(1)} - \frac{1}{4}P_{ja}^{(2)} \right) \log \frac{C_3^2}{b_0^2} \\
&\quad + \frac{1}{8}A^{(1,c)}P_{jb}^{(1)} \otimes P_{ba}^{(1)} \log^2 \frac{C_3^2}{b_0^2} - \frac{1}{4}B^{(1,c)}P_{ja}^{(1)} \log \left( \frac{b_0^2 C_2^2}{C_1^2} \right) \log \frac{C_3^2}{b_0^2} \\
&\quad + \frac{1}{8}A^{(1,c)}P_{ja}^{(1)} \log^2 \left( \frac{b_0^2 C_2^2}{C_1^2} \right) \log \frac{C_3^2}{b_0^2} - \frac{\beta_0}{4}P_{ja}^{(1)} \log^2 \frac{C_3^2}{b_0^2},
\end{aligned} \tag{3.104}$$

Comparing these results to that from Ref. [179], it is important to note the differences in the definition of  $\beta_0$  and  $\beta_1$ . In Ref. [179], the  $\beta$  functions are  $\beta_0 = (11C_A - 2n_f)/6$  and  $\beta_1 = (17C_A^2 - 5C_A n_f - 3C_F n_f)/6$ , while here  $\beta_0 = (11C_A - 2n_f)/12$  and  $\beta_1 = (17C_A^2 - 5C_A n_f - 3C_F n_f)/24$ . Note that this result is consistent with Ref. [179], except for the scale dependence in  $C^{(2)}$ . Additionally, the calculation is extended to include  $A^{(3)}$  and  $B^{(3)}$ . The maximum uncertainty for the Sudakov factor arises for the choice  $C_1 = b_0/2$  and  $C_2 = 2$  and  $C_1 = 2b_0$  and  $C_2 = 1/2$ , which can be understood from the fact that this has the largest impact on the value of the Sudakov integral. The dependence of  $C_3$  for the uncertainty is more complicated, because it deals with the complex energy and  $x$ -dependence of the PDFs.

With the these scale dependence calculations, and the calculations of the previous sections for the asymptotic piece, the comparison of the ResBos2 code to the LHC data for  $W$  and  $Z$  physics is possible to a higher precision then previously. The comparison to the LHC data can be found in Chap. 4 and 5, for the  $Z$  and  $W$  results respectively.



# Chapter 4

## $Z$ Boson Resummed Predictions

At the LHC, one of the most important precision Standard Model processes to study is Drell-Yan, specifically, with a focus on the  $Z$  boson mass peak. The precision of the data at the LHC is at the sub-percent precision for the normalized distributions, and a few percent for unnormalized distributions due to the luminosity uncertainty at the  $Z$ -peak. The transverse momentum distribution is important for the study of soft gluon resummation. However, a new observable was recently proposed at the Tevatron which has been shown to be more accurate, known as  $\phi_\eta^*$  [180, 25] and is discussed in Sec. 4.2.

### 4.1 $Z$ $p_T$ Distribution

As mentioned in Chapter 3, the transverse momentum of the  $Z$  boson requires resummation to describe the small  $p_T$  region. With the precision of the LHC data, the current ResBos code is insufficient, and the order of resummation needs to be increased, from NNLL to N<sup>3</sup>LL. A comparison of the calculation using NNLL resummation to the data at ATLAS at  $\sqrt{s} = 8$  TeV can be seen in Fig. 4.1. Clearly, there is a disagreement between the theory and the data. There are two regions of disagreement between the theory prediction and the data. These two regions can be categorized as: the intermediate transverse momentum region, between about 10 GeV and 100 GeV, and the high transverse momentum region,

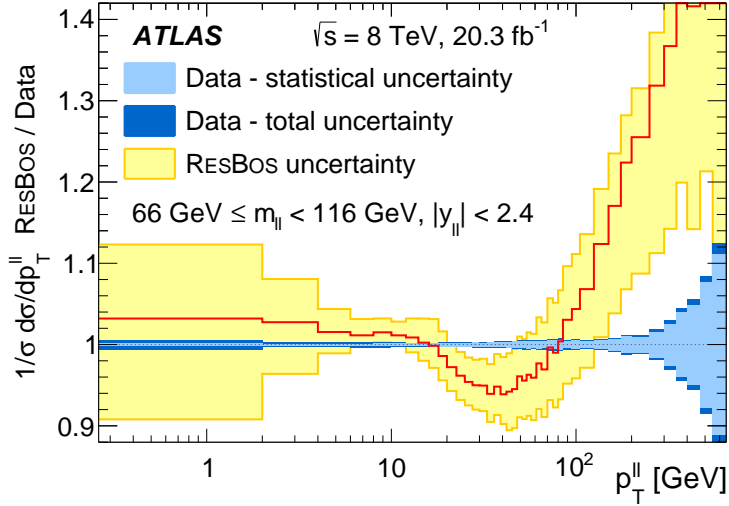


Figure 4.1: Comparison of  $p_T^{ll}$  data from ATLAS compared to ResBos predictions, reproduced from Ref. [23]

above 100 GeV. The resolution to each of these disagreements arises for different physics reasons.

Firstly, in the high transverse momentum region, the ResBos code used the invariant mass of the lepton pair for the factorization and renormalization scale. However, when the transverse momentum is above the mass of the  $Z$  boson, the major contribution comes from the process of a  $Z$  boson with one hard jet. In this process, the hard jet will have an energy close to that of the  $Z$  boson, and the scale that appears in the calculation is the transverse mass of the  $Z$  boson, defined as:

$$\mu^2 = M_{ll}^2 + p_T^2, \quad (4.1)$$

where  $M_{ll}$  is the invariant mass of the lepton pair, and  $p_T$  is the transverse momentum of the lepton pair. Changing the scale to the transverse mass results in better agreement between the theory prediction and the data as seen in Fig. 4.2.

However, in the intermediate transverse momentum region simply changing the scale

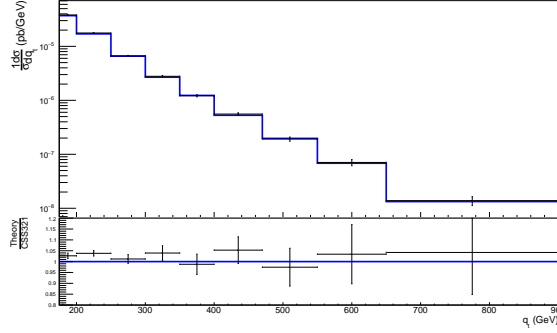


Figure 4.2: Comparison of the ResBos2 calculation with a scale choice of  $\mu^2 = M_\ell^2 + p_T^2$  to the ATLAS data given in Ref. [23], focusing on the high transverse momentum region

to the transverse mass does not resolve the problem. Therefore, the precision of the theory calculation needs to be improved. The order of the resummation calculation needs to be done to N<sup>3</sup>LL, which means that the  $A$  coefficient is done to  $\mathcal{O}(\alpha_s^3)$ , the  $B$  coefficient is done to  $\mathcal{O}(\alpha_s^3)$ , and the  $C$  coefficient is done to  $\mathcal{O}(\alpha_s^2)$ . The order of  $B$  needs to be one order higher than that of the  $C$  coefficient in order to have good agreement between the CSS and CFG prediction as seen in Fig. 4.3. In the previously mentioned figure, only the  $W$ -piece is included to focus solely on the difference between the two schemes (the  $Y$ -piece is the same in both schemes). The fixed order calculation for  $Z$ +jet at NLO is obtained from the Sherpa [178] program to correctly predict the angular distributions which is discussed in Section 4.3. Since the fixed order calculation contains a jet, the transverse momentum of the  $Z$  boson is required to be greater than 2 GeV to remove the singularity at  $p_T = 0$ . Additionally, it has been shown that at this order the fixed order and asymptotic calculations cancel to a sub-percent accuracy for  $p_T \approx 2$  GeV, as shown in Fig. 4.4. Finally, the matching of the resummed prediction to the fixed order prediction needs to be performed at high transverse momentum. In the ResBos2 code, matching occurs when the asymptotic expansion cancels with the resummed calculation, i.e.  $W - A = 0$ . As seen in Fig. 4.5, there are multiple

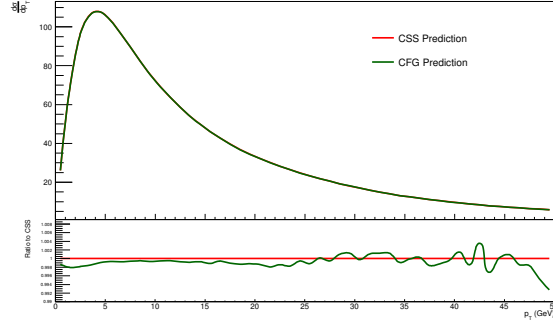


Figure 4.3: Comparison of the CSS and CFG formalisms, focusing on only the small transverse momentum, and not including the  $Y$ -piece.

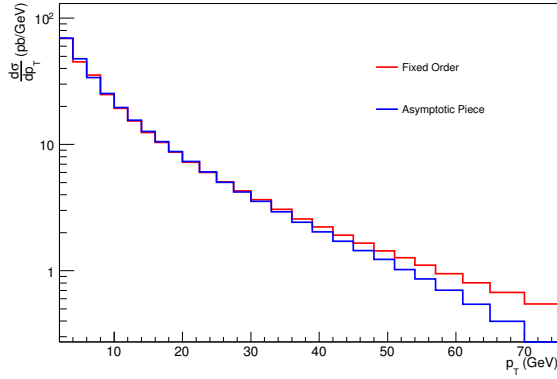


Figure 4.4: Comparison of the fixed order piece up to  $\mathcal{O}(\alpha_s^2)$  to the asymptotic piece up to  $\mathcal{O}(\alpha_s^2)$ . The cutoff on the transverse momentum of both calculations is set to 2 GeV.

crossing points, and the first crossing past the peak is used as the matching condition. Above the matching point, the prediction is set to be only the fixed order prediction. In this matching scheme, the crossing occurs approximately around 20 GeV for the invariant mass of the lepton pair near the  $Z$  peak, and in the central rapidity region, for a resummed order of  $N^3LL$  and an asymptotic order of  $\mathcal{O}(\alpha_s^3)$ . With the resummation calculation to  $N^3LL$ , asymptotic piece to  $\mathcal{O}(\alpha_s^2)$ , the fixed order to NNLO, and the matching procedure as described above, the ResBos2 code can be compared to the data.

The comparison of the ResBos2 code for both the CSS and CFG schemes to the ATLAS

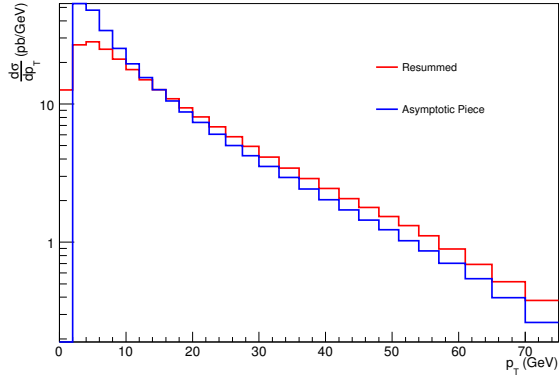


Figure 4.5: Comparison of the Asymptotic piece to  $\mathcal{O}(\alpha_s^3)$  to the N<sup>3</sup>LL resummed piece.

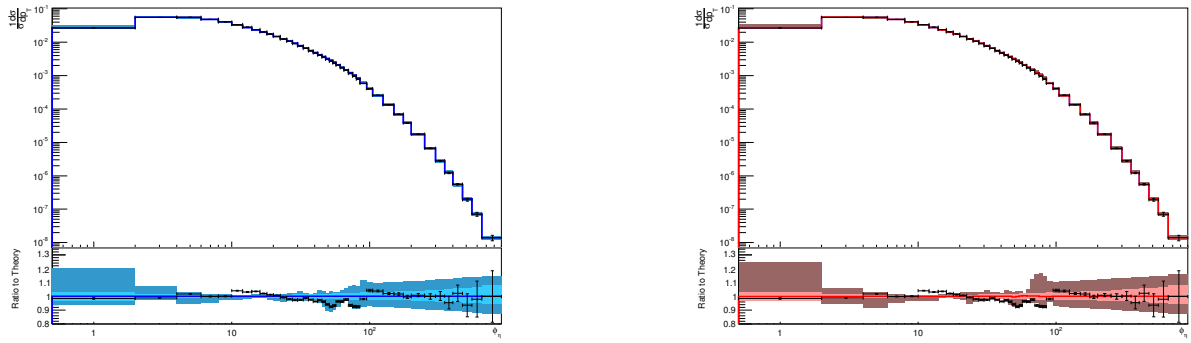


Figure 4.6: Comparison of both the CSS(left) and CFG(right) prediction to data. The PDF and scale uncertainty is given by the error bands. The lighter error band is the PDF uncertainty, and the darker error band is the combination of the scale and PDF uncertainty.

data [23] can be found in Fig. 4.6. In the figure, both the scale and PDF uncertainties are shown. As mentioned previously, the high transverse momentum region is resolved by switching the scale of the calculation, and this is supported by the results shown in the previously mentioned figure. Additionally, by increasing the order to N<sup>3</sup>LL accuracy, the intermediate transverse momentum is improved. There exists a calculation for  $Z$ +jet up to NNLO [24], however, their results are not public enough yet to perform a detailed comparison to the asymptotic piece up to  $\mathcal{O}(\alpha_s^3)$ . However, in their calculation, the k-factor is approximately flat above the matching region, in which the fixed order is the only calculation. To approximate these corrections at high transverse momentum, this k-factor is included. One step for the future of the ResBos2 calculation, is to perform a matching to the NNLO  $Z$ +jet calculation, when the results are public enough to check that the asymptotic piece cancels exactly in the limit of the transverse momentum going to zero. The results from the NNLO  $Z$ +jet calculation for the same data set as compared to above can be found in Fig. 4.7, and shows improvement in the intermediate transverse momentum region over the NLO result. Therefore, the matching to this prediction would further improve the prediction of the ResBos2 code.

## 4.2 $Z \phi_\eta^*$ Distribution

The  $\phi_\eta^*$  observable is a new observable proposed at the Tevatron [180, 25] that only depends on the angular distribution of the final state leptons, but directly correlates with the transverse momentum of the  $Z$  boson. The definition of this observable is given as:

$$\phi_\eta^* = \tan\left(\frac{\pi - \Delta\phi}{2}\right) \sin(\theta_\eta^*), \quad (4.2)$$

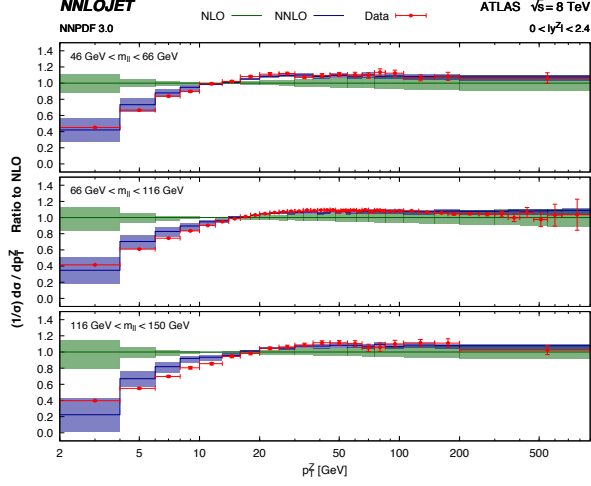


Figure 4.7: Comparison of the fixed order calculation of  $Z$ +jet to NNLO compared to the ATLAS data. Reproduced from [24].

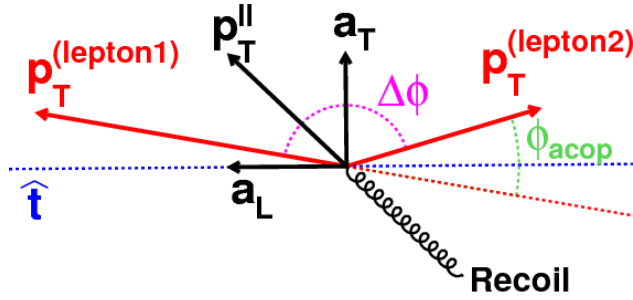


Figure 4.8: The frame definition for  $\phi_\eta^*$ , reproduced from [25].

where  $\Delta\phi$  is the azimuthal separation of the two leptons and  $\theta_\eta^*$  is the measurement of the scattering angle with respect to the proton beam direction in the rest frame of the  $Z$  boson.  $\theta_\eta^*$  is given in terms of lab observables as  $\cos(\theta_\eta^*) = \tanh\left(\frac{\eta^- - \eta^+}{2}\right)$ , where  $\eta^-$  and  $\eta^+$  are the pseudorapidities of the negatively and positively charged lepton respectively, see Fig. 4.8 for a depiction of the frame. Taking the limit of the transverse momentum to zero, the  $\phi_\eta^*$  prediction can be approximated by:

$$\phi_\eta^* \approx \frac{q_T}{M_{ll}} \sin \phi_{CS}, \quad (4.3)$$

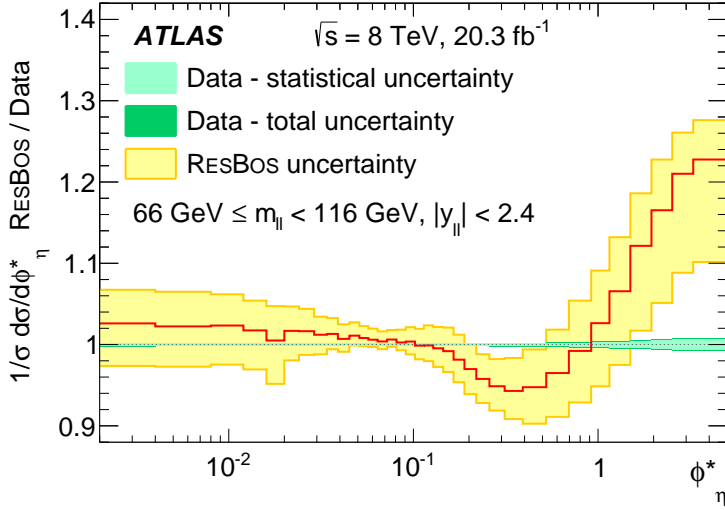


Figure 4.9: Comparison of  $\phi_\eta^*$  data from ATLAS compared to ResBos predictions, reproduced from Ref. [23]

where  $\phi_{CS}$  is the  $\phi$  angle in the Collins-Soper Frame,  $q_T$  is the transverse momentum of the  $Z$  boson, and  $M_{ll}$  is the invariant mass of the lepton pair. Using the equation above, the correspondence between the  $\phi_\eta^*$  distribution and the transverse momentum distribution may be approximated, e.g. for  $M_{ll} \approx M_Z$ , the range of  $10^{-3} \leq \phi_\eta^* \leq 0.1$  radians corresponds to a transverse momentum from 0.1 GeV to 10 GeV. From Eq. 4.3, the features can be mapped to Fig. 4.9, and therefore can be explained in the same manner as before. Looking first at the high  $\phi_\eta^*$  region, the disagreement is again resolved by a change of scale, from  $M_{ll}$  to  $M_T$ . For the intermediate  $\phi_\eta^*$  region ( $0.1 \leq \phi_\eta^* \leq 1$ ), the calculation needs to be improved as detailed above. Again Sherpa is used to obtain the perturbative prediction for  $Z$ +jet at NLO for the transverse momentum above 2 GeV. The matching is done in the same way as mentioned above, again matching in the transverse momentum distribution. Since the results are fully differentiable, the  $\phi_\eta^*$  distribution can be calculated from the lepton and anti-lepton momentums.

Similar to the discussion above for the transverse momentum distribution of the  $Z$  boson,



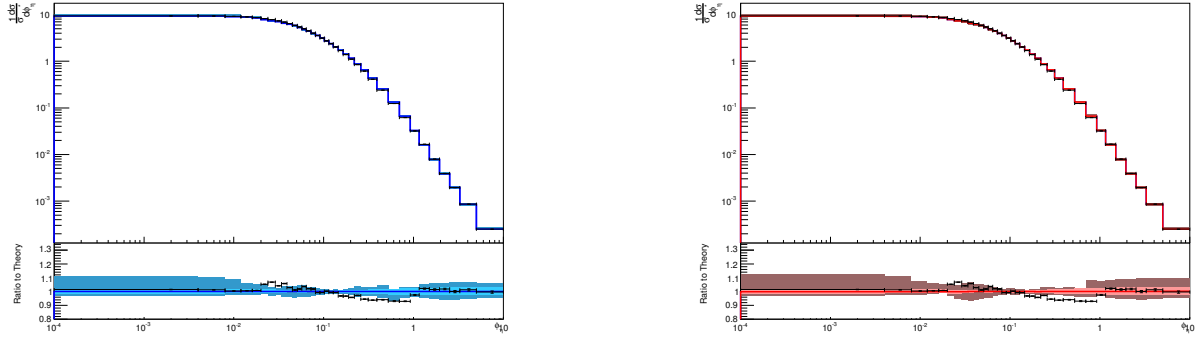


Figure 4.10: Comparison of both the CSS(left) and CFG(right) prediction to data. The PDF and scale uncertainty is given by the error bands. The lighter error band is the PDF uncertainty, and the darker error band is the combination of the scale and PDF uncertainty.

the improvement from the ResBos2 code is again noticeable. The PDF and scale uncertainties for the ResBos2 prediction of  $\phi_\eta^*$  can be found in Fig. 4.10. The improvement in the large  $\phi_\eta^*$  region is again due to using the correct scale for the calculation. Also, the improvement in the intermediate region is due to the increased accuracy of the ResBos2 code over the ResBos code. Finally, the  $Z$ +jet to NNLO fixed order calculation [24] compared to the data can be found in Fig. 4.11. The matching cannot yet be completed to this order, until the results of the group become more public. However, once the matching can be performed, the ResBos2 prediction should be even further improved.

### 4.3 Angular Functions

In Drell-Yan, the angular distributions of the charged lepton pairs allow for an additional handle on precision QCD studies. The fully differential cross-section describing the kinematics of the leptons can be decomposed into nine harmonic polynomials in the Collins-Soper Frame [181, 182, 183, 184]. It is convenient to factor out the unpolarized cross-section, and write the differential cross-section as a function of the harmonic polynomials and dimension-

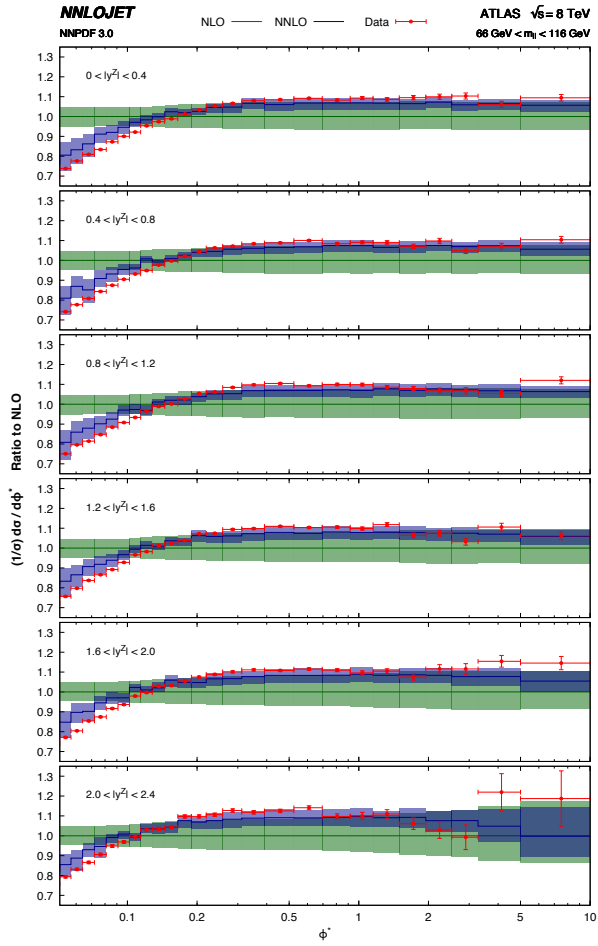


Figure 4.11: Comparison of the fixed order calculation of  $Z$ +jet to NNLO compared to the ATLAS data. Reproduced from [24].

less angular coefficients,  $A_{0-7}$  as:

$$\begin{aligned} \frac{d\sigma}{dp_T dy dQ^2 d \cos \theta d\phi} &= \frac{d\sigma}{dp_T dy dQ^2} \\ &\left[ \left(1 + \cos^2 \theta\right) + \frac{1}{2}A_0 \left(1 - 3 \cos^2 \theta\right) + A_1 \sin 2\theta \cos \phi \right. \\ &\quad + \frac{1}{2}A_2 \sin^2 \theta \cos 2\phi + A_3 \sin \theta \cos \phi + A_4 \cos \theta \\ &\quad \left. A_5 \sin^2 \theta \sin 2\phi + A_6 \sin 2\theta \sin \phi + A_7 \sin \theta \sin \phi \right]. \end{aligned} \quad (4.4)$$

It is important to note that only  $A_4$  is non-zero in the limit of  $p_T$  goes to zero. There is a well established relationship that states that  $A_0 - A_2 = 0$ , known as the Lam-Tung relation [142, 143, 144], and is expected to hold up to  $\mathcal{O}(\alpha_s)$ , but is known to break down at  $\mathcal{O}(\alpha_s^2)$  as will be shown later. The coefficients  $A_{5,6,7}$  are zero at NLO, and small at NNLO, and thus will not be included in the comparisons to data. The coefficients  $A_3$  and  $A_4$  depend on the relationship between the vector and axial couplings and are therefore sensitive to the weak mixing angle ( $\sin^2 \theta_W$ ).

To obtain the theory predictions for each of the angular coefficients, the moments of each coefficient are calculated by:

$$\langle P_i(\cos \theta, \phi) \rangle = \frac{\int P_i(\cos \theta, \phi) d\sigma d \cos \theta d\phi}{\int d\sigma d \cos \theta d\phi}, \quad (4.5)$$

where the  $P_i$ 's are the angular functions associated with each  $A_i$  respectively. There is a

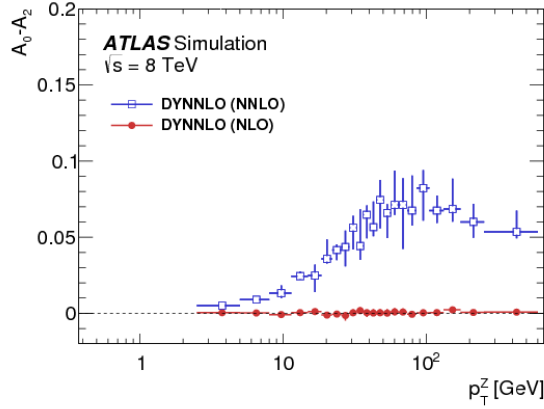


Figure 4.12: The predictions for  $A_2 - A_0$  for the DYNLO code [26], at NLO and NNLO. Reproduced from [27].

direct relationship between each moment and the angular coefficient given by:

$$\begin{aligned}
 \langle P_0(\cos\theta, \phi) \rangle &= \langle \frac{1}{2} (1 - 3\cos^2\theta) \rangle = \frac{3}{20} \left( A_0 - \frac{2}{3} \right), \\
 \langle P_1(\cos\theta, \phi) \rangle &= \langle \sin 2\theta \cos\phi \rangle = \frac{1}{5} A_1, \\
 \langle P_2(\cos\theta, \phi) \rangle &= \langle \sin^2\theta \cos 2\phi \rangle = \frac{1}{10} A_2, \\
 \langle P_3(\cos\theta, \phi) \rangle &= \langle \sin\theta \cos\phi \rangle = \frac{1}{4} A_3, \\
 \langle P_4(\cos\theta, \phi) \rangle &= \langle \cos\theta \rangle = \frac{1}{4} A_4, \\
 \langle P_5(\cos\theta, \phi) \rangle &= \langle \sin^2\theta \sin 2\phi \rangle = \frac{1}{5} A_5, \\
 \langle P_6(\cos\theta, \phi) \rangle &= \langle \sin 2\theta \sin\phi \rangle = \frac{1}{5} A_6, \\
 \langle P_7(\cos\theta, \phi) \rangle &= \langle \sin\theta \sin\phi \rangle = \frac{1}{4} A_7.
 \end{aligned} \tag{4.6}$$

The precision of the LHC shows the breaking of the Lam-Tung relation at large transverse momentum [27], as predicted by the NNLO calculation by DYNLO [26] of the angular

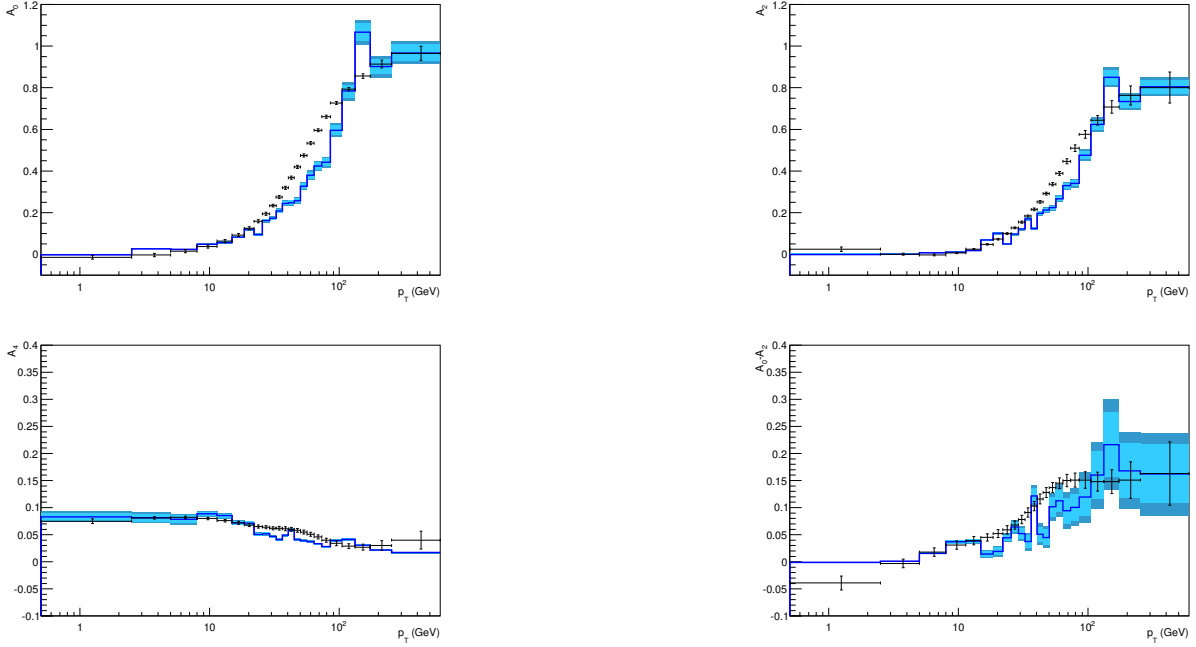


Figure 4.13: Theoretical prediction from the ResBos2 program for the angular coefficients of  $A_0$ ,  $A_2$ ,  $A_4$ , and the breaking of the Lam-Tung Relationship for the CSS Scheme. The lighter error band is the PDF uncertainty, and the darker error band is the combination of the scale and PDF uncertainty.

functions in Drell-Yan, see Fig. 4.12. The original ResBos code is unable to appropriately predict the angular coefficients to the precision required by the LHC, due to the fact that the k-factor obtained using the calculation by Arnold and Kauffman [177] can only be applied to the symmetric and anti-symmetric leading order angular functions ( $\mathcal{L}_0$  and  $A_4$ ), but not to the other angular distributions. To include these corrections in the ResBos2 code, the fixed order prediction is obtained by using the  $Z$ +jet prediction at NLO from the Sherpa code [178], which includes the full angular dependence.

From the prediction in Figs. 4.13 and 4.14, the ResBos2 prediction shows the Lam-Tung relationship breaking down, as expected at this order. Additionally,  $A_4$  is non-zero as expected. There is some disagreement with the data, but it should improve with the inclusion of higher order corrections.

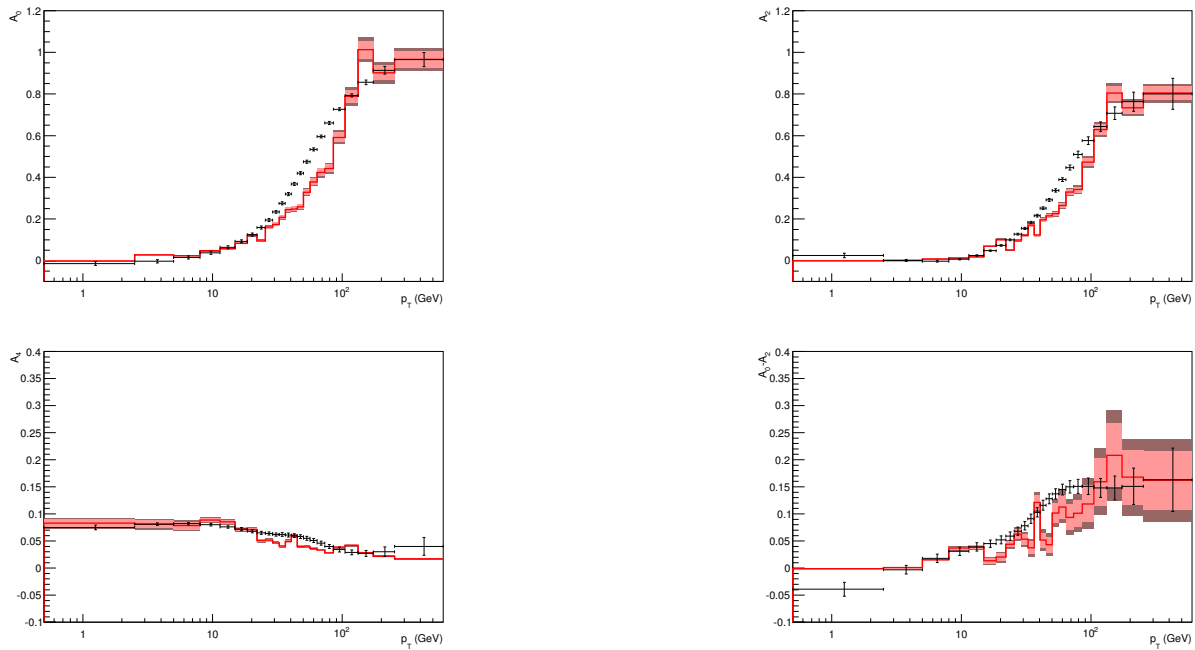


Figure 4.14: Theoretical prediction from the ResBos2 program for the angular coefficients of  $A_0$ ,  $A_2$ ,  $A_4$ , and the breaking of the Lam-Tung Relationship for the CFG Scheme. The lighter error band is the PDF uncertainty, and the darker error band is the combination of the scale and PDF uncertainty.

# Chapter 5

## $W$ Mass

One of the most interesting places to look for new physics signals is in the  $W$  mass. The precision of the Standard Model prediction of the mass is at the 0.01% level, and the experimental measurement is of similar precision. In order to improve the experimental measurement of the  $W$  boson, it is important to understand the transverse momentum of the  $W$  boson, and its relationship with the  $Z$  boson transverse momentum. Currently, the dominate uncertainty in the direct measurement of the  $W$  mass at the LHC arises from the theoretical predictions of the transverse mass of the  $W$  boson, or the transverse momentum of the lepton. In this chapter, the Standard Model prediction from Electroweak precision tests will be discussed, followed by a discussion of the experimental measurements at the Tevatron and the LHC. Finally, the improvements to the ResBos2 calculation for the  $W$  mass measurement are introduced.

### 5.1 SM EW Precision Fit

Using the Electroweak input scheme defined by on  $M_Z$ ,  $G_\mu$ , and  $\alpha$ , the  $W$  boson mass is a predicted parameter. The Standard Model calculation is detailed in Ref. [185], and is given by:

$$M_W^2 \left( 1 - \frac{M_W^2}{M_Z^2} \right) = \frac{\pi\alpha}{\sqrt{2}G_\mu} (1 + \Delta r), \quad (5.1)$$

with the loop corrections contained in  $\Delta r$ . At the one-loop order, the calculation of  $\Delta r$  is given as:

$$\Delta r = \Delta\alpha - \frac{c_W^2}{s_W^2} \Delta\rho + \Delta r_{rem}(M_H), \quad (5.2)$$

where  $c_W^2 = \frac{M_W^2}{M_Z^2}$ ,  $s_W^2 = 1 - c_W^2$ , and  $s_W$  is the Weinberg angle defined in Chap. 1 as the rotation angle needed to diagonalize the neutral boson sector of the Standard Model. The correction to  $\alpha$ , given by  $\Delta\alpha$  is due to light fermions and is proportional to the logarithm of their masses. Additionally, there is a modification to the  $\rho$  parameter as defined in Sec. 1.1.3. Finally, the last term contains all the dependence of the Higgs boson mass.

The calculation of  $\Delta r$  has been done to two-loops in the Electroweak coupling, contains the fermionic contributions [186, 187, 188] and the bosonic contributions [189, 190, 191, 192]. As for the QCD corrections to  $\Delta r$ , they are known to  $\mathcal{O}(\alpha\alpha_s^2)$  [193, 194, 195, 196]. Furthermore,  $\Delta\rho$  has been calculated to  $\mathcal{O}(\alpha\alpha_s^3)$  [197, 198, 199]. The fit to all of the Electroweak observables was done at NNLO in Ref. [5], and a summary of the results can be found reproduced in Table 5.1. The precision obtained by the global fit on the mass of the  $W$  boson sets the goal for the LHC. It is possible to break down the uncertainty of the fit to the  $W$  mass measurement into the contributions from the top mass, the theory uncertainty of the top mass, the  $Z$  mass,  $\Delta\alpha_{had}$ ,  $\alpha_s$ , the Higgs mass, and the theory uncertainty of the  $W$  mass. These contributions are broken down in Table 5.2. The largest uncertainties on the indirect determination of the  $W$  mass come from both the experimental and theoretical determination of the top quark mass, followed by the theory uncertainty on the  $W$  mass, and then the experimental measurement of the mass of the  $Z$  boson. The LHC should provide an improvement on the experimental measurement of the top quark mass, and should improve significantly at a future electron-positron collider. There is not going to be any improvement



Parameter	Input Value	Fit Result	w/o exp. input	w/o exp. input or theory unc.
$M_H$ [GeV] <sup>a</sup>	$125.14 \pm 0.24$	$125.14 \pm 0.24$	$93_{-21}^{+25}$	$93_{-20}^{+24}$
$M_W$ [GeV]	$80.385 \pm 0.015$	$80.364 \pm 0.007$	$80.358 \pm 0.008$	$80.358 \pm 0.006$
$\Gamma_W$ [GeV]	$2.085 \pm 0.042$	$2.091 \pm 0.001$	$2.091 \pm 0.001$	$2.091 \pm 0.001$
$M_Z$ [GeV]	$91.1875 \pm 0.0021$	$91.1880 \pm 0.0021$	$91.200 \pm 0.011$	$91.200 \pm 0.010$
$\Gamma_Z$ [GeV]	$2.4952 \pm 0.0023$	$2.4950 \pm 0.0014$	$2.4946 \pm 0.0016$	$2.4945 \pm 0.0016$
$m_t$ [GeV]	$173.34 \pm 0.76$	$173.81 \pm 0.85$	$170.0_{-2.4}^{+2.3}$ <sup>b</sup>	$177.0 \pm 2.3$ <sup>b</sup>

<sup>a</sup> Average of the ATLAS [200] and CMS [201] measurements, ignoring any correlation between systematic uncertainties

<sup>b</sup> The theoretical top-mass uncertainty is excluded.

Table 5.1: Electroweak fit. The fourth column gives the fit results without using any experimental or phenomenological estimate for the parameter when performing the fit. The fifth column is the same as the fourth, but ignores all theory uncertainties. The table is reproduced from Ref. [5].

Source	Value
$m_t$	0.0046
$\delta_{theory}m_t$	0.0030
$M_Z$	0.0026
$\Delta\alpha_{had}$	0.0018
$\alpha_s$	0.0020
$M_H$	0.0001
$\delta_{theory}M_W$	0.0040

Table 5.2: The values are reported in GeV, and taken from Ref. [5]

on the experimental measurement of the  $Z$  boson at the LHC or at a future electron-positron collider, due to the fact that the LEP measurements are very precise [202]. Finally, the experimental measurement of the  $W$  mass ideally should be close to the current uncertainty of the indirect measurement by the end of the LHC running [203, 204]. The details of the experimental goals and the limits that are expected are discussed in the following section.

## 5.2 Experimental Measurement

The experimental measurement of the  $W$  mass is one of the most important measurements at a hadron collider. The most precise channel to study the  $W$  mass at the LHC comes from the process,  $pp \rightarrow e\nu + X$ . However, the fact that there is a neutrino in the final state leads to the inability to directly reconstruct the invariant mass of the lepton-neutrino system. Therefore, two different observables are proposed to study the mass of the  $W$  boson. The first observable is the transverse mass of the  $W$  boson defined as:

$$M_T^2 = 2p_{T_l} \cancel{E}_T (1 - \cos \theta), \quad (5.3)$$

where  $p_{T_l}$  is the transverse momentum of the final state lepton,  $\cancel{E}_T$  is the missing transverse momentum (attributed to the neutrino), and  $\theta$  is the angle between the lepton and missing transverse momentum. The other observable is the transverse momentum of the lepton. Both of these observables are not accurately predicted by a fixed order calculation due to the dependence on the transverse momentum of the  $W$  boson, which requires resummation.

In measuring the  $W$  mass, an appropriate prediction of the Jacobian peak region for the lepton is important to obtain the correct mass. One of the most important features in determining the  $W$  mass is the tail of the distribution, and the Jacobian peak. Having an accurate theoretical prediction is required to match the shape of the data.

The traditional method of obtaining the  $W$  mass is through the use of a template fit technique. To estimate the uncertainty that arises from the PDF, the following 4 step method is used [205]<sup>1</sup>:

---

<sup>1</sup>For real data, a similar procedure is used to estimate the central value, but replacing the pseudodata with the actual data.

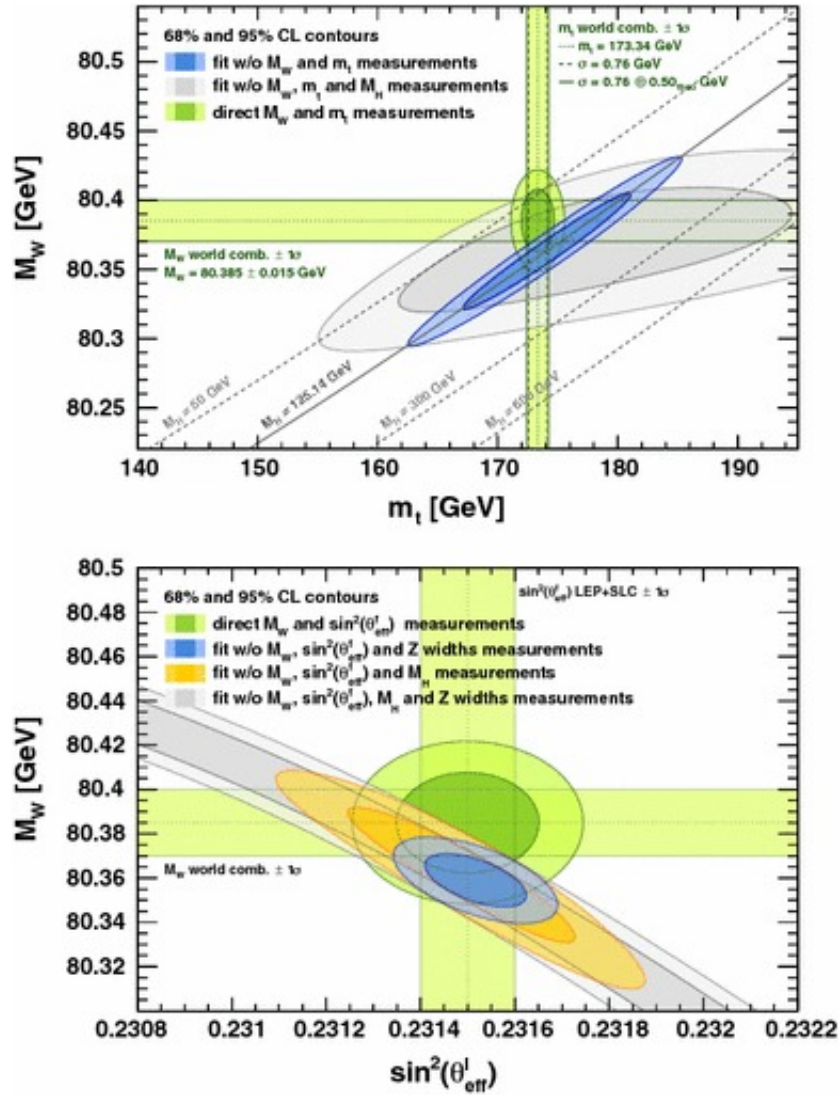


Figure 5.1: Results of the EW Fit, reproduced from Ref. [5]

1. Generate the observable to be used for the fitting for fixed  $W$  mass for each PDF error set of interest. Treat the generated observable as pseudodata.
2. Generate the mass templates for the distributions used to fit the pseudodata as a function of the  $W$  boson mass using the central prediction for the PDF.
3. Given the PDF set  $i$ , and the mass template  $j$ , calculate the  $\chi^2$  for each combination of  $i$  and  $j$ , given by:

$$\chi_{i,j}^2 = \frac{1}{N_{\text{bins}}} \sum_{k=1}^{N_{\text{bins}}} \frac{(O_k^j - O_k^i)^2}{(\sigma_k^i)^2 + (\sigma_k^j)^2}, \quad (5.4)$$

where  $O_k$  and  $\sigma_k$  are the value of the observable and the standard deviation of it in a given bin ( $k$ ), respectively.

4. The minimum of the  $\chi_{i,j}^2$  distribution for each PDF set  $i$  gives the mass  $j$  that the PDF best fits. The difference from the central value is the shift in the mass induced by PDF  $i$ . Combining all of the PDF sets, using the method to obtain the uncertainty as defined for the given PDF set, the allowed mass range is obtained.

This procedure will be demonstrated below for the CT14nnlo PDF set [10] for the lepton transverse momentum. Similar results are obtained if the transverse mass of the  $W$  boson is used. The CTEQ PDFs are based off of the Hessian method. Therefore, each eigenvector does not give the full uncertainty, and the uncertainty needs to be calculated by using the

master equation as given in [206] and below:

$$\Delta X^+ = \sqrt{\sum_i^n (\max(X_i^+ - X_0, X_i^- - X_0, 0))^2}, \quad (5.5)$$

$$\Delta X^- = \sqrt{\sum_i^n (\max(X_0 - X_i^+, X_0 - X_i^-, 0))^2}, \quad (5.6)$$

where  $i$  goes over each eigenvector, and the  $\pm$  refers to whether the shift is along the positive or negative direction respectively.

### 5.3 ResBos2 Results

One important prediction to make is the ratio of the transverse momentum of the  $Z$  boson to the transverse momentum of the  $W$  boson. With an accurate prediction of this ratio, the experimentalists can use data driven methods to obtain the transverse momentum predictions of the  $W$  boson through:

$$\frac{d\sigma}{dp_T^{(W)}} = \left( \frac{\frac{d\sigma}{dp_T^{(W)} \text{ th}}}{\frac{d\sigma}{dp_T^{(Z)} \text{ th}}} \right) \frac{d\sigma}{dp_T^{(Z)} \text{ data}}, \quad (5.7)$$

where  $\frac{d\sigma}{dp_T^{(W)}}$  is the data driven prediction for the  $W$  boson transverse momentum,  $\frac{d\sigma}{dp_T^{(W)} \text{ th}}$  is the theory prediction for the  $W$  boson transverse momentum,  $\frac{d\sigma}{dp_T^{(Z)} \text{ th}}$  is the theory prediction for the  $Z$  boson, and  $\frac{d\sigma}{dp_T^{(Z)} \text{ data}}$  is the  $Z$  boson transverse momentum data. An accurate prediction of this ratio allows to attempt to apply a transverse momentum cut on the  $W$  boson. This cut reduces the theoretical uncertainty arising from the PDFs greatly [205]. The normalized ratio ( $R_{W/Z}$ ) is shown in Fig. 5.2 for the ResBos2 prediction.

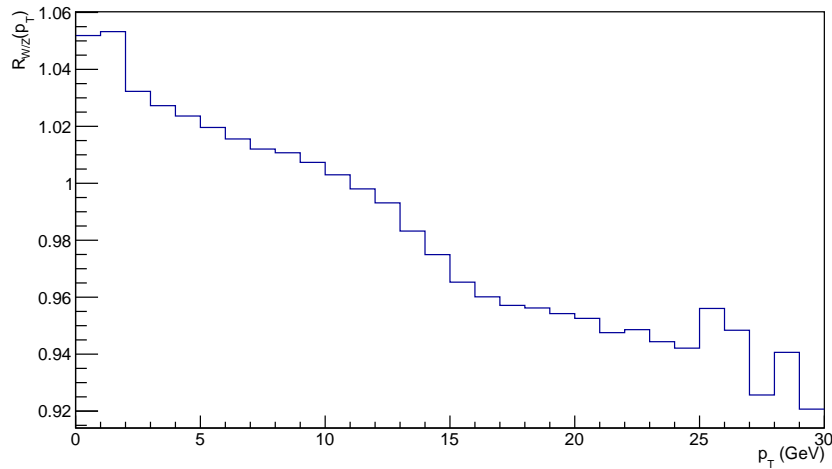


Figure 5.2: The ratio of the normalized transverse momentum distributions of the  $W$  boson to the  $Z$  boson.

The ResBos code can be used to calculate the theoretical uncertainty of the PDFs, as described in the section above. An example of the  $\chi^2$  distribution for one error set can be found in Fig. 5.3. After calculating the shift for all of the eigenvectors, and using the Hessian master equation as given in Eq. 5.5, the CT14nnlo PDF uncertainty can be calculated. For a collider center of mass energy of  $\sqrt{13}$  TeV, the  $W$  mass uncertainty is given as  $\delta^+ = 37$  MeV and  $\delta^- = 34$  MeV.

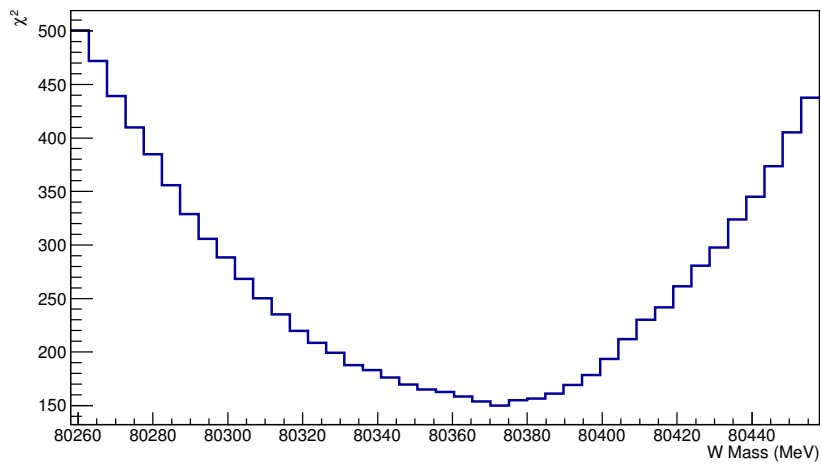


Figure 5.3: An example of the  $\chi^2$  distribution for an error set, others are similar to this. The central input mass was  $M_W = 80.358$  GeV. The minimum here occurs around 80.372, a shift of 14 MeV.

# Chapter 6

## Color Singlet Boson Plus Jet

### Resummation at Hadron Colliders

Soft gluon resummation for the class of color singlet boson plus jet processes has its own interest in perturbative QCD. To deal with the divergence in low transverse momentum hard processes, the transverse momentum resummation formalism is employed [138]. However, the  $q_T$  resummation formalism has been mainly applied to color-neutral particle production, such as inclusive vector boson  $W/Z$  and Higgs boson productions. Extensions to jet production in the final state has been limited, not only because of the technical issues associated with the jets in the final state, but also because jets carry color. Therefore, the soft gluon interactions are more complicated than those for color neutral particle production. Nevertheless, there has been progress made in the last few years on the  $q_T$  resummation for dijet production in hadronic collisions [207, 208, 209]. Here the details of expanding the calculation to single jets plus a color singlet boson are examined.

The resummation formula for  $V + j$  resummation can be summarized as

$$\frac{d^5\sigma}{dy_V dy_j dP_T^2 d^2q_\perp} = \sum_{ab} \sigma_0 \left[ \int \frac{d^2\vec{b}_\perp}{(2\pi)^2} e^{-i\vec{q}_\perp \cdot \vec{b}_\perp} W_{ab \rightarrow cd}(x_1, x_2, b_\perp) + Y_{ab \rightarrow cd} \right], \quad (6.1)$$

where  $y_V$  and  $y_j$  are rapidities for the boson and the jet, respectively,  $P_T$  is the jet transverse



momentum, and  $\vec{q}_\perp = \vec{P}_{V\perp} + \vec{P}_J$  is the total transverse momentum of the boson and the jet. The first term  $W$  contains the all order resummation, the second term  $Y$  comes from the difference between the fixed order corrections and the asymptotic piece, and  $\sigma_0$  represents the normalization of the differential cross section. Higgs plus jet  $q_T$  resummation will be used as an example of the procedure for calculating the resummation results for this class of processes.

## 6.1 Higgs Plus Jet Resummation

The effective Lagrangian in the heavy top quark mass limit is used to describe the coupling between the Higgs boson and gluon given by:

$$\mathcal{L}_{eff} = -\frac{\alpha_s}{12\pi v} F_{\mu\nu}^a F^{a\mu\nu} H, \quad (6.2)$$

where  $v$  is the vacuum expectation value,  $H$  the Higgs field,  $F^{\mu\nu}$  the gluon field strength tensor, and  $a$  the color index.

To begin, the  $W$  term can be written as:

$$W_{gg\rightarrow Hg}(x_1, x_2, b) = H_{gg\rightarrow Hg}(Q) x_1 f_g(x_1, \mu) x_2 f_g(x_2, \mu) e^{-S(Q^2, b_\perp)}, \quad (6.3)$$

$$W_{gq\rightarrow Hq}(x_1, x_2, b) = H_{gq\rightarrow Hq}(Q) x_1 f_g(x_1, \mu) x_2 f_q(x_2, \mu) e^{-S(Q^2, b_\perp)} + x_1 \leftrightarrow x_2, \quad (6.4)$$

$$W_{q\bar{q}\rightarrow Hg}(x_1, x_2, b) = H_{q\bar{q}\rightarrow Hg}(Q) x_1 f_q(x_1, \mu) x_2 f_{\bar{q}}(x_2, \mu) e^{-S(Q^2, b_\perp)} + x_1 \leftrightarrow x_2, \quad (6.5)$$

at the next-to-leading logarithmic (NLL) accuracy. Here  $Q^2 = s = x_1 x_2 S$  and represents the hard momentum scale,  $b_0 = 2e^{-\gamma_E}$ , with  $\gamma_E$  being the Euler constant,  $f_{a,b}(x, \mu)$  are the parton distributions for the incoming partons  $a$  and  $b$ , and  $x_{1,2}$  are momentum fractions of

the incoming hadrons carried by the partons. Beyond the NLL, a  $C$  function associated with the parton distribution functions will also need to be included.

The Sudakov form factor can be written as

$$S_{\text{Sud}}(Q^2, b_\perp) = \int_{C_1^2/b_\perp^2}^{C_2^2 Q^2} \frac{d\mu^2}{\mu^2} \left[ \ln \left( \frac{Q^2}{\mu^2} \right) A + B + D \ln \frac{1}{R^2} \right], \quad (6.6)$$

where  $R$  represents the cone size of the jet. Here the parameters  $A$ ,  $B$ ,  $D$  can be expanded perturbatively in  $\alpha_s$ , for example in the  $gg \rightarrow Hg$  channel,  $A = C_A \frac{\alpha_s}{\pi}$ ,  $B = -2C_A \beta_0 \frac{\alpha_s}{\pi}$ , and  $D = C_A \frac{\alpha_s}{2\pi}$ . The hard coefficient  $H$  can be calculated order by order, from the leading Born diagrams. For example, the gluon-gluon channel is given by:  $H^{(0)} = (s^4 + t^4 + u^4 + m_h^8) / (stu)$  [210, 211], where  $s = Q^2$ ,  $t$  and  $u$  are the Mandelstam variables for the partonic  $2 \rightarrow 2$  process.

### 6.1.1 Virtual Corrections

Firstly,  $W(b)$  needs to be calculated at the one-loop order and shown that it can be factorized into the parton distribution, jet, soft, and hard factors. The virtual corrections have been calculated in the literature, see for example Refs. [210, 212]. For convenience, the results are summarized below to demonstrate the resummation of the Higgs plus jet system. Since the virtual diagrams are proportional to  $\delta(q_T)$ , the  $b$ -space result can be expressed as

$$W_{ab}^{(1)v}(b_T) = x_1 f(x_1, \mu) x_2 f(x_2, \mu) \Gamma_{ab}^v, \quad (6.7)$$

where  $f_1$  and  $f_2$  are the PDFs,  $x_1$  and  $x_2$  are the momentum fractions of the partons from each hadron, and the expressions for  $\Gamma_{ab}^v$  can be extracted from the calculations in the

references mentioned above. For the gluon-gluon channel,

$$\begin{aligned}
\Gamma_{gg}^v &= H_{gg}^{(0)} \frac{\alpha_s C_A}{2\pi} \left[ -\frac{3}{\epsilon^2} + \frac{1}{\epsilon} \left( 2 \ln \frac{Q^2}{\mu^2} + \ln \frac{P_J^2}{\mu^2} \right) \right. \\
&\quad + \frac{1}{2} \left( \ln \frac{P_J^2}{\mu^2} \right)^2 - 2 \ln \frac{Q^2}{\mu^2} \ln \frac{P_J^2}{\mu^2} - 2 \ln \frac{Q^2}{-t} \ln \frac{Q^2}{-u} + \frac{11}{6} \pi^2 \\
&\quad + 2 \text{Li}_2 \left( 1 - \frac{M^2}{Q^2} \right) + 2 \text{Li}_2 \left( \frac{t}{M^2} \right) + 2 \text{Li}_2 \left( \frac{u}{M^2} \right) \\
&\quad \left. + \left( \ln \frac{\tilde{t}}{M^2} \right)^2 - \left( \ln \frac{\tilde{t}}{-t} \right)^2 + \left( \ln \frac{\tilde{u}}{M^2} \right)^2 - \left( \ln \frac{\tilde{u}}{-u} \right)^2 \right] \\
&\quad + \delta H_{gg}^{(1)} , \tag{6.8}
\end{aligned}$$

where  $\tilde{u}, \tilde{t} = M^2 - u, t$  respectively, and  $\delta H_{gg}^{(1)}$  is the finite term not proportional to  $H_{gg}^{(0)}$  and is given by:

$$\delta H_{gg}^{(1)} = (N - n_f) \frac{1}{3} N(N^2 - 1) \frac{M^2}{stu} \left[ stu + M^2 (st + su + tu) \right] . \tag{6.9}$$

For the quark-gluon channel,

$$\begin{aligned}
\Gamma_{qg}^v &= H_{qg}^{(0)} \frac{\alpha_s}{2\pi} \left\{ 4C_A \beta_0 \left( \frac{2}{\epsilon} + \ln \frac{-u}{\mu^2} - \frac{10}{3} \right) + C_A \left[ \frac{-2}{\epsilon^2} - \frac{2}{\epsilon} \left( \ln \frac{-u}{\mu^2} - \ln \frac{-t}{\mu^2} - \ln \frac{s}{\mu^2} \right) \right. \right. \\
&\quad + 2 \ln \frac{s}{\mu^2} \ln \frac{u}{t} + \ln^2 \frac{-u}{\mu^2} - \ln^2 \frac{-t}{\mu^2} - \ln^2 \frac{s}{\mu^2} - 2 \ln^2 \frac{\tilde{u}}{-u} + 2 \ln^2 \frac{\tilde{u}}{M^2} \\
&\quad \left. + 4 \text{Li}_2 \left( \frac{u}{M^2} \right) + 18 \zeta(2) - \frac{\pi^2}{3} + \frac{14}{3} \right] \\
&\quad + C_F \left[ \frac{-4}{\epsilon^2} - \frac{2}{\epsilon} \left( -2 \ln \frac{-u}{\mu^2} + 3 \right) - 2 \ln^2 \frac{-u}{\mu^2} + 2 \ln^2 \frac{s}{t} + 6 \ln \frac{-u}{\mu^2} \right. \\
&\quad \left. + 4 \text{Li}_2 \left( 1 - \frac{M^2}{s} \right) + 4 \text{Li}_2 \left( \frac{t}{M^2} \right) - 2 \ln^2 \frac{\tilde{t}}{-t} + 2 \ln^2 \frac{\tilde{t}}{M^2} + 4 \zeta(2) - \frac{2\pi^2}{3} - 16 \right] \left. \right\} \\
&\quad + \delta H_{qg}^{(1)} , \tag{6.10}
\end{aligned}$$

again with  $\delta H_{qg}^{(1)}$  analogous to  $\delta H_{gg}^{(1)}$  above, given by:

$$\delta H_{qg}^{(1)} = (C_A - C_F) C_A C_F (s + t) . \quad (6.11)$$

Finally, for the quark-anti-quark channel,

$$\begin{aligned} \Gamma_{q\bar{q}}^v = & H_{q\bar{q}}^{(0)} \frac{\alpha_s}{2\pi} \left\{ 4C_A \beta_0 \left( \frac{2}{\epsilon} - 2 \ln \frac{s}{\mu^2} + \frac{10}{3} \right) + C_A \left[ \frac{-2}{\epsilon^2} - \frac{2}{\epsilon} \ln \frac{s\mu^2}{ut} \right. \right. \\ & \ln^2 \frac{ut}{s\mu^2} + 2 \ln^2 \frac{s}{\mu^2} - 2 \ln^2 \frac{-t}{\mu^2} - 2 \ln^2 \frac{-u}{\mu^2} + 4 \text{Li}_2 \left( 1 - \frac{M^2}{s} \right) \\ & \left. \left. - 14\zeta(2) - \frac{\pi^2}{3} - 8 \right] + C_F \left[ \frac{-4}{\epsilon^2} - \frac{2}{\epsilon} \left( -2 \ln \frac{s}{\mu^2} + 3 \right) \right. \right. \\ & - 18 \ln \frac{-t}{\mu^2} \ln \frac{-u}{\mu^2} + 6 \ln \frac{s}{\mu^2} + 2 \ln^2 \frac{ut}{\mu^2 s} + 4 \ln \frac{s}{\mu^2} \ln \frac{ut}{s\mu^2} + 4 \text{Li}_2 \left( \frac{t}{M^2} \right) + 4 \text{Li}_2 \left( \frac{u}{M^2} \right) \\ & \left. \left. - 2 \ln^2 \frac{\tilde{t}}{-t} - 2 \ln^2 \frac{\tilde{u}}{-u} + 2 \ln^2 \frac{\tilde{t}}{M^2} + 2 \ln^2 \frac{\tilde{u}}{M^2} + 36\zeta(2) - \frac{2}{3}\pi^2 - 16 \right] \right\} \\ & + \delta H_{q\bar{q}}^{(1)} , \end{aligned} \quad (6.12)$$

with  $\delta H_{q\bar{q}}^{(1)}$  given as:

$$\delta H_{q\bar{q}}^{(1)} = (C_A - C_F) C_A C_F (-t - u) . \quad (6.13)$$

It is important to note the  $\frac{1}{\epsilon^2}$  and  $\frac{1}{\epsilon}$  divergences that appear in the above equations. These will be canceled by the divergences in the remaining terms.

At NLO, the strong coupling needs to be renormalized, yielding the following contribution:

$$\frac{\alpha_s C_A}{2\pi} \left( \frac{Q^2}{\mu^2} \right)^{-\epsilon} \left( -\frac{3}{\epsilon} \right) 2\beta_0 . \quad (6.14)$$

Here, the renormalization scale is set to  $Q^2$  to simplify the final expression.

### 6.1.2 Jet Corrections

Next, since this process contains a final state jet, the jet function needs to be applied in order to cancel out the collinear divergences from the final state. In order to perform this calculation, the Narrow Jet Approximation (NJA) is applied as derived in the calculation of inclusive jet production [213]. This approximation allows an analytic result for the jet production cross section to be obtained. For completeness, the quark and gluon jet contributions are listed below:

$$\begin{aligned}\mathcal{J}^g &= \frac{\alpha_s C_A}{2\pi} \left[ \frac{1}{\epsilon^2} + \frac{1}{\epsilon} \left( 2\beta_0 - \ln \frac{P_J^2 R^2}{\mu^2} \right) + I^g \right] , \\ \mathcal{J}^q &= \frac{\alpha_s C_F}{2\pi} \left[ \frac{1}{\epsilon^2} + \frac{1}{\epsilon} \left( \frac{3}{2} - \ln \frac{P_J^2 R^2}{\mu^2} \right) + I^q \right] ,\end{aligned}\tag{6.15}$$

where  $I^{g,q}$  depends on the jet algorithm used. For the  $k_t$ -family of jet algorithms the values of  $I^q$  and  $I^g$  are,

$$I^g = \frac{1}{2} \left( \ln \frac{P_J^2 R^2}{\mu^2} \right)^2 - 2\beta_0 \ln \frac{P_J^2 R^2}{\mu^2} + \frac{67}{9} - \frac{3}{4}\pi^2 - \frac{23}{54}N_f ,\tag{6.16}$$

$$I^q = \frac{1}{2} \left( \ln \frac{P_J^2 R^2}{\mu^2} \right)^2 - \frac{3}{2} \ln \frac{P_J^2 R^2}{\mu^2} + \frac{13}{2} - \frac{3}{4}\pi^2 .\tag{6.17}$$

Their contributions to  $W(b_\perp)$  can be included in the following manner,

$$W_{gg}^{(1)J}(b_\perp) = x_1 f_g(x_1, \mu) x_2 f_g(x_2, \mu) \mathcal{J}_g ,\tag{6.18}$$

$$W_{qg}^{(1)J}(b_\perp) = x_1 f_q(x_1, \mu) x_2 f_g(x_2, \mu) \mathcal{J}_q ,\tag{6.19}$$

$$W_{q\bar{q}}^{(1)J}(b_\perp) = x_1 f_q(x_1, \mu) x_2 f_{\bar{q}}(x_2, \mu) \mathcal{J}_g .\tag{6.20}$$

Again, there are divergences proportional to  $\frac{1}{\epsilon}$  as expected for a collinear jet function, which will be canceled with similar contributions from the soft corrections, see Sec. 6.1.4.

### 6.1.3 Collinear Corrections

Thirdly, the collinear radiation associated with the incoming partons needs to be calculated.

These contributions can be written in terms of parton splitting functions:

$$P_{qq} = \frac{\alpha_s}{2\pi^2} \frac{1}{q_{\perp}^2} C_F \int \frac{dx'}{x'} x' f_q(x', \mu) \frac{\xi(1+\xi^2)}{(1-\xi)_+}, \quad (6.21)$$

$$P_{gq} = \frac{\alpha_s}{2\pi^2} \frac{1}{q_{\perp}^2} C_F \int \frac{dx'}{x'} x' f_q(x', \mu) \left(1 + (1-\xi)^2\right), \quad (6.22)$$

$$P_{gg} = \frac{\alpha_s}{2\pi^2} \frac{1}{q_{\perp}^2} C_A \int \frac{dx'}{x'} x' f_g(x', \mu) \xi \left( \frac{2\xi}{(1-\xi)_+} + \frac{2(1-\xi)}{\xi} + 2\xi(1-\xi) \right), \quad (6.23)$$

$$P_{qg} = \frac{\alpha_s}{2\pi^2} \frac{1}{q_{\perp}^2} \frac{1}{2} \int \frac{dx'}{x'} x' f_g(x', \mu) \left( \xi^2 + (1-\xi)^2 \right). \quad (6.24)$$

where  $\xi = x/x'$ . Here the  $\xi \neq 1$  contributions are taken into consideration, whereas the  $\xi = 1$  part will be evaluated together with the soft gluon radiation contribution. These terms introduce divergences of the form  $\frac{1}{\epsilon} P_{ab}$  into  $W_{ab}(b)$ .

### 6.1.4 Soft Corrections

For soft gluon radiations, the leading power expansion can be applied to derive the dominant contribution by the Eikonal approximation, as discussed in Sec. F. This analysis has been applied in Ref. [214] to obtain the leading double logarithmic contributions to dijet production. For outgoing quark, antiquark, and gluon lines, the Eikonal approximation gives the

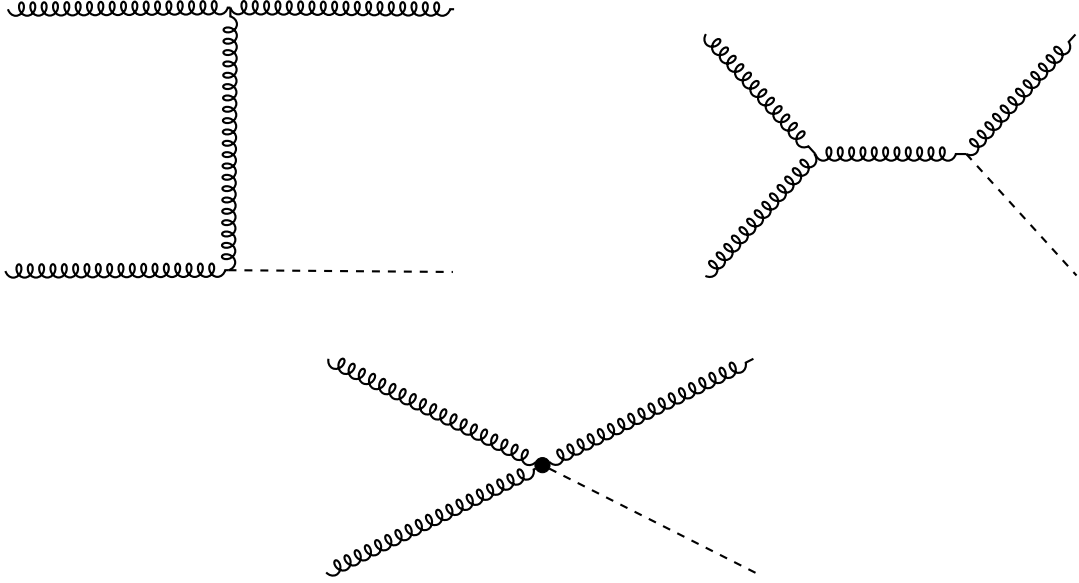


Figure 6.1: Feynman diagrams for the gluon-gluon scattering channel to a Higgs Boson.

following Feynman rules:

$$\frac{2k_i^\mu}{2k_i \cdot k_g + i\epsilon} g, \quad -\frac{2k_i^\mu}{2k_i \cdot k_g + i\epsilon} g, \quad \frac{2k_i^\mu}{2k_i \cdot k_g + i\epsilon} g, \quad (6.25)$$

respectively, where  $k_i$  represents the momentum of the outgoing particles. Similarly, for incoming quark, antiquark, and gluon lines, the rules are:

$$\frac{2p_1^\mu}{2p_1 \cdot k_g + i\epsilon} g, \quad -\frac{2p_1^\mu}{2p_1 \cdot k_g + i\epsilon} g, \quad \frac{2p_1^\mu}{2p_1 \cdot k_g - i\epsilon} g \quad (6.26)$$

respectively, where  $p_1$  represents the momentum for the incoming particle,  $g$  is the strong coupling constant, and  $k_g$  is the momentum of the soft gluon.

In the gluon-gluon scattering channel, the relevant Feynman diagrams can be found in

Fig. 6.1, from which the following contributions for soft gluon radiation can be calculated,

$$g^2 \int \frac{d^3 k_g}{(2\pi)^3 2E_{k_g}} \delta^{(2)}(q_\perp - k_{g\perp}) \frac{C_A}{2} [S_g(p_1, p_2) + S_g(k_1, p_1) + S_g(k_1, p_2)] \quad (6.27)$$

where  $S_g(p, q)$  is a short-handed notation for

$$S_g(p, q) = \frac{2p \cdot q}{p \cdot k_g q \cdot k_g} . \quad (6.28)$$

In order to evaluate the contributions from soft gluon radiation, the phase space of the gluon with restriction that gluon transverse momentum leads to the imbalance between the Higgs-jet system needs to be integrated out, i.e.,

$$g^2 \int \frac{d^3 k_g}{(2\pi)^3 2E_{k_g}} \delta^{(2)}(q_\perp - k_{g\perp}) S_g(p_1, p_2) . \quad (6.29)$$

The derivation of the above term is straightforward, by noticing that the lower limit in the longitudinal momentum fraction integral, is given by:

$$\int_{x_{min}}^1 \frac{dx}{x} \frac{1}{k_{g\perp}^2} , \quad (6.30)$$

where  $x$  is the momentum fraction of  $p_1$  carried by the soft gluon. Because of momentum conservation, the lower limit for the  $x$ -integral is given by:  $x_{min} = \frac{k_{g\perp}^2}{Q^2}$ . Therefore, the above integral leads to the following leading contribution,

$$\frac{1}{q_\perp^2} \ln \frac{Q^2}{q_\perp^2} . \quad (6.31)$$



Substituting the above equation into Eq. (6.29) results in,

$$g^2 \int \frac{d^3 k_g}{(2\pi)^3 2E_{k_g}} \delta^{(2)}(q_\perp - k_{g\perp}) S_g(p_1, p_2) = \frac{\alpha_s}{2\pi^2} \frac{1}{q_\perp^2} \left( 2 \ln \frac{Q^2}{q_\perp^2} \right). \quad (6.32)$$

The other terms are not as straightforward to calculate, because the simple phase space integral will contain jet contributions which have already been taken into account by the jet functions above (Sec. 6.1.2). Therefore, the jet contributions need to be subtracted in order to avoid double counting. That means the phase space integral has to exclude the jet region, noting that this exclusion does not depend on the jet algorithm at this order. This is because, this contribution arises from the soft gluon radiation, whereas the jet algorithm focuses on the collinear gluons associated with the jet.

As a general discussion, take the example of one term, given by:

$$\int \frac{d^3 k_g}{2E_{k_g}} \delta^{(2)}(q_\perp - k_{g\perp}) S_g(k_1, p_1) = \int d^2 k_{g\perp} \delta^{(2)}(q_\perp - k_{g\perp}) \int \frac{d\xi_1}{\xi_1} \frac{2}{(k_{g\perp} - \xi_1 k_{1\perp})^2}, \quad (6.33)$$

where  $k_{1\perp}$  represents the transverse momentum for the final state jet, and  $\xi_1 = k_g \cdot p_1 / k_1 \cdot p_1$ . Clearly, there is a collinear divergence associated with the jet, if the gluon radiation is within the jet cone a collinear divergence will be generated. In order to regulate this collinear jet divergence, the phase space integral can be limited to require that the gluon radiation be outside of the jet cone. Under this restriction, there will be no divergence associated with the jet, instead, the jet size  $R$  will be introduced to regulate the collinear divergence from the jet.

There are different ways to regulate the above integral. The central point is to identify the jet cone requirement. In the above example, a divergence exists when  $k_g$  is parallel to

$k_1$ , which means the invariant mass of  $k_1 + k_g$  is small. The out of cone radiation requires that the invariant mass has a minimum,

$$(k_1 + k_g)^2 > \Lambda^2 . \quad (6.34)$$

Clearly,  $\Lambda$  depends on the jet size, if  $(k_1 + k_g)^2$  is smaller than  $\Lambda^2$ , its contribution needs to be excluded, because it belongs to the jet contribution calculated in the previous section. Following a similar analysis as for the jet contribution, the size of  $\Lambda$  can be worked out. For example, if the kinematics of  $k_1$  and  $k_g$  are substituted into the above equation, the results are:

$$(k_1 + k_g)^2 \approx k_{1\perp} k_{g\perp} (e^{y_1 - y_g} + e^{y_g - y_1}) - 2k_{1\perp} k_{g\perp} \cos(\phi_1 - \phi_g) \approx k_{1\perp} k_{g\perp} R_{1g}^2 , \quad (6.35)$$

where  $y_1$  and  $y_g$  are rapidities for  $k_1$  and  $k_g$ ,  $\phi_1$  and  $\phi_g$  are the azimuthal angles, for the jet and additional gluon respectively, and  $R_{1g}$  represents the separation of  $k_1$  and  $k_g$  ( $R_{1g} = \sqrt{(y_1 - y_g)^2 + (\phi_1 - \phi_g)^2}$ ). In other words, if  $R_{1g}$  is smaller than  $R$ , the gluon radiation will be considered inside the jet cone and vice versa. Therefore, in the phase space integral of Eq. (6.33), the following kinematic restriction is imposed:  $\Theta(2k_1 \cdot k_g - \Lambda^2)$  with  $\Lambda^2 = k_{1\perp} k_{g\perp} R^2$ . Equivalently, a slight off-shell-ness for the jet momentum  $k_1$  can be adopted to regulate the divergence:  $k_1^2 = m_1^2 = k_{1\perp}^2 R^2$ . By doing so there is no need to impose any kinematic constraints, and the phase space integral can be carried out in a straightforward manner. The choice of  $m_1^2$  is made to ensure  $(k_1 + k_g)^2$  is always larger than

$\Lambda^2$ , shown by,

$$\begin{aligned}
(k_1 + k_g)^2 &= \sqrt{k_{1\perp}^2 + m_1^2} k_{g\perp} (e^{y_1 - y_g} + e^{y_g - y_1}) - 2k_{1\perp} k_{g\perp} \cos(\phi_1 - \phi_g) \quad (6.36) \\
&\approx \sqrt{k_{1\perp}^2 + m_1^2} k_{g\perp} (\Delta y)^2 + k_{1\perp} k_{g\perp} (\Delta \phi)^2 + 2k_{g\perp} \left( \sqrt{k_{1\perp}^2 + m_1^2} - k_{1\perp} \right) .
\end{aligned}$$

By choosing  $m_1^2 = k_{1\perp}^2 R^2$ ,  $(k_1 + k_g)^2$  is guaranteed to be larger than  $\Lambda^2$  for any values of  $\Delta y$  and  $\Delta \phi$ . In addition, the narrow jet approximation, i.e.,  $R \rightarrow 0$  limit, is taken. In this limit, the phase space cut-off technique results in the same leading contributions in terms of  $\ln(1/R)$ , as the introduction of a mass term.

After adding an off-shell-ness to the jet momentum, the above integral can be written as

$$\int \frac{d\xi_1}{\xi_1} \frac{2}{\xi_1^2 k_{1\perp}^2 (1 + R^2) + k_{g\perp}^2 - 2\xi_1 k_{1\perp} \cdot k_{g\perp}} . \quad (6.37)$$

To further integrate, the azimuthal angle of the jet is averaged over but the azimuthal angle is fixed for  $k_{g\perp}$ , giving:

$$\begin{aligned}
&\int \frac{d\xi_1}{\xi_1} \int_0^\pi \frac{d\phi}{\pi} \frac{2}{\xi_1^2 k_{1\perp}^2 (1 + R^2) + k_{g\perp}^2 - 2\xi_1 k_{1\perp} k_{g\perp} \cos(\phi)} , \\
&= \int \frac{d\xi_1}{\xi_1} \frac{1}{\sqrt{\left( \xi_1^2 k_{1\perp}^2 (1 + R^2) + k_{g\perp}^2 \right)^2 - 4\xi_1^2 k_{1\perp}^2 k_{g\perp}^2}} . \quad (6.38)
\end{aligned}$$

Again, the integration over  $\xi_1$  has a lower limit, and taking the limit of  $q_\perp \ll Q$  and  $R \rightarrow 0$ , the leading power contribution is:

$$\frac{1}{q_\perp^2} \frac{1}{2} \left[ \ln \frac{Q^2}{q_\perp^2} + \ln \left( \frac{t}{u} \right) + \ln \frac{1}{R^2} \right] . \quad (6.39)$$

Therefore, the final result for the  $S_g(k_1, p_1)$  term can be written as

$$g^2 \int \frac{d^3 k_g}{(2\pi)^3 2E_{k_g}} \delta^{(2)}(q_\perp - k_{g\perp}) S_g(k_1, p_1) = \frac{\alpha_s}{2\pi^2} \frac{1}{q_\perp^2} \left[ \ln \frac{Q^2}{q_\perp^2} + \ln \frac{1}{R_1^2} + \ln \left( \frac{t}{u} \right) \right]. \quad (6.40)$$

Evaluation of the other terms follow the same procedure, and the results are summarized below:

$$S_g(p_1, p_2) \Rightarrow \frac{\alpha_s}{2\pi^2} \frac{1}{q_\perp^2} \left( 2 \ln \frac{Q^2}{q_\perp^2} \right), \quad (6.41)$$

$$S_g(k_1, p_1) \Rightarrow \frac{\alpha_s}{2\pi^2} \frac{1}{q_\perp^2} \left[ \ln \frac{Q^2}{q_\perp^2} + \ln \frac{1}{R_1^2} + \ln \left( \frac{t}{u} \right) + \epsilon \left( \frac{1}{2} \ln^2 \frac{1}{R_1^2} + \frac{\pi^2}{6} \right) \right], \quad (6.42)$$

$$S_g(k_1, p_2) \Rightarrow \frac{\alpha_s}{2\pi^2} \frac{1}{q_\perp^2} \left[ \ln \frac{Q^2}{q_\perp^2} + \ln \frac{1}{R_1^2} + \ln \left( \frac{u}{t} \right) + \epsilon \left( \frac{1}{2} \ln^2 \frac{1}{R_1^2} + \frac{\pi^2}{6} \right) \right], \quad (6.43)$$

where the  $\epsilon$  terms are kept since they contribute to the finite piece after Fourier transforming into  $b_\perp$ -space<sup>1</sup>.

### 6.1.5 Total Real Correction

Combining the soft and collinear gluon radiation together, the asymptotic behavior at small  $q_T$  can be obtained. The gluon channel is given by:

$$\begin{aligned} & \frac{\alpha_s}{2\pi^2} \frac{H_{gg}^{(0)}}{q_T^2} \int \frac{dz_1 dz_2}{z_1 z_2} z_1 f_g(z_1) z_2 f_g(z_2) \left( \left( \delta(\xi_2 - 1) \xi_1 P^{(1)}(\xi_1) + \xi_1 \leftrightarrow \xi_2 \right) \right. \\ & \left. + \delta(\xi_1 - 1) \delta(\xi_2 - 1) C_A \left( 2 \ln \frac{Q^2}{q_T^2} - 4\beta_0 + \ln \frac{1}{R^2} + \epsilon \left( \frac{1}{2} \ln^2 \frac{1}{R^2} + \frac{\pi^2}{6} \right) \right) \right), \quad (6.44) \end{aligned}$$

---

<sup>1</sup>Details on Fourier transforming into  $b$ -space can be found in App. F

where  $\xi_i = x_i/z_i$ ,  $x_i$  is the momentum fraction of the gluon from the proton, and  $H_{gg}^{(0)}$  is the tree level contribution. Similar equations exist for the gluon-quark and the quark-anti-quark channel. Combining the three channels gives:

$$\begin{aligned}
& \frac{\alpha_s}{2\pi^2} \frac{1}{q_T^2} \int \frac{dz_1 dz_2}{z_1 z_2} z_1 f_a(z_1) z_2 f_b(z_2) \left\{ \left( \delta(\xi_2 - 1) \xi_1 P^{(1)}(\xi_1) + \xi_1 \leftrightarrow \xi_2 \right) \right. \\
& + \delta(\xi_1 - 1) \delta(\xi_2 - 1) \left[ H_{gg}^{(0)} C_A \left( 2 \ln \frac{Q^2}{q_T^2} - 4\beta_0 + \ln \frac{1}{R^2} \right) \right. \\
& + H_{qg}^{(0)} \left( (C_A + C_F) \ln \frac{Q^2}{q_T^2} - 2\beta_0 - \frac{3}{2} C_F + (C_A - C_F) \ln \frac{u}{t} + C_F \ln \frac{1}{R^2} \right) \\
& + H_{gq}^{(0)} \left( (C_A + C_F) \ln \frac{Q^2}{q_T^2} - 2\beta_0 - \frac{3}{2} C_F + (C_A - C_F) \ln \frac{u}{t} + C_F \ln \frac{1}{R^2} \right) \\
& \left. \left. + H_{q\bar{q}}^{(0)} \left( 2C_F \ln \frac{Q^2}{q_T^2} - 3C_F + C_A \ln \frac{1}{R^2} \right) \right] \right\}. \tag{6.45}
\end{aligned}$$

This will be compared to the fixed order calculation in the limit  $q_T$  goes to zero in Sec. 6.1.7. Now that the complete asymptotic piece is calculated, the Fourier Transform into  $b$ -space is performed. After the Fourier Transform, the poles from all of the different pieces cancel. The gluon-gluon channel is shown below, but similar results exist for the other channels, and can be found in App. G. The poles for the virtual correction are given by:

$$H^{(0)} \frac{\alpha_s C_A}{2\pi} \left( -\frac{3}{\epsilon^2} + \frac{1}{\epsilon} \left( 2 \ln \frac{Q^2}{\mu^2} + \ln \frac{P_J^2}{\mu^2} \right) \right), \tag{6.46}$$

the coupling renormalization is given in Eq. 6.14, and needs to be multiplied by the tree level matrix element ( $H^{(0)}$ ). The poles for the jet, collinear, PDF renormalization, and soft

corrections are given by:

$$H^{(0)} \frac{\alpha_s C_A}{2\pi} \left( \frac{1}{\epsilon^2} + \frac{1}{\epsilon} \left( 2\beta_0 - \ln \frac{P_J^2 R^2}{\mu^2} \right) \right), \quad (6.47)$$

$$- H^{(0)} \frac{\alpha_s C_A}{2\pi} \frac{1}{\epsilon} (\delta(\xi_2 - 1) \xi_1 P_{gg}(\xi_1) + \xi_1 \leftrightarrow \xi_2), \quad (6.48)$$

$$H^{(0)} \frac{\alpha_s C_A}{2\pi} \frac{1}{\epsilon} (\delta(\xi_2 - 1) (\xi_1 P_{gg}(\xi_1) + 2\beta_0 \delta(1 - \xi_1)) + \xi_1 \leftrightarrow \xi_2), \quad (6.49)$$

$$H^{(0)} \frac{\alpha_s C_A}{2\pi} \left( \frac{2}{\epsilon^2} + \frac{2}{\epsilon} \ln \frac{\mu^2}{Q^2} - \frac{1}{\epsilon} \ln \frac{1}{R^2} \right), \quad (6.50)$$

respectively. All the terms above are proportional to  $\delta(\xi_1 - 1)\delta(\xi_2 - 1)$  unless otherwise noted. Combining Eqs. 6.46, 6.14, and 6.50, it is clear that all of the poles cancel, and the remaining result is finite as required.

### 6.1.6 Resummation Calculation

After Fourier Transforming into  $b$ -space, the finite contribution at the one-loop order for the gluon-gluon channel is given as:

$$\begin{aligned} W_{gg \rightarrow Hg}^{(1)}(b) = & H_{gg}^{(0)} \frac{\alpha_s C_A}{2\pi} \left\{ \ln \frac{b_0^2}{b^2 \mu^2} \left[ \delta(\xi_2 - 1) \xi_1 P_{gg}^{(1)}(\xi_1) + (\xi_1 \leftrightarrow \xi_2) \right] + \delta(\xi_1 - 1) \delta(\xi_2 - 1) \right. \\ & \left. \times \left[ - \left( \ln \frac{Q^2 b_\perp^2}{b_0^2} \right)^2 + \left( 4\beta_0 - \ln \frac{1}{R^2} \right) \ln \frac{Q^2 b_\perp^2}{b_0^2} \right] \right\} + H_{gg}^{(1)} \delta(\xi_1 - 1) \delta(\xi_2 - 1), \end{aligned} \quad (6.51)$$

where the integral over the parton distributions is implicit, and similar results exist for the gluon-quark and quark-anti-quark channels. The hard coefficient,  $H^{(1)}$  for the gluon-gluon

channel is:

$$\begin{aligned}
H_{gg}^{(1)} = H_{gg}^{(0)} \frac{\alpha_s C_A}{2\pi} & \left[ \ln^2 \left( \frac{Q^2}{P_T^2} \right) + 2\beta_0 \ln \frac{Q^2}{P_T^2 R^2} + \ln \frac{1}{R^2} \ln \frac{Q^2}{P_T^2} - 2 \ln \frac{-t}{s} \ln \frac{-u}{s} \right. \\
& + \ln^2 \left( \frac{\tilde{t}}{m_h^2} \right) - \ln^2 \left( \frac{\tilde{t}}{-t} \right) + \ln^2 \left( \frac{\tilde{u}}{m_h^2} \right) - \ln^2 \left( \frac{\tilde{u}}{-u} \right) + 2\text{Li}_2 \left( 1 - \frac{m_h^2}{Q^2} \right) \\
& \left. + 2\text{Li}_2 \left( \frac{t}{m_h^2} \right) + 2\text{Li}_2 \left( \frac{u}{m_h^2} \right) + \frac{67}{9} + \frac{\pi^2}{2} - \frac{23}{54} N_f \right] + \delta H_{gg}^{(1)}, \tag{6.52}
\end{aligned}$$

where  $\tilde{t} = m_H^2 - t$ ,  $\tilde{u} = m_H^2 - u$ , and  $\delta H_{gg}^{(1)}$  can be found in Sec. 6.1.1. performing the calculation for the gluon-quark channel results in:

$$\begin{aligned}
H_{gq}^{(1)} = H_{gq}^{(0)} \frac{\alpha_s}{2\pi} & \left\{ C_A \left[ \frac{1}{2} \ln^2 \left( \frac{\hat{\mu}^2}{P_{J\perp}^2} \right) + \ln \left( \frac{P_{J\perp}^2}{\hat{\mu}^2} \right) \ln \left( \frac{u}{t} \right) + \ln \left( \frac{P_{J\perp}^2}{\hat{\mu}^2} \right) \ln \left( \frac{s}{\hat{\mu}^2} \right) \right. \right. \\
& \left. \left. - 2 \ln \frac{-t}{\hat{\mu}^2} \ln \frac{-u}{\hat{\mu}^2} - 4\beta_0 \ln \frac{-u}{\hat{\mu}^2} - 6\beta_0 \ln \frac{\hat{\mu}^2}{\tilde{\mu}^2} + 2\text{Li}_2 \left( \frac{u}{m_h^2} \right) - \ln^2 \frac{\tilde{u}}{-u} + \ln^2 \frac{\tilde{u}}{m_h^2} + \frac{7}{3} + \frac{4\pi^2}{3} \right] \right. \\
& + C_F \left[ \frac{1}{2} \ln^2 \left( \frac{\hat{\mu}^2}{P_{J\perp}^2} \right) + \frac{3}{2} \ln \frac{\hat{\mu}^2}{P_{J\perp}^2 R^2} + \ln \frac{1}{R^2} \ln \frac{\hat{\mu}^2}{P_{J\perp}^2} - \ln \frac{P_{J\perp}^2}{\hat{\mu}^2} \ln \frac{u}{t} - \ln \frac{P_{J\perp}^2}{\hat{\mu}^2} \ln \frac{s}{\hat{\mu}^2} \right. \\
& + 3 \ln \frac{-u}{\hat{\mu}^2} + 2\text{Li}_2 \left( 1 - \frac{m_h^2}{s} \right) + 2\text{Li}_2 \left( \frac{t}{m_h^2} \right) - \ln^2 \left( \frac{\tilde{t}}{-t} \right) + \ln^2 \left( \frac{\tilde{t}}{m_h^2} \right) - \frac{3}{2} \\
& \left. \left. - \frac{5\pi^2}{6} \right] + 20\beta_0 \right\} + \delta H_{gq}^{(1)}, \tag{6.53}
\end{aligned}$$

where  $\delta H_{qg}^{(1)}$  can again be found in Sec. 6.1.1. Finally, the quark-anti-quark channel is given by:

$$\begin{aligned}
H_{q\bar{q}}^{(1)} = & H_{q\bar{q}}^{(0)} \frac{\alpha_s}{2\pi} \left\{ C_A \left[ \frac{1}{2} \ln^2 \left( \frac{\hat{\mu}^2}{P_{J\perp}^2} \right) + \ln \left( \frac{P_{J\perp}^2}{\hat{\mu}^2} \right) \ln \left( \frac{u}{t} \right) + \ln \left( \frac{P_{J\perp}^2}{\hat{\mu}^2} \right) \ln \left( \frac{s}{\hat{\mu}^2} \right) \right. \right. \\
& - 2 \ln \frac{-t}{\hat{\mu}^2} \ln \frac{-u}{\hat{\mu}^2} - 4\beta_0 \ln \frac{-u}{\hat{\mu}^2} - 6\beta_0 \ln \frac{\hat{\mu}^2}{\tilde{\mu}^2} + 2\text{Li}_2 \left( \frac{u}{m_h^2} \right) \\
& \left. - \ln^2 \frac{\tilde{u}}{-u} + \ln^2 \frac{\tilde{u}}{m_h^2} + \frac{7}{3} + \frac{4\pi^2}{3} \right] \\
& + C_F \left[ \frac{1}{2} \ln^2 \left( \frac{\hat{\mu}^2}{P_{J\perp}^2} \right) + \frac{3}{2} \ln \frac{\hat{\mu}^2}{P_{J\perp}^2 R^2} + \ln \frac{1}{R^2} \ln \frac{\hat{\mu}^2}{P_{J\perp}^2} - \ln \frac{P_{J\perp}^2}{\hat{\mu}^2} \ln \frac{u}{t} - \ln \frac{P_{J\perp}^2}{\hat{\mu}^2} \ln \frac{s}{\hat{\mu}^2} \right. \\
& + 3 \ln \frac{-u}{\hat{\mu}^2} + 2\text{Li}_2 \left( 1 - \frac{m_h^2}{s} \right) + 2\text{Li}_2 \left( \frac{t}{m_h^2} \right) - \ln^2 \left( \frac{\tilde{t}}{-t} \right) + \ln^2 \left( \frac{\tilde{t}}{m_h^2} \right) - \frac{3}{2} - \frac{5\pi^2}{6} \left. \right] \\
& \left. + 20\beta_0 \right\} + \delta H_{gq}^{(1)}, \tag{6.54}
\end{aligned}$$

where  $\delta H_{q\bar{q}}^{(1)}$  is given in Sec. 6.1.1. With the above results, it is possible to calculate the resummation result in the CFG formalism by solving the evolution equations as discussed in Sec. 3.4. This results in a similar Sudakov factor to that for color singlet final states. however, the cone size needs to be introduced. This gives the following form:

$$S(b) = \int_{b_0^2/b^2}^{\hat{\mu}^2} \frac{d\mu^2}{\mu^2} \left( A \ln \frac{s}{\mu^2} + B + D \ln \frac{1}{R^2} \right), \tag{6.55}$$

where  $R$  is the cone size for the jet. The coefficients for A, B, and D depend on the process, and can be expanded order by order in perturbation theory. For the gluon-gluon channel,  $A^{(1)} = C_A$ ,  $B^{(1)} = -2\beta_0$ , and  $D = C_A$ . For the gluon-quark channel,  $A^{(1)} = \frac{1}{2}(C_A + C_F)$ ,  $B^{(1)} = -\beta_0 - \frac{3}{4}C_F - \frac{1}{2}(C_A - C_F) \ln \frac{u}{\tilde{t}}$ , and  $D = C_F$ . Finally, for the quark-anti-quark channel,  $A^{(1)} = C_F$ ,  $B^{(1)} = -\frac{3}{2}C_F$ , and  $D = C_A$ .



The dependence of  $\ln \frac{1}{R^2}$  in the Sudakov factor can be understood by looking at the soft radiation, which is what is contained in the Sudakov factor. As mentioned during the calculation of the soft factors (Sec. 6.1.4), the phase space needed to be separated to ensure that the soft gluons inside the jet were not double counted. This can also be understood by considering the contribution of the soft gluons inside the jet cone to the transverse momentum of the Higgs plus jet system. If the gluon falls within the jet cone, then the momentum of the gluon contributes to the jet, and does not contribute to the imbalance of transverse momentum between the jet and the Higgs boson. Instead, if it falls outside the cone it does contribute to the imbalance in transverse momentum.

It is interesting to note that many of the logarithms in  $H^{(1)}$  can be eliminated if the resummation scale  $\hat{\mu}$  is chosen to be  $P_{J\perp}$ . To illustrate this point, the ratio of  $H^{(1)}/H^{(0)}$  is plotted as functions of the Higg's rapidity ( $y_H$ ) as shown in Fig. 6.2 with the jet rapidity fixed at  $y_j = 0$ . This result shows that  $H^{(1)}$  is much larger than  $H^{(0)}$  in the large  $y_H$  region if  $\hat{\mu}^2 = s$ . In contrast, the ratio of  $H^{(1)}/H^{(0)}$  becomes less sensitive to  $y_H$  with  $\hat{\mu}^2 = P_{J\perp}^2$ . This is because when the difference of  $y_H$  and  $y_J$  becomes large, the invariant mass  $Q^2$  of the Higgs boson and the leading jet can become much larger than the transverse momentum of the jet. Hence, the scale of the results will be taken to be  $\hat{\mu} = P_{J\perp}$  in order to resum the large logarithms in the perturbative contributions. In the following, this scale choice is adopted in the theory predictions for comparison to fixed order and parton showers. However, results with  $\hat{\mu}^2 = s$  will be shown for the sake of comparison, and to support the choice of  $\hat{\mu}^2 = P_{J\perp}^2$ .

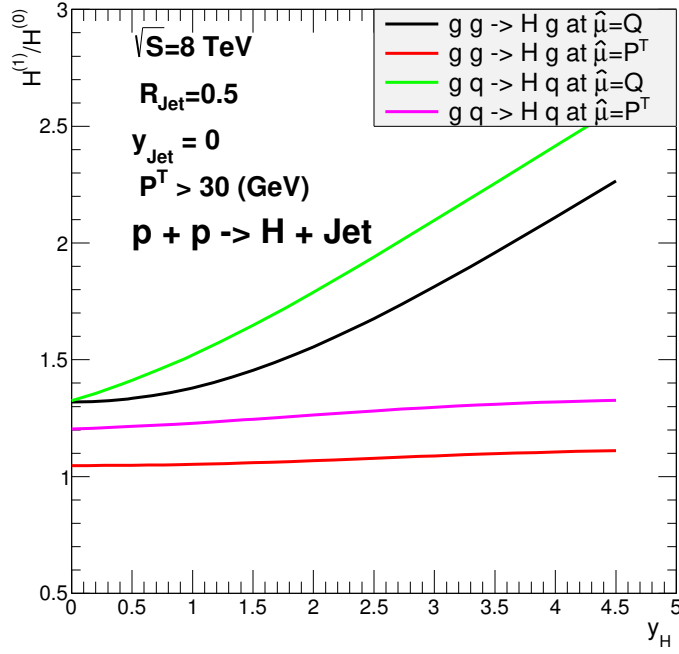


Figure 6.2: Rapidity dependence of the hard factor for Higgs+Jet for different scale choices

### 6.1.7 Results

The above resummation formula to compute the differential and total cross sections of the Higgs boson plus jet will be used to compare to both fixed order and parton shower results. While data exists for this process, it is currently not at an accuracy that will be able to discriminate against different predictions. In the numerical calculations shown, only the gluon-gluon and the gluon-quark channel are used. This is a valid approximation because the contribution for the quark-anti-quark channel is less than 1%, while the gluon-gluon and gluon-quark channels make up 71% and 29% respectively. The anti- $k_T$  algorithm is used in defining the jet with a cone size of  $R = 0.5$ .

Firstly, before the results are given, a cross check of the total cross-section is performed. This cross check is done in a manner similar to that described in Sec. 3.5. In this cross check,

it is evident that using the narrow jet approximation results in a 2% discrepancy between the fixed order result from MCFM, and the result from the calculation described here. This discrepancy varies as a function of  $R$  supporting the fact that it is due to the narrow jet approximation. Therefore, the correction is modeled by an additional  $R$ -dependent function inside of  $H^{(1)}$ . The correction is obtained by fitting the difference in cross section to a quadratic in  $R$ , giving a correction of  $H^{(0)} \frac{\alpha_s}{2\pi} (C_A R - 1.1R + 23.3R^2)$  and  $H^{(0)} \frac{\alpha_s}{2\pi} (C_F - 0.8 * R + 22.3R^2)$  for final state gluon and quark jets respectively. Additionally, for the resummation to be valid, the  $q_T$  needs to be smaller than  $P_{J\perp}$ , since the  $q_T$  is defined as the vector sum of the transverse momentum of the Higgs boson and the leading jet. If  $q_T$  is greater than  $P_{J\perp}$  it is not clear what the leading jet is, and the fixed order calculation needs to be used in this region. Finally, since  $A^{(2)}$  is global and only depends on the color factor in the initial state, this is also included into the calculation.

### 6.1.7.1 Comparison to Fixed Order

In Fig. 6.3, the comparison of the Higgs plus jet system at the LHC is shown for the total transverse momentum and the transverse momentum of the Higgs. The fixed order calculation is given by MCFM, while the resummation calculation is shown for the two scales discussed above.

For the total transverse momentum distribution, the leading order (LO) MCFM prediction is from the first non-zero prediction of the transverse momentum of the Higgs plus jet system, and the NLO result is the one-loop correction to that. In other words, the LO prediction is given by Higgs plus two jets, while the NLO prediction is given by Higgs plus two jets at NLO. The MCFM NLO prediction is cut-off at 20 GeV due to the numerical difficulties of obtaining an accurate prediction below this value. Comparing the total transverse

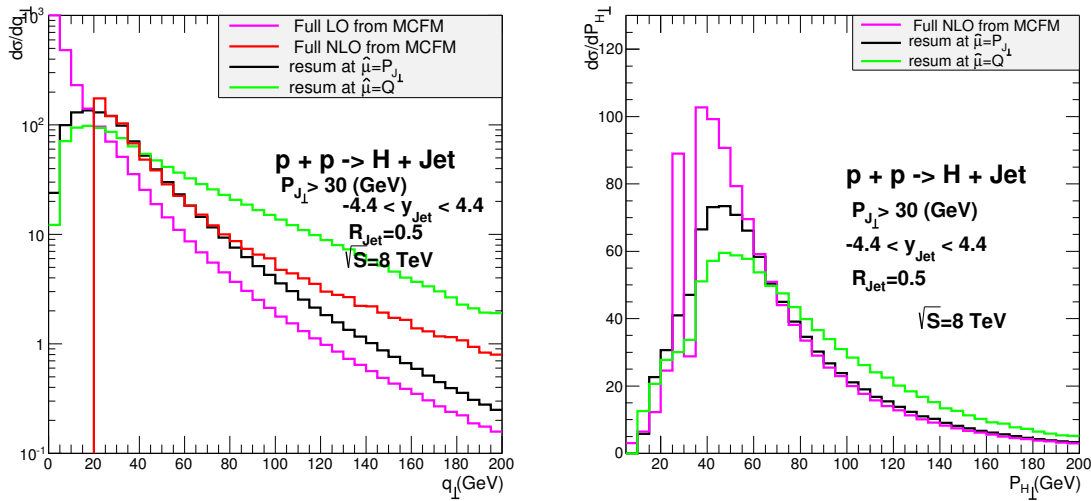


Figure 6.3: The differential cross sections of Higgs boson plus one jet production at the LHC as functions of the total transverse momentum  $q_{\perp}$  (left) and the Higgs boson transverse momentum  $P_{H\perp}$  (right). The resummation predictions (resum) with resummation scale set to be  $P_{J\perp}$  (black line) and  $Q$  (green line) respectively are compared to the LO result from MCFM (pink line) with non-zero  $q_{\perp}$ , and the NLO result from MCFM (red line) which is the production rate of Higgs boson plus two separate jets up to one-loop in QCD.

momentum distribution of the resummed and fixed order calculation, it is seen that the fixed order fails to describe the small  $q_T$  region. Additionally, it is clear that the scale choice of  $\hat{\mu} = Q$  results in a calculation that is too hard (too large of a cross-section for large  $q_T$ ), and can never be matched to fixed order. On the other hand, the scale choice of  $\hat{\mu} = P_{J\perp}$  gives a much more reasonable prediction.

For the transverse momentum of the Higgs boson, only the NLO prediction from MCFM is shown. This prediction is given by the  $\alpha_s$  corrections to the Higgs plus jet result. Again, the resummation calculation is given for the two different scale choices. The choice for  $\hat{\mu} = Q$  is too hard in the high transverse momentum region as also seen in the total transverse momentum distribution. Here, there is a discontinuity at the value of  $p_{H\perp} = p_{Jcut}$ , known as the Sudakov shoulder singularity. This is due to an integrable singularity that arises when the leading jet is close to back to back to the Higgs boson, or in other words, when  $q_T$  approaches zero. This is resolved in the resummation calculation, by appropriately resumming the logarithms to all orders that result in the divergence to give a finite result.

### 6.1.7.2 Comparison to Parton Showers

Similar to the fixed order calculation, the comparison of the resummation result can be compared to that from parton shower predictions. In this study, the Higgs boson was set to 125 GeV and left undecayed, the MMHT2014nlo68clas118 PDF set was used [215]. Finally, the theoretical uncertainties were estimated by varying the scales by factors of  $\frac{1}{2}$  and 2 around the central scale, but left the renormalization scale ( $\hat{\mu}$ ) fixed to  $P_{J\perp}$  as discussed above. The setup and details of the other predictions used in this comparison can be found in [28]. The jets for this calculation are taken to have a cone size of  $R = 0.4$ , with  $p_{J\perp} > 30$  GeV and  $|y_J| < 4.4$ . The codes that are used in this comparison are: SHERPA [178] plus

GOSAM [216, 217], MINLO [218], BFGLP [219], HEJ [220, 221, 222, 223, 224], Herwig 7.1 [225], Madgraph5\_aMC@NLO [226], POWHEG-BOX [227], STWZ [228], and SHERPA NNLOPS [229, 230]. Exact details of the setups for each of the individual codes can be found in [28].

Firstly, the total rates for the jet multiplicities are compared across all of the codes, shown in Fig. 6.4. The ResBos2 code is able to predict both the total inclusive rate for Higgs along with the inclusive rate for Higgs plus 1 jet. Comparing across all of the codes, it is clear that the ResBos2 prediction is consistent with the others as expected from the fixed order comparison above.

The differential distributions that are compared are the transverse momentum of the Higgs, the leading jet, the Higgs plus leading jet system, and the rapidity of the leading jet. Here the transverse momentum of the Higgs requires the presence of at least one hard jet.

The comparison of the transverse momentum of the Higgs boson in the presence of an additional jet can be seen in Fig. 6.5. The fixed order calculations again show the Sudakov shoulder singularity, but the all orders calculations do not have this singularity. In the ratio plot, at the high transverse momentum, there is a deviation of the resummation calculation from that of POWHEG due to a different choice of scales. In the RESBOS2 calculation, the central scale is  $\mu_0 = \frac{1}{2}m_h$  as mentioned above, but the scale choice for POWHEG is  $\mu_0 = \frac{1}{2}\sqrt{m_h^2 + p_T^2}$ . This scale choice softens the high transverse momentum tail as discussed in detail in Sec. 4.1.

Next, the comparison of the leading jet transverse momentum and rapidity distributions can be found in Fig. 6.6 and Fig. 6.7, respectively. Both of these distributions do not contain any large Sudakov effects, and therefore all the calculations should be close to that of the fixed order calculation. This is clearly seen in the aforementioned figures, with all the calculations falling within each others uncertainty bands. Additionally, the size of the uncertainty bands

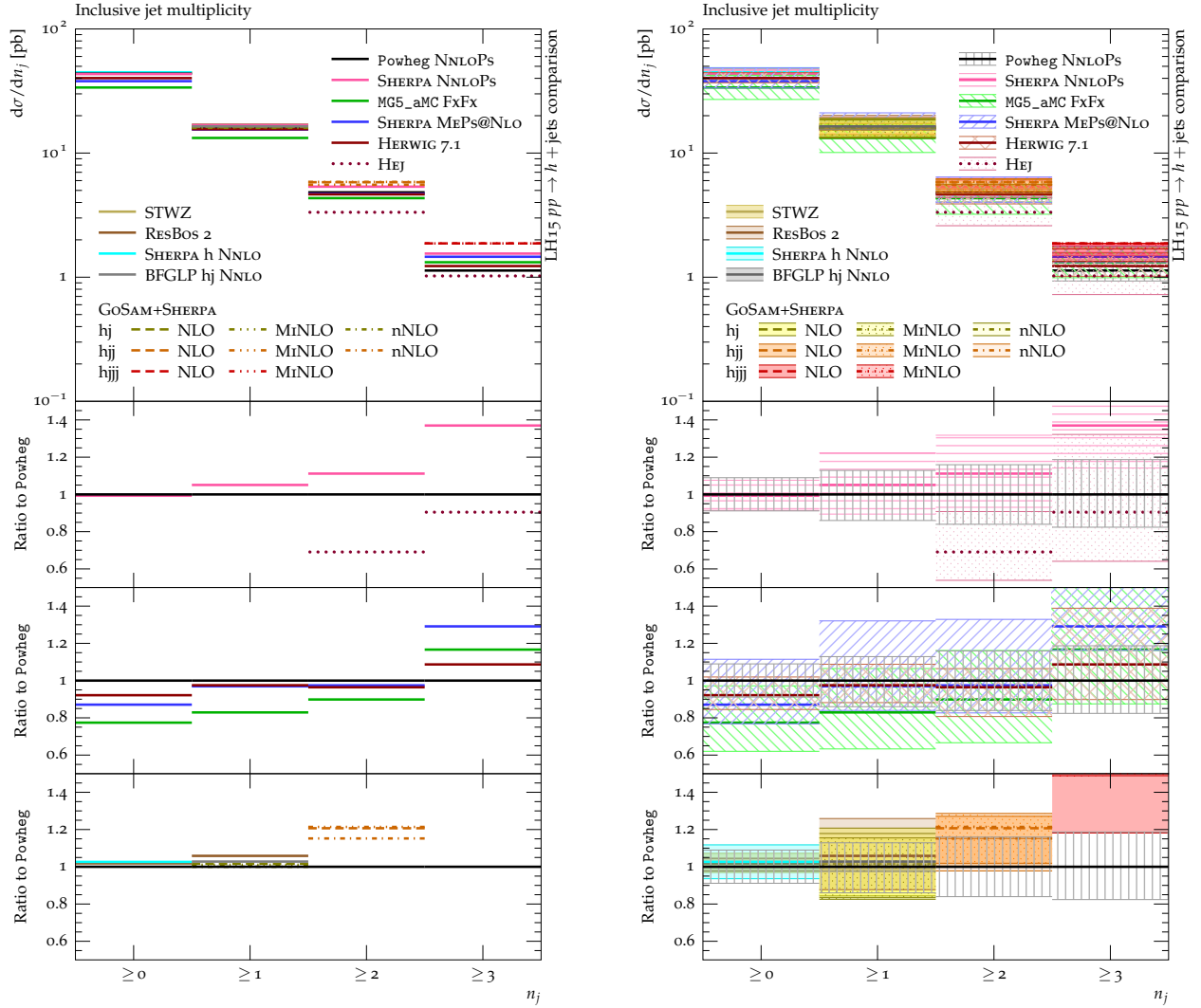


Figure 6.4: The central predictions(left panel) and with theoretical uncertainties (right panel) for the inclusive jet multiplicities as predicted by fixed-order calculations, resummed calculations, NNLO and NLO Monte Carols. The bottom panel is divided up into three subplots all showing the ratios with respect to the POWHEG NNLOPs prediction. The upper of these plots contains the HEJ and SHERPA NNLOPs ratios, while the middle one includes all NLO merged predictions (`Madgraph5_aMC@NLO`, `Herwig 7.1` and `SHERPA`) and the lower one shows all those listed in the bottom left legend of the main panel. Reproduced from [28].

are consistent with each other and are of the order of 20%. Again the difference in the high transverse momentum tail between the POWHEG and RESBOS2 calculations arise from the difference in scale choices. For the rapidity, the calculation is consistent throughout the rapidity range, and the offset between the POWHEG and RESBOS2 calculations is due to

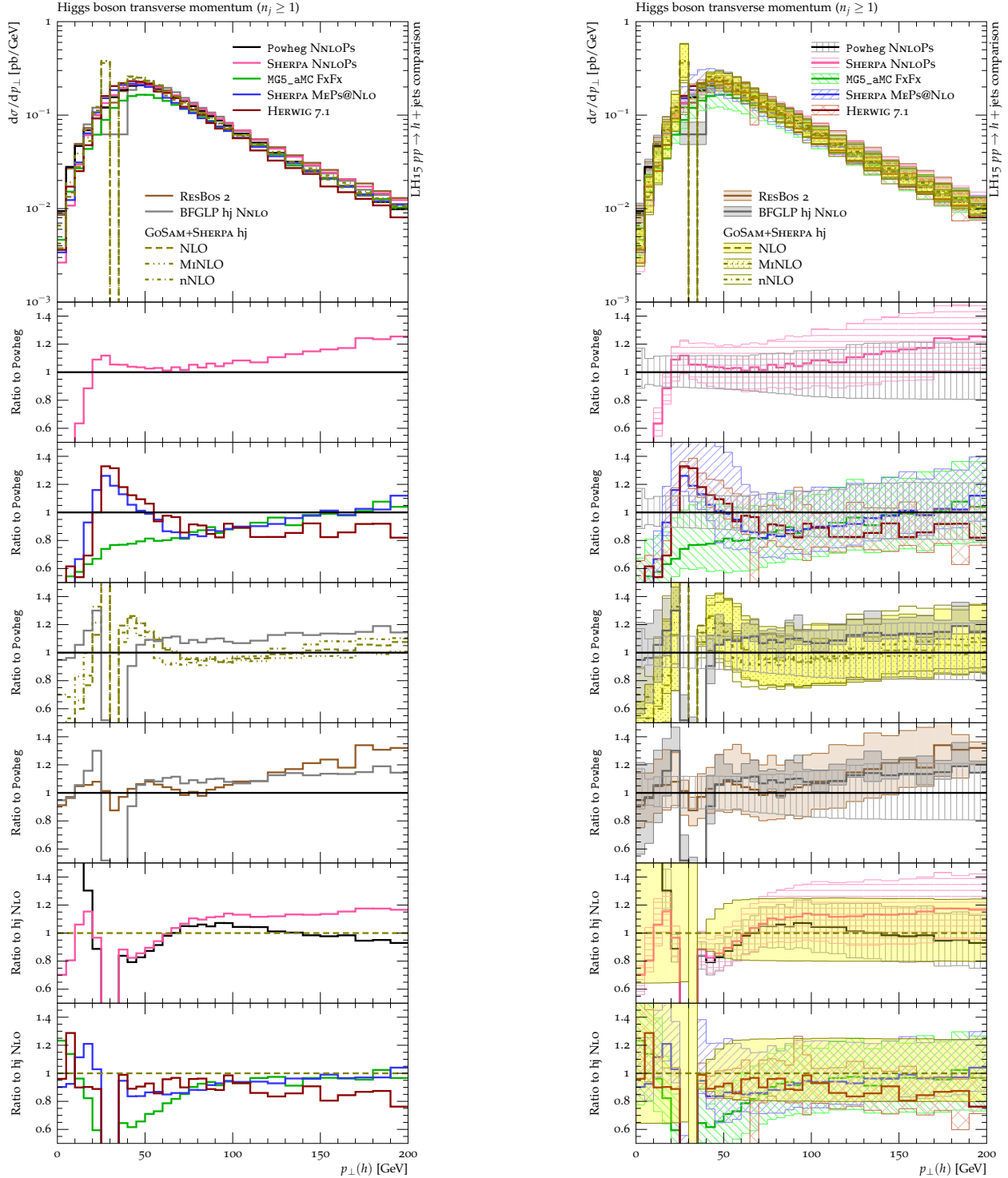


Figure 6.5: The Higgs boson transverse momentum in the presence of at least one jet central predictions(left) with uncertainty bands(right). The ratio plot panel is divided into six parts where the upper four exhibit the ratios to the POWHEG NNLOs result while the lower two show them to the NLO calculation for  $h + 1$  jet as provided by GOSAM+SHERPA.

Reproduced from [28].



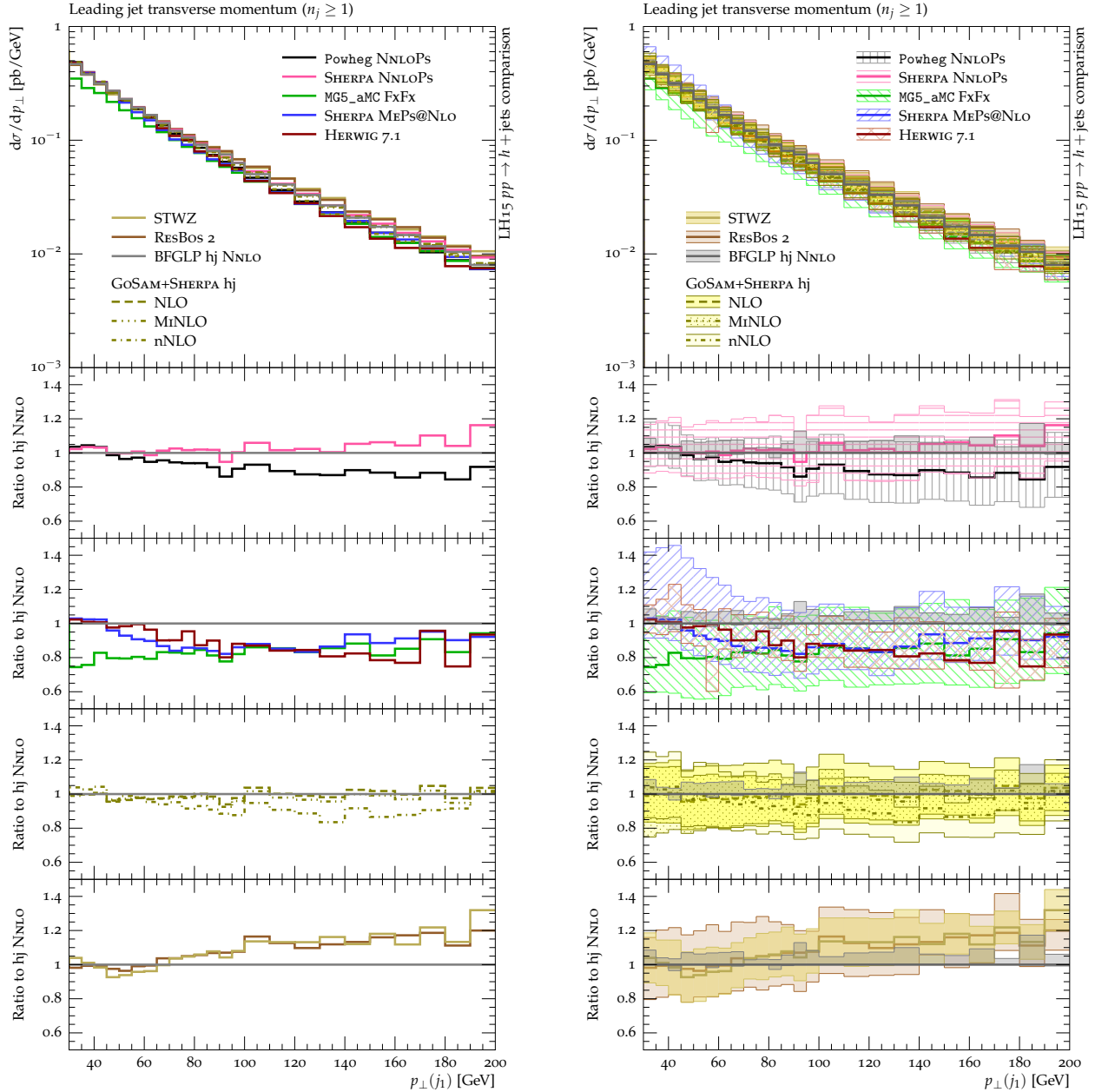


Figure 6.6: The leading jet transverse momentum distribution for  $h + \geq 1$ -jet production, to the right (left) shown with (without) the uncertainty bands provided by the various calculations. The part below the main plot contains four ratio plots taken wrt. the NNLO result of the BFGLP group following the same strategy for grouping the predictions as before (NNLOPs versus NLO ME+PS versus fixed-order and resummation results).

Reproduced from [28].

the fact that the total cross-sections differ by about 5%, which is within the theoretical uncertainty at this order, as seen when the uncertainty bands are overlaid.

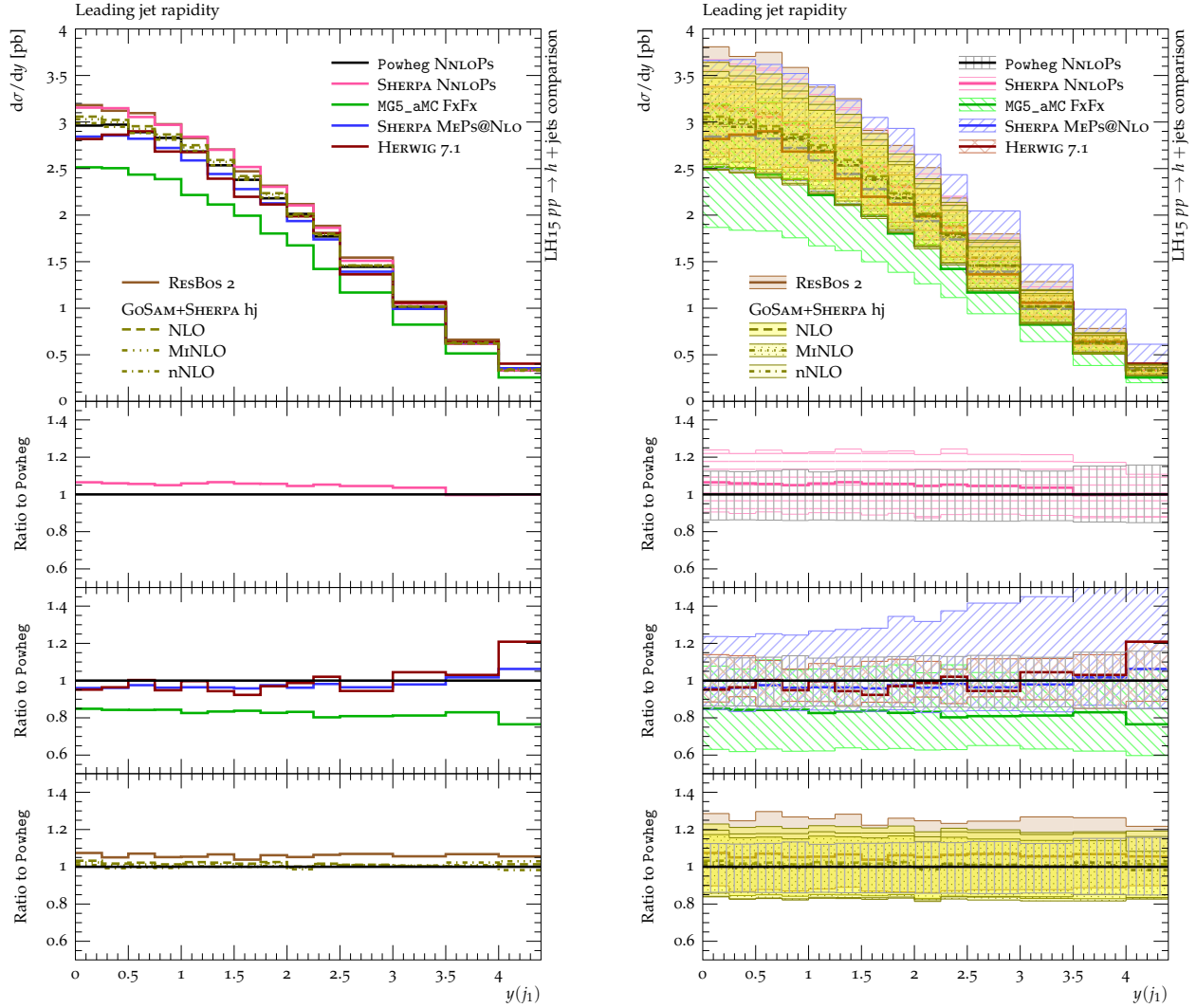


Figure 6.7: The rapidity distribution for the leading jet in  $h + \geq 1$ -jet production, shown without (left) and with (right) theoretical uncertainties. Ratio plots are displayed in the lower part of the plot using the POWHEG NNLOPS result for Higgs boson production as their reference. Predictions are grouped, from top to bottom, according to the categories NNLOPS, ME+PS at NLO and NLO fixed order as well as resummation. Reproduced from [28].

Finally, the transverse momentum of the Higgs plus jet system is examined. The comparison between the different results can be found in Fig. 6.8. Here comparing the RESBOS2 calculation to POWHEG has some interesting features that need to be discussed. In the high transverse momentum region, there is a discrepancy between the two calculations which arise from the fact that in the tail of the distribution, the RESBOS2 calculation only is matched to

the LO prediction for this observable as described in Sec. 6.1.7, and the agreement should be improved if the matching is done to a higher order prediction. Additionally, in the RESBOS2 calculation the logarithms dealing with the jet cone size are resummed as mentioned in Sec. 6.1.6. This results in a broader Sudakov peak than the other parton shower predictions, and an upward shift in the Sudakov peak value. When the LHC data becomes precise enough, this difference will be a strong test of the resummation formalism versus the parton shower model.

Overall, the parton shower predictions and the resummed predictions are consistent with each other. This was expected, since the formal accuracy of the two predictions for all observables with the exception of the transverse momentum of the Higgs plus jet system are of the same order. The major difference arises in the prediction of the Higgs plus jet system transverse momentum, due to the dependency of the jet cone size in the RESBOS2 prediction. Once the LHC data becomes precise enough, these codes and their differences can be tested against data.

### **6.1.8 Future of Higgs Plus Jet Resummation**

In this section, some brief future steps are discussed. Firstly, there has been some work to begin to extend this calculation from Higgs plus one jet to Higgs plus two jets [29]. Additionally, at higher order calculations for the Higgs plus one jet system non-global logarithms are introduced into the calculation.

The calculation of the Higgs plus two jets system is an important calculation to separate the vector boson fusion (VBF) production of the Higgs boson from the gluon fusion production of the Higgs boson. As shown in [29], the peak of the transverse momentum of the system peaks at drastically different values. This can be used to apply an additional cut

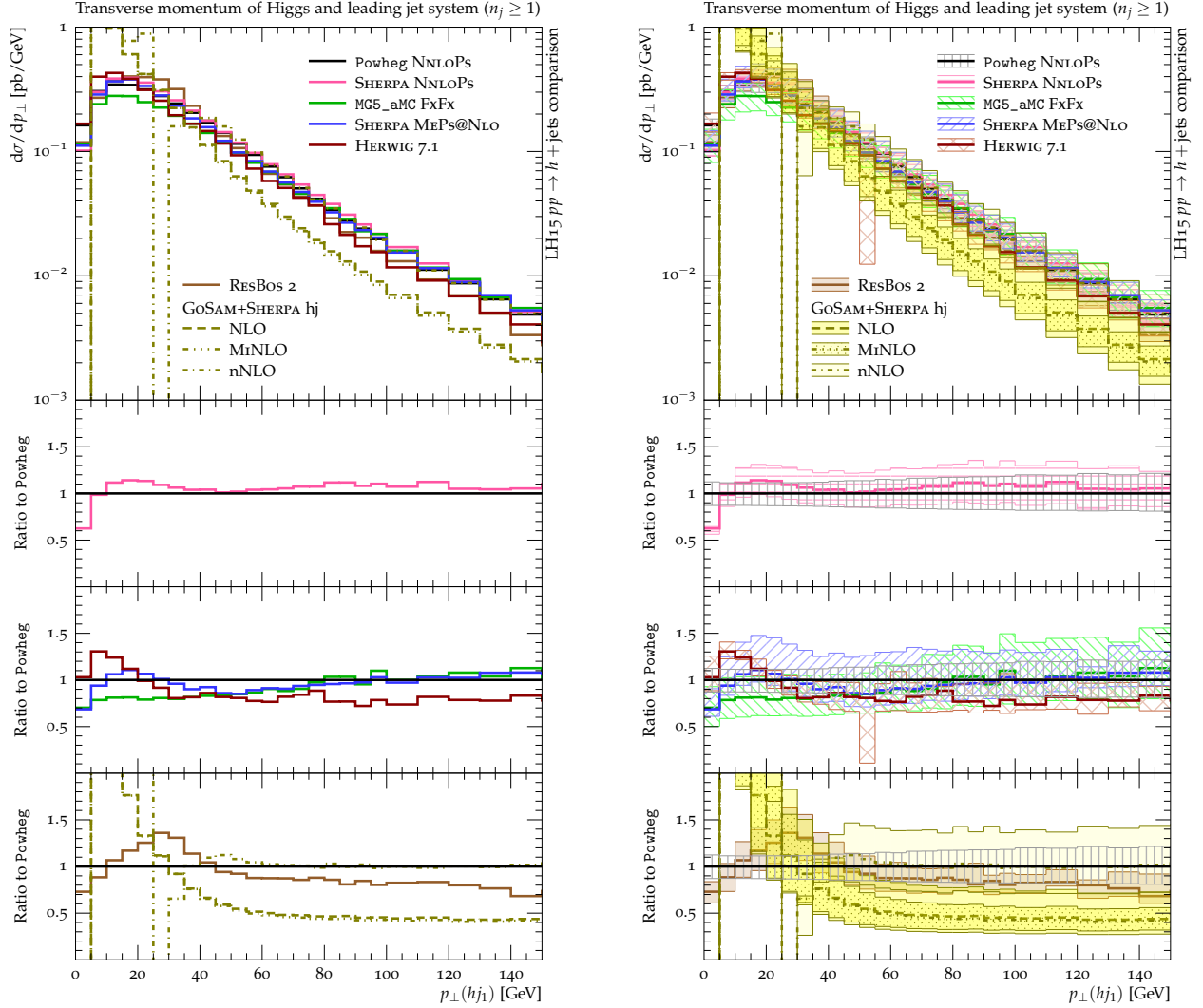


Figure 6.8: The transverse momentum of the Higgs-boson-leading-jet system in the presence of at least one jet. For better visibility, results are shown without (left) and with (right) theoretical uncertainties. The plot layout exactly corresponds to that of Figure 6.7, except for the extended  $\hat{y}$ -axis range in the ratio plots. Reproduced from [28].

on the Higgs production events to increase the purity of the VBF signal. The normalized distributions for this observable can be seen in Fig. 6.9.

Finally, the goal is to extend the Higgs plus one jet calculation to NNLL accuracy. However, going beyond NLL accuracy introduces what are known as non-global logarithms. Non-global logarithms are logarithms that may not appear at each order in the calculation, and do not have a specific form to predict the higher order coefficients of them. Therefore,

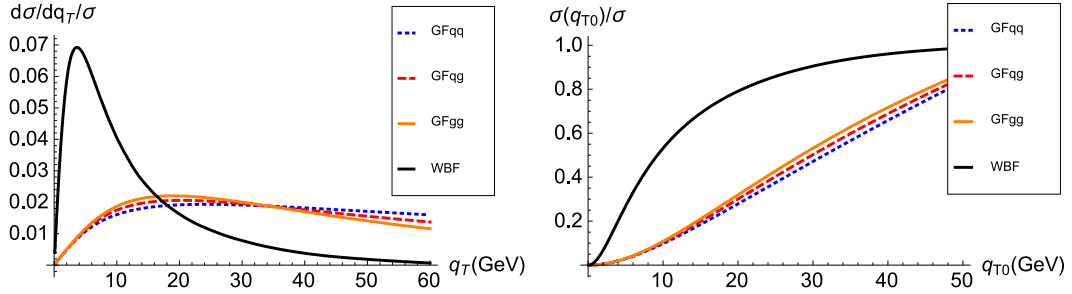


Figure 6.9: Normalized distributions of the vector boson fusion and gluon-fusion contributions to the Higgs boson plus two jets production in the typical kinematics at the LHC with  $\sqrt{S} = 13\text{TeV}$ , where the jet transverse momenta  $k_{1\perp} = k_{2\perp} = 30\text{GeV}$ ,  $y_{j1} = -y_{j2} = 2$  and  $y_h = 0$ : as functions of the total transverse momentum  $q_\perp$  (left); the total rate as function of the upper limit of  $q_\perp$  (right). Reproduced from [29].

it is not possible to resum these logarithms to all orders [231, 232, 11, 233]. This results in additional complications that need to be considered.

# Chapter 7

## Conclusion

The improvement of the ResBos code from the precision used for the Tevatron, to that of the new ResBos2 code, will allow for precision resummation calculations at the LHC. These improvements come from many different improved predictions, as mentioned above. Below a review of the improvements to the predictions, along with the experimental comparisons are summarized for the reader.

First, the improvements to color singlet resummation will be reviewed. In this section, the difference between schemes will again be pointed out. Also, the predictions for both the  $Z$  and  $W$  boson at the LHC will be reviewed. Finally, the future steps for this project will be outlined.

Afterwards, the addition of non-color singlet resummation calculation will be reviewed. In this section, the calculation for the Higgs plus jet system will be reviewed, along with some mentions of other works using these ideas. Finally, the future prospects for this new type of  $q_T$  resummation will be emphasized.

## 7.1 Color Singlet Resummation

### 7.1.1 Resummation Schemes

Two main schemes in  $q_T$  resummation are again the Collins-Soper-Sterman and the Catani-de-Florian-Grazzini schemes. The differences between these schemes have both an order by order, and an all orders relationship, to map from one scheme to the other. It was shown that as long as the calculation is performed such that the orders of the  $B$ ,  $C$ , and  $H$  coefficient are such that the order of  $B$  is one higher than  $C$  and  $H$ , then the two calculations are in very good agreement. This is supported by the conversion between the two schemes as seen in Eq. 3.73, and the results of Fig. 4.3.

### 7.1.2 $Z$ Boson Predictions

Previously at the LHC, the prediction of the ResBos code was unable to reproduce the data. The resolution to this issue took many different steps as outlined above. These steps, included the improvement of the precision of the calculation, and the change of the scale of the fixed order calculation.

The improvement in the precision of the calculation, was from NNLL to  $N^3LL$ , and the fixed order was improved from approximate NNLO to NNLO, with a k-factor included in the high transverse momentum region to match the NNLO  $Z$  plus jet calculation. One improvement that will be made to the ResBos2 code is the matching fully with the NNLO  $Z$  plus jet calculation. This will be included once the results of the NNLO  $Z$  plus jet calculation become sufficiently available.

The other improvement was the change of the fixed order scale from the invariant mass of the lepton pair to the transverse mass of the lepton pair, defined in the text above. This

choice of scale makes more sense for the high transverse momentum region due to the fact that at high transverse momentum, the energy of the jet is comparable to the invariant mass of the lepton pair.

Upon using these improvements to the ResBos prediction, the agreement between the theory prediction and the data is greatly improved. Further improvements will arise with the matching to the higher order fixed order calculation. However, this improvement will only help in the intermediate region.

One more improvement that can be made to the ResBos code, is to further improve the non-perturbative piece. Currently, the non-perturbative piece is fixed as a function of the resummation scales. This has recently been believed to give too conservative an estimate of the uncertainty of the prediction at small transverse momentum. Therefore, another future improvement is to include the resummation scale variations into the non-perturbative fit, allowing the non-perturbative function to depend on these scales, as makes physical sense.

### 7.1.3 $W$ Boson Predictions

The ResBos2 predictions for the  $W$ -transverse momentum, and the ability to use the code to help predict the  $W$  mass at the LHC will be helpful in understanding the EW sector of the SM. As mentioned in the text above, the indirect measurement is much smaller than the direct measurement of the  $W$  mass. It has been proposed to use resummation tools to improve the direct measurement, by predicting the ratio of the  $W$  transverse momentum to the  $Z$  transverse momentum. With these, the experimentalists will be able to reduce the uncertainties in the  $W$  mass measurement. These reductions will allow the measurement to be competitive with the indirect measurement.

Additionally, the ResBos2 prediction allows for a template fit of the experimental mea-



measurements of the transverse momentum of the leptons to the theoretical prediction. This will allow for a precise determination of the  $W$  mass.

Some future improvements that could be included into the ResBos2 prediction are again similar to that of the  $Z$  boson, from the matching to the higher order fixed order calculation, and improving the non-perturbative piece. While these may not have a large effect on the determination of the  $W$  boson mass, there are not any improvements that can be made in the theoretical prediction in the near future. The major improvements that would help, included calculations to much higher orders, which are not feasible at the writing of this thesis.

## 7.2 Non-Color Singlet Resummation

Recently, there has been work done to allow for non-color singlet  $q_T$  resummation in QCD. The first of these being the dijet calculation, and another related to the work of this thesis being the Higgs plus jet resummation as mentioned previously. With these calculations completed, a new set of processes are now able to be calculated that previously were thought not possible.

As mentioned above, the Higgs plus jet calculation was an important step in understanding QCD, and an important contribution towards obtaining the Higgs plus two jet resummation calculation. The Higgs plus two jet calculation is important in the study of the Higgs boson, in allowing one to separate the gluon-gluon fusion production mechanism of the Higgs boson from the EW production of the Higgs boson. Additionally, it is shown that the current prediction for the  $q_T$  resummed prediction for the Higgs plus jet system is consistent with the parton shower results. However, there is the one major difference in that

the analytic resummation knows about the cone size of the jet, resulting in a shape that differs from the parton shower codes. When the data becomes more precise, a great test of this method would be to see if the data can distinguish whether the paron shower method, or the analytic resummed method is correct.

### **7.3 Final Remarks**

In conclusion, the improvement of the  $q_T$  resummation calculations in QCD are included in the ResBos2 code. With these improvements, the calculations are now at a level that is sufficient for the precision required at the LHC. In the future, the ResBos2 will continue to improve building off of the work of this thesis, and the ideas that have formed as a result of this work.

## APPENDICES

# APPENDIX A

## The Dirac Equation and $\gamma$ Matrices

The Dirac equation is the equation of motion to describe fermions, and is given by:

$$\bar{\psi} (i\partial^\mu \gamma_\mu + m) \psi = 0, \quad (\text{A.1})$$

where  $\psi$  is the wavefunction of a fermion,  $m$  is the mass of that fermion, and  $\gamma_\mu$ <sup>1</sup> are the Dirac matrices defined by their anti-commutation relation:

$$\{\gamma^\mu, \gamma^\nu\} = 2g^{\mu\nu}, \quad (\text{A.2})$$

where  $g^{\mu\nu}$  is the metric tensor defined using the mostly negative choice,  $g^{\mu\nu} = \text{diag}(1, -1, -1, -1)$ , such that squares of time-like four momenta result in positive results.

The  $\gamma$  or Dirac matrices are used for infinitesimal transformations of spinors under spatial rotations and Lorentz boosts. There are many representations for these matrices. The Weyl representation is given by:

$$\gamma^0 = \begin{pmatrix} 0 & \mathbb{1} \\ \mathbb{1} & 0 \end{pmatrix}, \quad \gamma^i = \begin{pmatrix} 0 & \sigma^i \\ -\sigma^i & 0 \end{pmatrix}, \quad (\text{A.3})$$

---

<sup>1</sup>In Eq. A.1, it is common to rewrite  $\partial^\mu \gamma_\mu$  as  $\not{\partial}$ . This slashed notation will be used through the rest of this work. Also, additional details on the  $\gamma$  matrices, along with one representation of them can be found in App. A

where  $\sigma^i$  are the Pauli matrices, and  $\mathbb{1}$  is the  $2 \times 2$  Identity matrix. Additionally, a fifth  $\gamma$  matrix can be defined as:

$$\gamma^5 = i\gamma^0\gamma^1\gamma^2\gamma^3 = \begin{pmatrix} -\mathbb{1} & 0 \\ 0 & \mathbb{1} \end{pmatrix}. \quad (\text{A.4})$$

Important relationships of  $\gamma$  matrices are:

1.  $\gamma^\mu\gamma_\mu = 4\mathbb{1}_4$ ,
2.  $\gamma^\mu\gamma^\nu\gamma_\mu = -2\gamma^\nu$ ,
3.  $\gamma^\mu\gamma^\nu\gamma^\rho\gamma_\mu = 4g^{\nu\rho}\mathbb{1}_4$ ,
4.  $\gamma^\mu\gamma^\nu\gamma^\rho\gamma^\sigma\gamma_\mu = -2\gamma^\sigma\gamma^\rho\gamma^\nu$ ,
5. trace of any odd product of  $\gamma$  matrices excluding  $\gamma^5$  is zero,
6. trace of any odd product of  $\gamma$  matrices times  $\gamma^5$  is also zero,
7.  $\text{Tr}(\gamma^\mu\gamma^\nu) = 4g^{\mu\nu}$ ,
8.  $\text{Tr}(\gamma^\mu\gamma^\nu\gamma^\rho\gamma^\sigma) = 4(g^{\mu\nu}g^{\rho\sigma} - g^{\mu\rho}g^{\nu\sigma} + g^{\mu\sigma}g^{\nu\rho})$ ,
9.  $\text{Tr}(\gamma^5) = \text{Tr}(\gamma^\mu\gamma^\nu\gamma^5) = 0$ ,
10.  $\text{Tr}(\gamma^\mu\gamma^\nu\gamma^\rho\gamma^\sigma) = -4i\epsilon^{\mu\nu\rho\sigma}$ ,
11.  $\text{Tr}(\gamma^{\mu_1} \dots \gamma^{\mu_n}) = \text{Tr}(\gamma^{\mu_n} \dots \gamma^{\mu_1})$ ,

where  $\mathbb{1}_4$  is the  $4 \times 4$  unit matrix and  $\epsilon^{\mu\nu\rho\sigma}$  is the completely anti-symmetric Levi-Civita Tensor. When moving beyond 4 dimensions, the contraction identities are modified as follows:

1.  $\gamma^\mu \gamma_\mu = d \mathbb{1}_d,$
2.  $\gamma^\mu \gamma^\nu \gamma_\mu = -(d-2) \gamma^\nu,$
3.  $\gamma^\mu \gamma^\nu \gamma^\rho \gamma_\mu = 4g^{\nu\rho} - (4-d) \gamma^\nu \gamma^\rho,$
4.  $\gamma^\mu \gamma^\nu \gamma^\rho \gamma^\sigma \gamma_\mu = -2\gamma^\sigma \gamma^\rho \gamma^\nu + (4-d) \gamma^\nu \gamma^\rho \gamma^\sigma.$

The trace identities not involving  $\gamma^5$  are not modified since they are independent of dimensionality. There are many complications of dealing with  $\gamma^5$  in dimensions not equal to 4. There have been many discussions on the appropriate way to handle this situation. The reader is referred to [234, 235] for detailed discussions on this topic.

# APPENDIX B

## Spin, Helicity, and Chirality

### Spin

Spin is the eigenvalue of  $\vec{S}$ . For a fermion,  $\vec{S} = \frac{\vec{\sigma}}{2}$ . For a single particle, the spin and the angular momentum operators are the same. The scalar spin  $s$  is the eigenvalue in  $\vec{S}^2 = s(s+1)$ . When saying a particle is spin-1/2 refers to the value of  $s$ .

### Helicity

Helicity is the projection of the spin on the direction of momentum. Helicity eigenstates are given by the operator  $H = \frac{\vec{S} \cdot \vec{p}}{|\vec{p}|}$ , and exist for any spin particle.

### Chirality

Chirality is a concept that only exists for fermionic particles. A particle is chiral if it is not symmetric under a mirror symmetry. This leads to the definition of left-/right-handed particles. The projection of the fermionic wavefunction to the left-/right-handed components is given by:

$$P_L = \frac{1 + \gamma^5}{2}, \quad P_R = \frac{1 - \gamma^5}{2}. \quad (\text{B.1})$$

In the Weyl representation, the spinors can be represented by  $\begin{pmatrix} \psi_L \\ \psi_R \end{pmatrix}$ . In the massless limit chirality and helicity are the same.



# APPENDIX C

## Standard Model Higgs Boson and Higgs Mechanism

As discussed in Chapter 1, the Higgs Mechanism is used to introduce masses for vector bosons, in a manner that preserves the gauge theory. There, the calculation was demonstrated for a Higgs boson added to QED. The full details for adding a Higgs boson into  $SU(2)_L \times U(1)_Y$  is detailed below.

First, the addition of a scalar doublet is required to be added to the Standard Model, given by:

$$\phi = \frac{1}{\sqrt{2}} \begin{pmatrix} \phi_1 + i\phi_2 \\ \phi_3 + i\phi_4 \end{pmatrix}, \quad (\text{C.1})$$

which is a multiplet of  $SU(2)_L$  times  $U(1)_Y$ . The hypercharge of the above doublet is chosen to be  $Y = 1$ .

The potential for the scalar doublet that is responsible for the spontaneous breaking of the symmetry is the generalized form from that in Chapter 1, and is given as:

$$V(\phi) = \mu^2 (\phi^\dagger \phi) + \lambda (\phi^\dagger \phi)^2, \quad (\text{C.2})$$

where  $\mu^2 < 0$ . With a Lagrangian given as:

$$\mathcal{L} = (D^\mu \phi)^\dagger (D_\mu \phi) - V(\phi), \quad (\text{C.3})$$

where  $D_\mu$  is the covariant derivative given as:

$$D_\mu = \partial_\mu + ig \frac{1}{2} \vec{\tau} \cdot \vec{W}_\mu + ig' \frac{1}{2} Y B_\mu. \quad (\text{C.4})$$

The vacuum state ( $\phi_0$ ) is given by:

$$\phi_0 = \frac{1}{\sqrt{2}} \begin{pmatrix} 0 \\ v \end{pmatrix}, \quad (\text{C.5})$$

where  $v$  is known as the vacuum expectation value. With this choice of the vacuum,  $SU(2)_L \times U(1)_Y$  is broken, but since the vacuum has charge  $Q = I_3 + \frac{1}{2}Y = 0$ , there remains a  $U(1)_{EM}$  symmetry as required.

The Lagrangian above can be rewritten into terms of the physical gauge bosons ( $W^+, W^-, Z, \gamma$ ).

The  $W^\pm$  boson can be related to  $W^1$  and  $W^2$ , by the following relationship:

$$W^\pm = \frac{1}{\sqrt{2}} (W^1 \mp iW^2). \quad (\text{C.6})$$

Additionally, the  $Z$  and  $\gamma$  can be rewritten in terms of the  $W^3$  and  $B$  bosons as given by:

$$A = \frac{1}{\sqrt{g^2 + g'^2}} (g'W^3 + gB), \quad (\text{C.7})$$

$$Z = \frac{1}{\sqrt{g^2 + g'^2}} (gW^3 - g'B). \quad (\text{C.8})$$

Combining these relationships, the Lagrangian for the scalar can be rewritten as:

$$(D^\mu\phi)^\dagger (D_\mu\phi) = \frac{1}{8}v^2 \left( g^2 (W^+)^2 + g^2 (W^-)^2 + (g^2 + g'^2) Z^2 + 0 \cdot A^2 \right), \quad (\text{C.9})$$

plus terms that involve the Higgs boson. The rest of the results follow as discussed in Chapter 1.

# APPENDIX D

## Structure of $SU(3)$

A given representation of the Gell-Mann matrices is given by the following 8 matrices:

$$\begin{aligned}
 \lambda_1 &= \begin{pmatrix} 0 & 1 & 0 \\ 1 & 0 & 0 \\ 0 & 0 & 0 \end{pmatrix}, & \lambda_2 &= \begin{pmatrix} 0 & -i & 0 \\ i & 0 & 0 \\ 0 & 0 & 0 \end{pmatrix}, & \lambda_3 &= \begin{pmatrix} 1 & 0 & 0 \\ 0 & -1 & 0 \\ 0 & 0 & 0 \end{pmatrix}, \\
 \lambda_4 &= \begin{pmatrix} 0 & 0 & 1 \\ 0 & 0 & 0 \\ 1 & 0 & 0 \end{pmatrix}, & \lambda_5 &= \begin{pmatrix} 0 & 0 & -i \\ 0 & 0 & 0 \\ i & 0 & 0 \end{pmatrix}, & \lambda_6 &= \begin{pmatrix} 0 & 0 & 0 \\ 0 & 0 & 1 \\ 0 & 1 & 0 \end{pmatrix}, \\
 \lambda_7 &= \begin{pmatrix} 0 & 0 & 0 \\ 0 & 0 & -i \\ 0 & i & 0 \end{pmatrix}, & \lambda_8 &= \frac{1}{\sqrt{3}} \begin{pmatrix} 1 & 0 & 0 \\ 0 & 1 & 0 \\ 0 & 0 & -2 \end{pmatrix}.
 \end{aligned} \tag{D.1}$$

The structure functions are completely anti-symmetric in the choices of  $a, b$ , and  $c$ , and are a generalization of the Levi-Cevita Tensor from  $SU(2)$  to  $SU(3)$ . They are defined as:

$$f_{123} = 1, \quad f_{147} = f_{165} = f_{246} = f_{257} = f_{345} = f_{376} = \frac{1}{2}, \quad f_{458} = f_{678} = \frac{\sqrt{3}}{2}, \tag{D.2}$$

and in general they are zero, unless they contain an odd number from the set of  $\{2, 5, 7\}$ .

# APPENDIX E

## QCD Feynman Rules

### Fermion Lagrangian

To find the interaction terms for the fermions, we start from the free Lagrangian. For all of this, we will assume that the fermions are massless. It is easy for one to extend the following to include fermion masses.

$$\mathcal{L}_f = \bar{\psi} i \not{\partial} \psi \tag{E.1}$$

We will now require that the Lagrangian remain invariant under a SU(3) transformation.

To begin, a local SU(3) transformation can be written as:

$$X = e^{-iT^a \rho^a(x)} \tag{E.2}$$

Where  $\rho^a(x)$  are all real. We can then act this transformation on the above Lagrangian:

$$\psi \rightarrow X\psi \quad \partial_\mu \psi \rightarrow X\partial_\mu \psi + (\partial_\mu X)\psi \tag{E.3}$$

To bring back the desired SU(3) invariance, we introduce the covariant derivative which is defined such that:

$$D_\mu \psi \rightarrow XD_\mu \psi \tag{E.4}$$

Working through the equations above to find the definition of the covariant derivative, one finds that the form the covariant derivative must take is given by:

$$D_\mu = \partial_\mu + ig_s T^a A_\mu^a \quad (\text{E.5})$$

Where in the above equation,  $g_s$  is the strong coupling constant, and  $A_\mu^a$  are the vector boson fields for the strong force, known as gluons.

Therefore, the SU(3) invariant Lagrangian for fermions is defined as:

$$\mathcal{L}_f = \bar{\psi} (i\not{\partial} - g_s T^a \not{A}^a) \psi \quad (\text{E.6})$$

Looking at this equation, one can see where the interaction between the quarks and the gluons arises. Details on the interaction and the Feynman rules for QCD will be calculated in later sections.

## Vector Boson Lagrangian

The vector bosons, or gluons, are in the adjoint representation of SU(3). Therefore, under a SU(3) transformation the fields transform as:

$$A_\mu^{\prime a} = A_\mu^a - \partial_\mu \rho^a(x) + g_s f_{abc} \rho^b(x) A_\mu^c \quad (\text{E.7})$$

We can also define the field strength tensor for QCD in an analogous way to that of QED,

but we have to include additional terms since unlike QED, QCD is non-Abelian.

$$F_{\mu\nu}^a = \partial_\mu A_\nu^a - \partial_\nu A_\mu^a + g_s f^{abc} A_{\mu,b} A_{\nu,c} \quad (\text{E.8})$$

Also, similar to QED, the kinetic part of the Lagrangian is formed from a Lorentz invariant using two field strength tensors.

$$\mathcal{L}_{kin} = -\frac{1}{4} F^{\mu\nu,a} F_{\mu\nu}^a \quad (\text{E.9})$$

To simplify the expressions, we can define:  $\mathbb{A}_\mu \equiv -iT^a A_\mu^a$  and  $\mathbb{F}_{\mu\nu} \equiv -iT^a F_{\mu\nu}^a$ . Using these definitions, we can rewrite the kinetic part of the Lagrangian by using the following relations:

$$\mathbb{F}_{\mu\nu} = \partial_\mu \mathbb{A}_\nu - \partial_\nu \mathbb{A}_\mu + g_s [\mathbb{A}_\mu, \mathbb{A}_\nu] = \frac{1}{g_s} [D_\mu, D_\nu] \quad (\text{E.10})$$

Where  $D_\mu$  is the covariant derivative from Eq. E.5. Using the trace property of the  $T^a$ 's, one can rewrite the Lagrangian as:

$$\mathcal{L}_{kin} = -\frac{1}{2} \text{Tr}(\mathbb{F}^{\mu\nu} \mathbb{F}_{\mu\nu}) \quad (\text{E.11})$$

Putting the fermion Lagrangian E.6 together with the kinetic term for the boson Lagrangian E.9, one obtains the complete Lagrangian for QCD.

$$\mathcal{L}_{QCD} = -\frac{1}{4} F^{\mu\nu,a} F_{\mu\nu}^a + \bar{\psi} (i\not{D} - m) \psi \quad (\text{E.12})$$

## QCD Feynman Rules

In order to find the Feynman Rules for QCD, we first need to expand the kinetic term of the QCD Lagrangian in order to find the quartic, cubic, and quadratic terms for the vector bosons in the Lagrangian.

$$\begin{aligned}
F^{\mu\nu,a}F_{\mu\nu}^a &= \left( \partial^\mu A^{\nu,a} - \partial^\nu A^{\mu,a} + g_s f^{abc} A_b^\mu A_c^\nu \right) \left( \partial_\mu A_\nu^a - \partial_\nu A_\mu^a + g_s f^{ab'c'} A_{\mu,b'} A_{\nu,c'} \right) \\
&= \partial^\mu A^{\nu,a} \partial_\mu A_\nu^a - \partial^\mu A^{\nu,a} \partial_\nu A_\mu^a + g_s f^{ab'c'} \partial^\mu A^{\nu,a} A_{\mu,b'} A_{\nu,c'} \\
&\quad - \partial^\nu A^{\mu,a} \partial_\mu A_\nu^a + \partial^\nu A^{\mu,a} \partial_\nu A_\mu^a \\
&\quad - g_s f^{ab'c'} \partial^\nu A^{\mu,a} A_{\mu,b'} A_{\nu,c'} + g_s f^{abc} A_b^\mu A_c^\nu \partial_\mu A_\nu^a - g_s f^{abc} A_b^\mu A_c^\nu \partial_\nu A_\mu^a \\
&\quad + g_s^2 f^{abc} f^{ab'c'} A_b^\mu A_c^\nu A_{\mu,b'} A_{\nu,c'} \tag{E.13}
\end{aligned}$$

The equation above can be further simplified by noting:

$$\partial^\mu A^{\nu,a} \partial_\mu A_\nu^a = \partial^\nu A^{\mu,a} \partial_\nu A_\mu^a \text{ and } \partial^\mu A^{\nu,a} \partial_\nu A_\mu^a = \partial^\nu A^{\mu,a} \partial_\mu A_\nu^a$$

We can also interchange the A-fields since we represented them in terms of group components instead of matrices. Reorganizing the above equation and simplifying, one obtains:

$$\begin{aligned}
F^{\mu\nu,a}F_{\mu\nu}^a &= 2 \left[ \partial^\mu A^{\nu,a} \partial_\mu A_\nu^a - \partial^\mu A^{\nu,a} \partial_\nu A_\mu^a \right] \\
&\quad + 2g_s \left[ f_{abc} (\partial^\mu A^{\nu,a}) A_\mu^b A_\nu^c - f_{abc} (\partial^\nu A^{\mu,a}) A_\mu^b A_\nu^c \right] \\
&\quad + g_s^2 f_{abc} f_{ab'c'} A^{\mu,b} A^{\nu,c} A_{\mu,b'} A_{\nu,c'} \tag{E.14}
\end{aligned}$$



Putting this back into Eq. E.12, the Lagrangian can be written as:

$$\begin{aligned}
\mathcal{L}_{QCD} = & -\frac{1}{2} [\partial^\mu A^{\nu,a} \partial_\mu A_\nu^a - \partial^\mu A^{\nu,a} \partial_\nu A_\mu^a] \\
& - \frac{1}{2} g_s \left[ f_{abc} (\partial^\mu A^{\nu,a}) A_\mu^b A_\nu^c - f_{abc} (\partial^\nu A^{\mu,a}) A_\mu^b A_\nu^c \right] \\
& - \frac{1}{4} g_s^2 f_{abc} f_{ab'c'} A^{\mu,b} A^{\nu,c} A_\mu^{b'} A_\nu^{c'} \\
& + \bar{\psi} (i\not{\partial} - m) \psi - g_s T^a A_\mu^a \bar{\psi} \gamma^\mu \psi
\end{aligned} \tag{E.15}$$

Now that we have the Lagrangian in this form, we can begin calculating the Feynman Rules for QCD. We will calculate the Feynman Rules for:

1. Gluon propagator
2. Triple gluon coupling
3. Quartic gluon coupling
4. Fermion propagator
5. Fermion-gluon vertex

## Gluon Propagator

To find the gluon propagator Feynman Rule, one must first find all the quadratic terms in  $A_\mu^a$ . These terms are as follows:

$$\begin{aligned}
& -\frac{1}{2} [\partial^\mu A^{\nu,a} \partial_\mu A_\nu^a - \partial^\mu A^{\nu,a} \partial_\nu A_\mu^a] \\
& = -\frac{1}{2} A^{\mu,a} \left[ \partial^2 g_{\mu\nu} \delta_{ab} + \partial_\mu \partial_\nu \delta_{ab} \right] A^{\nu,b}
\end{aligned} \tag{E.16}$$

However, to find the propagator one needs to find the inverse of this operator, but due to gauge invariance this operator does not have an inverse. Therefore, in order to obtain the

gluon propagator we must first break the gauge invariance of the Lagrangian. To do this, we will insert a new term by hand, known as the gauge fixing term. Here we will use the following gauge breaking term:

$$\mathcal{L}_{gf} = -\frac{1}{2\alpha} (\partial_\mu A^{\mu,a})^2 = -\frac{1}{2\alpha} A_\mu^a (-\partial^\mu \partial^\nu \delta_{ab}) A_\nu^b \quad (\text{E.17})$$

Combining these two equations, we are able to find an operator that is invertible. The new term that we need to invert is given by:

$$-\frac{1}{2} A^{\mu,a} \left[ \partial^2 g_{\mu\nu} \delta_{ab} + \left(1 - \frac{1}{\alpha}\right) \partial_\mu \partial_\nu \delta_{ab} \right] A^{\nu,b} \quad (\text{E.18})$$

The propagator is found by taking two derivatives with respect to the Fourier transform of the Lagrangian.

$$\mathbb{P}^{-1} = -i \frac{\partial^2 \mathcal{F}(\mathcal{L})}{\partial A_\alpha^c \partial A_\beta^d} = -i \left( -k^2 g_{\alpha\beta} \delta_{cd} + \left(1 - \frac{1}{\alpha}\right) k_\alpha k_\beta \delta_{cd} \right) \quad (\text{E.19})$$

By observation, it is easy to see that the form that the inverse of this equation must take the form of:

$$\mathbb{P} = i \left( A g_{\mu\nu} + B \frac{k_\mu k_\nu}{k^2} \right) \delta_{ab} \quad (\text{E.20})$$

One can solve the equations for A and B to obtain the result for the propagator.

$$\mathbb{P} \mathbb{P}^{-1} = \mathbb{1} = g_{\sigma}^{\mu} \delta_{ab}$$

$$\begin{aligned}
&= \left( k^2 g_{\nu\sigma} - \left(1 - \frac{1}{\alpha}\right) k_\nu k_\sigma \right) \left( A g^{\mu\nu} + B \frac{k^\mu k^\nu}{k^2} \right) \delta_{ab} \\
&\Rightarrow -Ak^2 g_\sigma^\mu - Bk^\mu k_\sigma + A \left(1 - \frac{1}{\alpha}\right) k^\mu k_\sigma + B \left(1 - \frac{1}{\alpha}\right) k^\mu k_\sigma = g_\sigma^\mu \\
&\Rightarrow -Ak^2 = 1 \qquad -B + A \left(1 - \frac{1}{\alpha}\right) + B \left(1 - \frac{1}{\alpha}\right) = 0 \\
&\Rightarrow A = -\frac{1}{k^2} \qquad B = (1 - \alpha) \frac{1}{k^2}
\end{aligned} \tag{E.21}$$

Plugging the solutions to  $A$  and  $B$  back into Eq. E.20, we obtain the Feynman Rule for the gluon propagator.

$$\text{~~~~~} = i \frac{\delta_{ab}}{k^2} \left[ -g_{\mu\nu} + \frac{(1 - \alpha) k_\mu k_\nu}{k^2} \right] \tag{E.22}$$

### Triple Gluon Coupling

To find the triple gluon coupling, first we need to find all the terms that are cubic in the gauge fields. We will also be using the all incoming momentum convention when calculating the Feynman Rules. These terms are as follows:

$$\mathcal{L}_3 = -\frac{1}{2} g_s f_{abc} [\partial^\mu A^{\nu,a} - \partial^\nu A^{\mu,a}] A_\mu^b A_\nu^c \tag{E.23}$$

We then follow a similar procedure to that used for the propagator. We need to find:

$$\Gamma^{(3)} = \frac{-i \partial^3 \mathcal{F}(\mathcal{L}_3)}{\partial A_\alpha^l \partial A_\beta^m \partial A_\gamma^n} \tag{E.24}$$

The array of  $(l, m, n)$  has  $3! = 6$  permutations, but due to  $f_{abc}$  being antisymmetric, we can reduce the number of terms that need to be consider  $\frac{3!}{2} = 3$  cases. In deriving the Feynman rule, we will go through each of the three cases to determine it. Also, the gluons

will have the momenta  $p, k,$  and  $q,$  as seen in the diagram of the vertex below.

1. Consider  $(l, m, n) \rightarrow (a, b, c)$ :

The Fourier transform brings down the momentum associated with the gluon that has the derivative acting on it. So in this case we get factors of  $(ip).$

$$\frac{-i}{2} g_s f_{abc} \delta_{mb} g^{\beta\mu} \delta_{nc} g^{\gamma\nu} [\delta_{al} g_{\alpha\nu} (ip_\mu) - g_{\mu\alpha} \delta_{al} (ip_\nu)] = \frac{-i}{2} g_s f_{lmn} [(ip_\beta) g_{\alpha\gamma} - (ip_\gamma) g_{\alpha\beta}]$$

2. Consider  $(l, m, n) \rightarrow (b, c, a)$ :

Similar to above, but here the momentum factor is  $(ik).$

$$\frac{-i}{2} g_s f_{abc} \delta_{lb} g^{\alpha\mu} \delta_{mc} g^{\beta\nu} [\delta_{an} g_{\gamma\nu} (ik_\mu) - g_{\mu\gamma} \delta_{an} (ik_\nu)] = \frac{-i}{2} g_s f_{nlm} [(ik_\alpha) g_{\beta\gamma} - (ik_\beta) g_{\alpha\gamma}]$$

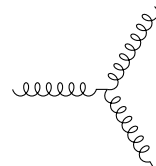
Note:  $f_{nlm} = -f_{lnm} = f_{lmn}$

3. Consider  $(l, m, n) \rightarrow (c, a, b)$ :

Here the momentum factor is  $(iq)$

$$\frac{-i}{2} g_s f_{abc} \delta_{nb} g^{\gamma\mu} \delta_{lc} g^{\alpha\nu} [\delta_{an} g_{\beta\nu} (iq_\mu) - g_{\mu\beta} \delta_{an} (iq_\nu)] = \frac{-i}{2} g_s f_{mnl} [(iq_\gamma) g_{\alpha\beta} - (ip_\alpha) g_{\gamma\beta}]$$

Putting the three terms together along with manipulating the structure constants to match, one obtains the Feynman rule for the 3 point function as:



$$= g_s f_{lmn} [(q - k)_\alpha \delta_{\beta\gamma} + (k - p)_\beta \delta_{\gamma\alpha} + (p - q)_\gamma \delta_{\alpha\beta}] \quad (\text{E.25})$$

## Quartic Gluon Coupling

The last piece that includes on the gauge field are terms that contain quartic terms in the fields. There is one such term shown below:

$$\mathcal{L}_4 = -\frac{1}{4}g_s^2 f_{abc}f_{ade}A^{\mu,b}A^{\nu,c}A_\mu^dA_\nu^e \quad (\text{E.26})$$

Therefore, following the same approach in the sections above, we will need to calculate the following term in order to get the Feynman rule:

$$\Gamma^{(4)} = \frac{i\partial^4 \mathcal{F}(\mathcal{L}_4)}{\partial A_\alpha^k \partial A_\beta^l \partial A_\gamma^m \partial A_\sigma^n} \quad (\text{E.27})$$

Here we can see that there will be  $4! = 24$  different permutations that can occur for the indices  $(k, l, m, n)$ . Again, due to the properties of the structure function we are able to relate  $(k, l, m, n)$  to  $(k, l, n, m)$ ,  $(k, m, l, n)$ , and  $(k, n, m, l)$ .

However, to illustrate the relationship, we will still show the work for all 24 permutations.

1. • Consider  $(k, l, m, n) \rightarrow (b, c, d, e)$

$$-\frac{i}{4}g_s^2 f_{abc}f_{ade}\delta_{bk}g^{\mu\alpha}\delta_{cl}g^{\nu\beta}\delta_{dm}g_{\mu\gamma}\delta_{en}g_{\nu\sigma} = -\frac{i}{4}g_s^2 f_{akl}f_{amn}g_{\alpha\gamma}g_{\beta\sigma}$$

- Consider  $(k, l, m, n) \rightarrow (b, c, d, e)$

$$-\frac{i}{4}g_s^2 f_{abc}f_{ade}\delta_{bk}g^{\mu\alpha}\delta_{cl}g^{\nu\beta}\delta_{dn}g_{\mu\sigma}\delta_{em}g_{\nu\gamma} = -\frac{i}{4}g_s^2 f_{akl}f_{anm}g_{\alpha\sigma}g_{\beta\gamma}$$

- Consider  $(k, m, l, n) \rightarrow (b, c, d, e)$

$$-\frac{i}{4}g_s^2 f_{abc}f_{ade}\delta_{bk}g^{\mu\alpha}\delta_{cm}g^{\nu\gamma}\delta_{dl}g_{\mu\beta}\delta_{en}g_{\nu\sigma} = -\frac{i}{4}g_s^2 f_{akm}f_{aln}g_{\alpha\beta}g_{\gamma\sigma}$$

- Consider  $(k, m, n, l) \rightarrow (b, c, d, e)$

$$-\frac{i}{4}g_s^2 f_{abc}f_{ade}\delta_{bk}g^{\mu\alpha}\delta_{cm}g^{\nu\gamma}\delta_{dn}g_{\mu\sigma}\delta_{el}g_{\nu\beta} = -\frac{i}{4}g_s^2 f_{akm}f_{aln}g_{\alpha\sigma}g_{\beta\gamma}$$

- Consider  $(k, n, m, l) \rightarrow (b, c, d, e)$

$$-\frac{i}{4}g_s^2 f_{abc}f_{ade}\delta_{bk}g^{\mu\alpha}\delta_{cn}g^{\nu\sigma}\delta_{dm}g_{\mu\gamma}\delta_{el}g_{\nu\beta} = -\frac{i}{4}g_s^2 f_{akn}f_{aml}g_{\alpha\gamma}g_{\beta\sigma}$$

- Consider  $(k, n, l, m) \rightarrow (b, c, d, e)$

$$-\frac{i}{4}g_s^2 f_{abc}f_{ade}\delta_{bk}g^{\mu\alpha}\delta_{cn}g^{\nu\sigma}\delta_{dl}g_{\mu\beta}\delta_{em}g_{\nu\gamma} = -\frac{i}{4}g_s^2 f_{akn}f_{alm}g_{\alpha\beta}g_{\gamma\sigma}$$

2. From here out, we will just write the result for each term. This can be done by recognizing the pattern of the terms above.

- Consider  $(l, m, n, k) \rightarrow (b, c, d, e)$

$$-\frac{i}{4}g_s^2 f_{alm}f_{ank}g_{\beta\sigma}g_{\gamma\alpha}$$

- Consider  $(l, m, k, n) \rightarrow (b, c, d, e)$

$$-\frac{i}{4}g_s^2 f_{alm}f_{akn}g_{\alpha\beta}g_{\gamma\sigma}$$

- Consider  $(l, n, m, k) \rightarrow (b, c, d, e)$

$$-\frac{i}{4}g_s^2 f_{aln} f_{amk} g_{\beta\gamma} g_{\alpha\sigma}$$

- Consider  $(l, k, n, m) \rightarrow (b, c, d, e)$

$$-\frac{i}{4}g_s^2 f_{alk} f_{anm} g_{\beta\sigma} g_{\alpha\gamma}$$

- Consider  $(l, n, k, m) \rightarrow (b, c, d, e)$

$$-\frac{i}{4}g_s^2 f_{aln} f_{akm} g_{\alpha\beta} g_{\gamma\sigma}$$

- Consider  $(l, k, m, n) \rightarrow (b, c, d, e)$

$$-\frac{i}{4}g_s^2 f_{alk} f_{amn} g_{\beta\gamma} g_{\alpha\sigma}$$

3. • Consider  $(m, n, k, l) \rightarrow (b, c, d, e)$

$$-\frac{i}{4}g_s^2 f_{amn} f_{akl} g_{\alpha\gamma} g_{\beta\sigma}$$

- Consider  $(m, n, l, k) \rightarrow (b, c, d, e)$

$$-\frac{i}{4}g_s^2 f_{amn} f_{alk} g_{\beta\gamma} g_{\alpha\sigma}$$

- Consider  $(m, k, n, l) \rightarrow (b, c, d, e)$

$$-\frac{i}{4}g_s^2 f_{amk} f_{anl} g_{\gamma\sigma} g_{\alpha\beta}$$

- Consider  $(m, l, k, n) \rightarrow (b, c, d, e)$

$$-\frac{i}{4}g_s^2 f_{aml} f_{akn} g_{\alpha\gamma} g_{\beta\sigma}$$

- Consider  $(m, k, l, n) \rightarrow (b, c, d, e)$

$$-\frac{i}{4}g_s^2 f_{amk} f_{aln} g_{\beta\gamma} g_{\alpha\sigma}$$

- Consider  $(m, l, n, k) \rightarrow (b, c, d, e)$

$$-\frac{i}{4}g_s^2 f_{aml} f_{ank} g_{\gamma\sigma} g_{\alpha\beta}$$

4. • Consider  $(n, k, l, m) \rightarrow (b, c, d, e)$

$$-\frac{i}{4}g_s^2 f_{ank} f_{alm} g_{\beta\sigma} g_{\alpha\gamma}$$

- Consider  $(n, k, m, l) \rightarrow (b, c, d, e)$

$$-\frac{i}{4}g_s^2 f_{ank} f_{aml} g_{\gamma\sigma} g_{\alpha\beta}$$



- Consider  $(n, l, k, m) \rightarrow (b, c, d, e)$

$$-\frac{i}{4}g_s^2 f_{anl} f_{akm} g_{\alpha\sigma} g_{\beta\gamma}$$

- Consider  $(n, m, l, k) \rightarrow (b, c, d, e)$

$$-\frac{i}{4}g_s^2 f_{anm} f_{alk} g_{\alpha\gamma} g_{\beta\sigma}$$

- Consider  $(n, l, m, k) \rightarrow (b, c, d, e)$

$$-\frac{i}{4}g_s^2 f_{anl} f_{amk} g_{\gamma\sigma} g_{\alpha\beta}$$

- Consider  $(n, m, k, l) \rightarrow (b, c, d, e)$

$$-\frac{i}{4}g_s^2 f_{anm} f_{akl} g_{\alpha\sigma} g_{\beta\gamma}$$

Combining the above 24 terms together, and simplifying the expressions, we get the following for the Feynman Rule:

$$\begin{aligned}
 \begin{array}{c} \text{-----} \\ | \\ \text{-----} \\ | \\ \text{-----} \\ | \\ \text{-----} \end{array} &= -ig_s^2 [f_{akl} f_{amn} (g_{\alpha\gamma} g_{\beta\sigma} - g_{\alpha\sigma} g_{\beta\gamma}) \\
 &+ f_{akm} f_{aln} (g_{\alpha\beta} g_{\sigma\gamma} - g_{\alpha\sigma} g_{\beta\gamma}) \\
 &+ f_{akn} f_{alm} (g_{\alpha\beta} g_{\sigma\gamma} - g_{\alpha\sigma} g_{\beta\gamma})] \tag{E.28}
 \end{aligned}$$

## Fermion Propagator

Now we will consider terms in the Lagrangian containing fermions. The first term that we will calculate is the fermion propagator. Unlike the gluon propagator, the fermion propagator does not have the issue of being zero due to gauge invariance. It is therefore, a straightforward calculation. The term needed in the Lagrangian is:

$$\mathcal{L}_f = \bar{\psi} (i\not{\partial} - m) \psi \quad (\text{E.29})$$

The propagator is found by the same method as above. In other words, we need to calculate:

$$\mathbb{P} = \left( -i \frac{\partial^2 \mathcal{F}(\mathcal{L}_f)}{\partial \bar{\psi} \partial \psi} \right)^{-1} \quad (\text{E.30})$$

Performing this calculation, one obtains:

$$\mathbb{P} = i (\not{p} - m)^{-1} = \frac{i}{\not{p} - m} = \frac{i(\not{p} + m)}{p^2 - m^2} \quad (\text{E.31})$$

Where to get to the last equation, we multiplied the top and the bottom by  $\not{p} + m$  to bring it to the typical form. Thus, the Feynman rule for the Fermion propagator is given by:

$$\longrightarrow = \frac{i(\not{p} + m)}{p^2 - m^2} \quad (\text{E.32})$$

## Fermion-Gluon Vertex

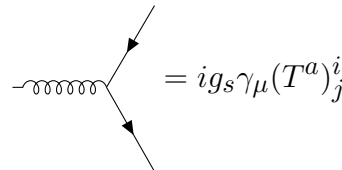
The remaining term that has not been accounted for in the Lagrangian thus far is the interaction term between gluons and fermions. This term is given by:

$$\mathcal{L}_{int} = g_s T^a A_\mu^a \bar{\psi} \gamma^\mu \psi = g_s A_\mu^a \bar{\psi}_i \gamma^\mu (T^a)^i_j \psi_j \quad (\text{E.33})$$

Where in the second equation we wrote in the indices corresponding to the color of the fermions. The index  $a$  goes from 1 to 8, where the indices  $i, j$  can be 1, 2, or 3. Again, we perform the same procedure as before:

$$\Gamma^{int} = \frac{i \partial^3 \mathcal{F}(\mathcal{L}_{int})}{\partial \bar{\psi} \partial \psi \partial A_\mu^a} \quad (\text{E.34})$$

This gives us the Feynman rule, which is shown below:



$$= i g_s \gamma_\mu (T^a)^i_j \quad (\text{E.35})$$

Note: The order of  $(ij)$  is important because  $T^a$  is not a symmetric matrix.

## Faddeev-Popov Ghost Fields

Arising from an artifact of insisting on Lorentz invariance and unitarity for massless spin-1 particles are unphysical particles known as Faddeev-Popov ghosts. These also arise in QED, but since the theory is Abelian, they do not couple to the photon. Here in the non-Abelian theory they do couple to the gluon, but only appear at higher orders, since they are non-

physical. There are ways to derive the Feynman rules to not have any ghost fields known as Axial gauges and a discussion on these can be found in [236].

The gauge fixing term can be expressed as:

$$\mathcal{L}_{gf} = -\frac{1}{2\alpha}(c^a)^2 \quad (\text{E.36})$$

The ghost Lagrangian is defined as:

$$\mathcal{L}_{FP} = \bar{\chi}^a M_{ab} \chi^b \quad (\text{E.37})$$

where  $M_{ab} = \frac{\delta c^a}{\delta \Lambda^b}$ . We can see that there will be one ghost and one anti-ghost for each of the gluons. Therefore, there will be 8 ghost fields and 8 anti-ghost fields. Let us examine how the  $c^a$  fields change under a local gauge transformation.

$$c^a = \partial^\mu A_\mu^a \rightarrow \partial^\mu (A_\mu^a + \delta A_\mu^a) = c^a + \delta c^a \quad (\text{E.38})$$

To find the equation for  $M_{ab}$  we will need to calculate the  $\delta C^a$  term in the above equation.

The derivation is shown in the equations below.

$$\begin{aligned} \delta C^a &= \partial^\mu (\delta A_\mu^a) = \partial^\mu (-\partial_\mu \Lambda^a + g_s f_{abc} \Lambda^b A_\mu^c) \\ &= -\partial^2 \Lambda^a + g_s f_{abc} \partial^\mu (\Lambda^b A_\mu^c) \end{aligned} \quad (\text{E.39})$$

$$\begin{aligned} &= \left[ -\partial^2 \delta^{ab} + g_s f_{abc} (A_\mu^c \partial^\mu + \partial^\mu A_\mu^c) \right] \Lambda^b \\ \Rightarrow M_{ab} &= \frac{\delta c^a}{\delta \Lambda^b} = -\partial^2 \delta_{ab} + g_s f_{abc} (A_\mu^c \partial^\mu + \partial^\mu A_\mu^c) \end{aligned} \quad (\text{E.40})$$

Plugging the above result into Eq. E.37, we get the resulting ghost Lagrangian.

$$\begin{aligned}\mathcal{L}_{FP} &= \bar{\chi}^a \left[ -\partial^2 \delta_{ab} + g_s f_{abc} (A_\mu^c \partial^\mu + \partial^\mu A_\mu^c) \right] \chi^b \\ &= (\partial_\mu \bar{\chi}^a) (\partial^\mu \chi^a) - g_s f_{abc} (\partial^\mu \bar{\chi}^a) A_\mu^c \chi^b\end{aligned}\tag{E.41}$$

Now we will begin to calculate the Feynman rules for the ghost fields. We begin with the calculation of the propagator.

$$\mathbb{P} = \left( \frac{-i\partial^2 \mathcal{F}(-\bar{\chi}^a \partial^2 \delta_{ab} \chi^b)}{\partial \bar{\chi}^a \partial \chi^b} \right)^{-1}\tag{E.42}$$

$$\dots\dots\dots = -i \frac{1}{k^2} \delta_{ab}\tag{E.43}$$

The only remaining Feynman rule for QCD to calculate is the ghost-gluon interaction term. This term is given by the same procedure as above, giving:



$$\dots\dots\dots = g_s f_{abc} p_\mu\tag{E.44}$$

It is important to note that the anti-ghost fields are not the anti-particles of the ghost fields.

## QCD $\beta$ Functions

The  $\beta$  functions in QCD arise from the calculation of the renormalization of the strong coupling constant. They have been calculated up to four-loops [237, 238]. The results up to that order are listed below:

$$\beta_0 = \frac{11}{3}C_A - \frac{4}{3}T_F n_F, \quad (\text{E.45})$$

$$\beta_1 = \frac{34}{3}C_A^2 - \frac{20}{3}C_A T_F n_F - 4C_F T_F n_F, \quad (\text{E.46})$$

$$\begin{aligned} \beta_2 = & \frac{2857}{54}C_A^3 - \frac{1415}{27}C_A^2 T_F n_F + \frac{158}{27}C_A T_F^2 n_F^2 + \frac{44}{9}C_F T_F^2 n_F^2 \\ & - \frac{205}{9}C_A C_F T_F n_F + 2C_F^2 T_F n_F, \end{aligned} \quad (\text{E.47})$$

$$\begin{aligned} \beta_3 = & C_A C_F T_F^2 n_F^2 \left( \frac{17152}{243} + \frac{448}{9}\zeta_3 \right) + C_A C_F^2 T_F n_F \left( -\frac{4204}{27} + \frac{352}{9}\zeta_3 \right) + \frac{424}{243}C_A T_F^3 n_F^3 \\ & + C_A^2 C_F T_F n_F \left( \frac{7073}{243} - \frac{656}{9}\zeta_3 \right) + C_A^2 T_F^2 n_F^2 \left( \frac{7930}{81} + \frac{224}{9}\zeta_3 \right) + \frac{1232}{243}C_F T_F^3 n_F^3 \\ & C_A^3 T_F n_F \left( -\frac{39143}{81} + \frac{136}{3}\zeta_3 \right) + C_A^4 \left( \frac{150653}{486} - \frac{44}{9}\zeta_3 \right) + C_F^2 T_F^2 n_F^2 \left( \frac{1352}{27} - \frac{704}{9}\zeta_3 \right) \\ & + 46C_F^3 T_F n_F + n_F \frac{d_F^{abcd} d_A^{abcd}}{N_A} \left( \frac{512}{9} - \frac{1664}{3}\zeta_3 \right) + n_F^2 \frac{d_F^{abcd} d_F^{abcd}}{N_A} \left( -\frac{704}{9} + \frac{512}{3}\zeta_3 \right) \\ & + \frac{d_A^{abcd} d_A^{abcd}}{N_A} \left( -\frac{80}{9} + \frac{704}{3}\zeta_3 \right), \end{aligned} \quad (\text{E.48})$$

where the coefficients in the  $\beta$  equations can be expressed in the specific values for an  $SU(N)$  group are:

$$\begin{aligned} T_F = \frac{1}{2}, \quad C_F = \frac{N^2 - 1}{2N}, \quad C_A = N, \quad \frac{d_F^{abcd} d^{abcd}_F}{N_A} = \frac{N^4 - 6N^2 + 18}{96N^2}, \\ \frac{d_F^{abcd} d^{abcd}_A}{N_A} = \frac{N(N^2 + 6)}{48}, \quad \frac{d_A^{abcd} d^{abcd}_A}{N_A} = \frac{N^2(N^2 + 36)}{24}, \quad N_A = N^2 - 1. \end{aligned} \quad (\text{E.49})$$

# APPENDIX F

## Calculation Details

### Plus Functions

The Plus function is a distribution to handle singularities of functions that occur for  $x = 1$ .

Given the function  $F(x)$  which is singular for  $x = 1$ , the plus function is defined as:

$$F(x)_+ \equiv \lim_{\beta \rightarrow 0} \left( F(x)\Theta(1-x-\beta) - \delta(1-x-\beta) \int_0^{1-\beta} dy F(y) \right). \quad (\text{F.1})$$

When a plus function is convoluted with a test function, the final result is well defined. For example, given a test function  $G(x)$ , the convolution is given by:

$$\int_0^1 dx F(x)_+ G(x) = \int_0^1 dx F(x) (G(x) - G(1)). \quad (\text{F.2})$$

Additionally, a property of the plus function is:

$$\int_0^1 dx F(x)_+ = 0, \quad (\text{F.3})$$

which can be easily derived with a choice of  $G(x) = 1$ . Finally, it is possible to obtain the result for a lower bound that is non-zero by:

$$\int_a^1 dx F(x)_{+G(x)} = \int_a^1 dx F(x) (G(x) - G(1)) + G(1) \int_0^a F(x). \quad (\text{F.4})$$

## NLO Real Corrections to Drell-Yan

Similar to the quark-anti-quark channel, the singular terms for the (anti-)quark-gluon channel are given by:

$$\left(|M|_{gq}^2\right)_{\text{sing}} = 64 \left(\frac{Q^2}{2}\right) \left( (g_L^2 + g_R^2) (f_L^2 + f_R^2) \mathcal{K}_3 \mathcal{L}_0 - (g_L^2 - g_R^2) (f_L^2 - f_R^2) \mathcal{K}_4 (2A_4) \right), \quad (\text{F.5})$$

with

$$\begin{aligned} \mathcal{K}_3 &= \frac{1}{q_T^2} \left( z_A^2 + (1 - z_A)^2 \right) \delta(1 - z_B) \\ &\quad - \epsilon \frac{1}{q_T^2} \delta(1 - z_B) z_A (1 - z_A) + z_A \leftrightarrow z_B, \end{aligned} \quad (\text{F.6})$$

$$\mathcal{K}_4 = \frac{1}{q_T^2} \left( z_A^2 + (1 - z_A)^2 \right) \delta(1 - z_B) + z_A \leftrightarrow z_B. \quad (\text{F.7})$$

## Loop Integrals

Here a brief discuss of loop integrals is given, along with the calculation of the loop integral involved in calculating the NLO correction to Drell-Yan. For additional discussions of loop integrals, and the more modern approach that has been developed to tackle the calculations of higher number of loops can be found in [239, 240, 241].



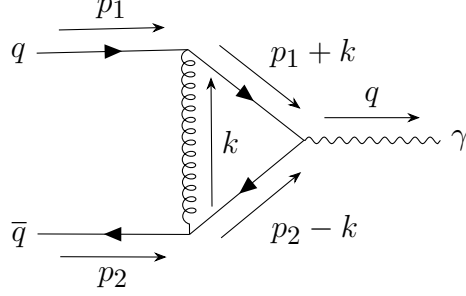


Figure F.1: The hadronic virtual correction Feynman Diagram to Drell-Yan at NLO.

For Drell-Yan at NLO accuracy, there is only one virtual diagram to calculate if dimensional regularization is used. The hadronic component of the calculation is given the following Feynman diagram in Fig. F.1. Since this diagram is  $\mathcal{O}(\alpha_s)$ , the matrix element squared will be of  $\mathcal{O}(\alpha_s^2)$ . Since this is a higher order correction, only the cross term of the virtual diagram and the tree level diagram are used up to NLO. The result is obtained from  $2\text{Re} \left( M_{\text{born}} M_{\text{virt}}^\dagger \right)$ . Using the Feynman rules, the virtual correction is given as:

$$2\text{Re} \left( M_{\text{born}} M_{\text{virt}}^\dagger \right) = \int \frac{d^d k}{(2\pi)^d} \text{Tr} \left( \not{p}_2 \gamma^\alpha (\not{p}_2 - \not{k}) \gamma^\mu (\not{p}_1 + \not{k}) \gamma^\beta \not{p}_1 \gamma^\nu \right) C_F \frac{i g_{\alpha\beta}}{k^2} \frac{i}{(p_2 - k)^2} \frac{i}{(p_1 + k)^2} g_{\mu\nu} (2\pi) g_s^2 Q^2 e^2, \quad (\text{F.8})$$

where  $C_F$  is the color factor,  $g_s$  is the strong coupling constant,  $Q$  is the charge of the quark, and  $e$  is the electric charge. Consider the integral:

$$\int \frac{d^d k}{(2\pi)^d} \frac{\text{Tr} \left( \not{p}_2 \gamma^\alpha (\not{p}_2 - \not{k}) \gamma^\mu (\not{p}_1 + \not{k}) \gamma^\beta \not{p}_1 \gamma^\nu \right)}{k^2 (p_2 - k)^2 (p_1 + k)^2}. \quad (\text{F.9})$$

Using the Feynman parameter trick<sup>1</sup>, gives:

$$I = \int dx dy \frac{d^d k}{(2\pi)^d} \frac{\text{Tr} \left( \not{p}_2 \gamma^\alpha (\not{p}_2 - \not{k}) \gamma^\mu (\not{p}_1 + \not{k}) \gamma^\beta \not{p}_1 \gamma^\nu \right)}{k^2(1-x-y) + (p_2 - k)^2 x + (p_1 + k)^2 y}. \quad (\text{F.10})$$

The denominator of the above equation can be simplified, using the substitution:  $l^\mu = k^\mu - p_2^\mu x + p_1^\mu y$ , and the definition  $q^2 = 2p_1 \cdot p_2$ , giving:

$$D = l^2 + q^2 xy. \quad (\text{F.11})$$

Now consider the numerator of Eq. F.10, the numerator can be simplified, using the substitution for  $l$  given above, to:

$$\begin{aligned} N = & -4q^4 \left[ (1-y-x)(1-\epsilon) + xy - 2\epsilon^2 xy \right] \\ & + 8 \frac{1-2\epsilon}{2(2-\epsilon)} q^2 l^2 - 8\epsilon(1-\epsilon) q^2 l^2. \end{aligned} \quad (\text{F.12})$$

Combining the numerator and the denominator and putting the integrals back, gives three unique integrals to calculate. The first integral is:

$$\begin{aligned} I_1 = & \int_0^1 dx \int_0^{1-x} dy \int \frac{d^d l}{(2\pi)^d} \frac{1-y-x}{(l^2 + q^2 xy)^3} \\ = & \frac{-i}{16\pi^2 q^2} \left( \frac{4\pi}{-q^2} \right)^\epsilon \frac{1}{2} \frac{1}{\Gamma(1-\epsilon)} \left( \frac{1}{\epsilon^2} + \frac{2}{\epsilon} + 4 + \mathcal{O}(\epsilon) \right), \end{aligned} \quad (\text{F.13})$$

---

<sup>1</sup>Details on the Feynman parameter trick can be found in Appendix A.4 of [42]

the second is:

$$\begin{aligned}
I_2 &= \int_0^1 dx \int_0^{1-x} dy \int \frac{d^d l}{(2\pi)^d} \frac{l^2}{(l^2 + q^2 xy)^3} \\
&= \frac{-i}{16\pi^2} \frac{2-\epsilon}{2} \left( \frac{4\pi}{-q^2} \right)^\epsilon \frac{1}{\Gamma(1-\epsilon)} \left( \frac{1}{2\epsilon} + \frac{3}{2} + \frac{7\epsilon}{2} + \mathcal{O}(\epsilon^2) \right), \tag{F.14}
\end{aligned}$$

and finally, the third is:

$$\begin{aligned}
I_3 &= \int_0^1 dx \int_0^{1-x} dy \int \frac{d^d l}{(2\pi)^d} \frac{xy}{(l^2 + q^2 xy)^3} \\
&= \frac{-i}{16\pi^2 q^2} \frac{1}{2} \left( \frac{4\pi}{-q^2} \right)^\epsilon \left( \frac{1}{2} + \frac{3\epsilon}{2} + \mathcal{O}(\epsilon^2) \right). \tag{F.15}
\end{aligned}$$

Plugging all of the results back into Eq. F.10, gives:

$$I = \frac{iq^2}{16\pi^2} \left( \frac{4\pi}{q^2} \right)^\epsilon \frac{1}{\Gamma(1-\epsilon)} \left( \frac{-2}{\epsilon^2} - \frac{3}{\epsilon} - 8 + \pi^2 + \mathcal{O}(\epsilon) \right). \tag{F.16}$$

Finally, substituting the result of the integral back into Eq. F.8, gives the desired result found in Eq. 3.18.

## Phase Space In D-Dimensions

When working outside of  $d = 4 - 2\epsilon$  dimensions, the integrals over the phase space need to be modified. The major calculation that is needed, is the area of a unit sphere in  $d$  dimensions.

This can be calculated by using the following trick:

$$\begin{aligned}
(\sqrt{\pi})^d &= \left( \int dx e^{-x^2} \right)^d = \int d^d x \exp \left( - \sum_{i=1}^d x_i^2 \right) \\
&= \int d\Sigma_d \int_0^\infty dx x^{d-1} e^{-x^2} = \left( \int d\Sigma_d \right) \frac{1}{2} \Gamma \left( \frac{d}{2} \right).
\end{aligned}$$

Solving for  $\int d\Sigma_d$  gives:

$$\int d\Sigma_d = \frac{2\pi^{d/2}}{\Gamma(d/2)}. \tag{F.17}$$

Using Eq. F.17 reproduces the expected results for the familiar integer dimensions as seen in Table F.1.

$d$	$\Gamma(d/2)$	$\int d\Sigma_d$
1	$\sqrt{\pi}$	2
2	1	$2\pi$
3	$\sqrt{\pi}/2$	$4\pi$
4	1	$2\pi^2$

Table F.1: Table of the results of calculating the area of a  $d$ -Sphere

## Resummation Coefficients to N<sup>3</sup>LL

The coefficients up to NNLL can be found in Section 3.4.1 and 3.4.2 for the CSS and CFG formalisms respectively. For the additional terms that appear at N<sup>3</sup>LL, they can be found in [167, 168], and are reproduced here for ease.

The  $B$  anomalous dimension in CSS at  $\mathcal{O}(\alpha_s^3)$  is given as:

$$B_3^{DY} = \gamma_2^{DY} - \gamma_2^r + \beta_1 c_1^{DY} + 2\beta_0 \left( c_2^{DY} - \frac{1}{2} \left( c_1^{DY} \right)^2 \right), \tag{F.18}$$

substituting the numbers into the equation above, the numerical result is given as:

$$B_3^{DY} = 114.98 - 11.27n_f + 0.32n_f^2, \quad (\text{F.19})$$

where  $n_f$  is the number of active flavors. Note the above equation differs from that in [167], since the expansion in [167] is for  $\frac{\alpha_s}{4\pi}$ , while this work uses  $\frac{\alpha_s}{\pi}$ .

The hard-collinear coefficient at the NNLO for vector boson production is given by five different initial states:  $q\bar{q}$ ,  $q\bar{q}'$ ,  $qq$ ,  $qq'$ , and  $qg$ . These coefficients are given as:

$$\begin{aligned} 2C_{q\bar{q}}^{(2)}(z) + \delta(1-z) & \left[ H_q^{DY(2)} - \frac{3}{4} \left( H_q^{DY(1)} \right)^2 + \frac{C_F}{4} (\pi^2 - 8) H_q^{DY(1)} \right] \\ & + \frac{1}{2} C_F H_q^{DY(1)} (1-z) \\ & = \mathcal{H}_{q\bar{q} \leftarrow q\bar{q}}^{DY(2)}(z) - \frac{C_F^2}{4} \left[ \delta(1-z) \frac{(\pi^2 - 8)^2}{4} + (\pi^2 - 10)(1-z) - (1+z) \ln z \right], \end{aligned} \quad (\text{F.20})$$

$$\begin{aligned} C_{qg}^{(2)}(z) + \frac{1}{4} H_q^{DY(1)} z(1-z) & = \mathcal{H}_{q\bar{q} \leftarrow qg}^{DY(2)}(z) \\ & - \frac{C_F}{4} \left[ z \ln z + \frac{1}{2} (1-z^2) + \left( \frac{\pi^2}{4} - 4 \right) z(1-z) \right], \end{aligned} \quad (\text{F.21})$$

$$C_{qq}^{(2)}(z) = \mathcal{H}_{q\bar{q} \leftarrow qq}^{DY(2)}(z), \quad (\text{F.22})$$

$$C_{qq'}^{(2)}(z) = \mathcal{H}_{q\bar{q} \leftarrow qq'}^{DY(2)}(z), \quad (\text{F.23})$$

$$C_{q\bar{q}'}^{(2)}(z) = \mathcal{H}_{q\bar{q} \leftarrow q\bar{q}'}^{DY(2)}(z), \quad (\text{F.24})$$

where the  $\mathcal{H}$  coefficients are given by:

$$\begin{aligned}
\mathcal{H}_{q\bar{q} \leftarrow q\bar{q}}^{DY(2)}(z) = & C_A C_F \left\{ \left( \frac{7\zeta_3}{2} - \frac{101}{27} \right) \left( \frac{1}{1-z} \right)_+ + \left( \frac{59\zeta_3}{18} - \frac{1535}{192} + \frac{215\pi^2}{216} - \frac{\pi^4}{240} \right) \delta(1-z) \right. \\
& + \frac{1+z^2}{1-z} \left( -\frac{\text{Li}_3(1-z)}{2} + \text{Li}_3(z) - \frac{\text{Li}_2(z)\log(z)}{2} - \frac{1}{2}\text{Li}_2(z)\log(1-z) \right. \\
& - \frac{1}{24}\log^3(z) - \frac{1}{2}\log^2(1-z)\log(z) + \frac{1}{12}\pi^2\log(1-z) - \frac{\pi^2}{8} \Big) \\
& + \frac{1}{1-z} \left( -\frac{1}{4}(11-3z^2)\zeta_3 - \frac{1}{48}(-z^2+12z+11)\log^2(z) \right. \\
& - \frac{1}{36}(83z^2-36z+29)\log(z) + \frac{\pi^2 z}{4} \Big) \\
& + (1-z) \left( \frac{\text{Li}_2(z)}{2} + \frac{1}{2}\log(1-z)\log(z) \right) + \frac{z+100}{27} + \frac{1}{4}z\log(1-z) \Big\} \\
& + C_F n_F \left\{ \frac{14}{27} \left( \frac{1}{1-z} \right)_+ + \frac{1}{864} (192\zeta_3 + 1143 - 152\pi^2) \delta(1-z) \right. \\
& + \frac{(1+z^2)}{72(1-z)} \log(z)(3\log(z)+10) + \frac{1}{108}(-19z-37) \Big\} \\
& + C_F^2 \left\{ \frac{1}{4} \left( -15\zeta_3 + \frac{511}{16} - \frac{67\pi^2}{12} + \frac{17\pi^4}{45} \right) \delta(1-z) \right. \\
& + \frac{1+z^2}{1-z} \left( \frac{\text{Li}_3(1-z)}{2} - \frac{5\text{Li}_3(z)}{2} + \frac{1}{2}\text{Li}_2(z)\log(1-z) + \frac{3\text{Li}_2(z)\log(z)}{2} \right. \\
& + \frac{3}{4}\log(z)\log^2(1-z) + \frac{1}{4}\log^2(z)\log(1-z) - \frac{1}{12}\pi^2\log(1-z) + \frac{5\zeta_3}{2} \Big) \\
& + (1-z) \left( -\text{Li}_2(z) - \frac{3}{2}\log(1-z)\log(z) + \frac{2\pi^2}{3} - \frac{29}{4} \right) + \frac{1}{24}(1+z)\log^3(z) \\
& + \frac{1}{1-z} \left( \frac{1}{8}(-2z^2+2z+3)\log^2(z) + \frac{1}{4}(17z^2-13z+4)\log(z) \right. \\
& \left. - \frac{z}{4}\log(1-z) \right\} \\
& + C_F \left\{ \frac{1}{z}(1-z)(2z^2-z+2) \left( \frac{\text{Li}_2(z)}{6} + \frac{1}{6}\log(1-z)\log(z) - \frac{\pi^2}{36} \right) \right. \\
& + \frac{1}{216z}(1-z)(136z^2-143z+172) - \frac{1}{48}(8z^2+3z+3)\log^2(z) \\
& \left. + \frac{1}{36}(32z^2-30z+21)\log(z) + \frac{1}{24}(1+z)\log^3(z) \right\}, \tag{F.25}
\end{aligned}$$

$$\begin{aligned}
\mathcal{H}_{q\bar{q}\leftarrow q\bar{q}'}^{DY(2)}(z) = C_F \left\{ \frac{1}{12z}(1-z)(2z^2-z+2) \left( \text{Li}_2(z) + \log(1-z)\log(z) - \frac{\pi^2}{6} \right) \right. \\
+ \frac{1}{432z}(1-z)(136z^2-143z+172) + \frac{1}{48}(1+z)\log^3(z) \\
\left. - \frac{1}{96}(8z^2+3z+3)\log^2(z) + \frac{1}{72}(32z^2-30z+21)\log(z) \right\}, \quad (\text{F.26})
\end{aligned}$$

$$\begin{aligned}
\mathcal{H}_{q\bar{q}\leftarrow q\bar{q}}^{DY(2)}(z) = C_F \left( C_F - \frac{1}{2}C_A \right) \left\{ \frac{1+z^2}{1+z} \left( \frac{3\text{Li}_3(-z)}{2} + \text{Li}_3(z) + \text{Li}_3\left(\frac{1}{1+z}\right) - \frac{\text{Li}_2(-z)\log(z)}{2} \right. \right. \\
- \frac{\text{Li}_2(z)\log(z)}{2} - \frac{1}{24}\log^3(z) - \frac{1}{6}\log^3(1+z) + \frac{1}{4}\log(1+z)\log^2(z) \\
+ \frac{\pi^2}{12}\log(1+z) - \frac{3\zeta_3}{4} \left. \right) + (1-z) \left( \frac{\text{Li}_2(z)}{2} + \frac{1}{2}\log(1-z)\log(z) + \frac{15}{8} \right) \\
- \frac{1}{2}(1+z)(\text{Li}_2(-z) + \log(z)\log(1+z)) + \frac{\pi^2}{24}(z-3) + \frac{1}{8}(11z+3)\log(z) \left. \right\} \\
+ C_F \left\{ \frac{1}{12z}(1-z)(2z^2-z+2) \left( \text{Li}_2(z) + \log(1-z)\log(z) - \frac{\pi^2}{6} \right) \right. \\
+ \frac{1}{432z}(1-z)(136z^2-143z+172) - \frac{1}{96}(8z^2+3z+3)\log^2(z) \\
\left. + \frac{1}{72}(32z^2-30z+21)\log(z) + \frac{1}{48}(1+z)\log^3(z) \right\}, \quad (\text{F.27})
\end{aligned}$$

$$\mathcal{H}_{q\bar{q}\leftarrow q\bar{q}'}^{DY(2)}(z) = \mathcal{H}_{q\bar{q}\leftarrow q\bar{q}}^{DY(2)}(z), \quad (\text{F.28})$$

$$\begin{aligned}
\mathcal{H}_{q\bar{q}\leftarrow qg}^{DY(2)}(z) = & C_A \left\{ -\frac{1}{12z}(1-z) \left( 11z^2 - z + 2 \right) \text{Li}_2(1-z) \right. \\
& + \left( 2z^2 - 2z + 1 \right) \left( \frac{\text{Li}_3(1-z)}{8} - \frac{1}{8} \text{Li}_2(1-z) \log(1-z) + \frac{1}{48} \log^3(1-z) \right) \\
& + \left( 2z^2 + 2z + 1 \right) \left( \frac{3\text{Li}_3(-z)}{8} + \frac{\text{Li}_3\left(\frac{1}{1+z}\right)}{4} - \frac{\text{Li}_2(-z) \log(z)}{8} - \frac{1}{24} \log^3(1+z) \right. \\
& + \left. \frac{1}{16} \log^2(z) \log(1+z) + \frac{1}{48} \pi^2 \log(1+z) \right) + \frac{1}{4} z(1+z) \text{Li}_2(-z) + z \text{Li}_3(z) \\
& - \frac{1}{2} z \text{Li}_2(1-z) \log(z) - z \text{Li}_2(z) \log(z) - \frac{3}{8} \left( 2z^2 + 1 \right) \zeta_3 - \frac{149z^2}{216} \\
& - \frac{1}{96} \left( 44z^2 - 12z + 3 \right) \log^2(z) + \frac{1}{72} \left( 68z^2 + 6\pi^2 z - 30z + 21 \right) \log(z) \\
& + \frac{\pi^2 z}{24} + \frac{43z}{48} + \frac{43}{108z} + \frac{1}{48} (2z+1) \log^3(z) - \frac{1}{2} z \log(1-z) \log^2(z) \\
& - \frac{1}{8} (1-z) z \log^2(1-z) + \frac{1}{4} z(1+z) \log(1+z) \log(z) \\
& + \left. \frac{1}{16} (3-4z) z \log(1-z) - \frac{35}{48} \right\} \\
& + C_F \left\{ \left( 2z^2 - 2z + 1 \right) \left( \zeta_3 - \frac{\text{Li}_3(1-z)}{8} - \frac{\text{Li}_3(z)}{8} + \frac{1}{8} \text{Li}_2(1-z) \log(1-z) \right. \right. \\
& + \left. \frac{\text{Li}_2(z) \log(z)}{8} - \frac{1}{48} \log^3(1-z) + \frac{1}{16} \log(z) \log^2(1-z) \right. \\
& + \left. \frac{1}{16} \log^2(z) \log(1-z) \right) \\
& - \frac{3z^2}{8} - \frac{1}{96} \left( 4z^2 - 2z + 1 \right) \log^3(z) + \frac{1}{64} \left( -8z^2 + 12z + 1 \right) \log^2(z) \\
& + \frac{1}{32} \left( -8z^2 + 23z + 8 \right) \log(z) + \frac{5}{24} \pi^2 (1-z) z + \frac{11z}{32} + \frac{1}{8} (1-z) z \log^2(1-z) \\
& - \left. \frac{1}{4} (1-z) z \log(1-z) \log(z) - \frac{1}{16} (3-4z) z \log(1-z) - \frac{9}{32} \right\}, \quad (\text{F.29})
\end{aligned}$$

$$\mathcal{H}_{q\bar{q}\leftarrow gg}^{DY(2)}(z) = -\frac{z}{2} \left( 1-z + \frac{1}{2} (1+z) \log(z) \right), \quad (\text{F.30})$$



where  $\text{Li}_k(z)$  ( $k = 2, 3$ ) are the polylogarithm functions,

$$\text{Li}_2(z) = - \int_0^z \frac{dt}{t} \ln(1-t) \ , \quad \text{Li}_3(z) = \int_0^1 \frac{dt}{t} \ln(t) \ln(1-zt) \ , \quad (\text{F.31})$$

and the  $H$  factors are the scheme dependent resummation factors. For CSS,  $H$  is 1 to all orders, while for CFG,  $H$  has  $\alpha_s$  dependence.

## Fit to SIDIS Data

The universality of the parton distribution is a powerful prediction from QCD factorization. According to the TMD factorization, the universality of the TMD parton distributions should exist between SIDIS and Drell-Yan processes as well. Therefore, the non-perturbative functions determined for the TMD parton distributions from the Drell-Yan type of processes shall apply to that in the SIDIS. Of course, the transverse momentum distribution of hadron production in DIS processes also depends on the final state TMD fragmentation functions, which need to be determined by fitting to existing experimental data. Following the universality arguments, the following parameterizations for the non-perturbative form factors for SIDIS process can be assumed, in contrast to Eq. 3.77 for Drell-Yan process,

$$S_{NP}^{(DIS)} = \frac{g_1}{2} b^2 + g_2 \ln(b/b_*) \ln(Q/Q_0) + g_3 b^2 (x_0/x_B)^\lambda + \frac{g_h}{z_h^2} b^2 \ . \quad (\text{F.32})$$

In the above parameterization,  $g_1$  and  $g_2$  have been determined from the experimental data of Drell-Yan lepton pair production. The factor of 1/2 in front of the  $g_1$  term is due the fact that there is only one incoming hadron in the SIDIS process, while there are two incoming hadrons in the Drell-Yan process. Although there has been evidence from recent studies [242, 243] that

$g_h$  could be different for the so-called favored and dis-favored fragmentation functions, they will be taken to be the same in this study for simplicity. When more precise data become available, a global analysis with two separate  $g_h$  parameters may need to be performed.

In principle,  $g_1$ ,  $g_2$ , and  $g_h$  may be fitted to both Drell-Yan and SIDIS data simultaneously. However, the SIDIS data from HERMES and COMPASS mainly focus in the relative low  $Q^2$  range. Because of that, the theoretical uncertainty of the CSS prediction is not well under control, particularly, from the  $Y$ -term contribution. There have been several successful phenomenological studies to describe the experimental data from HERMES and COMPASS experiments, using the leading order TMD formalism [242, 244]. The goal of this paper is to check if the non-perturbative form factors determined in the Drell-Yan process can be applied to the SIDIS processes. As shown in Ref. [171], fitting both is not possible with the original BLNY or KN fit, where it was found that the extrapolation of these fits to the kinematic region of HERMES and COMPASS is in conflict with the experimental data. However, it will be shown that the SIYY form will be able to extend to SIDIS experiments from HERMES and COMPASS Collaborations.

Therefore, in the following, the parameters ( $g_{1,2}$ ) are set to the fitted values from the Drell-Yan data and compared to the SIDIS data for consistency. In Fig. F.2, the comparisons between the theory predictions with  $g_h = 0.042$  and the SIDIS data from HERMES is given, with a total  $\chi^2$  around 180. This parameter is consistent with previous analysis when the leading order TMD formalism is considered [242, 244]. It is also consistent with the TMD formalism with truncated evolution effects in Ref. [171]. The differential cross section for the SIDIS process depends on the hadron fragmentation functions, for which the parameterization from the new DSS fit [245, 246] is used here. A normalization factor about 2.0 in the calculation of the multiplicity distributions shown in Fig. F.2 is used, which

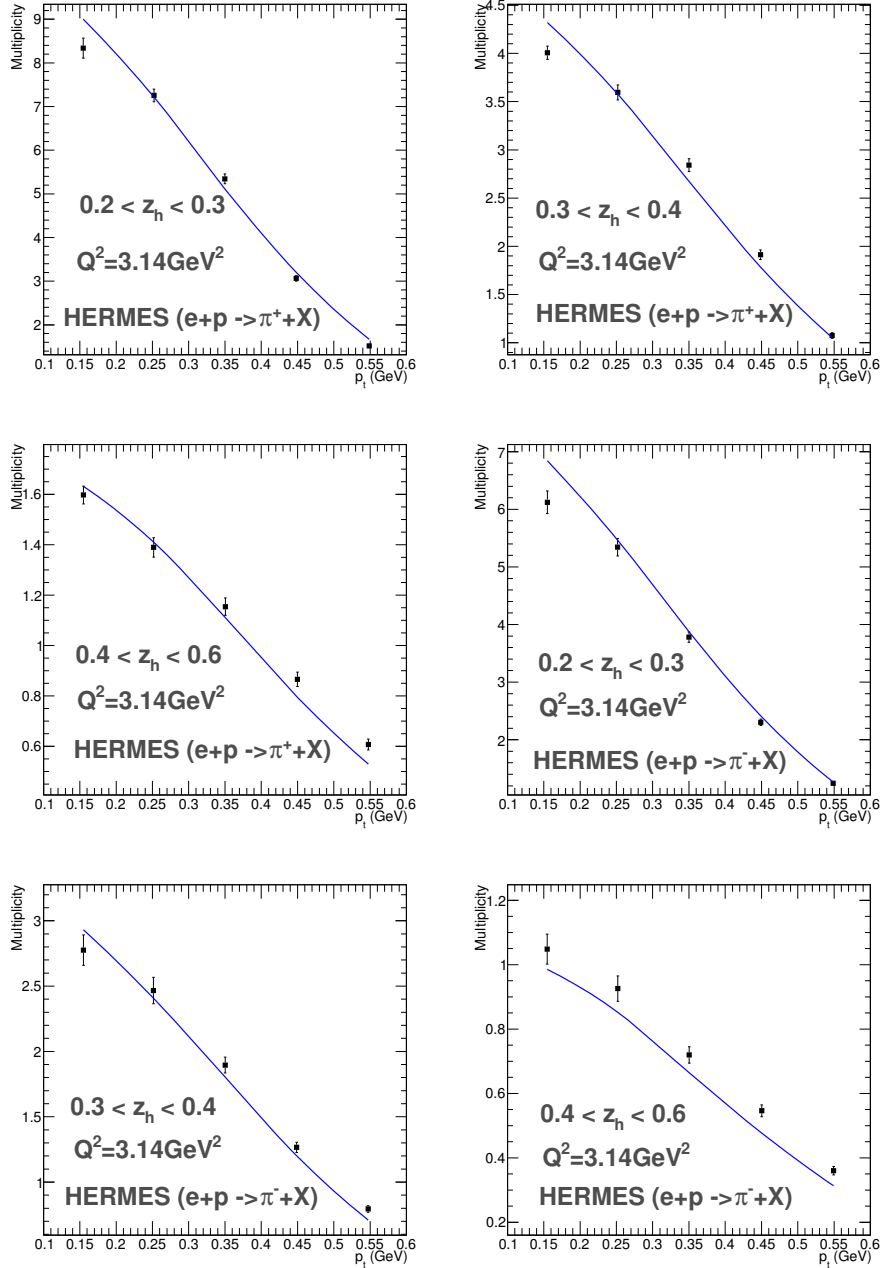


Figure F.2: Multiplicity distribution as function of transverse momentum in semi-inclusive hadron production in deep inelastic scattering compared to the experimental data from HERMES Collaboration at  $Q^2 = 3.14 \text{ GeV}^2$ .

accounts for theoretical uncertainties from higher order corrections for both differential and inclusive cross sections <sup>2</sup>. Here, the  $Y$ -term contribution is not included, for the reasons mentioned above.

The figures in Sec. 3.4.4 and Fig.F.2 clearly illustrate that the SIYY non-perturbative function is a universal non-perturbative TMD function which can be used to describe both Drell-Yan lepton pair production and semi-inclusive hadron production in DIS processes in the CSS resummation framework. Also, note that that the new functional form for the non-perturbative function is crucial to achieve this conclusion as given in Eqs. (3.77) and (F.32).

## $\alpha_s$ Expansion

The Taylor series expansion of  $\alpha_s$  around some fixed scale  $\mu_0$  is given by:

$$\frac{\alpha_s(\mu)}{\pi} = \frac{\alpha_s(\mu_0)}{\pi} + \left. \frac{\partial \frac{\alpha_s(\mu)}{\pi}}{\partial \log \mu^2} \right|_{\mu=\mu_0} \log \frac{\mu^2}{\mu_0^2} + \frac{1}{2} \left. \frac{\partial^2 \frac{\alpha_s(\mu)}{\pi}}{\partial (\log \mu^2)^2} \right|_{\mu=\mu_0} \log^2 \frac{\mu^2}{\mu_0^2} + \mathcal{O}(\alpha_s^3). \quad (\text{F.33})$$

To obtain the final result, we need to calculate the derivatives. However, the first derivative is exactly related to the  $\beta$  function for the running of the coupling,

$$\frac{\partial \frac{\alpha_s(\mu)}{\pi}}{\partial \log \mu^2} = \beta(\alpha_s(\mu)), \quad (\text{F.34})$$

---

<sup>2</sup>Compared to the leading order TMD fit of Ref. [244] where there is no normalization factor, the  $C^{(1)}$  coefficient is large and negative in the CSS resummation application to the SIDIS. Phenomenologically, that is the reason to include a factor of 2 in the comparison to the SIDIS data. This could be improved if the differential cross section (instead of multiplicity distributions) are measured in the future.

with

$$\beta(\alpha_s(\mu)) = - \sum_{k=1}^{\infty} \left( \frac{\alpha_s(\mu)}{\pi} \right)^{k+1} \beta_{k-1}. \quad (\text{F.35})$$

For the second derivative,

$$\frac{\partial^2 \frac{\alpha_s(\mu)}{\pi}}{\partial (\log \mu^2)^2} = \frac{\partial \beta(\alpha_s(\mu))}{\partial \frac{\alpha_s(\mu)}{\pi}} \beta(\alpha_s(\mu)) = -\beta(\alpha_s(\mu)) \sum_{k=1}^{\infty} (k+1) \left( \frac{\alpha_s(\mu)}{\pi} \right)^k \beta_{k-1}. \quad (\text{F.36})$$

Inputting these results into Eq. F.33, and keeping terms only up to  $\mathcal{O}(\alpha_s^3)$ , the expansion of  $\alpha_s$  is:

$$\frac{\alpha_s(\mu)}{\pi} = \frac{\alpha_s(\mu_0)}{\pi} \left( 1 - \frac{\alpha_s(\mu_0)}{\pi} \beta_0 \log \frac{\mu^2}{\mu_0^2} + \left( \frac{\alpha_s(\mu_0)}{\pi} \right)^2 \left( \beta_0^2 \log^2 \frac{\mu^2}{\mu_0^2} - \beta_1 \log \frac{\mu^2}{\mu_0^2} \right) + \mathcal{O}(\alpha_s^3) \right). \quad (\text{F.37})$$

## PDF Expansion

The Taylor series expansion of the parton distribution function around some fixed scale  $\mu_F$  is given by:

$$f_i(x, \mu) = f_i(x, \mu_F) + \frac{\partial f_i(x, \mu)}{\partial \log \mu^2} \Big|_{\mu=\mu_F} \log \frac{\mu^2}{\mu_0^2} + \frac{1}{2} \frac{\partial^2 f_i(x, \mu)}{\partial (\log \mu^2)^2} \Big|_{\mu=\mu_F} \log^2 \frac{\mu^2}{\mu_F^2} + \frac{1}{6} \frac{\partial^3 f_i(x, \mu)}{\partial (\log \mu^2)^3} \Big|_{\mu=\mu_F} \log^3 \frac{\mu^2}{\mu_F^2} + \mathcal{O}(\alpha_s^4). \quad (\text{F.38})$$

To obtain the final result, the derivatives need to be calculated. However, the first derivative is exactly related to the DGLAP evolution equations,

$$\begin{aligned} \frac{\partial f_i(x, \mu)}{\partial \log \mu^2} &= \frac{\alpha_s(\mu)}{2\pi} P^{(1)} \otimes f_i(x, \mu) \\ &+ \left( \frac{\alpha_s(\mu)}{2\pi} \right)^2 P^{(2)} \otimes f_i(x, \mu) + \left( \frac{\alpha_s(\mu)}{2\pi} \right)^3 P^{(3)} \otimes f_i(x, \mu) + \mathcal{O}(\alpha_s^4), \end{aligned} \quad (\text{F.39})$$

When calculating the second derivative, it is also necessary to expand  $\alpha_s(\mu)$  around  $\mu_R$  as shown in the previous section. Only up to  $\mathcal{O}(\alpha_s^3)$  will be kept to keep the equations short. The second derivative is given as,

$$\begin{aligned} \frac{\partial^2 f_i(x, \mu)}{\partial (\log \mu^2)^2} &= \left( \frac{\alpha_s}{\pi} \right)^2 \left( \frac{1}{4} P^{(1)} \otimes P^{(1)} \otimes f(\mu) - \frac{1}{2} \beta_0 P^{(1)} \otimes f(\mu) \right) \\ &+ \left( \frac{\alpha_s}{\pi} \right)^3 \left( \frac{1}{8} P^{(1)} \otimes P^{(2)} \otimes f(\mu) + \frac{1}{8} P^{(2)} \otimes P^{(1)} \otimes f(\mu) + \beta_0^2 \ln \frac{\mu^2}{\mu_R^2} P^{(1)} \otimes f(\mu) \right. \\ &\left. - \frac{1}{2} \beta_0 \ln \frac{\mu^2}{\mu_R^2} P^{(1)} \otimes P^{(1)} \otimes f(\mu) - \frac{1}{2} \beta_1 P^{(1)} \otimes f(\mu) - \frac{1}{2} \beta_0 P^{(2)} \otimes f(\mu) \right) + \mathcal{O}(\alpha_s^4), \end{aligned} \quad (\text{F.40})$$

and the third derivative is given as,

$$\begin{aligned} \frac{\partial^3 f_i(x, \mu)}{\partial (\log \mu^2)^3} &= \left( \frac{\alpha_s}{\pi} \right)^3 \left( \beta_0^2 P^{(1)} \otimes f(\mu) - \frac{3}{4} \beta_0 P^{(1)} \otimes P^{(1)} \otimes f(\mu) \right. \\ &\left. + \frac{1}{8} P^{(1)} \otimes P^{(1)} \otimes P^{(1)} \otimes f(\mu) \right) + \mathcal{O}(\alpha_s^4). \end{aligned} \quad (\text{F.41})$$

Inputting these results into Eq. F.38, and keeping terms only up to  $\mathcal{O}(\alpha_s^3)$ , the expansion of

the PDF is:

$$\begin{aligned}
f(\mu) = & f(\mu_F) + \frac{1}{2} \frac{\alpha_s(\mu_R)}{\pi} \ln \frac{\mu^2}{\mu_F^2} P^{(1)} \otimes f(\mu_F) \\
& + \left( \frac{\alpha_s(\mu_R)}{\pi} \right)^2 \left( -\frac{1}{2} \beta_0 \ln \frac{\mu^2}{\mu_F^2} \ln \frac{\mu_F^2}{\mu_R^2} P^{(1)} \otimes f(\mu_F) - \frac{1}{4} \beta_0 \ln^2 \frac{\mu^2}{\mu_F^2} P^{(1)} \otimes f(\mu_F) \right. \\
& \left. + \frac{1}{8} \ln^2 \frac{\mu^2}{\mu_F^2} P^{(1)} \otimes P^{(1)} \otimes f(\mu_F) + \frac{1}{4} \ln \frac{\mu^2}{\mu_F^2} P^{(2)} \otimes f(\mu_F) \right) \\
& + \left( \frac{\alpha_s(\mu_R)}{\pi} \right)^3 \left( \frac{1}{16} \ln^2 \frac{\mu^2}{\mu_F^2} P^{(1)} \otimes P^{(2)} \otimes f(\mu_F) + \frac{1}{16} \ln^2 \frac{\mu^2}{\mu_F^2} P^{(2)} \otimes P^{(1)} \otimes f(\mu_F) \right. \\
& + \frac{1}{2} \beta_0^2 \ln^2 \frac{\mu^2}{\mu_F^2} \ln \frac{\mu_F^2}{\mu_R^2} P^{(1)} \otimes f(\mu_F) + \frac{1}{2} \beta_0^2 \ln \frac{\mu^2}{\mu_F^2} \ln^2 \frac{\mu_F^2}{\mu_R^2} P^{(1)} \otimes f(\mu_F) \\
& - \frac{1}{4} \beta_0 \ln^2 \frac{\mu^2}{\mu_F^2} \ln \frac{\mu_F^2}{\mu_R^2} P^{(1)} \otimes P^{(1)} \otimes f(\mu_F) - \frac{1}{2} \beta_1 \ln \frac{\mu^2}{\mu_F^2} \ln \frac{\mu_F^2}{\mu_R^2} P^{(1)} \otimes f(\mu_F) \\
& + \frac{1}{6} \beta_0^2 \ln^3 \frac{\mu^2}{\mu_F^2} P^{(1)} \otimes f(\mu_F) - \frac{1}{8} \beta_0 \ln^3 \frac{\mu^2}{\mu_F^2} P^{(1)} \otimes P^{(1)} \otimes f(\mu_F) - \frac{1}{4} \beta_1 \ln^2 \frac{\mu^2}{\mu_F^2} P^{(1)} \otimes f(\mu_F) \\
& + \frac{1}{48} \ln^3 \frac{\mu^2}{\mu_F^2} P^{(1)} \otimes P^{(1)} \otimes P^{(1)} \otimes f(\mu_F) - \frac{1}{2} \beta_0 \ln \frac{\mu^2}{\mu_F^2} \ln \frac{\mu_F^2}{\mu_R^2} P^{(2)} \otimes f(\mu_F) \\
& \left. - \frac{1}{4} \beta_0 \ln^2 \frac{\mu^2}{\mu_F^2} P^{(2)} \otimes f(\mu_F) + \frac{1}{8} \ln \frac{\mu^2}{\mu_F^2} P^{(3)} \otimes f(\mu_F) \right) + \mathcal{O}(\alpha_s^4). \tag{F.42}
\end{aligned}$$

## $\mathcal{O}(\alpha_s^3)$ Asymptotic Piece

Continuing on to  $\mathcal{O}(\alpha_s^3)$ , the calculations become extremely complex. The asymptotic piece can be given by:

$$\begin{aligned}
{}_3C_5^{(i,j)} &= \frac{1}{4} \left( A^{(1)} \right)^3 f_i f_j, \\
{}_3C_4^{(i,j)} &= \left( A^{(1)} \right)^2 \left( \frac{5}{4} B^{(1)} f_i f_j - \frac{5}{3} \beta_0 f_i f_j + \frac{5}{8} f_i P^{(1)} \otimes f_j + \frac{5}{8} A^{(2(1)} f_j P^{(1)} \otimes f_i \right), \\
{}_3C_3^{(i,j)} &= A^{(1)} \left( \left( \left( B^{(1)} \right)^2 - \frac{7}{3} \beta_0 B^{(1)} - A^{(2)} + \beta_0^2 \right) f_i f_j + 2B^{(1)} f_j P^{(1)} \otimes f_i - \frac{7}{3} \beta_0 f_j P^{(1)} \otimes f_i \right. \\
&\quad \left. + \frac{1}{2} P^{(1)} \otimes f_i P^{(1)} \otimes f_j + \frac{1}{2} f_j P^{(1)} \otimes P^{(1)} \otimes f_i \right) \\
&\quad - \left( A^{(1)} \right)^2 \left( f_j C^{(1)} \otimes f_i - \frac{1}{2} f_j P^{(1)} \otimes f_i \log \left( \frac{Q^2}{\mu_F^2} \right) - \beta_0 f_i f_j \log \left( \frac{Q^2}{\mu_R^2} \right) \right) + i \leftrightarrow j, \\
{}_3C_2^{(i,j)} &= \left( 2\beta_0 A^{(2)} + B^{(1)} \left( \beta_0^2 - \frac{3}{2} A^{(2)} \right) + A^{(1)} \left( -\frac{3}{2} B^{(2)} + \beta_1 - 2\beta_0^2 \log \left( \frac{Q^2}{\mu_R^2} \right) \right) \right. \\
&\quad \left. + 3\beta_0 B^{(1)} \log \left( \frac{Q^2}{\mu_R^2} \right) \right) \\
&\quad - 5 \left( A^{(1)} \right)^3 \zeta_3 + \frac{1}{2} \left( B^{(1)} \right)^3 - \frac{3}{2} \beta_0 \left( B^{(1)} \right)^2 \right) f_i f_j - \frac{3}{2} A^{(2)} f_j P^{(1)} \otimes f_i \\
&\quad + A^{(1)} \left( 5\beta_0 f_j C^{(1)} \otimes f_i + B^{(1)} \left( -3f_j C^{(1)} \otimes f_i - \frac{3}{2} f_j P^{(1)} \otimes f_i \log \left( \frac{Q^2}{\mu_F^2} \right) \right) \right) \\
&\quad - \frac{3}{2} C^{(1)} \otimes f_i P^{(1)} \otimes f_j - \frac{3}{2} f_j C^{(1)} \otimes P^{(1)} \otimes f_i + \beta_0 f_j P^{(1)} \otimes f_i \log \left( \frac{Q^2}{\mu_F^2} \right) \\
&\quad - \frac{3}{4} P^{(1)} \otimes f_i P^{(1)} \otimes f_j \log \left( \frac{Q^2}{\mu_F^2} \right) - \frac{3}{4} P^{(1)} \otimes P^{(1)} \otimes f_i f_j \log \left( \frac{Q^2}{\mu_F^2} \right) \\
&\quad + 3\beta_0 f_j P^{(1)} \otimes f_i \log \left( \frac{Q^2}{\mu_R^2} \right) - \frac{3}{4} f_j P^{(2)} \otimes f_i \right) \\
&\quad + \beta_0^2 f_j P^{(1)} \otimes f_i - \frac{3}{4} \beta_0 P^{(1)} \otimes f_i P^{(1)} \otimes f_j - \frac{3}{4} \beta_0 f_j P^{(1)} \otimes P^{(1)} \otimes f_i \\
&\quad + \frac{3}{2} \left( B^{(1)} \right)^2 f_j P^{(1)} \otimes f_i \\
&\quad + B^{(1)} \left( -3\beta_0 f_j P^{(1)} \otimes f_i + \frac{3}{4} P^{(1)} \otimes f_i P^{(1)} \otimes f_j + \frac{3}{4} f_j P^{(1)} \otimes P^{(1)} \otimes f_i \right)
\end{aligned}$$



$$+ \frac{3}{8}P^{(1)} \otimes P^{(1)} \otimes f_i P^{(1)} \otimes f_j + \frac{1}{8}f_j P^{(1)} \otimes P^{(1)} \otimes P^{(1)} \otimes f_i$$

$$+ i \leftrightarrow j,$$

$$\begin{aligned} {}_3C_1^{(i,j)} &= \left( -2\beta_0 A^{(2)} \log \left( \frac{Q^2}{\mu_R^2} \right) + A^{(3)} - 2B^{(1)}B^{(2)} + 2B^{(2)}\beta_0 + 2 \left( B^{(1)} \right)^2 \beta_0 \log \left( \frac{Q^2}{\mu_R^2} \right) \right. \\ &+ B^{(1)} \left( \beta_1 - 2\beta_0^2 \log \left( \frac{Q^2}{\mu_R^2} \right) \right) + A^{(1)} \left( \beta_0^2 \log \left( \frac{Q^2}{\mu_R^2} \right) - \beta_1 \log \left( \frac{Q^2}{\mu_R^2} \right) \right) \\ &+ \left( A^{(1)} \right)^2 \left( \frac{40}{3}\beta_0 - 10B^{(1)} \right) \zeta_3 \Big) f_i f_j + A^{(2)} \left( 2f_j C^{(1)} \otimes f_i + f_j P^{(1)} \otimes f_i \log \left( \frac{Q^2}{\mu_F^2} \right) \right) \\ &- 4\beta_0^2 f_j C^{(1)} \otimes f_i - 2\beta_0^2 f_j P^{(1)} \otimes f_i \log \left( \frac{Q^2}{\mu_R^2} \right) - \frac{1}{2}P^{(2)} \otimes f_i P^{(1)} \otimes f_j \\ &- C^{(1)} \otimes P^{(1)} \otimes f_i P^{(1)} \otimes f_j - \frac{1}{2}C^{(1)} \otimes f_i P^{(1)} \otimes P^{(1)} \otimes f_j \\ &- \frac{3}{4}P^{(1)} \otimes P^{(1)} \otimes f_i P^{(1)} \otimes f_j \log \left( \frac{Q^2}{\mu_F^2} \right) - 2B^{(2)}f_j P^{(1)} \otimes f_i - \frac{1}{4}f_j P^{(1)} \otimes P^{(2)} \otimes f_i \\ &- \frac{1}{4}f_j P^{(2)} \otimes P^{(1)} \otimes f_i - \frac{1}{2}f_j C^{(1)} \otimes P^{(1)} \otimes P^{(1)} \otimes f_i \\ &- \frac{1}{4}f_j P^{(1)} \otimes P^{(1)} \otimes P^{(1)} \otimes f_i \log \left( \frac{Q^2}{\mu_F^2} \right) \\ &+ \left( B^{(1)} \right)^2 \left( -2f_j C^{(1)} \otimes f_i - f_j P^{(1)} \otimes f_i \log \left( \frac{Q^2}{\mu_F^2} \right) \right) \\ &+ 3\beta_0 C^{(1)} \otimes f_i P^{(1)} \otimes f_j + \frac{1}{2}\beta_0 P^{(1)} \otimes f_i P^{(1)} \otimes f_j \left( \log \left( \frac{Q^2}{\mu_F^2} \right) + 2 \log \left( \frac{Q^2}{\mu_R^2} \right) \right) \\ &+ \beta_0 f_j P^{(2)} \otimes f_i + 3f_j C^{(1)} \otimes P^{(1)} \otimes f_i + \frac{1}{2}\beta_0 f_j P^{(1)} \otimes P^{(1)} \otimes f_i \log \left( \frac{Q^2}{\mu_F^2} \right) \\ &+ \beta_0 f_j P^{(1)} \otimes P^{(1)} \otimes f_i \log \left( \frac{Q^2}{\mu_R^2} \right) \end{aligned}$$

$$\begin{aligned}
& + B^{(1)} \left( -2C^{(1)} \otimes f_i P^{(1)} \otimes f_j - P^{(1)} \otimes f_i P^{(1)} \otimes f_j \log \left( \frac{Q^2}{\mu_F^2} \right) \right. \\
& + \beta_0 f_j P^{(1)} \otimes f_i \log \left( \frac{Q^2}{\mu_F^2} \right) \\
& + 4\beta_0 f_j P^{(1)} \otimes f_i \log \left( \frac{Q^2}{\mu_R^2} \right) - f_j P^{(2)} \otimes f_i - 2f_j C^{(1)} \otimes P^{(1)} \otimes f_i \\
& - f_j P^{(1)} \otimes P^{(1)} \otimes f_i \log \left( \frac{Q^2}{\mu_F^2} \right) \\
& + 6\beta_0 f_j C^{(1)} \otimes f_i + \beta_0 f_j P^{(1)} \otimes f_i \left( \log \left( \frac{Q^2}{\mu_F^2} \right) + 4 \log \left( \frac{Q^2}{\mu_R^2} \right) \right) \\
& + A^{(1)} \left( \frac{1}{4} P^{(1)} \otimes f_i P^{(1)} \otimes f_j \log^2 \left( \frac{Q^2}{\mu_F^2} \right) + \frac{1}{4} f_j P^{(1)} \otimes P^{(1)} \otimes f_i \log^2 \left( \frac{Q^2}{\mu_F^2} \right) \right. \\
& + \frac{1}{2} \beta_0 f_j P^{(1)} \otimes f_i \log^2 \left( \frac{Q^2}{\mu_F^2} \right) + C^{(1)} \otimes f_i P^{(1)} \otimes f_j \log \left( \frac{Q^2}{\mu_F^2} \right) \\
& + \frac{1}{2} f_j P^{(2)} \otimes f_i \log \left( \frac{Q^2}{\mu_F^2} \right) \\
& + f_j C^{(1)} \otimes P^{(1)} \otimes f_i \log \left( \frac{Q^2}{\mu_F^2} \right) - 2\beta_0 f_j P^{(1)} \otimes f_i \log \left( \frac{Q^2}{\mu_F^2} \right) \log \left( \frac{Q^2}{\mu_R^2} \right) \\
& + C^{(1)} \otimes f_i C^{(1)} \otimes f_j + 2f_j C^{(2)} \otimes f_i - 4\beta_0 f_j C^{(1)} \otimes f_i \log \left( \frac{Q^2}{\mu_R^2} \right) \\
& + \beta_1 f_j P^{(1)} \otimes f_i - 10 \left( A^{(1)} \right)^2 \zeta_3 f_j P^{(1)} \otimes f_i \\
& + i \leftrightarrow j,
\end{aligned}$$

$$\begin{aligned}
{}_3C_0^{(i,j)} & = 2C^{(1)} \otimes f_j f_i B^{(2)} + P^{(1)} \otimes f_j \log \left( \frac{Q^2}{\mu_F^2} \right) f_i B^{(2)} + 2C^{(1)} \otimes f_i f_j B^{(2)} \\
& + P^{(1)} \otimes f_i \log \left( \frac{Q^2}{\mu_F^2} \right) f_j B^{(2)} + \frac{3}{8} P^{(1)} \otimes f_j P^{(1)} \otimes P^{(1)} \otimes f_i \log^2 \left( \frac{Q^2}{\mu_F^2} \right) \\
& + \frac{3}{8} P^{(1)} \otimes f_i P^{(1)} \otimes P^{(1)} \otimes f_j \log^2 \left( \frac{Q^2}{\mu_F^2} \right) + P^{(1)} \otimes f_j \log^2 \left( \frac{Q^2}{\mu_R^2} \right) f_i \beta_0^2 \\
& + 4C^{(1)} \otimes f_j \log \left( \frac{Q^2}{\mu_R^2} \right) f_i \beta_0^2 + P^{(1)} \otimes f_i \log^2 \left( \frac{Q^2}{\mu_R^2} \right) f_j \beta_0^2
\end{aligned}$$

$$\begin{aligned}
& + 4C^{(1)} \otimes f_i \log \left( \frac{Q^2}{\mu_R^2} \right) f_j \beta_0^2 + C^{(2)} \otimes f_j P^{(1)} \otimes f_i + C^{(2)} \otimes f_i P^{(1)} \otimes f_j \\
& + \frac{1}{2} C^{(1)} \otimes f_j P^{(2)} \otimes f_i + \frac{1}{2} C^{(1)} \otimes f_i P^{(2)} \otimes f_j \\
& + C^{(1)} \otimes f_j C^{(1)} \otimes P^{(1)} \otimes f_i + C^{(1)} \otimes f_i C^{(1)} \otimes P^{(1)} \otimes f_j \\
& + \frac{1}{2} P^{(1)} \otimes f_j P^{(2)} \otimes f_i \log \left( \frac{Q^2}{\mu_F^2} \right) + \frac{1}{2} P^{(1)} \otimes f_i P^{(2)} \otimes f_j \log \left( \frac{Q^2}{\mu_F^2} \right) \\
& + P^{(1)} \otimes f_j C^{(1)} \otimes P^{(1)} \otimes f_i \log \left( \frac{Q^2}{\mu_F^2} \right) + P^{(1)} \otimes f_i C^{(1)} \otimes P^{(1)} \otimes f_j \log \left( \frac{Q^2}{\mu_F^2} \right) \\
& + \frac{1}{2} C^{(1)} \otimes f_j P^{(1)} \otimes P^{(1)} \otimes f_i \log \left( \frac{Q^2}{\mu_F^2} \right) + \frac{1}{2} C^{(1)} \otimes f_i P^{(1)} \otimes P^{(1)} \otimes f_j \log \left( \frac{Q^2}{\mu_F^2} \right) \\
& + \frac{1}{8} P^{(1)} \otimes P^{(1)} \otimes P^{(1)} \otimes f_j \log^2 \left( \frac{Q^2}{\mu_F^2} \right) f_i - 2\beta_1 C^{(1)} \otimes f_j f_i \\
& + \frac{1}{4} P^{(3)} \otimes f_j f_i + \frac{1}{2} C^{(1)} \otimes P^{(2)} \otimes f_j f_i + C^{(2)} \otimes P^{(1)} \otimes f_j f_i \\
& + \frac{1}{4} P^{(1)} \otimes P^{(2)} \otimes f_j \log \left( \frac{Q^2}{\mu_F^2} \right) f_i + \frac{1}{4} P^{(2)} \otimes P^{(1)} \otimes f_j \log \left( \frac{Q^2}{\mu_F^2} \right) f_i \\
& + \frac{1}{2} C^{(1)} \otimes P^{(1)} \otimes P^{(1)} \otimes f_j \log \left( \frac{Q^2}{\mu_F^2} \right) f_i - \beta_1 P^{(1)} \otimes f_j \log \left( \frac{Q^2}{\mu_R^2} \right) f_i \\
& + \frac{1}{8} P^{(1)} \otimes P^{(1)} \otimes P^{(1)} \otimes f_i \log^2 \left( \frac{Q^2}{\mu_F^2} \right) f_j - 2\beta_1 C^{(1)} \otimes f_i f_j \\
& + \frac{1}{4} P^{(3)} \otimes f_i f_j + \frac{1}{2} C^{(1)} \otimes P^{(2)} \otimes f_i f_j \\
& + C^{(2)} \otimes P^{(1)} \otimes f_i f_j + \frac{1}{4} P^{(1)} \otimes P^{(2)} \otimes f_i \log \left( \frac{Q^2}{\mu_F^2} \right) f_j + \frac{1}{4} P^{(2)} \otimes P^{(1)} \otimes f_i \log \left( \frac{Q^2}{\mu_F^2} \right) f_j \\
& + \frac{1}{2} C^{(1)} \otimes P^{(1)} \otimes P^{(1)} \otimes f_i \log \left( \frac{Q^2}{\mu_F^2} \right) f_j - \beta_1 P^{(1)} \otimes f_i \log \left( \frac{Q^2}{\mu_R^2} \right) f_j \\
& + \frac{1}{2} P^{(1)} \otimes f_i P^{(1)} \otimes f_j \log^2 \left( \frac{Q^2}{\mu_F^2} \right) \beta_0 - 4C^{(1)} \otimes f_i C^{(1)} \otimes f_j \beta_0 \\
& - C^{(1)} \otimes f_j P^{(1)} \otimes f_i \log \left( \frac{Q^2}{\mu_F^2} \right) \beta_0 - C^{(1)} \otimes f_i P^{(1)} \otimes f_j \log \left( \frac{Q^2}{\mu_F^2} \right) \beta_0 \\
& - 2C^{(1)} \otimes f_j P^{(1)} \otimes f_i \log \left( \frac{Q^2}{\mu_R^2} \right) \beta_0 - 2C^{(1)} \otimes f_i P^{(1)} \otimes f_j \log \left( \frac{Q^2}{\mu_R^2} \right) \beta_0
\end{aligned}$$

$$\begin{aligned}
& -2P^{(1)} \otimes f_i P^{(1)} \otimes f_j \log \left( \frac{Q^2}{\mu_F^2} \right) \log \left( \frac{Q^2}{\mu_R^2} \right) \beta_0 \\
& + \frac{1}{4} P^{(1)} \otimes P^{(1)} \otimes f_j \log^2 \left( \frac{Q^2}{\mu_F^2} \right) f_i \beta_0 - 4C^{(2)} \otimes f_j f_i \beta_0 - C^{(1)} \otimes P^{(1)} \otimes f_j \log \left( \frac{Q^2}{\mu_F^2} \right) f_i \beta_0 \\
& - P^{(2)} \otimes f_j \log \left( \frac{Q^2}{\mu_R^2} \right) f_i \beta_0 - 2C^{(1)} \otimes P^{(1)} \otimes f_j \log \left( \frac{Q^2}{\mu_R^2} \right) f_i \beta_0 \\
& - P^{(1)} \otimes P^{(1)} \otimes f_j \log \left( \frac{Q^2}{\mu_F^2} \right) \log \left( \frac{Q^2}{\mu_R^2} \right) f_i \beta_0 + \frac{1}{4} P^{(1)} \otimes P^{(1)} \otimes f_i \log^2 \left( \frac{Q^2}{\mu_F^2} \right) f_j \beta_0 \\
& - 4C^{(2)} \otimes f_i f_j \beta_0 - C^{(1)} \otimes P^{(1)} \otimes f_i \log \left( \frac{Q^2}{\mu_F^2} \right) f_j \beta_0 - P^{(2)} \otimes f_i \log \left( \frac{Q^2}{\mu_R^2} \right) f_j \beta_0 \\
& - 2C^{(1)} \otimes P^{(1)} \otimes f_i \log \left( \frac{Q^2}{\mu_R^2} \right) f_j \beta_0 - P^{(1)} \otimes P^{(1)} \otimes f_i \log \left( \frac{Q^2}{\mu_F^2} \right) \log \left( \frac{Q^2}{\mu_R^2} \right) f_j \beta_0 \\
& + \left( B^{(1)} \right) \left( \frac{1}{2} P^{(1)} \otimes f_i P^{(1)} \otimes f_j \log^2 \left( \frac{Q^2}{\mu_F^2} \right) + \frac{1}{4} P^{(1)} \otimes P^{(1)} \otimes f_j f_i \log^2 \left( \frac{Q^2}{\mu_F^2} \right) \right) \\
& + \frac{1}{4} P^{(1)} \otimes P^{(1)} \otimes f_i f_j \log^2 \left( \frac{Q^2}{\mu_F^2} \right) + \frac{1}{2} P^{(1)} \otimes f_j f_i \beta_0 \log^2 \left( \frac{Q^2}{\mu_F^2} \right) \\
& + \frac{1}{2} P^{(1)} \otimes f_i f_j \beta_0 \log^2 \left( \frac{Q^2}{\mu_F^2} \right) + \frac{1}{2} P^{(2)} \otimes f_j f_i \log \left( \frac{Q^2}{\mu_F^2} \right) \\
& + C^{(1)} \otimes f_j P^{(1)} \otimes f_i \log \left( \frac{Q^2}{\mu_F^2} \right) + C^{(1)} \otimes f_i P^{(1)} \otimes f_j \log \left( \frac{Q^2}{\mu_F^2} \right) \\
& + C^{(1)} \otimes P^{(1)} \otimes f_j f_i \log \left( \frac{Q^2}{\mu_F^2} \right) + C^{(1)} \otimes P^{(1)} \otimes f_i f_j \log \left( \frac{Q^2}{\mu_F^2} \right) \\
& + \frac{1}{2} P^{(2)} \otimes f_i f_j \log \left( \frac{Q^2}{\mu_F^2} \right) + 2C^{(1)} \otimes f_i C^{(1)} \otimes f_j \\
& - 2P^{(1)} \otimes f_j \log \left( \frac{Q^2}{\mu_R^2} \right) f_i \beta_0 \log \left( \frac{Q^2}{\mu_F^2} \right) - 2P^{(1)} \otimes f_i \log \left( \frac{Q^2}{\mu_R^2} \right) f_j \beta_0 \log \left( \frac{Q^2}{\mu_F^2} \right) \\
& + 2C^{(2)} \otimes f_j f_i + 2C^{(2)} \otimes f_i f_j - 4C^{(1)} \otimes f_j \log \left( \frac{Q^2}{\mu_R^2} \right) f_i \beta_0 - 4C^{(1)} \otimes f_i \log \left( \frac{Q^2}{\mu_R^2} \right) f_j \beta_0 \\
& + \left( A^{(1)} \right)^2 \left( 4C^{(1)} \otimes f_j \zeta(3) f_i + 2P^{(1)} \otimes f_j \log \left( \frac{Q^2}{\mu_F^2} \right) \zeta(3) f_i + 4C^{(1)} \otimes f_i f_j \zeta(3) \right) \\
& + 2P^{(1)} \otimes f_i \log \left( \frac{Q^2}{\mu_F^2} \right) f_j \zeta(3)
\end{aligned}$$

$$\begin{aligned}
& + \left( A^{(1)} \right) \left( -4P^{(1)} \otimes f_i \zeta(3) P^{(1)} \otimes f_j + \frac{28}{3} f_i \beta_0 \zeta(3) P^{(1)} \otimes f_j \right. \\
& + \left( B^{(1)} \right) \left( -8P^{(1)} \otimes f_j \zeta(3) f_i - 8P^{(1)} \otimes f_i f_j \zeta(3) \right) - 2P^{(1)} \otimes P^{(1)} \otimes f_j f_i \zeta(3) \\
& \left. - 2P^{(1)} \otimes P^{(1)} \otimes f_i f_j \zeta(3) + \frac{28}{3} P^{(1)} \otimes f_i f_j \beta_0 \zeta(3) \right) \\
& + f_i f_j \left( -4 \log \left( \frac{Q^2}{\mu_R^2} \right) \beta_0 B^{(2)} + 2B^{(3)} \right. \\
& + \left. \left( B^{(1)} \right) \left( 2 \log^2 \left( \frac{Q^2}{\mu_R^2} \right) \beta_0^2 - 2\beta_1 \log \left( \frac{Q^2}{\mu_R^2} \right) \right) + \left( A^{(1)} \right) \left( -8\zeta(3) \left( B^{(1)} \right)^2 \right. \right. \\
& + \left. \frac{56}{3} \beta_0 \zeta(3) \left( B^{(1)} \right) - 8\beta_0^2 \zeta(3) \right) - 12 \left( A^{(1)} \right)^3 \zeta(5) + 8A^{(1)+(2)} \zeta(3) \\
& \left. - 8 \left( A^{(1)} \right)^2 \log \left( \frac{Q^2}{\mu_R^2} \right) \beta_0 \zeta(3) \right),
\end{aligned}$$

Similarly, the singular piece to  $\mathcal{O}(\alpha_s^3)$  can be calculated in a similar method. However,  $C^{(3)}$  has not yet been calculated, and involves a complex three-loop calculation. Therefore, it is not possible to obtain the  $\alpha_s^3$  cross-section at this point, and there is no need for the singular piece to be calculated.

## Eikonal Approximation

### Eikonalization in the Collinear Limit

Given a collinear gluon of momentum  $l$  connecting two fermions of momentum  $p_1$  and  $p_2$ , as shown in Fig. F.3, the matrix element can be given as:

$$\mathcal{M} = \bar{v}(p_1) \gamma_\alpha \frac{(\not{p}_1 - \not{l})}{(p_1 - l)^2} \cdots \frac{(\not{p}_2 - \not{l})}{(p_2 - l)^2} \gamma^{\alpha u}(p_2), \quad (\text{F.43})$$

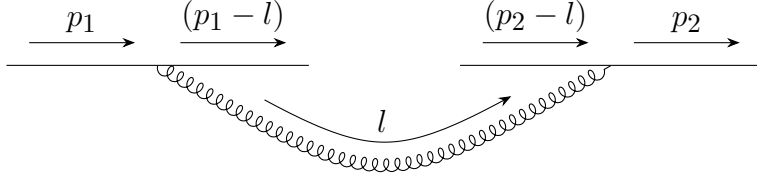


Figure F.3: Connection of a soft/collinear gluon between two colored particles.

where the dots represent any allowed processes between the two fermions. If  $l$  is collinear to  $p_2$ , then

$$(\not{p}_2 - \not{l}) \gamma^\alpha u(p_2) = (p_2 - l)^+ \gamma^- \gamma^\alpha u(p_2), \quad (\text{F.44})$$

where the coordinate system being used is the light-cone coordinates, and the  $+/-$  refers to the plus or minus component of the momentum defined as:  $p^\pm = E \pm p_z$ . Consider the  $\gamma$  matrices in the above equation. If  $\alpha = -$ , then  $\gamma^- u(p_2) = 0$  from the on-shell condition. If  $\alpha = T$ , then  $\gamma^- \gamma^T = -\gamma^T \gamma^-$  from the anti-commutation relations, and therefore also gives zero. Hence, the only non-vanishing term is for  $\alpha = +$ , giving:

$$\mathcal{M} = \bar{v}(p_1) \frac{\gamma^- (\not{p}_1 - \not{l})}{(p_1 - l)^2} \dots \frac{(p_2 - l)^+ \gamma^- \gamma^+}{(p_2 - l)^2} u(p_2). \quad (\text{F.45})$$

Using the on-shell condition and commutation relation, the part before the dots can be simplified to:

$$\bar{v}(p_1) \frac{2p_1^-}{(p_1 - l)^2}, \quad (\text{F.46})$$

and furthermore, if  $p_2 = (p^+, 0, 0)$ , and  $p_1^\alpha = p_1^+ \bar{n}^\alpha + p_1^- n_\alpha + p_1^T \underline{n}^T$ , where  $\bar{n}_\mu = (1, 0, 0)$ ,  $n_\mu = (0, 1, 0)$ , and  $\underline{n}_T = (0, 0, \underline{1})$ , then the equation can be shown to factorize, giving:

$$\bar{v}(p_1) \frac{n_\alpha}{(-n \cdot l) + i\epsilon}. \quad (\text{F.47})$$

## Eikonalization in the Soft Limit

Similar to the collinear limit, the process can be factorized if the gluon connecting the particles is soft. Again, starting from Eq. F.43, taking the limit  $l \leftarrow 0$ , gives:

$$\frac{(p_2 - l)}{(p_2 - l)^2} \gamma^\alpha u(p_2) \rightarrow \left[ \frac{p_2^\alpha}{(-p_2 \cdot l) + i\epsilon} \right]. \quad (\text{F.48})$$

Which can be calculated by using the on-shell condition, and properties of the  $\gamma$  matrices. It is important to note, that in calculations the sign of the  $\epsilon$  term is important to keep straight, and must always be positive when using this approach. Again, the final result factorizes the left-hand side of Fig. F.3 from the right-hand side.

## Fourier Transform Details

The Fourier Transform in  $d - 2$  dimensions from transverse momentum space to impact parameter space is given by:

$$\int \frac{e^{i\vec{k}_T \cdot b}}{(k_T^2)^\alpha} d^{2-2\epsilon} k_T = \left( \frac{b^2}{4\pi} \right)^{\epsilon + \alpha - 1} \pi^\alpha \frac{\Gamma(1 - \epsilon - \alpha)}{\Gamma(\alpha)}. \quad (\text{F.49})$$

To obtain the Fourier Transform for functions of the form  $\frac{1}{k_T^2} \log^n k_T^2$ , derivatives with respect to  $\alpha$  are taken of the previous equation, and then  $\alpha$  is taken to one. The derivation of the above equation can be found below, and requires the use of the following identity:

$$(k_T^2)^{-\alpha} = \frac{1}{\Gamma(\alpha)} \int_0^\infty x^{\alpha-1} e^{-xk_T^2} dx, \quad (\text{F.50})$$

using this identity, the first equation is derived as follows:

$$\begin{aligned}
\int \frac{e^{i\vec{k}_T \cdot \vec{b}}}{(k_T^2)^\alpha} d^{2-2\epsilon} k_T &= \frac{1}{\Gamma(\alpha)} \int e^{i\vec{k}_T \cdot b} d^{2-2\epsilon} k_T \int_0^\infty x^{\alpha-1} e^{-xk_T^2} dx \\
&= \frac{1}{\Gamma(\alpha)} \int_0^\infty x^{\alpha-1} dx \int d\Omega \int_0^\infty k_T^{2-2\epsilon-1} e^{ik_T b \cos(\theta) - xk_T^2} dk_T \\
&= \frac{1}{\Gamma(\alpha)} \int_0^\infty x^{\alpha-1} dx \int_0^\infty k_T^{2-2\epsilon-1} dk_T \int d\Omega_{2-2\epsilon} \sin^{-2\epsilon} \theta e^{ik_T b \cos(\theta) - xk_T^2} \\
&= \frac{1}{\Gamma(\alpha)} \int_0^\infty x^{\alpha-1} dx \int_0^\infty k_T^{2-2\epsilon-1} dk_T \frac{2\pi^{1-\epsilon}}{\Gamma(1-\epsilon)} {}_0F_1 \left( 1-\epsilon; -\frac{1}{4}b^2 k_T^2 \right) e^{-xk_T^2} \\
&= \left( \frac{b^2}{4\pi} \right)^{\epsilon+\alpha-1} \pi^\alpha \frac{\Gamma(1-\epsilon-\alpha)}{\Gamma(\alpha)},
\end{aligned}$$

where  ${}_0F_1 \left( 1-\epsilon; -\frac{1}{4}b^2 k_T^2 \right)$  is the confluent hypergeometric function. Using this relationship, we can easily derive the Fourier Transform of all the terms needed to check the asymptotic contribution up through  $\mathcal{O}(\alpha_s^3)$ . Here are a list of the results for completeness:

$$I^{(0)} = \pi \left( \frac{b^2}{4\pi} \right)^\epsilon \Gamma(-\epsilon) \quad (\text{F.51})$$

$$I^{(1)} = -\pi \left( \frac{b^2}{4\pi} \right)^\epsilon \Gamma(-\epsilon) \left( \gamma_E + \log \frac{b^2}{4} - \psi_0(-\epsilon) \right) \quad (\text{F.52})$$

$$I^{(2)} = \pi \left( \frac{b^2}{4\pi} \right)^\epsilon \Gamma(-\epsilon) \left( \left( \gamma_E + \log \frac{b^2}{4} - \psi_0(-\epsilon) \right)^2 - \frac{\pi^2}{6} + \psi_1(-\epsilon) \right) \quad (\text{F.53})$$

$$\begin{aligned}
I^{(3)} &= -\pi \left( \frac{b^2}{4\pi} \right)^\epsilon \Gamma(-\epsilon) \left( \left( \gamma_E + \log \frac{b^2}{4} - \psi_0(-\epsilon) \right)^3 - \frac{\pi^2}{2} \left( \gamma_E + \log \frac{b^2}{4} - \psi_0(-\epsilon) \right) \right. \\
&\quad \left. + 3\psi_1(-\epsilon) \left( \gamma_E + \log \frac{b^2}{4} - \psi_0(-\epsilon) \right) - 2(\psi_2(1) + \psi_2(-\epsilon)) \right) \quad (\text{F.54})
\end{aligned}$$



$$\begin{aligned}
I^{(4)} = & \pi \left( \frac{b^2}{4\pi} \right)^\epsilon \Gamma(-\epsilon) \left( \left( \gamma_E + \log \frac{b^2}{4} - \psi_0(-\epsilon) \right)^4 - \pi^2 \left( \gamma_E + \log \frac{b^2}{4} - \psi_0(-\epsilon) \right)^2 \right. \\
& - \pi^2 \psi_1(-\epsilon) + 6\psi_1(-\epsilon) \left( \gamma_E + \log \frac{b^2}{4} - \psi_0(-\epsilon) \right)^2 + \frac{\pi^4}{60} + \psi_3(-\epsilon) \\
& \left. - 4(\psi_2(1) + \psi_2(-\epsilon)) \left( \gamma_E + \log \frac{b^2}{4} - \psi_0(-\epsilon) \right) \right) \quad (\text{F.55})
\end{aligned}$$

$$\begin{aligned}
I^{(5)} = & \pi \left( \frac{b^2}{4\pi} \right)^\epsilon \Gamma(-\epsilon) \left( \left( \gamma_E + \log \frac{b^2}{4} - \psi_0(-\epsilon) \right)^5 - \frac{5\pi^2}{3} \left( \gamma_E + \log \frac{b^2}{4} - \psi_0(-\epsilon) \right)^3 \right. \\
& + 10\psi_1(-\epsilon) \left( \gamma_E + \log \frac{b^2}{4} - \psi_0(-\epsilon) \right)^3 - 10\pi^2 \left( \gamma_E + \log \frac{b^2}{4} - \psi_0(-\epsilon) \right) \psi_1(-\epsilon) \\
& - 10(\psi_2(1) + \psi_2(-\epsilon)) \left( \left( \gamma_E + \log \frac{b^2}{4} - \psi_0(-\epsilon) \right)^2 + \psi_1(-\epsilon) - \frac{\pi^2}{6} \right) \\
& + 15 \left( \frac{\pi^2}{6} + \psi_1(-\epsilon) \right)^2 \left( \gamma_E + \log \frac{b^2}{4} - \psi_0(-\epsilon) \right) \\
& - 30\zeta(4) \left( \gamma_E + \log \frac{b^2}{4} - \psi_0(-\epsilon) \right) + 5 \left( \gamma_E + \log \frac{b^2}{4} - \psi_0(-\epsilon) \right) \psi_3(-\epsilon) \\
& \left. - (\psi_4(1) + \psi_4(-\epsilon)) \right) \quad (\text{F.56})
\end{aligned}$$

where  $I^{(n)} = \int \frac{d^{2-2\epsilon} q_t}{q_t^2} \log^n(q_t^2) e^{-i\vec{q}_t \cdot \vec{b}}$ , and  $\psi_n$  is the  $n^{\text{th}}$  polygamma function defined as:

$$\psi_n(z) = \frac{d^{n+1}}{dz^{n+1}} \log(\Gamma(z)) \quad (\text{F.57})$$

# APPENDIX G

## Higgs Plus Jet Resummation

### Calculation Details

The poles for the quark-gluon channel are given for the virtual, renormalization, jet, collinear, PDF renormalization, and soft corrections as:

$$H^{(0)} \frac{\alpha_s}{2\pi} \left( \frac{24}{\epsilon} \beta_0 + C_A \left( \frac{-2}{\epsilon^2} - \frac{2}{\epsilon} \left( \ln \frac{-u}{\mu^2} - \ln \frac{-t}{\mu^2} - \ln \frac{s}{\mu^2} \right) \right) + C_F \left( -\frac{4}{\epsilon^2} - \frac{2}{\epsilon} \left( -2 \ln \frac{-u}{\mu^2} + 3 \right) \right) \right), \quad (\text{G.1})$$

$$- H^{(0)} \frac{\alpha_s}{2\pi} \frac{18}{\epsilon} 2\beta_0, \quad (\text{G.2})$$

$$H^{(0)} \frac{\alpha_s C_F}{2\pi} \left( \frac{2}{\epsilon^2} + \frac{2}{\epsilon} \left( \frac{3}{2} - \ln \frac{P_J^2 R^2}{\mu^2} \right) \right), \quad (\text{G.3})$$

$$H^{(0)} \frac{\alpha_s}{2\pi} \frac{-2}{\epsilon} (C_F \delta(\xi_2 - 1) \xi_1 P_{qq}(\xi_1) + C_A \delta(\xi_1 - 1) \xi_2 P_{gg}(\xi_2)), \quad (\text{G.4})$$

$$H^{(0)} \frac{\alpha_s}{2\pi} \left( \frac{2C_F}{\epsilon} \left( P_{qq}(\xi_1) + \frac{3}{2} \delta(xi_1 - 1) \right) + \frac{2C_A}{\epsilon} (P_{gg}(\xi_2) + 2\beta_0 \delta(xi_2 - 1)) \right), \quad (\text{G.5})$$

$$H^{(0)} \frac{\alpha_s}{2\pi} \left( 2(C_A + C_F) \left( \frac{1}{\epsilon^2} + \frac{1}{\epsilon} \ln \frac{\mu^2}{s} \right) - \frac{2}{\epsilon} \left( (C_A - C_F) \ln \frac{t}{u} + C_F \ln \frac{1}{R^2} \right) \right), \quad (\text{G.6})$$

‘respectively. Similarly, for the quark-anti-quark channel, the poles are in the same order as above, and are given as:

$$H^{(0)} \frac{\alpha_s}{2\pi} \left( 24\beta_0 \frac{1}{\epsilon} + C_A \left( \frac{-2}{\epsilon^2} - \frac{2}{\epsilon} \ln \frac{s\mu^2}{ut} \right) + C_F \left( \frac{-4}{\epsilon^2} - \frac{2}{\epsilon} \left( -2 \ln \frac{s}{\mu^2} + 3 \right) \right) \right), \quad (\text{G.7})$$

$$H^{(0)} \frac{\alpha_s}{2\pi} \left( \frac{-6C_A}{\epsilon} 2\beta_0 \right), \quad (\text{G.8})$$

$$H^{(0)} \frac{\alpha_s}{2\pi} 2C_A \left( \frac{1}{\epsilon^2} + \frac{1}{\epsilon} \left( 2\beta_0 - \ln \frac{P_T^2}{\mu^2} + \ln \frac{1}{R^2} \right) \right), \quad (\text{G.9})$$

$$H^{(0)} \frac{\alpha_s}{2\pi} \frac{-2}{\epsilon} C_F (\delta(\xi_2 - 1) \xi_1 P_{qq}(x) + \xi_1 \leftrightarrow \xi_2), \quad (\text{G.10})$$

$$H^{(0)} \frac{\alpha_s}{2\pi} \frac{2C_F}{\epsilon} \left( P_{qq}(\xi_1) \xi_1 + \frac{3}{2} \delta(\xi_1 - 1) + \xi_1 \leftrightarrow \xi_2 \right), \quad (\text{G.11})$$

$$H^{(0)} \frac{\alpha_s}{2\pi} 2 \left( C_F \left( \frac{2}{\epsilon^2} + \frac{2}{\epsilon} \ln \frac{\mu^2}{s} \right) - \frac{1}{\epsilon} C_A \ln \frac{1}{R^2} \right). \quad (\text{G.12})$$

In both of the above set of equations, all the terms are proportional to  $\delta(\xi_1 - 1)\delta(\xi_2 - 1)$  unless otherwise noted. Looking at the above equations, all of the poles cancel, leaving a finite result, and validating the results of the calculations.

## BIBLIOGRAPHY

## BIBLIOGRAPHY

- [1] M. Baak, M. Goebel, J. Haller, A. Hoecker, D. Kennedy, R. Kogler, K. Mönig, M. Schott, and J. Stelzer. The electroweak fit of the standard model after the discovery of a new boson at the lhc. *The European Physical Journal C*, 72(11):2205, Nov 2012.
- [2] A. Korytov. Experimental Methods at the LHC. In L. Dixon and et al., editors, *Journeys Through the Precision Frontier: Amplitudes for Colliders (TASI 2014)*, pages 99–181, 2016.
- [3] John M. Campbell, R. Keith Ellis, and Walter T. Giele. A Multi-Threaded Version of MCFM. *Eur. Phys. J.*, C75(6):246, 2015.
- [4] Ryan Gavin, Ye Li, Frank Petriello, and Seth Quackenbush. FEWZ 2.0: A code for hadronic Z production at next-to-next-to-leading order. *Comput. Phys. Commun.*, 182:2388–2403, 2011.
- [5] M. Baak, J. Cúth, J. Haller, A. Hoecker, R. Kogler, K. Mönig, M. Schott, and J. Stelzer. The global electroweak fit at nnlo and prospects for the lhc and ilc. *The European Physical Journal C*, 74(9):3046, 2014.
- [6] C. Patrignani et al. Review of Particle Physics. *Chin. Phys.*, C40(10):100001, 2016.
- [7] Robert Hofstadter. Electron scattering and nuclear structure. *Rev. Mod. Phys.*, 28:214–254, 1956.
- [8] S. Chekanov et al. A ZEUS next-to-leading-order QCD analysis of data on deep inelastic scattering. *Phys. Rev.*, D67:012007, 2003.
- [9] Henry W. Kendall. Deep inelastic scattering: Experiments on the proton and the observation. *Rev. Mod. Phys.*, 63:597–614, 1991.
- [10] Sayipjamal Dulat, Tie-Jiun Hou, Jun Gao, Marco Guzzi, Joey Huston, Pavel Nadolsky, Jon Pumplin, Carl Schmidt, Daniel Stump, and C. P. Yuan. New parton distribution functions from a global analysis of quantum chromodynamics. *Phys. Rev.*, D93(3):033006, 2016.

- [11] Matteo Cacciari, Gavin P. Salam, and Gregory Soyez. The Anti-k(t) jet clustering algorithm. *JHEP*, 04:063, 2008.
- [12] Siona Ruth Davis. Interactive Slice of the CMS detector. Aug 2016.
- [13] Serguei Chatrchyan et al. Identification of b-quark jets with the CMS experiment. *JINST*, 8:P04013, 2013.
- [14] B. Pasquini and P. Schweitzer. Pion transverse momentum dependent parton distributions in a light-front constituent approach, and the Boer-Mulders effect in the pion-induced Drell-Yan process. *Phys. Rev.*, D90(1):014050, 2014.
- [15] Stefano Catani, Daniel de Florian, Giancarlo Ferrera, and Massimiliano Grazzini. Vector boson production at hadron colliders: transverse-momentum resummation and leptonic decay. *JHEP*, 12:047, 2015.
- [16] A. S. Ito et al. Measurement of the Continuum of Dimuons Produced in High-Energy Proton - Nucleus Collisions. *Phys. Rev.*, D23:604–633, 1981.
- [17] G. Moreno et al. Dimuon production in proton - copper collisions at  $\sqrt{s} = 38.8$ -GeV. *Phys. Rev.*, D43:2815–2836, 1991.
- [18] D. Antreasyan et al. Production Dynamics of High Mass Muon Pairs. *Phys. Rev. Lett.*, 47:12–15, 1981.
- [19] T. Affolder et al. The transverse momentum and total cross section of  $e^+e^-$  pairs in the  $Z$  boson region from  $p\bar{p}$  collisions at  $\sqrt{s} = 1.8$  TeV. *Phys. Rev. Lett.*, 84:845–850, 2000.
- [20] B. Abbott et al. Measurement of the inclusive differential cross section for  $Z$  bosons as a function of transverse momentum in  $\bar{p}p$  collisions at  $\sqrt{s} = 1.8$  TeV. *Phys. Rev.*, D61:032004, 2000.
- [21] V. M. Abazov et al. Measurement of the shape of the boson transverse momentum distribution in  $p\bar{p} \rightarrow Z/\gamma^* \rightarrow e^+e^- + X$  events produced at  $\sqrt{s}=1.96$ -TeV. *Phys. Rev. Lett.*, 100:102002, 2008.
- [22] T. Aaltonen et al. Transverse momentum cross section of  $e^+e^-$  pairs in the  $Z$ -boson region from  $p\bar{p}$  collisions at  $\sqrt{s} = 1.96$  TeV. *Phys. Rev.*, D86:052010, 2012.

- [23] Georges Aad et al. Measurement of the transverse momentum and  $\phi_\eta^*$  distributions of Drell-Yan lepton pairs in proton-proton collisions at  $\sqrt{s} = 8$  TeV with the ATLAS detector. *Eur. Phys. J.*, C76(5):291, 2016.
- [24] A. Gehrmann-De Ridder, T. Gehrmann, E. W. N. Glover, A. Huss, and T. A. Morgan. NNLO QCD corrections for Drell-Yan  $p_T^Z$  and  $\phi^*$  observables at the LHC. *JHEP*, 11:094, 2016.
- [25] Victor Mukhamedovich Abazov et al. Precise study of the  $Z/\gamma^*$  boson transverse momentum distribution in  $p\bar{p}$  collisions using a novel technique. *Phys. Rev. Lett.*, 106:122001, 2011.
- [26] Stefano Catani, Leandro Cieri, Giancarlo Ferrera, Daniel de Florian, and Massimiliano Grazzini. Vector boson production at hadron colliders: a fully exclusive QCD calculation at NNLO. *Phys. Rev. Lett.*, 103:082001, 2009.
- [27] Georges Aad et al. Measurement of the angular coefficients in  $Z$ -boson events using electron and muon pairs from data taken at  $\sqrt{s} = 8$  TeV with the ATLAS detector. *JHEP*, 08:159, 2016.
- [28] J. R. Andersen et al. Les Houches 2015: Physics at TeV Colliders Standard Model Working Group Report. In *9th Les Houches Workshop on Physics at TeV Colliders (PhysTeV 2015) Les Houches, France, June 1-19, 2015*, 2016.
- [29] Peng Sun, C. P. Yuan, and Feng Yuan. Long Range Correlation in Higgs Boson Plus Two Jets Production at the LHC. *Phys. Lett.*, B762:47–51, 2016.
- [30] Georges Aad et al. Observation of a new particle in the search for the Standard Model Higgs boson with the ATLAS detector at the LHC. *Phys. Lett.*, B716:1–29, 2012.
- [31] Serguei Chatrchyan et al. Observation of a new boson at a mass of 125 GeV with the CMS experiment at the LHC. *Phys. Lett.*, B716:30–61, 2012.
- [32] Georges Aad et al. Combined Measurement of the Higgs Boson Mass in  $pp$  Collisions at  $\sqrt{s} = 7$  and 8 TeV with the ATLAS and CMS Experiments. *Phys. Rev. Lett.*, 114:191803, 2015.
- [33] R. P. Woodard. How Far Are We from the Quantum Theory of Gravity? *Rept. Prog. Phys.*, 72:126002, 2009.

- [34] P. Cushman et al. Working Group Report: WIMP Dark Matter Direct Detection. In *Proceedings, 2013 Community Summer Study on the Future of U.S. Particle Physics: Snowmass on the Mississippi (CSS2013): Minneapolis, MN, USA, July 29-August 6, 2013*, 2013.
- [35] Jessica Goodman, Masahiro Ibe, Arvind Rajaraman, William Shepherd, Tim M. P. Tait, and Hai-Bo Yu. Constraints on Dark Matter from Colliders. *Phys. Rev.*, D82:116010, 2010.
- [36] Jim Alexander et al. Dark Sectors 2016 Workshop: Community Report. 2016.
- [37] Alessandro Strumia and Francesco Vissani. Neutrino masses and mixings and... 2006.
- [38] Laurent Canetti, Marco Drewes, and Mikhail Shaposhnikov. Matter and Antimatter in the Universe. *New J. Phys.*, 14:095012, 2012.
- [39] Steven Weinberg. Gauge Hierarchies. *Phys. Lett.*, 82B:387–391, 1979.
- [40] Andre de Gouvea, Daniel Hernandez, and Tim M. P. Tait. Criteria for Natural Hierarchies. *Phys. Rev.*, D89(11):115005, 2014.
- [41] Michael Dine. TASI lectures on the strong CP problem. In *Flavor physics for the millennium. Proceedings, Theoretical Advanced Study Institute in elementary particle physics, TASI 2000, Boulder, USA, June 4-30, 2000*, pages 349–369, 2000.
- [42] Michael E Peskin and Daniel V Schroeder. *An Introduction to Quantum Field Theory; 1995 ed.* Westview, Boulder, CO, 1995. Includes exercises.
- [43] Emmy Noether. Invariant Variation Problems. *Gott. Nachr.*, 1918:235–257, 1918. [Transp. Theory Statist. Phys.1,186(1971)].
- [44] P. A. M. Dirac. The quantum theory of the emission and absorption of radiation. *Proceedings of the Royal Society of London A: Mathematical, Physical and Engineering Sciences*, 114(767):243–265, 1927.
- [45] W. Heisenberg and W. Pauli. On Quantum Field Theory. (In German). *Z. Phys.*, 56:1–61, 1929.
- [46] W. Heisenberg and W. Pauli. On Quantum Field Theory. 2. (In German). *Z. Phys.*, 59:168–190, 1930.



- [47] Enrico Fermi. Quantum theory of radiation. *Rev. Mod. Phys.*, 4:87–132, Jan 1932.
- [48] D. Hanneke, S. Fogwell, and G. Gabrielse. New Measurement of the Electron Magnetic Moment and the Fine Structure Constant. *Phys. Rev. Lett.*, 100:120801, 2008.
- [49] Eduardo de Rafael. Update of the Electron and Muon g-Factors. 2012. [Nucl. Phys. Proc. Suppl.234,193(2013)].
- [50] Henri Becquerel. On the rays emitted by phosphorescence. *Compt. Rend. Hebd. Seances Acad. Sci.*, 122(8):420–421, 1896.
- [51] E. Fermi. An attempt of a theory of beta radiation. 1. *Z. Phys.*, 88:161–177, 1934.
- [52] Sheldon L. Glashow and Steven Weinberg. Natural Conservation Laws for Neutral Currents. *Phys. Rev.*, D15:1958, 1977.
- [53] Abdus Salam and John Clive Ward. Electromagnetic and weak interactions. *Phys. Lett.*, 13:168–171, 1964.
- [54] Abdus Salam. Weak and Electromagnetic Interactions. *Conf. Proc.*, C680519:367–377, 1968.
- [55] F. J. Hasert et al. Observation of Neutrino Like Interactions Without Muon Or Electron in the Gargamelle Neutrino Experiment. *Phys. Lett.*, 46B:138–140, 1973.
- [56] G. Arnison et al. Experimental Observation of Isolated Large Transverse Energy Electrons with Associated Missing Energy at  $s^{**}(1/2) = 540\text{-GeV}$ . *Phys. Lett.*, 122B:103–116, 1983. [,611(1983)].
- [57] G. Arnison et al. Experimental Observation of Lepton Pairs of Invariant Mass Around  $95\text{-GeV}/c^{**2}$  at the CERN SPS Collider. *Phys. Lett.*, 126B:398–410, 1983.
- [58] P. Bagnaia et al. Evidence for  $Z^0 \rightarrow e^+ e^-$  at the CERN anti-p p Collider. *Phys. Lett.*, B129:130–140, 1983.
- [59] M. Banner et al. Observation of Single Isolated Electrons of High Transverse Momentum in Events with Missing Transverse Energy at the CERN anti-p p Collider. *Phys. Lett.*, 122B:476–485, 1983.
- [60] Gerard 't Hooft and M. J. G. Veltman. Regularization and Renormalization of Gauge Fields. *Nucl. Phys.*, B44:189–213, 1972.

- [61] Peter W. Higgs. Broken symmetries and the masses of gauge bosons. *Phys. Rev. Lett.*, 13:508–509, Oct 1964.
- [62] Yoichiro Nambu. Quasi-particles and gauge invariance in the theory of superconductivity. *Phys. Rev.*, 117:648–663, Feb 1960.
- [63] F. Englert and R. Brout. Broken symmetry and the mass of gauge vector mesons. *Phys. Rev. Lett.*, 13:321–323, Aug 1964.
- [64] G. S. Guralnik, C. R. Hagen, and T. W. B. Kibble. Global conservation laws and massless particles. *Phys. Rev. Lett.*, 13:585–587, Nov 1964.
- [65] J. Goldstone. Field theories with superconductor solutions. *Il Nuovo Cimento (1955-1965)*, 19(1):154–164, Jan 1961.
- [66] Andre de Gouvea. TASI lectures on neutrino physics. In *Physics in D  $\dot{=} 4$ . Proceedings, Theoretical Advanced Study Institute in elementary particle physics, TASI 2004, Boulder, USA, June 6-July 2, 2004*, pages 197–258, 2004.
- [67] Michael E. Peskin and Tatsu Takeuchi. Estimation of oblique electroweak corrections. *Phys. Rev. D*, 46:381–409, Jul 1992.
- [68] S. Alioli et al. Precision studies of observables in  $pp \rightarrow W \rightarrow l\nu_l$  and  $pp \rightarrow \gamma, Z \rightarrow l^+l^-$  processes at the LHC. *Eur. Phys. J.*, C77(5):280, 2017.
- [69] Doreen Wackerroth and Wolfgang Hollik. Electroweak radiative corrections to resonant charged gauge boson production. *Phys. Rev.*, D55:6788–6818, 1997.
- [70] Stefan Dittmaier and Max Huber. Radiative corrections to the neutral-current Drell-Yan process in the Standard Model and its minimal supersymmetric extension. *JHEP*, 01:060, 2010.
- [71] A. Sirlin. Radiative corrections in the  $SU(2)_L \times U(1)$  theory: A simple renormalization framework. *Phys. Rev. D*, 22:971–981, Aug 1980.
- [72] C. G. Bollini and J. J. Giambiagi. Dimensional renormalization : The number of dimensions as a regularizing parameter. *Il Nuovo Cimento B (1971-1996)*, 12(1):20–26, Nov 1972.
- [73] Joshua Ellis. TikZ-Feynman: Feynman diagrams with TikZ. *Comput. Phys. Commun.*, 210:103–123, 2017.

- [74] G. 't Hooft. Dimensional regularization and the renormalization group. *Nuclear Physics B*, 61:455 – 468, 1973.
- [75] Steven Weinberg. New approach to the renormalization group. *Phys. Rev. D*, 8:3497–3509, Nov 1973.
- [76] Gerard 't Hooft. Renormalizable Lagrangians for Massive Yang-Mills Fields. *Nucl. Phys.*, B35:167–188, 1971.
- [77] N. N. Bogoliubov and O. S. Parasiuk. On the Multiplication of the causal function in the quantum theory of fields. *Acta Math.*, 97:227–266, 1957.
- [78] Klaus Hepp. Proof of the Bogolyubov-Parasiuk theorem on renormalization. *Commun. Math. Phys.*, 2:301–326, 1966.
- [79] W. Zimmermann. Convergence of Bogolyubov's method of renormalization in momentum space. *Commun. Math. Phys.*, 15:208–234, 1969. [Lect. Notes Phys.558,217(2000)].
- [80] Steven Weinberg. *The Quantum theory of fields. Vol. 1: Foundations*. Cambridge University Press, 2005.
- [81] M. Gell-Mann. A schematic model of baryons and mesons. *Physics Letters*, 8(3):214 – 215, 1964.
- [82] G Zweig. An  $SU_3$  model for strong interaction symmetry and its breaking; Version 2. (CERN-TH-412):80 p, Feb 1964. Version 1 is CERN preprint 8182/TH.401, Jan. 17, 1964.
- [83] L D Landau, A A Abrikosov, and I M Khalatnikov. The removal of infinities in quantum electrodynamics. *Collected Papers of L.D. Landau*, page 607610, 1965.
- [84] David J. Gross and Frank Wilczek. Ultraviolet behavior of non-abelian gauge theories. *Phys. Rev. Lett.*, 30:1343–1346, Jun 1973.
- [85] H. David Politzer. Reliable perturbative results for strong interactions? *Phys. Rev. Lett.*, 30:1346–1349, Jun 1973.
- [86] G. Ecker. Chiral perturbation theory. *Prog. Part. Nucl. Phys.*, 35:1–80, 1995.
- [87] Kenneth G. Wilson. Confinement of Quarks. *Phys. Rev.*, D10:2445–2459, 1974. [,45(1974)].

- [88] J. Gasser and H. Leutwyler. Chiral Perturbation Theory to One Loop. *Annals Phys.*, 158:142, 1984.
- [89] Steven Weinberg. Effective chiral Lagrangians for nucleon - pion interactions and nuclear forces. *Nucl. Phys.*, B363:3–18, 1991.
- [90] Christof Gattringer and Christian B. Lang. Quantum chromodynamics on the lattice. *Lect. Notes Phys.*, 788:1–343, 2010.
- [91] H. J. Rothe. Lattice gauge theories: An Introduction. *World Sci. Lect. Notes Phys.*, 43:1–381, 1992. [World Sci. Lect. Notes Phys.82,1(2012)].
- [92] J. Smit. Introduction to quantum fields on a lattice: A robust mate. *Cambridge Lect. Notes Phys.*, 15:1–271, 2002.
- [93] I. Montvay and G. Munster. *Quantum fields on a lattice*. Cambridge University Press, 1997.
- [94] O. V. Tarasov, A. A. Vladimirov, and A. Yu. Zharkov. The Gell-Mann-Low Function of QCD in the Three Loop Approximation. *Phys. Lett.*, B93:429–432, 1980.
- [95] Richard P. Feynman. Very high-energy collisions of hadrons. *Phys. Rev. Lett.*, 23:1415–1417, 1969.
- [96] J. D. Bjorken. Asymptotic Sum Rules at Infinite Momentum. *Phys. Rev.*, 179:1547–1553, 1969.
- [97] N. F. Mott. The scattering of fast electrons by atomic nuclei. *Proceedings of the Royal Society of London. Series A, Containing Papers of a Mathematical and Physical Character*, 124(794):425–442, 1929.
- [98] Curtis G. Callan, Jr. and David J. Gross. High-energy electroproduction and the constitution of the electric current. *Phys. Rev. Lett.*, 22:156–159, 1969.
- [99] Bo Andersson, G. Gustafson, G. Ingelman, and T. Sjostrand. Parton Fragmentation and String Dynamics. *Phys. Rept.*, 97:31–145, 1983.
- [100] Bo Andersson. The Lund model. *Camb. Monogr. Part. Phys. Nucl. Phys. Cosmol.*, 7:1–471, 1997.

- [101] Yuri L. Dokshitzer. Calculation of the Structure Functions for Deep Inelastic Scattering and  $e^+ e^-$  Annihilation by Perturbation Theory in Quantum Chromodynamics. *Sov. Phys. JETP*, 46:641–653, 1977. [Zh. Eksp. Teor. Fiz.73,1216(1977)].
- [102] V. N. Gribov and L. N. Lipatov. Deep inelastic  $e p$  scattering in perturbation theory. *Sov. J. Nucl. Phys.*, 15:438–450, 1972. [Yad. Fiz.15,781(1972)].
- [103] Guido Altarelli and G. Parisi. Asymptotic Freedom in Parton Language. *Nucl. Phys.*, B126:298–318, 1977.
- [104] S. Moch, J. A. M. Vermaseren, and A. Vogt. The Three loop splitting functions in QCD: The Nonsinglet case. *Nucl. Phys.*, B688:101–134, 2004.
- [105] A. Vogt, S. Moch, and J. A. M. Vermaseren. The Three-loop splitting functions in QCD: The Singlet case. *Nucl. Phys.*, B691:129–181, 2004.
- [106] S. Catani, Yuri L. Dokshitzer, M. Olsson, G. Turnock, and B. R. Webber. New clustering algorithm for multi - jet cross-sections in  $e^+ e^-$  annihilation. *Phys. Lett.*, B269:432–438, 1991.
- [107] Yuri L. Dokshitzer, G. D. Leder, S. Moretti, and B. R. Webber. Better jet clustering algorithms. *JHEP*, 08:001, 1997.
- [108] M. Wobisch and T. Wengler. Hadronization corrections to jet cross-sections in deep inelastic scattering. In *Monte Carlo generators for HERA physics. Proceedings, Workshop, Hamburg, Germany, 1998-1999*, pages 270–279, 1998.
- [109] Joshua Isaacson, Hsiang-nan Li, Zhao Li, and C. P. Yuan. Factorization for substructures of boosted Higgs jets. *Phys. Lett.*, B771:619–623, 2017.
- [110] Matteo Cacciari, Gavin P. Salam, and Gregory Soyez. FastJet User Manual. *Eur. Phys. J.*, C72:1896, 2012.
- [111] Jesse Thaler and Ken Van Tilburg. Identifying Boosted Objects with N-subjettiness. *JHEP*, 03:015, 2011.
- [112] David E. Kaplan, Keith Rehermann, Matthew D. Schwartz, and Brock Tweedie. Top Tagging: A Method for Identifying Boosted Hadronically Decaying Top Quarks. *Phys. Rev. Lett.*, 101:142001, 2008.

- [113] Stephen D. Ellis, Christopher K. Vermilion, and Jonathan R. Walsh. Recombination Algorithms and Jet Substructure: Pruning as a Tool for Heavy Particle Searches. *Phys. Rev.*, D81:094023, 2010.
- [114] Andrew J. Larkoski, Simone Marzani, Gregory Soyez, and Jesse Thaler. Soft Drop. *JHEP*, 05:146, 2014.
- [115] R. Brun, F. Bruyant, M. Maire, A. C. McPherson, and P. Zancarini. GEANT3. 1987.
- [116] G Aad and etal. Atlas pixel detector electronics and sensors. *Journal of Instrumentation*, 3(07):P07007, 2008.
- [117] The barrel modules of the ATLAS semiconductor tracker. *Nucl. Instrum. Meth.*, A568:642–671, 2006.
- [118] The ATLAS semiconductor tracker end-cap module. *Nucl. Instrum. Meth.*, A575:353–389, 2007.
- [119] Ahmet Bingul. The atlas trt and its performance at lhc. *Journal of Physics: Conference Series*, 347(1):012025, 2012.
- [120] The ATLAS TRT barrel detector. *JINST*, 3:P02014, 2008.
- [121] The ATLAS TRT end-cap detectors. *JINST*, 3:P10003, 2008.
- [122] G Piacquadio, K Prokofiev, and A Wildauer. Primary vertex reconstruction in the atlas experiment at lhc. *Journal of Physics: Conference Series*, 119(3):032033, 2008.
- [123] V Karimki, M Mannelli, P Siegrist, H Breuker, A Caner, R Castaldi, K Freudenreich, G Hall, R Horisberger, M Huhtinen, and A Cattai. *The CMS tracker system project: Technical Design Report*. Technical Design Report CMS. CERN, Geneva, 1997.
- [124] *The CMS tracker: addendum to the Technical Design Report*. Technical Design Report CMS. CERN, Geneva, 2000.
- [125] The CMS Collaboration. Description and performance of track and primary-vertex reconstruction with the cms tracker. *Journal of Instrumentation*, 9(10):P10009, 2014.
- [126] Serguei Chatrchyan et al. Energy Calibration and Resolution of the CMS Electromagnetic Calorimeter in  $pp$  Collisions at  $\sqrt{s} = 7$  TeV. *JINST*, 8:P09009, 2013. [JINST8,9009(2013)].

- [127] G. Aad and et. al. Readiness of the atlas liquid argon calorimeter for lhc collisions. *The European Physical Journal C*, 70(3):723–753, 2010.
- [128] W. Ralph Nelson, H. Hirayama, and David W. O. Rogers. The Egs4 Code System. 1985.
- [129] S. Abdullin and etal. The cms barrel calorimeter response to particle beams from 2 to 350 gev/c. *The European Physical Journal C*, 60(3):359–373, 2009.
- [130] S. Akhmadaliev et al. Results from a new combined test of an electromagnetic liquid argon calorimeter with a hadronic scintillating-tile calorimeter. *Nuclear Instruments and Methods in Physics Research Section A: Accelerators, Spectrometers, Detectors and Associated Equipment*, 449(3):461 – 477, 2000.
- [131] *ATLAS muon spectrometer: Technical Design Report*. Technical Design Report ATLAS. CERN, Geneva, 1997.
- [132] M Bontenackels. The CMS Muon Spectrometer. Technical Report CMS-CR-2005-020, CERN, Geneva, Sep 2005.
- [133] Georges Aad et al. Performance of  $b$ -Jet Identification in the ATLAS Experiment. *JINST*, 11(04):P04008, 2016.
- [134] D. Buskulic and et. al. A precise measurement of  $zbb/z$ hadrons. *Physics Letters B*, 313(3):535 – 548, 1993.
- [135] G. Aad et al. Expected Performance of the ATLAS Experiment - Detector, Trigger and Physics. 2009.
- [136] Mark Hodgkinson. Missing ET Performance in ATLAS. 2008.
- [137] H. Pi, P. Avery, D. Green, J. Rohlf, and C. Tully. Measurement of missing transverse energy with the cms detector at the lhc. *The European Physical Journal C - Particles and Fields*, 46(1):45–56, 2006.
- [138] John C. Collins, Davison E. Soper, and George F. Sterman. Transverse Momentum Distribution in Drell-Yan Pair and W and Z Boson Production. *Nucl.Phys.*, B250:199, 1985.
- [139] John C. Collins and Davison E. Soper. Angular Distribution of Dileptons in High-Energy Hadron Collisions. *Phys. Rev.*, D16:2219, 1977.

- [140] Toichiro Kinoshita. Mass singularities of feynman amplitudes. *Journal of Mathematical Physics*, 3(4):650–677, 1962.
- [141] T. D. Lee and M. Nauenberg. Degenerate systems and mass singularities. *Phys. Rev.*, 133:B1549–B1562, Mar 1964.
- [142] C. S. Lam and Wu-Ki Tung. A Systematic Approach to Inclusive Lepton Pair Production in Hadronic Collisions. *Phys. Rev.*, D18:2447, 1978.
- [143] C. S. Lam and Wu-Ki Tung. A Parton Model Relation Sans QCD Modifications in Lepton Pair Productions. *Phys. Rev.*, D21:2712, 1980.
- [144] C. S. Lam and Wu-Ki Tung. Structure Function Relations at Large Transverse Momenta in Lepton Pair Production Processes. *Phys. Lett.*, B80:228–231, 1979.
- [145] R. Hamberg, W. L. van Neerven, and T. Matsuura. A complete calculation of the order  $\alpha - s^2$  correction to the Drell-Yan  $K$  factor. *Nucl. Phys.*, B359:343–405, 1991. [Erratum: *Nucl. Phys.*B644,403(2002)].
- [146] T. Gehrmann, E. W. N. Glover, T. Huber, N. Ikizlerli, and C. Studerus. Calculation of the quark and gluon form factors to three loops in QCD. *JHEP*, 06:094, 2010.
- [147] A. Gehrmann-De Ridder, T. Gehrmann, E. W. N. Glover, Alexander Huss, and T. A. Morgan. Z+jet production at NNLO. *PoS*, ICHEP2016:594, 2016.
- [148] Radja Boughezal, Xiaohui Liu, and Frank Petriello. Phenomenology of the Z-boson plus jet process at NNLO. *Phys. Rev.*, D94(7):074015, 2016.
- [149] George F. Sterman. Summation of Large Corrections to Short Distance Hadronic Cross-Sections. *Nucl. Phys.*, B281:310–364, 1987.
- [150] S. Catani and L. Trentadue. Resummation of the QCD Perturbative Series for Hard Processes. *Nucl. Phys.*, B327:323–352, 1989.
- [151] S. Catani and L. Trentadue. Comment on QCD exponentiation at large x. *Nucl. Phys.*, B353:183–186, 1991.
- [152] S. Catani, L. Trentadue, G. Turnock, and B. R. Webber. Resummation of large logarithms in e+ e- event shape distributions. *Nucl. Phys.*, B407:3–42, 1993.



- [153] Edmond L. Berger and Rui-bin Meng. Transverse momentum distributions for heavy quark pairs. *Phys. Rev.*, D49:3248–3260, 1994.
- [154] Stefano Catani, Leandro Cieri, Daniel de Florian, Giancarlo Ferrera, and Massimiliano Grazzini. Universality of transverse-momentum resummation and hard factors at the NNLO. *Nucl. Phys.*, B881:414–443, 2014.
- [155] G. Parisi and R. Petronzio. Small Transverse Momentum Distributions in Hard Processes. *Nucl. Phys.*, B154:427–440, 1979.
- [156] C. T. H. Davies and W. James Stirling. Nonleading Corrections to the Drell-Yan Cross-Section at Small Transverse Momentum. *Nucl. Phys.*, B244:337–348, 1984.
- [157] F. Landry, R. Brock, Pavel M. Nadolsky, and C. P. Yuan. Tevatron Run-1  $Z$  boson data and Collins-Soper-Sterman resummation formalism. *Phys. Rev.*, D67:073016, 2003.
- [158] Anton V. Konychev and Pavel M. Nadolsky. Universality of the Collins-Soper-Sterman nonperturbative function in gauge boson production. *Phys. Lett.*, B633:710–714, 2006.
- [159] Jian-wei Qiu and Xiao-fei Zhang. Role of the nonperturbative input in QCD resummed Drell-Yan  $Q_T$  distributions. *Phys. Rev.*, D63:114011, 2001.
- [160] Gregory P. Korchemsky and George F. Sterman. Nonperturbative corrections in resummed cross-sections. *Nucl. Phys.*, B437:415–432, 1995.
- [161] Jiro Kodaira and Luca Trentadue. Summing soft emission in qcd. *Physics Letters B*, 112(1):66 – 70, 1982.
- [162] S. Catani, E. D’Emilio, and L. Trentadue. The gluon form factor to higher orders: Gluon-gluon annihilation at small qt. *Physics Letters B*, 211(3):335 – 342, 1988.
- [163] Hua Xing Zhu, Chong Sheng Li, Hai Tao Li, Ding Yu Shao, and Li Lin Yang. Transverse-momentum resummation for top-quark pairs at hadron colliders. *Phys. Rev. Lett.*, 110(8):082001, 2013.
- [164] Daniel de Florian and Massimiliano Grazzini. Next-to-next-to-leading logarithmic corrections at small transverse momentum in hadronic collisions. *Phys. Rev. Lett.*, 85:4678–4681, 2000.

- [165] Daniel de Florian and Massimiliano Grazzini. The Structure of large logarithmic corrections at small transverse momentum in hadronic collisions. *Nucl. Phys.*, B616:247–285, 2001.
- [166] Thomas Becher and Matthias Neubert. Drell-Yan Production at Small  $q_T$ , Transverse Parton Distributions and the Collinear Anomaly. *Eur. Phys. J.*, C71:1665, 2011.
- [167] Ye Li and Hua Xing Zhu. Bootstrapping Rapidity Anomalous Dimensions for Transverse-Momentum Resummation. *Phys. Rev. Lett.*, 118(2):022004, 2017.
- [168] Stefano Catani, Leandro Cieri, Daniel de Florian, Giancarlo Ferrera, and Massimiliano Grazzini. Vector boson production at hadron colliders: hard-collinear coefficients at the NNLO. *Eur. Phys. J.*, C72:2195, 2012.
- [169] Stefano Catani, Daniel de Florian, and Massimiliano Grazzini. Universality of non-leading logarithmic contributions in transverse momentum distributions. *Nucl. Phys.*, B596:299–312, 2001.
- [170] F. Landry, R. Brock, G. Ladinsky, and C. P. Yuan. New fits for the nonperturbative parameters in the CSS resummation formalism. *Phys. Rev.*, D63:013004, 2001.
- [171] Peng Sun and Feng Yuan. Energy Evolution for the Sivers Asymmetries in Hard Processes. *Phys. Rev.*, D88:034016, 2013.
- [172] Peng Sun and Feng Yuan. Transverse momentum dependent evolution: Matching semi-inclusive deep inelastic scattering processes to Drell-Yan and W/Z boson production. *Phys. Rev.*, D88(11):114012, 2013.
- [173] Hung-Liang Lai, Marco Guzzi, Joey Huston, Zhao Li, Pavel M. Nadolsky, Jon Pumplin, and C. P. Yuan. New parton distributions for collider physics. *Phys. Rev.*, D82:074024, 2010.
- [174] Jian-wei Qiu and Xiao-fei Zhang. QCD prediction for heavy boson transverse momentum distributions. *Phys. Rev. Lett.*, 86:2724–2727, 2001.
- [175] Peter B. Arnold and Russel P. Kauffman. W and z production at next-to-leading order: From large  $q_T$  to small. *Nuclear Physics B*, 349(2):381 – 413, 1991.
- [176] Csaba Balazs. *Soft gluon effects on electroweak boson production in hadron collisions*. PhD thesis, Michigan State U., 1999.

- [177] Peter Brockway Arnold and Russel P. Kauffman.  $W$  and  $Z$  production at next-to-leading order: From large  $q(t)$  to small. *Nucl. Phys.*, B349:381–413, 1991.
- [178] T. Gleisberg, Stefan. Hoeche, F. Krauss, M. Schonherr, S. Schumann, F. Siegert, and J. Winter. Event generation with SHERPA 1.1. *JHEP*, 02:007, 2009.
- [179] Marco Guzzi, Pavel M. Nadolsky, and Bowen Wang. Nonperturbative contributions to a resummed leptonic angular distribution in inclusive neutral vector boson production. *Phys. Rev.*, D90(1):014030, 2014.
- [180] A. Banfi, S. Redford, M. Vesterinen, P. Waller, and T. R. Wyatt. Optimisation of variables for studying dilepton transverse momentum distributions at hadron colliders. *Eur. Phys. J.*, C71:1600, 2011.
- [181] E. Mirkes. Angular decay distribution of leptons from  $w$ -bosons at nlo in hadronic collisions. *Nuclear Physics B*, 387(1):3 – 85, 1992.
- [182] E. Mirkes and J. Ohnemus. Angular distributions of drell-yan lepton pairs at the fermilab tevatron: Order  $\alpha_s^2$  corrections and monte carlo studies. *Phys. Rev. D*, 51:4891–4904, May 1995.
- [183] E. Mirkes and J. Ohnemus. Polarization effects in Drell-Yan type processes  $h_1 + h_2 \rightarrow j$  ( $W, Z, \gamma^*, J / \psi$ ) +  $x$ . In *The Albuquerque meeting. Proceedings, 8th Meeting, Division of Particles and Fields of the American Physical Society, Albuquerque, USA, August 2-6, 1994. Vol. 1,2*, pages 1721–1723, 1994.
- [184] E. Mirkes and J. Ohnemus.  $W$  and  $Z$  polarization effects in hadronic collisions. *Phys. Rev.*, D50:5692–5703, 1994.
- [185] M. Awramik, M. Czakon, A. Freitas, and G. Weiglein. Precise prediction for the  $W$  boson mass in the standard model. *Phys. Rev.*, D69:053006, 2004.
- [186] A. Freitas, W. Hollik, W. Walter, and G. Weiglein. Complete fermionic two loop results for the  $M(W) - M(Z)$  interdependence. *Phys. Lett.*, B495:338–346, 2000. [Erratum: *Phys. Lett.*B570,no.3-4,265(2003)].
- [187] Ayres Freitas, W. Hollik, W. Walter, and Georg Weiglein. Electroweak two loop corrections to the  $M_W - M_Z$  mass correlation in the standard model. *Nucl. Phys.*, B632:189–218, 2002. [Erratum: *Nucl. Phys.*B666,305(2003)].
- [188] M. Awramik and M. Czakon. Complete two loop electroweak contributions to the muon lifetime in the standard model. *Phys. Lett.*, B568:48–54, 2003.

- [189] M. Awramik and M. Czakon. Complete two loop bosonic contributions to the muon lifetime in the standard model. *Phys. Rev. Lett.*, 89:241801, 2002.
- [190] M. Awramik and M. Czakon. Two loop electroweak bosonic corrections to the muon decay lifetime. *Nucl. Phys. Proc. Suppl.*, 116:238–242, 2003. [238(2002)].
- [191] A. Onishchenko and O. Veretin. Two loop bosonic electroweak corrections to the muon lifetime and  $M(Z) - M(W)$  interdependence. *Phys. Lett.*, B551:111–114, 2003.
- [192] M. Awramik, M. Czakon, A. Onishchenko, and O. Veretin. Bosonic corrections to  $\Delta r$  at the two loop level. *Phys. Rev.*, D68:053004, 2003.
- [193] L. Avdeev, J. Fleischer, S. Mikhailov, and O. Tarasov.  $\mathcal{O}(\alpha\alpha_s^2)$  correction to the electroweak  $\rho$  parameter. *Phys. Lett.*, B336:560–566, 1994. [Erratum: *Phys. Lett.*B349,597(1995)].
- [194] K. G. Chetyrkin, Johann H. Kuhn, and M. Steinhauser. Corrections of order  $\mathcal{O}(G_F M_t^2 \alpha_s^2)$  to the  $\rho$  parameter. *Phys. Lett.*, B351:331–338, 1995.
- [195] K. G. Chetyrkin, Johann H. Kuhn, and M. Steinhauser. QCD corrections from top quark to relations between electroweak parameters to order  $\alpha_s^2$ . *Phys. Rev. Lett.*, 75:3394–3397, 1995.
- [196] K. G. Chetyrkin, Johann H. Kuhn, and M. Steinhauser. Three loop polarization function and  $\mathcal{O}(\alpha_s^2)$  corrections to the production of heavy quarks. *Nucl. Phys.*, B482:213–240, 1996.
- [197] Y. Schroder and M. Steinhauser. Four-loop singlet contribution to the rho parameter. *Phys. Lett.*, B622:124–130, 2005.
- [198] K. G. Chetyrkin, M. Faisst, Johann H. Kuhn, P. Maierhofer, and Christian Sturm. Four-Loop QCD Corrections to the Rho Parameter. *Phys. Rev. Lett.*, 97:102003, 2006.
- [199] R. Boughezal and M. Czakon. Single scale tadpoles and  $\mathcal{O}(G_F m(t)^2 \alpha_s^3)$  corrections to the rho parameter. *Nucl. Phys.*, B755:221–238, 2006.
- [200] Georges Aad et al. Measurement of the Higgs boson mass from the  $H \rightarrow \gamma\gamma$  and  $H \rightarrow ZZ^* \rightarrow 4\ell$  channels with the ATLAS detector using  $25 \text{ fb}^{-1}$  of  $pp$  collision data. *Phys. Rev.*, D90(5):052004, 2014.

- [201] CMS Collaboration. Precise determination of the mass of the Higgs boson and studies of the compatibility of its couplings with the standard model. 2014.
- [202] K. Agashe et al. Working Group Report: Top Quark. In *Proceedings, 2013 Community Summer Study on the Future of U.S. Particle Physics: Snowmass on the Mississippi (CSS2013): Minneapolis, MN, USA, July 29-August 6, 2013*, 2013.
- [203] V. Buge, C. Jung, G. Quast, A. Ghezzi, M. Malberti, and T. Tabarelli de Fatis. Prospects for the precision measurement of the W mass with the CMS detector at the LHC. *J. Phys.*, G34:N193–N220, 2007.
- [204] Nathalie Besson, Maarten Boonekamp, Esben Klinkby, Sascha Mehlhase, and Troels Petersen. Re-evaluation of the LHC potential for the measurement of  $M_W$ . *Eur. Phys. J.*, C57:627–651, 2008.
- [205] Giuseppe Bozzi, Luca Citelli, and Alessandro Vicini. Parton density function uncertainties on the W boson mass measurement from the lepton transverse momentum distribution. *Phys. Rev.*, D91(11):113005, 2015.
- [206] J. Pumplin, D. Stump, R. Brock, D. Casey, J. Huston, J. Kalk, H. L. Lai, and W. K. Tung. Uncertainties of predictions from parton distribution functions. 2. The Hessian method. *Phys. Rev.*, D65:014013, 2001.
- [207] Andrea Banfi, Mrinal Dasgupta, and Yazid Delenda. Azimuthal decorrelations between QCD jets at all orders. *Phys. Lett.*, B665:86–91, 2008.
- [208] A. H. Mueller, Bo-Wen Xiao, and Feng Yuan. Sudakov double logarithms resummation in hard processes in the small-x saturation formalism. *Phys. Rev.*, D88(11):114010, 2013.
- [209] Peng Sun, C. P. Yuan, and Feng Yuan. Soft Gluon Resummations in Dijet Azimuthal Angular Correlations in Hadronic Collisions. *Phys. Rev. Lett.*, 113(23):232001, 2014.
- [210] V. Ravindran, J. Smith, and W. L. Van Neerven. Next-to-leading order QCD corrections to differential distributions of Higgs boson production in hadron hadron collisions. *Nucl. Phys.*, B634:247–290, 2002.
- [211] Christopher J. Glosser and Carl R. Schmidt. Next-to-leading corrections to the Higgs boson transverse momentum spectrum in gluon fusion. *JHEP*, 12:016, 2002.
- [212] Carl R. Schmidt.  $H \rightarrow g g g$  ( $g q$  anti- $q$ ) at two loops in the large  $M(t)$  limit. *Phys. Lett.*, B413:391–395, 1997.

- [213] Asmita Mukherjee and Werner Vogelsang. Jet production in (un)polarized pp collisions: dependence on jet algorithm. *Phys. Rev.*, D86:094009, 2012.
- [214] Peng Sun, C. P. Yuan, and Feng Yuan. Transverse Momentum Resummation for Dijet Correlation in Hadronic Collisions. *Phys. Rev.*, D92(9):094007, 2015.
- [215] L. A. Harland-Lang, A. D. Martin, P. Motylinski, and R. S. Thorne. Parton distributions in the LHC era: MMHT 2014 PDFs. *Eur. Phys. J.*, C75(5):204, 2015.
- [216] Gavin Cullen et al. GOSAM-2.0: a tool for automated one-loop calculations within the Standard Model and beyond. *Eur. Phys. J.*, C74(8):3001, 2014.
- [217] Gavin Cullen, Nicolas Greiner, Gudrun Heinrich, Gionata Luisoni, Pierpaolo Mastrolia, Giovanni Ossola, Thomas Reiter, and Francesco Tramontano. Automated One-Loop Calculations with GoSam. *Eur. Phys. J.*, C72:1889, 2012.
- [218] Keith Hamilton, Paolo Nason, and Giulia Zanderighi. MINLO: Multi-Scale Improved NLO. *JHEP*, 10:155, 2012.
- [219] Radja Boughezal, Christfried Focke, Xiaohui Liu, and Frank Petriello.  $W$ -boson production in association with a jet at next-to-next-to-leading order in perturbative QCD. *Phys. Rev. Lett.*, 115(6):062002, 2015.
- [220] Jeppe R. Andersen and Jennifer M. Smillie. Constructing All-Order Corrections to Multi-Jet Rates. *JHEP*, 01:039, 2010.
- [221] Jeppe R. Andersen and Jennifer M. Smillie. The Factorisation of the  $t$ -channel Pole in Quark-Gluon Scattering. *Phys. Rev.*, D81:114021, 2010.
- [222] Jeppe R. Andersen and Jennifer M. Smillie. Multiple Jets at the LHC with High Energy Jets. *JHEP*, 06:010, 2011.
- [223] Jeppe R. Andersen and Chris D. White. A New Framework for Multijet Predictions and its application to Higgs Boson production at the LHC. *Phys. Rev.*, D78:051501, 2008.
- [224] Jeppe R. Andersen, Vittorio Del Duca, and Chris D. White. Higgs Boson Production in Association with Multiple Hard Jets. *JHEP*, 02:015, 2009.
- [225] Johannes Bellm et al. Herwig 7.0/Herwig++ 3.0 release note. *Eur. Phys. J.*, C76(4):196, 2016.

- [226] J. Alwall, R. Frederix, S. Frixione, V. Hirschi, F. Maltoni, O. Mattelaer, H. S. Shao, T. Stelzer, P. Torrielli, and M. Zaro. The automated computation of tree-level and next-to-leading order differential cross sections, and their matching to parton shower simulations. *JHEP*, 07:079, 2014.
- [227] John M. Campbell, R. Keith Ellis, Rikkert Frederix, Paolo Nason, Carlo Oleari, and Ciaran Williams. NLO Higgs Boson Production Plus One and Two Jets Using the POWHEG BOX, MadGraph4 and MCFM. *JHEP*, 07:092, 2012.
- [228] Iain W. Stewart, Frank J. Tackmann, Jonathan R. Walsh, and Saba Zuberi. Jet  $p_T$  resummation in Higgs production at  $NNLL' + NNLO$ . *Phys. Rev.*, D89(5):054001, 2014.
- [229] Stefan Hche, Ye Li, and Stefan Prestel. Drell-Yan lepton pair production at NNLO QCD with parton showers. *Phys. Rev.*, D91(7):074015, 2015.
- [230] Stefan Hche, Ye Li, and Stefan Prestel. Higgs-boson production through gluon fusion at NNLO QCD with parton showers. *Phys. Rev.*, D90(5):054011, 2014.
- [231] Andrea Banfi, Mrinal Dasgupta, Kamel Khelifa-Kerfa, and Simone Marzani. Non-global logarithms and jet algorithms in high- $p_T$  jet shapes. *JHEP*, 08:064, 2010.
- [232] Andrew Hornig, Christopher Lee, Iain W. Stewart, Jonathan R. Walsh, and Saba Zuberi. Non-global Structure of the  $O(\alpha_s^2)$  Dijet Soft Function. *JHEP*, 08:054, 2011.
- [233] R. B. Appleby and M. H. Seymour. Nonglobal logarithms in interjet energy flow with kt clustering requirement. *JHEP*, 12:063, 2002.
- [234] Andrzej J. Buras and Peter H. Weisz. QCD Nonleading Corrections to Weak Decays in Dimensional Regularization and 't Hooft-Veltman Schemes. *Nucl. Phys.*, B333:66–99, 1990.
- [235] S. A. Larin. The Renormalization of the axial anomaly in dimensional regularization. *Phys. Lett.*, B303:113–118, 1993.
- [236] Daniel F. Litim and Jan M. Pawłowski. On general axial gauges for QCD. *Nucl. Phys. Proc. Suppl.*, 74:329–332, 1999.
- [237] T. van Ritbergen, J. A. M. Vermaseren, and S. A. Larin. The Four loop beta function in quantum chromodynamics. *Phys. Lett.*, B400:379–384, 1997.

- [238] M. Czakon. The Four-loop QCD beta-function and anomalous dimensions. *Nucl. Phys.*, B710:485–498, 2005.
- [239] Stefan Weinzierl. The Art of computing loop integrals. In *Universality and renormalization: From stochastic evolution to renormalization of quantum fields. Proceedings, Workshop on 'Percolation, SLE and related topics', Toronto, Canada, September 20-24, 2005, and Workshop on 'Renormalization and universality in mathematical physics', Toronto, Canada, October 18-22, 2005*, pages 345–395, 2006.
- [240] R. Keith Ellis, Zoltan Kunszt, Kirill Melnikov, and Giulia Zanderighi. One-loop calculations in quantum field theory: from Feynman diagrams to unitarity cuts. *Phys. Rept.*, 518:141–250, 2012.
- [241] Johannes M. Henn. Lectures on differential equations for Feynman integrals. *J. Phys.*, A48:153001, 2015.
- [242] Andrea Signori, Alessandro Bacchetta, Marco Radici, and Gunar Schnell. Investigations into the flavor dependence of partonic transverse momentum. *JHEP*, 11:194, 2013.
- [243] C. A. Aidala, B. Field, L. P. Gamberg, and T. C. Rogers. Limits on transverse momentum dependent evolution from semi-inclusive deep inelastic scattering at moderate  $Q$ . *Phys. Rev.*, D89(9):094002, 2014.
- [244] M. Anselmino, M. Boglione, J. O. Gonzalez Hernandez, S. Melis, and A. Prokudin. Unpolarised Transverse Momentum Dependent Distribution and Fragmentation Functions from SIDIS Multiplicities. *JHEP*, 04:005, 2014.
- [245] Daniel de Florian, Rodolfo Sassot, and Marco Stratmann. Global analysis of fragmentation functions for pions and kaons and their uncertainties. *Phys. Rev.*, D75:114010, 2007.
- [246] Daniel de Florian, R. Sassot, Manuel Epele, Roger J. Hernandez-Pinto, and Marco Stratmann. Parton-to-Pion Fragmentation Reloaded. *Phys. Rev.*, D91(1):014035, 2015.